Physik

Interface-Driven Modulation of Ultrafast Charge-Carrier Dynamics in Graphene/Ferromagnetic Metal-Organic Heterostructures

Dissertation

Eva Sophia Walther

Mai 2025

Rheinland-Pfälzische
Technische Universität
Kaiserslautern
Landau

Interface-Driven Modulation of Ultrafast Charge-Carrier Dynamics in Graphene/Ferromagnetic Metal-Organic Heterostructures

Dissertation

Eva Sophia Walther

Vom Fachbereich Physik der Rheinland-Pfälzischen Technischen Universität Kaiserslautern-Landau
zur Verleihung des akademischen Grades “Doktor der Naturwissenschaften” genemigte Dissertation

Betreuer: **Prof. Dr. Benjamin Stadtmüller**
Zweitgutachter: **Prof. Dr. Martin Aeschlimann**

Datum der wissenschaftlichen Aussprache: 2025-05-30
DE - 386

Abstract

Graphene's extraordinary electronic and spin transport properties make it a promising material for future technologies, yet its intrinsic lack of a band gap and weak spin-orbit coupling pose significant challenges.

This dissertation investigates how engineered interfaces can overcome these limitations and actively modulate ultrafast charge-carrier dynamics in graphene-based heterostructures.

Specifically, I study graphene on ferromagnetic Ni(111) and two derived hybrids: one with an **intercalated monolayer of lead (Pb)** between graphene and Ni, and another with a **layer of organic molecules (coronene)** coupled via a graphene buffer to Ni. Using **time- and angle-resolved photoemission spectroscopy (Tr-ARPES)**, I directly observe how these different interface configurations influence electronic structure and femtosecond carrier dynamics.

In the graphene/Nickel system, strong hybridisation with the Nickel substrate obliterates graphene's Dirac cone. By contrast, intercalating Pb under graphene is shown to restore graphene's Dirac band structure and open a $\sim 300\,\mathrm{meV}$ band gap at the Dirac point. This is one of the largest proximity-induced gaps reported in graphene, effectively transforming it into a **quasi-semiconductor** while it remains adjacent to a ferromagnetic substrate. Time-resolved measurements indicate that **optical excitation can transiently perturb the gapped Dirac bands**, highlighting the potential for all-optical tuning of graphene's electronic structure in such heterostructures.

Concurrently, I examine the **ultrafast demagnetisation dynamics of the Nickel substrate** through its exchange-split band structure. I find that capping Nickel with graphene accelerates the demagnetisation (from $\sim 170\,\mathrm{fs}$ to $\sim 120\,\mathrm{fs}$), consistent with a graphene-mediated spin flux away from the metal. Strikingly, the Nickel film demagnetises an order of magnitude faster (down to $\sim 50\,\mathrm{fs}$) when the graphene/Nickel interface includes an intercalated Pb layer. This **ultra-rapid magnetic quench** – accompanied by a complete collapse of Ni's spin polarisation – is attributed to the heavy metal layer acting as an efficient spin sink, siphoning spin-polarised electrons out of Nickel and facilitating spin scattering via Pb's strong spin-orbit coupling. However, the presence of Pb also prolongs the magnetisation recovery, reflecting a trade-off between the speed and reversibility of magnetic switching. These findings underscore how interface engineering (e.g., adding atomic layers of heavy elements) can drastically manipulate spin dynamics, in agreement with super-diffusive spin transport models.

The third part of the study focuses on a **graphene/metal–organic heterostructure**: coronene molecules adsorbed on graphene/Ni. Here, graphene serves as a one-atom-thick interlayer that electronically decouples the molecules from the metal substrate. Static photoemission confirms that the graphene buffer preserves the molecular orbital features of coronene close to its free-standing form, which would otherwise be energetically shifted by direct metal contact.

Upon optical excitation, I observe an ultrafast injection of electrons from the Ni/graphene substrate into the unoccupied molecular orbitals of coronene. Notably, a transient population appears in the area of coronene's lowest unoccupied molecular orbital (LUMO), and a lower-energy feature is detected that is consistent with a long-lived excited state in the coronene or at the graphene–coronene interface. These excited molecular-state populations persist for hundreds of femtoseconds, outliving the initial hot electron decay in the graphene/Nickel substrate. Furthermore, at delays of one to a few picoseconds, a secondary rise in the molecular signal is observed, suggesting subsequent charge redistribution or a delayed excitation mechanism within the interface. The time-resolved spectral shifts (including a transient lowering of the graphene/Nickel Fermi level) indicate that photoexcitation drives a charge transfer from the metal into the molecule, momentarily altering the interfacial band alignment. My results provide a direct, momentum-resolved view of charge transfer and excited-state dynamics in a graphene-protected organic layer, demonstrating the feasibility of using graphene to mediate and control ultrafast electronic processes at a metal–molecule junction.

Together, these studies illustrate that the ultrafast behaviour of graphene – whether it be electronic band structure responses or spin and charge transfer processes – can be profoundly tuned by interface design. By introducing targeted interlayers (heavy metals or 2D materials), one can impart

new functionalities to graphene: a sizeable band gap with strong spin-orbit coupling, enhanced or accelerated spin flow, or efficient photo-carrier injection into molecular orbitals. These findings have broad implications. For spintronics, the graphene/Pb/Nickel results suggest a pathway to ultrafast magnetic switches and spin-current generators that leverage heavy-element proximity effects. For optoelectronics and photochemistry, the graphene/coronene results highlight how graphene can serve as a transparent conduit for charges and potentially preserve long-lived excited states at a normally quenching interface.

More generally, this work showcases time-resolved ARPES as a powerful technique to capture microscopic dynamics in complex materials and supports the paradigm that by engineering interfaces – "where the action happens" – one can direct and control materials' behaviour on the fundamental timescale of electronic and spin motions.

AI-Involvement

The entire text of this dissertation was corrected for style, spelling, and grammar, and partly for translations, using the AI-supported software DeepL and ChatGPT. More detailed information can be found in the Appendix, Section B.1.

Kurzzusammenfassung

Diese Dissertation untersucht, wie sich gezielt entwickelte Grenzflächen nutzen lassen, um bestehende Einschränkungen zu überwinden und die ultraschnelle Ladungsträgerdynamik in graphene-basierten Heterostrukturen aktiv zu steuern.

Graphen besitzt außergewöhnliche elektronische und spinabhängige Transporteigenschaften und gilt daher als vielversprechendes Material für zukünftige Technologien. Das intrinsische Fehlen einer Bandlücke am Dirac-Punkt sowie die schwache Spin-Bahn-Kopplung stellen jedoch erhebliche Herausforderungen dar. In dieser Arbeit untersuche ich Graphen auf ferromagnetischem Ni(111) sowie zwei daraus abgeleitete Hybridsysteme: ein System mit einer **interkalierten Monolage aus Blei (Pb)** zwischen Graphen und Ni und ein weiteres mit einer **Schicht organischer Moleküle (Coronen)**, die über einen Graphenpuffer an Ni gekoppelt ist. Mithilfe von **zeit- und winkelaufgelöster Photoemissionsspektroskopie (Tr-ARPES)** beobachte ich direkt, wie diese verschiedenen Grenzflächenkonfigurationen die elektronische Struktur und die Dynamik der Ladungsträger im Femtosekundenbereich beeinflussen.

Im Graphen/Ni-System führt die starke Hybridisierung mit dem Substrat zur vollständigen Aufhebung des Dirac-Kegels von Graphen. Demgegenüber zeigt sich, dass die Interkalation von Pb unterhalb von Graphen die Dirac-Bandstruktur wiederherstellt und eine Bandlücke von etwa $\sim 300\,\mathrm{meV}$ am Dirac-Punkt öffnet. Diese zählt zu den größten bislang beobachteten, induzierten Bandlücken in Graphen und verwandelt es effektiv in einen **Quasi-Halbleiter**, obwohl es weiterhin in direktem Kontakt zu einem ferromagnetischen Substrat steht. Zeitaufgelöste Messungen zeigen, dass **optische Anregung die durch eine Bandlücke getrennten Dirac-Bänder vorübergehend beeinflussen kann**, was das Potenzial einer rein optischen Kontrolle der elektronischen Struktur in solchen Heterostrukturen unterstreicht.

Parallel dazu untersuche ich die **ultraschnelle Demagnetisierungsdynamik des Ni-Substrats** anhand seiner austauschgespaltenen Bandstruktur. Die Ergebnisse zeigen, dass eine Graphen-Bedeckung die Demagnetisierung beschleunigt (von $\sim 170\,\mathrm{fs}$ auf $\sim 120\,\mathrm{fs}$), was auf einen durch Graphen vermittelten Spintransport in das Metall hindeutet. Auffällig ist, dass der Ni-Film eine Größenordnung schneller demagnetisiert (bis zu $\sim 50\,\mathrm{fs}$), wenn eine interkalierte Pb-Schicht in die Graphen/Ni-Grenzfläche eingebracht wird. Diese **ultraschnelle Demagnetisierung** – verbunden mit einem vollständigen Zusammenbruch der Spinpolarisation – wird auf die Schwermetallschicht zurückgeführt, die als effiziente Spinsenke wirkt. Abgeleitete spinpolarisierte Elektronen erfahren durch die starke Spin-Bahn-Kopplung von Pb intensive Spinstreuung, was eine starke Spin-Durchmischung ermöglicht und zudem die Remagnetisierungszeit verlängert. Für technische Anwendungen bedeutet dies einen Konflikt zwischen e.g. optisch induzierter Magnetisierungsschaltung und der Reversibilität bzw. "Tod-Zeit" des Systems. Die Ergebnisse dieser Untersuchungen belegen, dass gezieltes Grenzflächendesign – etwa durch Einbringen schwerer Elemente – die Spindynamik wesentlich beeinflussen kann (im Einklang mit theoretischen Modellen zum superdiffusiven Spintransports).

Im dritten Teil der Arbeit steht eine **Graphen/Metall–organische Heterostruktur** im Fokus: Coronen-Moleküle, adsorbiert auf Graphen/Ni. Graphen fungiert hierbei als einatomige Zwischenschicht, welche die Moleküle elektronisch vom Metallsubstrat entkoppelt. Statische Photoemissionsdaten zeigen, dass die molekularen Orbitalstrukturen von Coronen durch die Graphen-Zwischenschicht nahezu in ihrer freistehenden Form erhalten bleiben, während direkter Kontakt zu Nickel diese durch Hybridisierung energetisch stark verschieben würde.
Nach optischer Anregung beobachte ich eine ultraschnelle Injektion von Elektronen aus dem Ni/Graphen-Substrat in die unbesetzten molekularen Orbitale von Coronen. Besonders hervorzuheben ist das Auftreten einer transienten Besetzung im Bereich des niedrigsten unbesetzten Molekülorbitals (LUMO) die einem langlebigen angeregten Zustandes im Coronene oder an der Graphen-Coronen-Schnittstelle zugeordnet werden könnte. Diese angeregten molekularen Zustände bleiben über mehrere Hundert Femtosekunden bestehen und überdauern den Zerfall der heißen Elektronen im Graphen/Ni-Substrat. Darüber hinaus zeigt sich im Bereich von ein bis wenigen Pikosekunden ein sekundärer Anstieg des molekularen Signals, was auf eine spätere Ladungsumverteilung oder eine verzögerte Anregungsdynamik a der Grenzschicht hinweist. Die zudem beobachteten spektralen Verschiebun-

gen – einschließlich einer transienten Absenkung des Fermi-Niveaus von Graphen/Ni – deuten auf einen durch Photoanregung induzierten Ladungstransfer vom Metall zum Molekül hin, der die Bandausrichtung an der Grenzfläche vorübergehend beeinflusst. Meine Ergebnisse liefern eine direkte, impulsaufgelöste Darstellung des Ladungstransfers und der Dynamik angeregter Zustände in einer durch Graphen "geschützten" organischen Schicht und belegen die Möglichkeit, Graphen zur Steuerung ultraschneller elektronischer Prozesse an Metall–Molekül-Grenzflächen einzusetzen.

Insgesamt zeigen diese Studien, dass das ultraschnelle Verhalten von Graphen – sowohl hinsichtlich seiner elektronischen Bandstruktur, als auch bezüglich Spin- und Ladungstransportprozessen – durch gezielte Gestaltung von Grenzflächen maßgeblich beeinflusst werden kann. Durch das Einbringen spezifischer Zwischenschichten (etwa aus Schwermetallen oder 2D-Materialien) lassen sich neue Funktionalitäten in Graphen realisieren: eine ausgeprägte Bandlücke mit starker Spin-Bahn-Kopplung, beschleunigter Spintransport oder effiziente Injektion Licht-induzierter Ladungsträger in molekulare Zustände. Diese Erkenntnisse haben weiterreichende Bedeutung: Für die Spintronik eröffnen die Ergebnisse zum Graphen/Pb/Ni-System Perspektiven für ultraschnelle magnetische Schalter und Spinstromquellen, die Proximitätseffekte schwerer Elemente nutzen. Für Optoelektronik und Photochemie zeigen die Resultate der Graphen/Coronen-Heterostruktur, wie Graphen als transparente Leitungsschicht fungieren und angeregte Zustände an einer Grenzfläche stabilisieren kann.

Allgemein demonstriert diese Arbeit das Potenzial zeit- und winkel aufgelöster Photoelektronen Spektroskopie als leistungsstarke Methode zur Untersuchung mikroskopischer Dynamiken in komplexen Materialien und unterstützt das Paradigma, dass sich durch gezieltes Design von Grenzflächen das Materialverhalten auf der fundamentalen Zeitskala elektronischer und spinabhängiger Prozesse steuern lässt.

KI-Unterstützung

Der gesamte Text in dieser Dissertation wurde mit hilfe der KI-basierten Software ChatGPT und DeepL, stylistisch, gramatikalisch und bezüglich Rechtschreibung optimiert. Genauere Informationen befinden sich in Sektion B.1 im Anhang.

Contents

1.Introduction

Modern electronics have been driven for decades by the pursuit of faster operation speeds, further miniaturisation, and greater data storage densities. Historically, these advances often came at the cost of higher power consumption and heat dissipation, with energy efficiency and sustainability only secondary considerations. It has become clear that continued progress must confront fundamental limitations in materials and energy usage. Thus, a shift is underway toward new materials and device concepts that can deliver improved performance without exacerbating resource constraints or environmental impact. In this context, fields like spintronics and quantum computing have emerged as promising paradigms to complement or even replace conventional silicon-based electronics, aiming to utilise electron spin or quantum coherence for processing information with potentially lower dissipation. Crucially, the performance of such novel devices often hinges on the properties of **interfaces** between different materials. As Herbert Kroemer famously stated, "**the interface is the device**" [1], and this maxim remains true today [1, 2]: the atomic-scale coupling at an interface can govern charge and spin transport, energy dissipation, and functionality in ways that bulk properties alone cannot. Developing next-generation electronics and spintronics therefore requires both discovering new materials and mastering interface engineering.

1.1. Graphene - a material with endless possibilities

One material that has attracted enormous interest in this quest is **graphene** – a two-dimensional monolayer of carbon atoms in a honeycomb lattice (see Figure 1.1). The utilization of carbon-based nanomaterials like graphene is appealing from both a technological and an environmental standpoint. Carbon is earth-abundant and recyclable, and graphene itself exhibits a combination of exceptional properties that are rare in traditional materials.

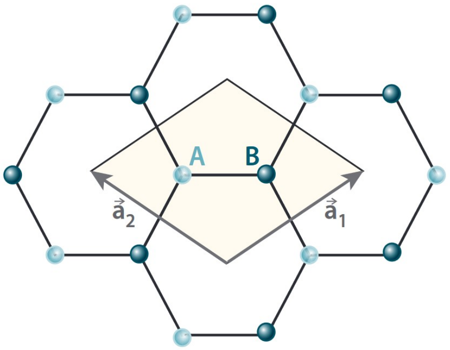

Figure (1.1) Atomic structure of graphene: The unit cell of graphene is spanned by two lattice vectors with a length of $a_{1,2} = 2.46\,\text{Å}$ and an angle of $\theta = 60°$ between them. It includes two atoms, located at (0, 0) and (1=3, 1=3) [3]. Figure used with permission of Annual Reviews, Inc., from [4]; permission conveyed through Copyright Clearance Centre, Inc.

For example, charge carriers in graphene behave as massless Dirac fermions, yielding ultra-high room-temperature mobilities on the order of $2.5 \times 10^5\,\frac{\text{cm}}{\text{V}^2\,\text{s}}$ [5] (in comparison, Cu has ~43 $\frac{\text{cm}}{\text{V}^2\,\text{s}}$ - 50 $\frac{\text{cm}}{\text{V}^2\,\text{s}}$ [1]). Each atom-thin layer absorbs about 2.3 % of incident white light. Although this is remarkably high, it is endowing graphene with ~ 97.8 % optical transparency [6]. Its in-plane thermal conductivity (3000 $\frac{\text{W m}}{\text{K}}$ - 5000 $\frac{\text{W m}}{\text{K}}$) far exceeds that of copper (20 times) [7, 8], and its mechanical strength (tensile strength 130 GPa [7], Young's modulus 1 TPa [9]) rivals the best known materials [5, 9]. These outstanding electrical, optical, and mechanical properties, combined with the atomic thickness and flexibility of graphene, make it a candidate for a wide range of applications. Proposed uses span from transparent electrodes in displays and solar cells to high-frequency transistors, ultra-capacitors, and spin-logic devices. Indeed, graphene's high charge carrier mobility and stability suggest it could play a major role in future interconnects and transistors as silicon technology approaches its limits

---

[1] the still very high conductivity results from its high electron density.

[10]. Furthermore, the ability to support ballistic transport and spin-polarised currents in graphene has drawn interest for integrating it into spintronic circuits.

However, integrating graphene into practical device architectures also poses significant challenges. Foremost among these is the fact that pristine graphene is a zero-band gap semimetal. The π and π^* bands in free-standing graphene meet at the Dirac points (K/K$'$ points of the Brillouin zone) with linear dispersion and no energy gap, depicted in Figure 1.2.

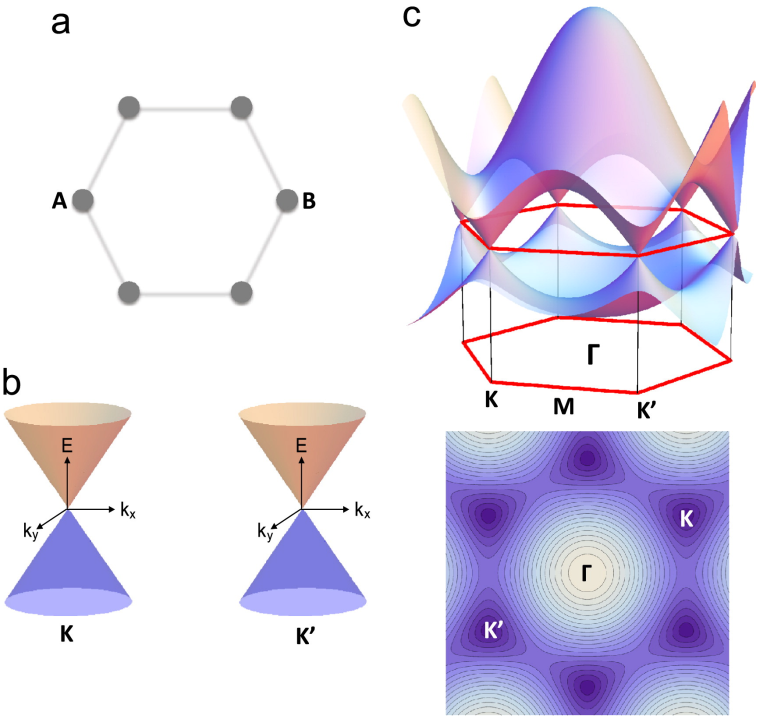

Figure (1.2) Electronic structure of graphene: (a) the honeycomb lattice structure of graphene with the two inequivalent sites A and B occupied by carbon atoms, (b) the exact energy degeneracy at the K and K' points of the Brillouin zone guarantees a linear energy-momentum dispersion (the massless spectrum of the Dirac cone) near the two inequivalent valleys, (c) the full electronic dispersion of the π-bands in the graphene Brillouin zone, showing the trigonal warping effects away from the K- and K'-points and the saddle point singularity at the M-point. The equivalent-energy contour lines of the conduction band are also displayed. The figure is used with permission of PERGAMON, from [11]; permission conveyed through Copyright Clearance Centre, Inc.

While this band structure underlies graphene's remarkable carrier mobility and allows phenomena like the half-integer quantum Hall effect and Klein tunnelling (unimpeded transmission of electrons through potential barriers) [12], the lack of an energy gap prevents a clear "on-off" switching behaviour required for logic transistors and many optoelectronic applications. In essence, graphene cannot be turned "off" which leads to leakage currents in transistor channels. Creating a band gap in graphene *without* degrading its other desirable properties has therefore been a central theme in graphene research. Numerous strategies have been explored, such as constraining graphene laterally in narrow nano-ribbons or quantum dots (to induce quantum confinement gaps), stacking graphene in bilayers and breaking inversion symmetry with an external field, chemically functionalise the lattice (e.g. partial hydrogenation), or exploiting substrate interactions to break the sublattice symmetry. Each approach has met with limited success: for instance, patterning graphene into nanostructures can open gaps but at the cost of edge disorder and scattering, whereas chemical modifications or certain substrates perturb the Dirac cone but often introduce defects or only small gaps on the order of a few tens of meV.

Graphene on interfaces - benefits and challenges

A particularly promising route is to interface graphene with other materials in ways that tailor its band structure through proximity effects. In this regard, the choice of substrate or interfacing layer is crucial.

Graphene on metals is a prototypical example: **graphene/metal** interfaces can dramatically alter graphene's electronic structure depending on the interaction strength. On inert, lattice-mismatched substrates such as Ir(111), Au(111) or Pt(111), graphene is bound weakly by van-der-Waals forces. It retains an almost pristine linear dispersion (the Dirac cone), albeit usually with some charge transfer (doping) and minor distortions such as small band gaps or warping due to Moiré superlattices [3, 13]. On the other hand, on certain transition-metal surfaces that form strong covalent bonds to carbon (so-called "chemisorption" interaction), graphene's π orbitals hybridise with metal d-states, and its band structure is radically changed.

An important case is **graphene on Ni(111)**, a ferromagnetic metal with a nearly perfect lattice match to graphene. Epitaxial growth of monolayer graphene on Ni(111) is straightforward and yields large, high-quality films, which is advantageous for device fabrication. But due to strong C–Ni bonding, the Dirac point of graphene on Ni(111) is shifted about 2.7 eV below the Fermi level (shown in Figure 1.3) and the bands lose their linear dispersion, becoming parabolic near E_F as they mix with Ni states [14, 15]. In essence, pristine graphene's semi-metallic character is quenched on Ni(111), a potentially negative outcome.

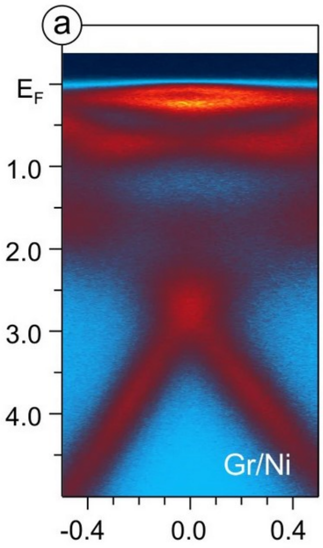

Figure (1.3) The sequence of ARPES data for graphene on Ni(111). The figure is used with permission of Nature Publishing Group, from [15]; permission conveyed through Copyright Clearance Centre, Inc.

On the positive side, this intimate contact with a ferromagnet endows graphene with **magnetic** properties: a partial spin polarisation is induced in graphene's π band due to exchange coupling with Ni [16, 17]. X-ray magnetic circular dichroism (XMCD) and spin-resolved photoemission studies have shown that the carbon atoms in graphene/Ni(111) acquire a magnetic moments of their own, effectively making the graphene layer an "extension" of the Ni substrate's magnetic moment.

The graphene layer also mediates interesting interface effects such as an inversion of the Ni surface spin polarisation and the emergence of a short-lived image-potential-derived interface state that can serve as a source of spin-polarised electrons [18, 19]. These properties suggest graphene/Ni interfaces could be useful as spin filters or spin injectors.

The trade-off, however, is that the strong hybridisation which induces magnetism also destroys graphene's massless carrier dispersion and high mobility. The very phenomenon (Klein tunnelling suppression) that confers high mobility in free-standing graphene is eliminated when the sublattice symmetry is broken by a strongly interacting substrate [3]. This exemplifies a common situation in materials science: **the need to balance competing interactions to achieve optimal functionality.** In the graphene/Ni case, we gain magnetic functionality but lose the superior electronic properties.

Heavy-metal intercalation as a means to take the best of both worlds

To **combine the best of both worlds** – preserving graphene's extraordinary band structure while still reaping benefits of a chosen substrate (be it magnetism or other functionality) – one effective strategy is to introduce an ultrathin spacer layer between graphene and the substrate. This approach is known as **intercalation** when done after graphene growth (inserting atoms underneath the graphene), or one can directly grow graphene on a pre-deposited interlayer. The idea is to **de-**

couple graphene from detrimental substrate interactions, restoring its Dirac cone, while using the intercalant to impart new properties (such as enhanced spin-orbit coupling or modified magnetism). Prior studies have demonstrated the feasibility of this approach. For example, intercalating a monolayer of gold between graphene and Ni(111) recovers a nearly free-standing graphene band structure (Dirac point at E_F with linear dispersions, Figure 1.4) and induces a strong Rashba-type spin splitting of the graphene bands due to the high atomic number of Au [20]. Notably, in that case no sizeable band gap was opened at the Dirac point, since the induced spin-orbit coupling (SOC) primarily manifested as band splitting rather than a gap.

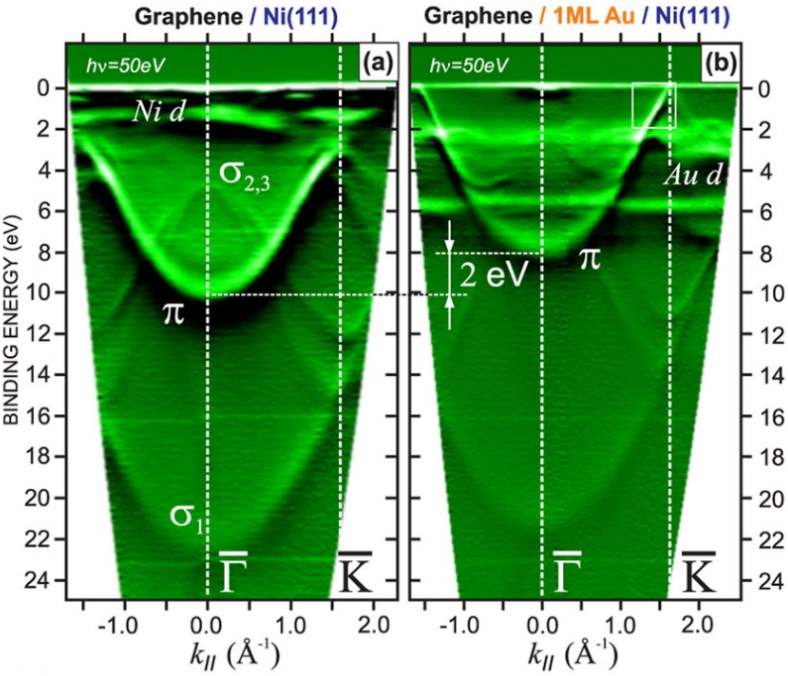

Figure (1.4) Electronic structure of graphene on Ni(111) before and after 1ML Au intercalation leading to a 2eV shift and a band gab closing at the K-Point. Reprinted with permission from [14]. Copyright 2008 by the American Physical Society.

More generally, intercalation of various metals (Au, Cu, Al, etc.) under graphene on metals yields chemical decoupling (graphene's v_F and linear bands are restored) but often leaves the Dirac cone gapless or only weakly perturbed [13]. Moreover, if the intercalant is a simple metal without magnetism, it might also "cut off" or dampen the direct exchange coupling between graphene and a ferromagnetic substrate, thus removing the induced magnetic moment in graphene [13]. This presents a dilemma: **inserting a decoupling layer can re-establish graphene's superior electronic traits, but one might lose the very spintronic functionality (proximity magnetism) that was sought by using a ferromagnetic substrate.**

To overcome this, researchers have started exploring **intercalation with heavy elements or compound layers** that can provide additional functionalities. One avenue is to leverage elements with strong SOC to induce a band gap in graphene via the **proximity spin-orbit effect**. Theory by Kane and Mele predicted that if graphene's weak intrinsic SOC (on the order of 10×10^{-5} eV [21]) were enhanced, graphene could support a quantum spin Hall phase — a topological insulator with an SOC-induced gap and spin-polarised edge states [22]. While intrinsic graphene is topologically trivial (gapless), the introduction of an SOC gap of even a few tens of meV could drastically change its transport properties, introducing spin-momentum locking and opening the door to dissipationless spin currents.

Heavy adatoms or under-layers (such as Pb, Bi, W, etc.) are prime candidates to boost graphene's SOC.

Experimentally, **graphene/heavy metal interfaces** have shown intriguing results: Intercalating Pb under graphene on Pt(111) reportedly opened a ~200 meV band gap at the Dirac point, accompanied by emergent topological surface-state features, suggesting a transition toward a 2D topological

insulator state [23]. (Note: This interpretation has been debated, and alternative studies argued the observed gap might be due to a structural distortion rather than a pure SOC effect [24].) Intercalation of a Bi–Au alloy under graphene/Ni was found to produce a strong spin splitting of the Dirac bands (hundreds of meV Rashba-type splitting) without opening a gap [25], whereas intercalation of Eu (which oxidise to EuO) under graphene/Ni induced a spin-selective gap of order $\sim$100 meV due to exchange splitting from the magnetic EuO layer [26].
These studies highlight that by choosing different intercalant materials, one can prioritise certain effects: **a non-magnetic heavy metal emphasises SOC-induced phenomena, while a magnetic insulator emphasises exchange coupling — both can modify graphene's Dirac bands in useful ways.**

In this work, I focus on using lead (Pb) as an intercalation layer for graphene on Ni(111). Lead is a heavy element (high atomic number $Z = 82$) providing strong spin-orbit interaction, but it is non-magnetic (Pb is a $6p$ metal with negligible magnetic moment). This combination makes Pb an intriguing choice: it can potentially open a sizeable SOC gap in graphene, yet its presence at the interface with Ni might also influence magnetism by acting as a spacer or **spin sink**. Prior to this thesis, it was known that Pb intercalation can induce large SOC effects in graphene [27]. For example, Pb islands under graphene were observed to cause local enhancements of SOC leading to quasi-Landau level formations without external magnetic fields (due to the giant Rashba effect at island edges). Theoretical work also suggested that Pb chemically bonds to graphene and could turn it into a semiconductor with a moderate band gap [28]. But this finding might not be accurate in the light of the findings of C. Schott [29], describing the graphene layer as "free floating" after Pb intercalation.

Open questions remained regarding a continuous Pb monolayer under graphene: Would it indeed open a significant Band gap on a ferromagnetic substrate? If so, what is the nature of this gap (pure SOC-driven vs. sublattice symmetry breaking)? And how would such a system behave under ultrafast optical excitation? These questions are at the heart of Chapter 3 of this thesis.

Ultrafast spin-dynamics in graphene-heavy-metal-ferromagnet interfaces - a way to high-speed demagnetisation?

Another major thrust of this thesis concerns ultrafast spin dynamics at graphene/ferromagnet interfaces. Since the landmark discovery by Beaurepaire *et al.* (1996) that ferromagnetic metals can demagnetise on sub-picosecond timescales upon laser excitation, a great deal of effort has gone into understanding the mechanisms of ultrafast demagnetisation. One mechanism involves the flow of spin-polarised electrons out of the ferromagnet, carrying angular momentum with them (often termed super-diffusive spin transport or spin currents) [30]. If a ferromagnet is adjacent to a material that can accept and quickly dissipate these spin currents (for instance, a heavy metal layer with strong spin-orbit scattering), the demagnetisation of the ferromagnet can be markedly accelerated.
This has been demonstrated experimentally: for example, Ni films capped with a heavy metal like Au show faster demagnetisation than bare Ni, as the Au layer absorbs spin-polarised electrons emitted from Ni and randomise their spins after a certain time [31]. In the context of graphene/Ni interfaces, an interesting scenario arises. Graphene is only one atom thick and has negligible spin-orbit coupling itself, so one might expect it to be a nearly transparent membrane for spin flows. Indeed, graphene's high conductivity and low atomic number imply that it can transmit spin-polarised electrons ballistically. Recent studies have hinted that the presence of a graphene monolayer can modify the demagnetisation behaviour of Ni, consistent with a partial spin current into the graphene layer on femtosecond timescales. Additionally, if a heavy layer like Pb is intercalated, it could dramatically enhance spin dissipation at the interface by providing strong spin-flip scattering.
The combined graphene/Pb sandwich on Ni is thus hypothesized to act as a composite spin sink, where graphene shuttles spins into the Pb, and Pb's SOC dissipates them. How this manifests in the time domain, in the ultrafast demagnetisation kinetics of Ni, had not been experimentally explored before.

Chapter 4 of this thesis addresses this gap by comparing the demagnetisation dynamics of pristine Ni(111), graphene-covered Ni(111), and Pb-intercalated graphene/Ni(111)

using time-resolved photoemission measurements of the Ni $3d$ band exchange splitting.

Beyond inorganic interfaces: hybrid organic–inorganic heterostructures

Organic molecular semiconductors are attractive for applications in flexible electronics, photovoltaics, and spintronics, but their performance when interfaced with metals is often compromised by strong chemisorption and charge transfer at the metal surface.
A single layer of graphene can function as an atomic-scale buffer layer: it binds to metal surfaces on one side, while presenting a relatively inert face on the other side for molecule adsorption. The molecule then experiences a mostly van-der-Waals interaction with graphene, rather than directly bonding to the metal, which helps preserve the molecule's intrinsic electronic structure (molecular orbital alignment, band gap, etc.) [32]. Meanwhile, graphene's conductivity can still electronically connect the molecule and metal, enabling charge transfer but in a controlled fashion. This kind of structure—molecule on graphene on metal—has become a model system for studying charge and energy transfer across hybrid interfaces. For instance, ultrafast spectroscopy on graphene-coated metal surfaces with adsorbed molecules has revealed that photo-excited electrons can transfer from the substrate, through graphene, into the molecular layer on a sub-picosecond timescale [33]. Moreover, the presence of the graphene spacer can introduce new dynamics: in some graphene/semiconductor heterostructures, electrons and holes excited in different layers form interfacial excitons or become trapped in separate layers, leading to lifetimes of the separated charges on the order of picoseconds [34]. Such long-lived charge-separated states would normally be unexpected for a molecule directly on a metal (where an excited electron in the molecule would rapidly decay into the metal within tens of femtoseconds). Graphene thus not only shields the molecule from chemical interactions with the metal, but also potentially provides an electronic decoupling that can sustain excited-state species longer, which is advantageous for photo-conversion and possibly for spintronic applications if spin-polarised carriers can be maintained.

In this thesis, Chapter 5 focuses on a model hybrid system consisting of a Ni(111) surface, a monolayer graphene buffer, and an adsorbed polycyclic aromatic hydrocarbon molecule (coronene). The goal is to elucidate how ultrafast photo-induced charge transfer occurs from the metal/graphene substrate into the molecular layer, and whether graphene enables any unique intermediate states or prolonged carrier lifetimes that could be harnessed in future devices.

1.2. Research objectives

From the above background, it is evident that **interface-driven effects** in graphene-based heterostructures are critical to both fundamental science and potential applications in ultrafast electronics and spintronics. The present work is motivated by several open questions in this area, which we address with the technique of time- and angle-resolved photoemission spectroscopy (TR-ARPES) combined with static surface-sensitive methods. In particular, the key objectives of this PhD project are as follows:

Band gap engineering in graphene via intercalation:

Can intercalating a heavy element into the graphene/Ni(111) interface restore graphene's Dirac band structure and open a substantial band gap at the Dirac point?
I aim to create a graphene/ferromagnet heterostructure that retains graphene's high Fermi velocity and linear bands while inducing a gap large enough to be technologically relevant. Lead (Pb) was chosen as the intercalant. A related question is the mechanism of any observed gap: is it driven by enhanced spin-orbit coupling (potentially leading to a topological state) or by symmetry breaking (a "trivial" gap)? Furthermore, I seek to determine whether such a proximity-induced gap can be dynamically modulated. In other words:
If a band gap is present in graphene/Pb/Ni, how does it respond to ultrafast optical excitation?
Understanding the transient behaviour of the Dirac gap under non-equilibrium conditions is important for evaluating the prospects of high-speed optical or electrical switching in graphene-based devices.

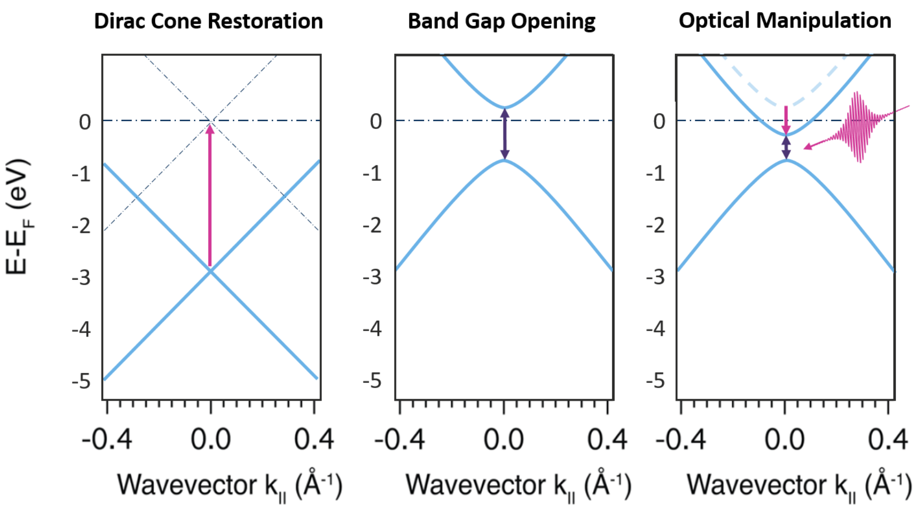

Figure (1.5) Research Objective - Band gap Engineering in Graphene: From restoring the Dirac Cone back to E_F over the introduction of a band gap to the optical manipulation of the gap.

Ultrafast magnetisation dynamics at graphene–ferromagnet interfaces

How does the presence of graphene, and an intercalated heavy metal layer, influence the femtosecond demagnetisation of a ferromagnetic substrate?
I address this by comparing Ni(111) in three scenarios: a clean Ni surface (from literature), a Ni surface covered by one layer of graphene, and a Ni surface with graphene and an intercalated Pb layer. By monitoring the time-dependent collapse and recovery of Ni's spin-split band structure (exchange splitting) after an ultrafast laser excitation, I can infer the relative efficiency of spin-angular-momentum dissipation in each case. This study tests whether graphene can act as a conduit for spin currents (thereby moderately accelerating demagnetisation via spin transport into graphene) and whether adding Pb provides an even more efficient spin dissipation channel (via spin-orbit scattering). The ultimate objective is to discern how interface engineering at the atomic scale can control magnetic relaxation processes, which is of great relevance for the design of high-speed spintronic devices (e.g. magnetic memory elements) with tailored switching dynamics.

Light-induced charge transfer in a graphene-buffered metal–organic interface

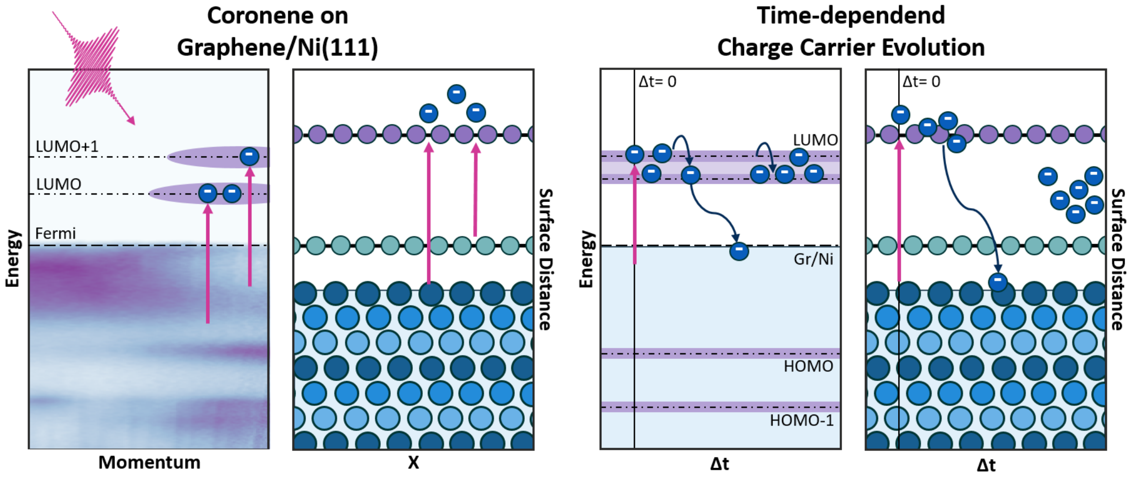

Figure (1.6) Research Objective: Light induced charge carrier injection from the graphene/Ni interface into a molecular system and their time-resolved evolution.

Can a graphene monolayer facilitate the injection of photo-excited charge carriers from

a metal into an adsorbed molecular semiconductor, and what are the ultrafast dynamics of such charge-transfer processes?
I investigate this question using coronene molecules on graphene/Ni(111) as a model system, illustrated in Figure 1.6. The goals are to determine whether the graphene buffer layer enables population of the molecule's formerly unoccupied orbitals (in essence, creating a transient negative charging of the molecule) upon excitation of the substrate, and to characterise the lifetime and decay pathways of these induced populations. Of particular interest is the emergence of any long-lived excited state, such as an interfacial or interlayer states trapped by momentum mismatch, which could signify a partial separation of charge across the interface. Insights from this study will improve the understanding of energy and charge flow in hybrid nanostructures and could inform strategies for optimising charge separation in molecular electronics or organic spintronics.

Summary

In summary, this dissertation is driven by the overarching vision of
understanding and controlling electronic and spin-dependent phenomena at graphene interfaces on ultrafast timescales.
By focusing on the specific objectives above, the work connects fundamental concepts—such as band topology, spin currents, and excitonic coupling—to practical considerations for future devices. All experiments were performed using ultrahigh vacuum surface science techniques. In particular, time-resolved ARPES (utilise femtosecond extreme-UV pulses as probes) is a central tool in this thesis, as it allows direct mapping of the evolving band structure and occupancy of electronic states after photoexcitation. This approach provides a window into transient states of matter that cannot be accessed by steady-state measurements alone, thereby shedding light on the dynamic interplay between electrons, spins, and lattice at complex interfaces.

1.3. Outline of the thesis

Chapter 2: Methods: From Sample preparation to presented results describes the experimental setup and analytical methodologies, including the sample preparation, the generation of ultrafast pump and probe pulses and the operation of the time-resolved ARPES apparatus. The analytical methods employed throughout this work are the focus of this chapter. A detailed introduction in the handling of time- and angle- resolved data will be given, accompanied by diagrams and code examples, detailing the complex data analysis routines.

Chapter 3: Lead intercalated graphene on the nickel(111) surface - a material system for the future? presents a study of lead-intercalated graphene on Ni(111). I demonstrate that intercalating a monolayer of Pb between graphene and Ni(111) effectively decouples the graphene from the metal, restoring a high-quality Dirac cone electronic structure. Notably, a band gap of hundreds of meV is opened at the Dirac point (at E_D). This result shows that heavy atom intercalation can overcome graphene's gaplessness while largely preserving its band dispersion – an important proof-of-concept for graphene-based electronics. In the second part of Chapter 3, I explore the ultrafast dynamics of the gapped Dirac cone using TR-ARPES. I find that optical excitation (with an 1.58 eV pump pulse) leads to a transient modulation of the Dirac gap: specifically, the gap size is partially reduced on a sub-picosecond timescale. While the graphene layer remains intact and no permanent damage occurs, the observation of a transient band gap renormalization indicates that the electronic structure of graphene/Pb/Ni can be actively tuned by light. I discuss potential mechanisms for this effect and suggest how such ultrafast control of a band gap could be leveraged in opto-spintronic device concepts.

Chapter 4: Modulation of nickel magnetisation dynamics at the graphene/Ni and graphene/Pb/Ni interface investigates ultrafast magnetisation dynamics at Ni(111) interfaces by comparing three cases: a clean Ni(111) surface (from literature), a graphene-covered Ni(111), and a graphene/Pb/Ni(111) tri-layer (with Pb intercalated). Using time- and angle-resolved photoemission to track the exchange-split Ni 3d bands (in particular, the spin splitting of the Ni minority and majority d-band peaks near E_F), I quantify the demagnetisation time τ_M and the maximum reduction in spin polarisation for each sample upon femtosecond laser excitation. I find that graphene on Ni slightly accelerates the demagnetisation of Ni compared to the bare surface. This is consistent with a scenario in which excited spin-polarised electrons can flow into the graphene layer, causing a modest increase in the demagnetisation rate by carrying angular momentum away from the Ni layer (a form of super-diffusive spin transport across the interface). The effect is not dramatic, but it suggests that even a one-atom-thick carbon layer can partake in ultrafast spin currents. Strikingly, for the Pb-intercalated interface (Ni/Pb/Gr), I observe a much more rapid and extensive demagnetisation. The Ni exchange splitting collapses almost completely within tens of femtoseconds of excitation—about three times faster as in Ni/Gr—and the subsequent recovery of magnetisation is also modified. I interpret this behaviour as evidence that the intercalated Pb monolayer acts as an efficient sink for spin angular momentum. My experimental findings align well with theoretical predictions of spin super-diffusion [30] and with earlier element-specific studies (e.g. X-ray probing of Ni/Au interfaces [31]) that showed enhanced demagnetisation in the presence of heavy metal contacts. This study underscores the principle that by engineering the interface (in this case adding two different layers to Ni), one can widely tune the spin relaxation behaviour of a ferromagnet on ultrafast timescales.

Chapter 5: Light driven charge carrier injection from graphene/Ni interface into organic molecular systems turns to the graphene-buffered metal–organic interface of coronene on Ni(111). First, the static electronic structure of coronene adsorbed directly on Ni(111) is compared to that with a graphene interlayer. On bare Ni, coronene molecules chemisorp strongly. In contrast, with a monolayer of graphene between coronene and Ni, coronene retains sharp molecular orbital features close to its gas-phase frontier orbital energies, confirming that graphene effectively decouples the molecule from the metal substrate and prevents strong hybridisation. Building on this, the chapter then presents time-resolved measurements of the coronene/Gr/Ni sample following optical excitation. By using a photon energy below the HOMO-to-LUMO-transition, predominantly electrons in the metal substrate (Ni and graphene) are excited and I aim to observe how they populate the unoccupied states of the adsorbed coronene layer via the graphene spacer. The Tr-ARPES data reveal a two-step dynamics: an initial ultrafast injection of electrons into the coronene LUMO (within ∼100 fs after excitation), followed by a secondary, much longer-lived population of the LUMO that persists for several hundred femtoseconds to a few picoseconds. I interpret the prompt LUMO population as direct evidence of charge transfer from the Ni/graphene substrate into the molecular orbital, analogous to observations in other molecule-on-graphene systems [33]. The subsequent long-lived component is an unexpected but crucial observation. I propose a plausible mechanisms to explain the LUMO population's longevity:
A momentum-space bottleneck, wherein the electron in the coronene LUMO cannot easily scatter into the substrate because of momentum mismatch or lack of available empty states at the same energy in the Ni/graphene bands. Graphene's presence can impose additional momentum filtering (due to its two-dimensional band structure and the requirement for conservation at the interface), meaning the electron might be trapped in the molecular layer until it can find a decay pathway that satisfies both energy and momentum conservation. Analogous phenomena have been reported in other van-der-Waals heterostructures, such as WS_2/graphene, where interlayer excitons have lifetimes on the order of 1 ps due to momentum mismatch between the layers' band extrema [34]. The findings illustrate how incorporating a single graphene layer can fundamentally alter charge-transfer dynamics at a molecule–metal interface, creating opportunities to harvest or manipulate excited charges before they thermalise or being screened. Such insights are valuable for the design of graphene-based molecular electronics, where one might, for example, exploit long-lived charge separation for photodetectors or use the spin-character of such interfacial excitons in future organic spintronic devices.

Chapter 6: Conclusion and outlook Finally, Chapter 6 summarises the main findings of the thesis and provides an outlook on possible future research directions. Key results from the three study areas are synthesised to highlight the overarching themes: the critical role of interfaces in enabling or limiting material functionalities, and the power of ultrafast measurements to reveal microscopic processes in complex heterostructures.
I discuss remaining open questions – such as the exact nature (topological or trivial) of the induced band gap in graphene/Pb/Ni, the potential to generalise the spin sink effect with other heavy elements or to tune it with layer thickness, and the prospect of exploiting interfacial excitons in graphene-mediated systems.
I also suggest possible next steps, for instance, spin-resolved photoemission to directly measure spin effects in the graphene layer, or exploring different molecular systems on graphene to see how universal the observed long-lived charge separation is, and further investigate its origin.

Through these studies, the thesis contributes to a deeper fundamental understanding of ultrafast phenomena at surfaces and interfaces, and paves the way toward tailoring interface properties for advanced functional devices in the realms of electronics, spintronics, and photonics.

The work remains grounded in an experimental physics approach. In essence, the chapters that follow will show how a single layer of carbon atoms — when combined with careful interface engineering and examined with ultrafast spectroscopy — can yield rich physics, from the opening of new energy gaps to the quenching of magnetism and the mediation of novel excited states. Each of these findings underscores the enduring truth of Kroemer's adage:
It is at interfaces where materials can be profoundly transformed, and where future device innovations are likely to emerge.

2. Methods: From Sample Preparation to Presented Results

Introduction

The goal of this chapter is to provide a concise yet comprehensive overview of all experimental and analytical methods employed to generate and interpret the data presented in this thesis. I begin by detailing the ultra-high vacuum sample preparation protocols — cleaning of Ni(111) single crystals, chemical-vapour deposition of graphene, intercalation of lead monolayers, and vapour deposition of coronene — as well as the surface-structure verification by low-energy electron diffraction (LEED). Next, I describe the angle-resolved photoemission spectroscopy (ARPES) and time-resolved ARPES setups used for all measurements: the electron analyser and detector configuration, the light sources (He-discharge lamp and high-harmonic generation driven by an ultrafast laser), and the pump-probe scheme that yields femtosecond time resolution. As many of the techniques are well established within the surface science community, only a concise description is given here, more detailed information can be found elsewhere (Surface science: [35, 36]; Photoemission: [37]; Chemical Vapour Deposition: [38]).
Finally, I outline my data-analysis framework, implemented in MATLAB, which encompasses raw-data handling, normalisation (total-counts and flat-field corrections), stitching of angular sweeps, momentum space transformations, and both static and time-resolved spectral fitting routines.
Together, these methods form a robust workflow that takes photoemission spectra from raw-data all the way to the extraction of quantitative parameters — band gaps, exchange splitting, electron temperatures, and transient carrier dynamics — on the fundamental timescale of electronic and spin motions.

The explanatory experimental results presented have partly been taken with contributions of several colleagues, whose support I gratefully acknowledge.
Firstly, LEED images of the sample systems used: Measurements from the graphene/Pb/nickel(111) and the coronene/graphene/nickel(111) sample system have been taken from [29], all others were taken and analysed by myself. For the crystal high axes orientation comparison, low-energy electron diffraction images of graphene/nickel(111) from a measurement campaign at the ELI-ALPS nanoscale electron spectroscopy for chemical analysis (nanoESCA) end-station were used, here the sample preparation was supported by Martin Mitkov and Alexander Schmid, and the data acquisition by Martin Mitkov, Gyula Halasi, Nikolett Olah, Csaba Vass and Alexander Schmid. For the exemplary shown time-resolved measurements, I kindly refer to the beginning of the experimental chapters where detailed work distribution is explained.

2.1. Sample preparation

The ARPES techniques used here are highly surface-sensitive measurements that require ultra-high vacuum (ultra-high vacuum, vacuum enviroment with extremely low pressure below 1×10^{-9} mbar (UHV)) conditions to prevent contamination and molecular adsorption. Ensuring a clean sample surface is particularly critical for reactive surfaces such as nickel(111) as used in this thesis. The following sections detail the cleaning procedures, the preparation of two-dimensional graphene layers, the intercalation of Pb atoms, and the vapour deposition of coronene. LEED was employed to verify the sample structure and quality in comparison to previous work by our group. For a more detailed description and detailed geometrical analysis of the sample systems, see [29].

2.1.1. Creating a pristine Ni(111) surface

The Ni(111) single crystal was cleaned by repeated cycles of sputtering with focused Ar^+ ions (energy ranging from 1.0 keV to 2.5 keV) at an Ar pressure of 2.5 mbar for durations between 20 min and 60 min, followed by annealing at approximately 750 °C for 20 min - 120 min under UHV conditions. Typically, the process begins with a cycle of "hot-sputtering" (sputtering at elevated sample temperatures). The complete procedure generally yields an atomically flat, contamination-free surface.

However, due to the high solubility of carbon in Ni(111), residual carbon remains. For graphene growth, this residual carbon acts as condensation centres, thereby assisting in the formation of a large single-domain graphene sheet. Figure 2.1 shows the LEED images taken after sample cleaning.

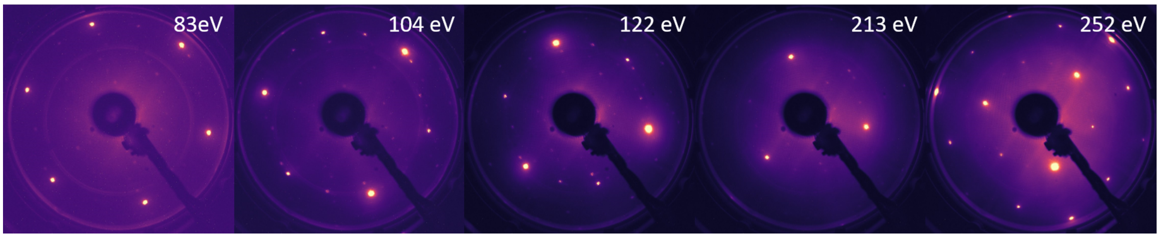

Figure (2.1) LEED images of the pristine Ni(111) surface. In addition to the clear Ni(111) spots, residual carbon contamination is visible. The images were acquired at electron beam energies of 83 eV, 104 eV, 122 eV, 213 eV and 252 eV.

2.1.2. Growing one ML graphene on a nickel(111) crystal

Graphene was synthesised via chemical vapour deposition (CVD) on the cleaned Ni(111) surface. The crystal was heated to 750 °C and exposed to ethylene (C_2H_4) at a pressure between 2.6×10^{-6} mbar - 3.5×10^{-6} mbar for 120 min, followed by a 15-minute post-annealing at the same temperature. To accelerate cooling and protect the heating stage, a constant airflow of 1.1 bar was applied at the UHV-sample manipulator cooling system. Preliminary assessment of the sample quality was carried out using low-energy electron diffraction, and the results are displayed in Figure 2.2. The low-energy electron diffraction pattern of the graphene monolayer on nickel(111) (graphene/Ni(111)) system closely mirrors that of pure Ni(111) resulting from the minimal lattice mismatch and commensurate structure. The only observable difference is an intensity modulation with varying electron beam energies (beforehand Ni(111) shows a clear 3-fold symmetry), indicative of the additional graphene layer. A high-quality film shows no extra spots or modulations that might suggest bilayer growth or rotational domains. Methods to further check the sample quality if needed, e.g. by using X-ray photoelectron spectroscopy (XPS), are explained in [29].

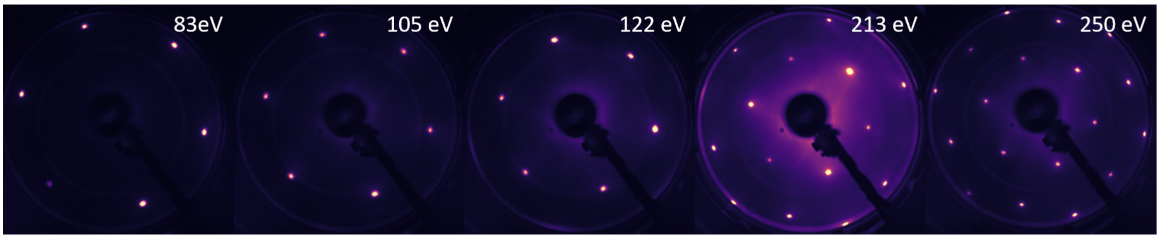

Figure (2.2) LEED images of the graphene/Ni(111) surface. A clear six-fold symmetry, typical for graphene is visible. The graphene spots coincide with the Ni(111) spots. Therefore no additional spots are visible. It is noteworthy to mention here, that the residual carbon clusters from the Ni(111) surface were condensation centres for the graphene-sheet formation, therefore these spots are no longer visible. The images were taken at 83eV, 104eV, 122eV, 213eV and 252eV electron beam energy.

2.1.3. Lead intercalation

Pb atoms were intercalated into the graphene/Ni(111) system (graphene/Ni(111)) by evaporating Pb onto the sample maintained at approximately 220 °C. This process was repeated until sufficient Pb coverage was achieved. After each evaporation step (lasting between 5 min and 10 min), the sample was post-annealed at temperatures between 250 °C and 550 °C to facilitate intercalation and remove residual Pb atoms. The intercalation was confirmed by LEED (see Figure 2.3) and corroborated by complementary techniques such as scanning tunneling microscopy (STM), normal incidence X-ray standing wave and XPS, in previous studies within our group [29].

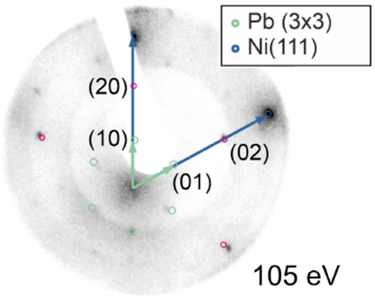

Figure (2.3) LEED images of the lead intercalated graphene ML on nickel(111) (graphene/Pb/Ni(111)) surface. The image was taken at 105eV and shows the determined superstructure vectors. Reprinted with kind permission of the author from [29].

2.1.4. Evaporation of coronene on graphene/Ni(111)

To evaluate graphene's role as a buffer layer between a ferromagnet and an organic molecular film, coronene was evaporated onto the graphene/Ni(111) sample. This deposition was carried out in two steps using a Knudsen-type evaporator at 155 °C. In the first step, the evaporation lasted 6 min and 30 s, and in the second step, 1 min and 20 s. The resulting coronene film was characterised using LEED. Figure 2.4 shows representative LEED patterns for the coronene/graphene/Ni(111) interface.

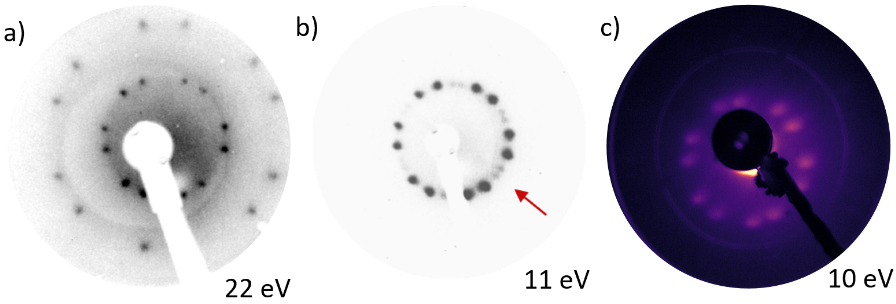

Figure (2.4) Different coronene/graphene/Ni(111) LEED patterns. (a) shows a LEED image of a sub-Mono Layer (ML) coronene/graphene/Ni(111) sample at 22eV. In (b) the same sample system at 11eV is depicted but with a visible coronen multilayer. The 2nd layer spots are marked with a red arrow. The LEED pattern at 10eV of sample used in this thesis is shown in (c). A clearly ordered coronen layer is visible but no 2nd layer sports. Image (a) and (b) were reprinted with kind permission of the author from [29].

Image (a) demonstrates an optimised layered system, while (b) shows a multilayer coronene preparation. These images, reprinted from [29], result from extensive sample preparation and analysis. In comparison, image (c) represents the sample used in the time-resolved experiments of this thesis, exhibiting a well-ordered LEED pattern with no second-layer peaks, which indicates nearly full monolayer coronene coverage. Despite the suboptimal quality of the LEED image itself, the measurement confirmed high sample quality, as further evidenced by subsequent ARPES data. Samples that met the quality criteria, as determined by LEED, were then transferred under UHV conditions to the analysis chamber for further characterisation and measurements.

2.2. Measurement setup

2.2.1. The angle-resolved photoemission spectroscopy setup

The majority of the data presented in this thesis were obtained using an angle-resolved photoemission spectroscopy setup at the **RPTU Kaiserslautern-Landau in Kaiserslautern** in the group of **Prof. Martin Aeschlimann**. The instrument and its peripherals were assembled under the coordination of Johannes Stöckl. Detailed descriptions of the setup can be found in the dissertation of Johannes Stöckl [39] and the diploma thesis of Anatol Jurenkow [40]. This section is based on the work of Johannes Stöckl and the SPECS user manual.

The electron detector used is the PHOIBOS 150 from SPECS GmbH, a hemispherical electron analyser that separates electrons entering the entrance slit by their momentum and energy. It was operated in **fixed analyser transmission (FAT)** mode. By adjusting the electrons' kinetic energy with electron optics preceding the hemisphere, the pass energy — and thereby the energy resolution — remains constant while obtaining a spectral scan over all desired energies. The electron distribution is measured by an micro channel plate (MCP)-enhanced CCD detector or, alternatively, with spin resolution using the FERRUM spin-filter from FOCUS GmbH (the spin-filter was not used in this dissertation). A schematic of the analyser setup is shown in Figure 2.5.

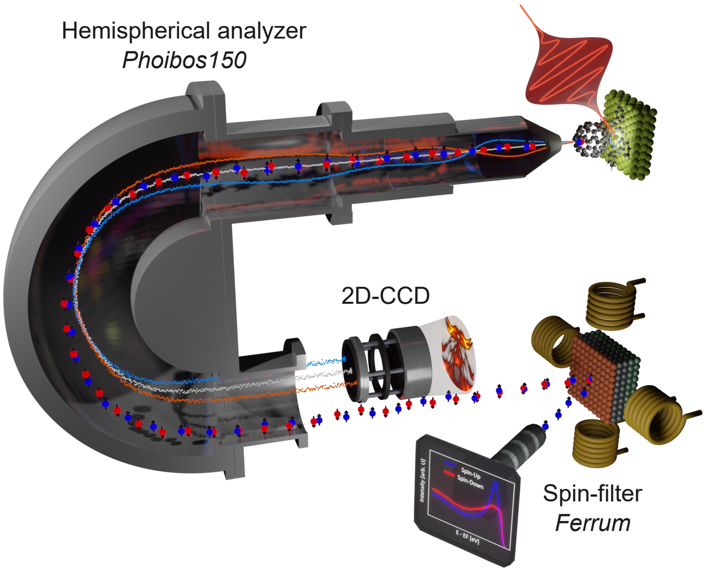

Figure (2.5) Schematic of the detector system of the spin- and angle-resolved photoelectron spectroscopy (S-ARPES) setup. Reprinted with kind permission of the author from [41].

The setup was mainly operated in the **wide angle mode (WAD)**, which provides an angular acceptance of $\alpha = 26°$ and an angular resolution of $\Delta\alpha = 0.3°$. The energy resolution was experimentally determined to be $\Delta E_{analyser} = 23\,\text{meV}$ using an entrance slit size of $S_{entry} = 0.5\,\text{mm}$ and a pass energy of $E_{pass} = 10\,\text{eV}$ [39]. For other settings, the energy resolution can be estimated by

$$\Delta E_{analyser} = E_{pass} \frac{S_{entry} + S_{exit}}{4D_{analyser}} \tag{2.1}$$

were $D_{analyser} = 150\,\text{cm}$ is the radius of the hemisphere and S_{exit} the exit slit. During the time-resolved HHG data acquisition pass-energies of 48.20 eV, 64.27 eV and 74.98 eV were used resulting in energy resolutions of 0.08 eV, 0.11 eV and 0.12 eV. For the setup as used here S_{exit} can be neglected, since the single channels of the MCP are the respective exit slits and in comparison to the entrance slit are multiple orders of magnitude smaller.

As is customary for ARPES instruments, accessing the full k-space requires precise sample positioning relative to the detector. The setup is equipped with a six-axis manipulator that allows translation in x, y, and z, as well as rotations in polar, azimuth, and tilt angles, with a positional accuracy of 10 µm and an angular precision of 0.05°. The electron momentum component parallel to the surface is determined by the sample's exit angle and can be calculated as

$$k_{||} = \hbar^{-1}\sqrt{2m_e E_{kin}} \cdot \sin(\theta). \tag{2.2}$$

The setup is connected to multiple light sources used during this thesis were:

1) The VUV lamp lamp (VUV5000 from SCIENTA OMICRON) is a helium discharge lamp optimised to emit the HeI_α and $HeII_\alpha$ lines. Specifically, $\lambda_{He2} = 30.56\,\text{nm}$ corresponds to a photon energy of $E_{Ph-He2} = 40.57\,\text{eV}$, and $\lambda_{He1} = 58.46\,\text{nm}$ corresponds to $E_{Ph-He1} = 21.21\,\text{eV}$. Both lines exhibit a spectral width of less than 2 meV [39].

2) The KM-Wyvern Ti:sapphire laser amplifier system (KM-labs in Boulder, Co., USA)

has a fundamental wavelength of approximately 782.5nm (photon energy ∼1.584 eV) and a temporal FWHM of 55 fs. It is used as a pump pulse as well as to drive a high-harmonic generation (HHG) process. The generated 7th harmonic, with a wavelength of approximately 55.73 nm (photon energy ∼22.247 eV) and the same temporal FWHM of 55 fs (same as the driving laser), is utilise for the measurements.

2.2.2. Adding time resolution

Time- and angle-resolved photoelectron spectroscopy (Tr-ARPES) is a well-established technique for investigating electron dynamics on a femtosecond timescale. In this work, ARPES is combined with a pump-probe technique that employs two ultrafast laser pulses to capture ultrafast transient processes in materials. Figure 2.6 schematically illustrates the laser beam path from the KM-Wyvern Ti:sapphire laser amplifier system laser to the experiment.

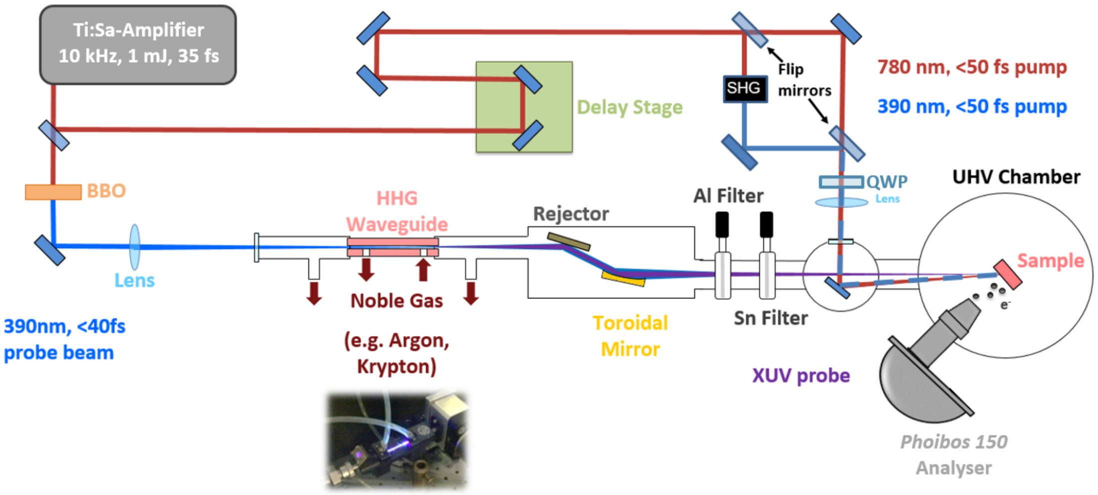

Figure (2.6) Diagram of the laser beam path as well as the HHG setup. Shown are the Wyvern laser, the module for generating extreme ultraviolet light, the translation stage of the pump-probe system, and the detector system within the UHV chamber. Reprinted with kind permission of the author from [42].

Initially, the high-photon-flux pulse is split by a beam-splitter (90:10 reflection/transmission ratio) into pump and probe branches. The weaker pump pulse is directed to a translation stage that adjusts its optical path length relative to the probe beam. Its intensity is set using a half-wave plate (HWP) and polariser (optimised for the laser wavelength), with an optional quarter-wave plate (QWP) available to convert linear (p) polarisation into circular (σ) polarisation. The sample is excited by either the fundamental of the Wyvern laser (1.584 eV) or its second harmonic (3.168 eV), thereby triggering electronic transitions or other rapid phenomena.

Meanwhile, the probe beam is routed to the high-harmonic generation (HHG) section, where it first passes through a BBO crystal to generate the second harmonic. The frequency-doubled pulses with 3.168 eV photon-energy are then injected into the vacuum and focused by a lens into the entrance of a krypton-filled glass fibre capillary. Inside the capillary, the HHG process produces a spectrum of higher-energy radiation that is focused by a toroidal mirror and spectrally filtered by ∼ 100 nm aluminium and tin thin-film filters to isolate the 7th harmonic at 22.247eV. Finally, the selected EUV pulse is directed onto the sample surface to trigger photoelectron emission.

By varying the delay between the pump and probe, snapshots of the transient electronic structure with femtosecond resolution can be captured. The energy and momentum of the emitted electrons are analysed using the above mentioned angle-resolved photoemission spectroscopy setup, to reveal detailed information about electron dynamics and relaxation processes.

The high probe photon energy not only enables the study of electrons with higher binding energies but also covers a momentum space larger than 1.5 Å^{-1}, exceeding the Brillouin zone of most materials. Additionally, the pump penetration depth is approximately 13nm [43], comparable to the EUV probe depth of 10nm [44]. Importantly, the probing depth of photoelectrons is close to a monolayer for the resulting maximal photoemitted electron energy of $\sim$ 16eV [45]. Hence the time- and angle-resolved photoelectron spectroscopy (Tr-ARPES) signal mainly probes the **individual surface layer** of the samples 4.2.

In conclusion, the Tr-ARPES approach is a highly surface-sensitive tool essential for investigating ultrafast phenomena such as charge-carrier dynamics, phase transitions, and non-equilibrium states in complex solid-state systems.

2.2.3. Laser fluence calculation

Laser fluence critically influences the observed changes in exchange splitting and remagnetisation time, as shown in Chapter 4 and Figure A.7. The laser fluence of the pump pulse at the sample surface is calculated following the method in [44]:

$$F_0 = \frac{2E(1-R)}{\pi\sigma^2} \tag{2.3}$$

where E is the pump pulse energy, R the surface reflectivity, and σ the Gaussian beam radius at the $1/e^2$ intensity level [44]. This fluence represents the peak intensity of the laser pulse. For multilayer systems, it is important to note that the penetration depth is approximately 13nm [43] and that a single graphene layer, as investigated in this thesis, absorbs about 2.3% of incident visible light [11]. The in-situ fluence for a nickel substrate is given by

$$F(z) = 0.977 \cdot F_0 \exp^{\frac{-z}{13\mathrm{nm}}} . \tag{2.4}$$

For the Wyvern laser system used here, the pump pulse energy E is approximately 1 $\frac{\mathrm{mJ}}{\mathrm{cm}^2}$ at 10W, with a reflectivity R of approximately 0.74 for p-polarised light and 0.64 for s-polarised light [44]. The laser spot radius σ is estimated to be 0.25 ± 0.02 mm. For the graphene/Pb/Ni(111) measurements a pump power of 400mW was used, and for graphene/Ni(111) 250mW. Consequently, the applied laser fluence ranges between 0.66 and 2.65 $\frac{\mathrm{mJ}}{\mathrm{cm}^2}$, with an estimated average value of 1.18 $\frac{\mathrm{mJ}}{\mathrm{cm}^2}$. Of this, approximately 0.03 $\frac{\mathrm{mJ}}{\mathrm{cm}^2}$ (around 2.3% [11]) is absorbed by the graphene layer. According to [44] (see appendix A.6 for fluence-dependent magnetisation dynamics), the absorbed laser fluence exceeds the critical fluence F_C of 0.59 $\frac{\mathrm{mJ}}{\mathrm{cm}^2}$, leading to heating of the nickel electron system above its Curie temperature T_C and thereby demagnetisation.

2.3. Analytical methods

In this section, I describe the comprehensive analytical procedures applied to the acquired ARPES data. A major component of this work is the data analysis, which was performed primarily in **MATLAB** [1] using custom routines. The data analysis framework was started by Johannes Stöckl and further developed by him and Benito Arnoldi. While singular functionalities, like importing the data into the MATLAB environment and the angle-to-k-parallel transformation were taken from the framework, almost every other function, that is not a MATLAB build-in function was developed specifically for the needed data analysis in this thesis. These routines encompass raw-data handling, normalisation, transformation, peak finding, and time-resolved fitting procedures. The following text details each analytical step and the associated **MATLAB** functions, with code examples provided in **MATLAB** syntax.
Following the “production” of samples and data acquisition, the analysis workflow proceeds as outlined below.

2.3.1. Pre-analysis raw-data handling

After importing the measurement raw-data, a specific sequence of pre-analysis steps is executed to produce datasets ready for detailed analysis. Figure 2.7 schematically illustrates the standard operations applied to all ARPES measurement data.

---

[1] **MATLAB** is a high-level language and interactive environment developed by **MathWorks** for numerical computation, visualisation, and programming. It offers extensive built-in functions and toolboxes that support data analysis, simulation, and algorithm development.

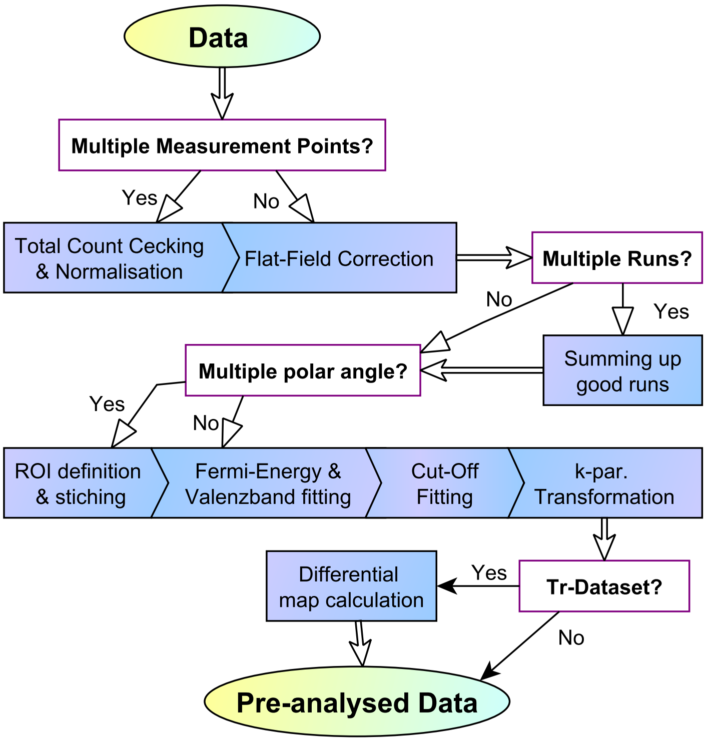

Figure (2.7) Schematic showing the **standard operations** conducted on the raw angle-resolved photoemission spectroscopy data, from import to creation of analysis-ready datasets.

Counts-per-measurement-point behaviour and normalisation Due to possible variations in light intensity when using the high harmonic generation setup, the total count per measurement point may fluctuate between different images steps taken. In time-resolved experiments, where up to 70 runs with 43 delay points are recorded, distinguishing between laser intensity fluctuations, periodic disturbances, or genuine transient band shifts is challenging. To address this, the TrHHG_calculate_TotalCountsPerMeasurementstep function calculates the total counts for individual measurement steps and runs. Figure 2.8 shows an exemplary output plot (generated by the function if demanded) in which the raw counts (blue) and a smoothed version (orange) are overlaid, green lines indicate t_0 and black lines mark the beginning of new runs.

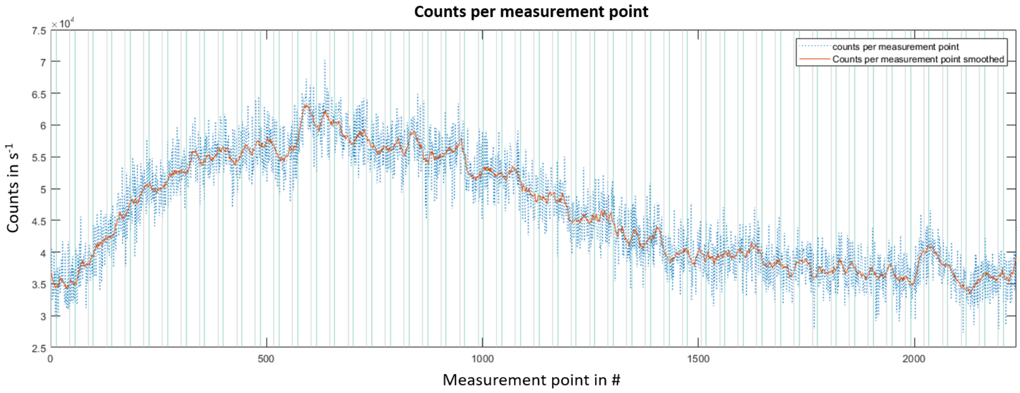

Figure (2.8) Explanatory plot from the TrHHG_calculate_TotalCountsPerMeasurementstep function for a Tr-ARPES dataset of graphene/Ni(111). The blue curve shows the calculated counts, while the orange curve represents the smoothed version. Green lines mark t_0 and black lines indicate the start of a new run.

For snapshots covering a range of 26° in angle and up to 10 eV in energy, the total counts should remain nearly constant between measurement snapshots. Fluctuations are therefore attributed to laser intensity changes and corrected using the TrHHG_Analysis_Norm_TotalCountsPerMeasurementstep function (if no anomalies or periodic behaviour are detected). This routine divides every pixel by the sum of the counts of the corresponding measurement and multiplies by the median total snapshot count-rate (to avoid small numbers). This normalisation is not applied when different regions of k-space are measured in separate steps because in those cases one can not differentiate between intensity loss and signal change due to changes in the depicted electronic band structure.

Flat-field normalisation MCP-based 2D detectors may develop spatially inhomogeneous sensitivity over time. To correct for such effects, a flat-field image — recorded with homogeneous illumination of the detector, were damages and insensitivities will show as artificial structures — is used to normalise the data. The TrHHG_normalise_data_with_Flatfield function interpolates the flat-field image to match the pixel dimensions of the measurement data and divides each pixel value by the corresponding flat-field value.

Summing of multiple measurement runs To improve the signal-to-noise ratio, multiple measurement runs are often summed up. Runs meeting quality criteria (e.g., absence of beam damage) are combined into a single dataset using the TrHHG_Analysis_Calculate_Sum function.

ROI definition and data stitching In ARPES experiments, different areas of k-space are recorded by translating the sample. The regions of interest (ROI) are first defined using Define_ROI_from_xyfile to exclude distortions (e.g., from the entrance slit). Subsequently, the stitch_polarsweep function automatically sorts the measurements by their polar angles and creates a composite dataset. In overlapping areas, the data are averaged and can be interpolated (using stitch_polarsweep_interpol). The final dataset may then be smoothed using an Savitzky–Golay smoothing filter (an example of this is Figure 3.4).

Fermi distribution and valence band fitting For accurate energy calibration, the Fermi distribution is fitted to an extracted spectrum. In metallic systems, the presence of metal peaks near the Fermi edge necessitates simultaneous fitting of the Fermi distribution and the adjacent peaks. The integrated MATLAB curve fitting application is used for **simple** fits. Figure 2.9 shows an exemplary screenshot from this tool, where the photoemission yield versus energy is plotted (black) with the fitted curve (blue). The tool also provides the 99% confidence interval and statistical parameters such as the R-squared value. The resulting fit code can be exported as executable MATLAB code.

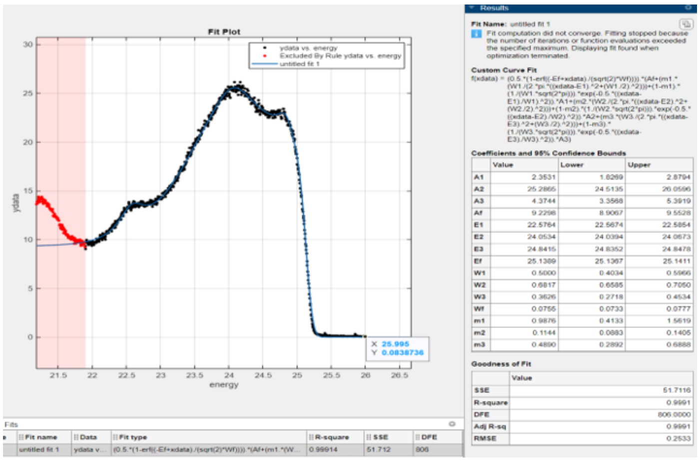

Fit Name: untitled fit 1

Fit computation did not converge. Fitting stopped because the number of iterations or function evaluations exceeded the specified maximum. Displaying fit found when optimization terminated.

Custom Curve Fit

```
f(xdata) = (0.5.*(1-erf((-Ef+xdata)./(sqrt(2)*Wf)))).*(Af+(m1.*
           (W1./(2.*pi.*((xdata-E1).^2+(W1./2).^2)))+(1-m1).*
           (1./(W1.*sqrt(2*pi))).*exp(-0.5.*((xdata-
           E1)./W1).^2)).*A1+(m2.*(W2./(2.*pi.*((xdata-E2).^2+
           (W2./2).^2)))+(1-m2).*(1./(W2.*sqrt(2*pi))).*exp(-0.5.*
           ((xdata-E2)./W2).^2)).*A2+(m3.*(W3./(2.*pi.*((xdata-
           E3).^2+(W3./2).^2)))+(1-m3).*
           (1./(W3.*sqrt(2*pi))).*exp(-0.5.*((xdata-
           E3)./W3).^2)).*A3)
```

Coefficients and 95% Confidence Bounds

	Value	Lower	Upper
A1	2.3531	1.8269	2.8794
A2	25.2865	24.5135	26.0596
A3	4.3744	3.3568	5.3919
Af	9.2298	8.9067	9.5528
E1	22.5764	22.5674	22.5854
E2	24.0534	24.0394	24.0673
E3	24.8415	24.8352	24.8478
Ef	25.1389	25.1367	25.1411
W1	0.5000	0.4034	0.5966
W2	0.6817	0.6585	0.7050
W3	0.3626	0.2718	0.4534
Wf	0.0755	0.0733	0.0777
m1	0.9876	0.4133	1.5619
m2	0.1144	0.0883	0.1405
m3	0.4890	0.2892	0.6888

Goodness of Fit

	Value
SSE	51.7116
R-square	0.9991
DFE	806.0000
Adj R-sq	0.9991
RMSE	0.2533

Fit name	Data	Fit type	R-square	SSE	DFE
untitled fit 1	ydata v...	(0.5.*(1-erf((-Ef+xdata)./(sqrt(2)*Wf)))).*(Af+(m1.*(W...	0.99914	51.712	806

Figure (2.9) Explanatory screenshot of the MATLAB Curve Fitting tool. The black plot represents the data (photoemission yield vs. energy), the blue curve is the fitted function, and the red-marked section was excluded from the fit. The displayed fit function and results (on the right hand side), including the 99% confidence interval and R-squared value, demonstrate the fit quality.

The tool was set to employ the **trust-region algorithm** and to reduce the free parameter space starting parameters and coefficient constraints (upper and lower bounds) were set. The results, residual, exitflags, etc. can be exported to the MATLAB workspace as well as the complete fit-setup (executable MATLAB code). In the given example the Fermi-Distribution and three Voigt peaks were fitted using

```matlab
% Extracting Angle integrated Spectrum for fit:
    ydata = (squeeze(mean(NiCor_VUV.channeldata,1,'omitnan')));
% Energy axis - xdata - for fit:
    energy = NiCor_VUV.axes.energy.data;

FittingFunction = @(xdata) (...
    (m1 .* (W1./(2.*pi.*((xdata - E1).^2 + (W1./2).^2))) + (1 - m1) .* (1./(W1 .* sqrt(2*pi))).*
        exp( -0.5 .* ((xdata - E1)./W1).^2 )).*A1 + ... % Peak 1
    (m2 .* (W2./(2.*pi.*((xdata - E2).^2 + (W2./2).^2))) + (1 - m2) .* (1./(W2 .* sqrt(2*pi))).*
        exp( -0.5 .* ((xdata - E2)./W2).^2 )).*A2 + ... % Peak 2
    (m3 .* (W3./(2.*pi.*((xdata - E3).^2 + (W3./2).^2))) + (1 - m3) .* (1./(W3 .* sqrt(2*pi))).*
        exp( -0.5 .* ((xdata - E3)./W3).^2 )).*A3 + ... % Peak 3
    Af ).* (0.5.*(1-erf((-Ef+xdata)./(sqrt(2) * Wf )))); % Fermi distribution
```

Listing (2.1) Example Code: Fermi and Voight peaks fitting function

k-parallel transformation Using the results from the Fermi distribution fit, the work function and the cut-off can be calculated. These values are then used for the polar-angle to k_{II} transformation, following Equation 2.2. A function implemented by Benito Arnoldi automatically transforms the dataset and adjusts the image distortion if a bias voltage U_{Bias} is applied. According to Hengsberger *et al.* [41], the bias potential is given by

$$U_t = U_{Bias} + (\Phi_{analyser} - \Phi_{WF}),$$

which is used to calculate a correction angle θ_{cor} via

$$\sin(\theta_x) = \left(\frac{eU_t}{E_{kin}} \left[1 - \frac{\sqrt{1-\theta_m^2}}{2} - \frac{\arcsin(\theta_m)}{2\theta_m} \right] \right)^{\frac{1}{2}}. \tag{2.5}$$

The sum $\theta_{cor} + \theta_m$ is then substituted into Equation 2.2 to obtain accurate momentum values.

Differential Map Calculation For time- and angle-resolved photoelectron spectroscopy data, especially when using high harmonic generation radiation, the excited-state signal can be very weak relative to the occupied states. Often instead of looking at the raw data, differential data will be consulted. Differential maps are generated by subtracting an averaged reference dataset (typically 4–6 measurements taken well before t_0) from each time step. The TrHHG_Analysis_Calculate_DifferentialMap function performs this subtraction and normalise the result, thereby enhancing the contrast of time-dependent changes. Examples are presented in Figure 3.13.

2.3.2. Sample specific corrections

2.3.2.1. Rotation correction

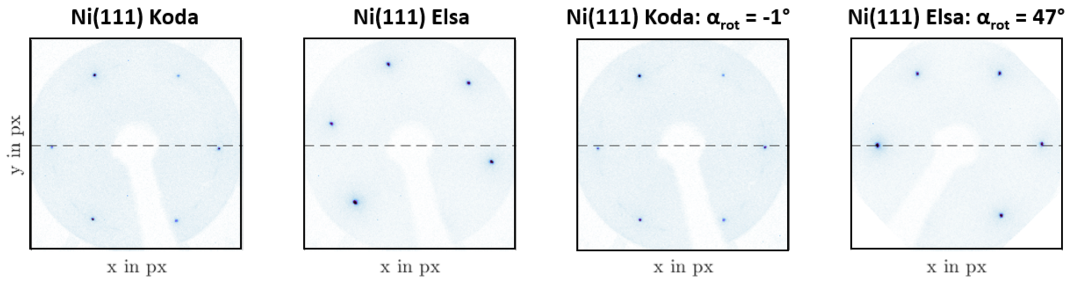

Figure (2.10) low-energy electron diffraction measurements of the graphene/Ni(111) system on the Ni(111)-Koda and Ni(111)-Elsa crystals. The left images show the original LEED patterns recorded using an MCP-LEED at the ELI-ALPS Nano-ESCA endstation, and the right images display the datasets after rotation using the angles α_{rot} (1° for Ni(111)-Koda and 47° for Ni(111)-Elsa), resulting in a relative rotation of 46°. This rotation must be taken into account during analysis.

Due to the manual mounting of different Ni(111) crystals on UHV sample plates, the high-symmetry axes of the samples may be rotated relative to one another. In this work, the crystals (internally designated as Ni(111)-Koda and Ni(111)-Elsa) were rotated by $\alpha_{rot,KODA} = -1°$ and $\alpha_{rot,ELSA} = 106°$, respectively, as illustrated in Figure 2.10. Before detailed analysis, the datasets are rotated such that the high-symmetry directions (of nickel) align consistently.

2.3.3. Semi-static angle-resolved photoemission spectroscopy data analysis

2.3.3.1. Excited states spectrum extraction

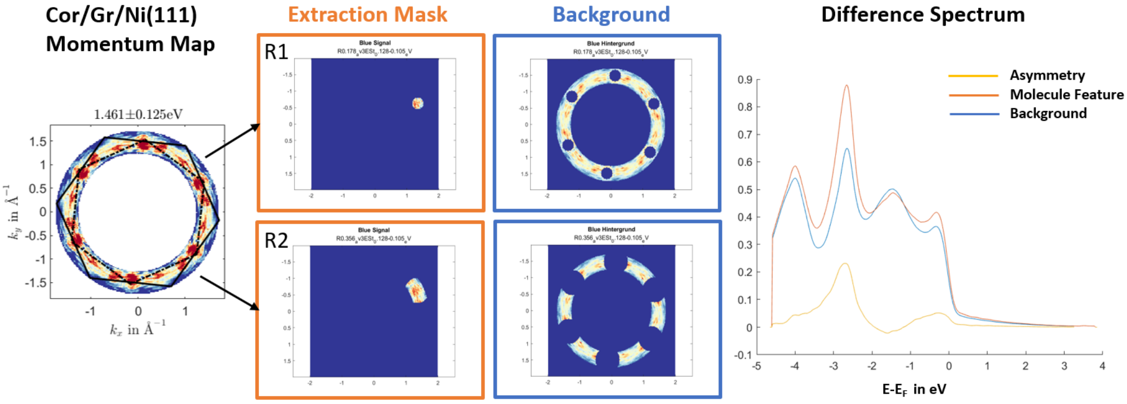

Figure (2.11) Illustration of the spectral feature signature extraction for two different extraction mask radii. From the left: Explanatory momentum map of the blue-pumped coronene/graphene/nickel(111) system; Resulting data for the extraction-mask and background averaging; Difference spectrum, showing the feature, the background and the **asymmetry** spectra after extraction for all energies.

To extract a differential spectrum for a specific area in k-space, as was done for the coronene/-graphene/Ni(111) stationary-delay configuration data, an extraction mask was used. This mask is applied to all energy steps, removing all data surrounding the specified region. Averaging yield the “spectral feature signature”, while average of the removed data forms the “Background”. By calculating the difference between the datasets, spectral signatures originating from the specified region can be identified. Figure 2.11 showcases this procedure.

2.3.4. Time-resolved angle-resolved photoemission spectroscopy data analysis

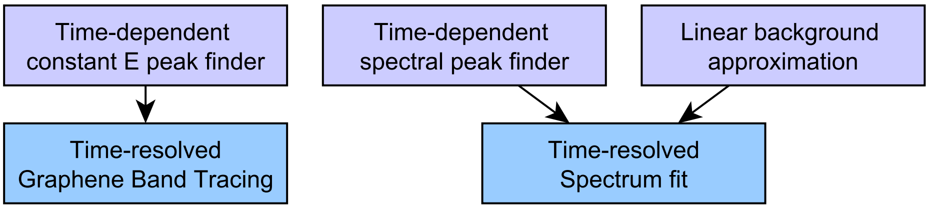

Figure (2.12) Schematic of the Tr-ARPES analysis workflow. The blue boxes denote the principal fitting functions and their dependencies on pre-fit results.

For time-resolved pump-probe ARPES experiments, additional analytical steps are required to distinguish between overall band shifts (e.g., due to space-charge effects) and intrinsic light-induced modifications of the band structure. Moreover, by extracting the time-dependent evolution of the Fermi function (including its position, width, and amplitude), changes in physical parameters such as the chemical potential and electron temperature can be deduced. Figure 2.12 schematically presents the key functions employed in the time-resolved analysis; the two most important fitting functions and their dependencies on pre-fit results are depicted in blue.

2.3.4.1. Tr-Pre-Analyse Tools

Linear background approximation When using HHG radiation as a probe due to the used experimental setup an additional signal causes a non-zero background (likely from leakage of the 9th harmonic) best visible in the unoccupied region of the spectrum. A simple linear function, $f(E) = p_1 \cdot E + p_2$, is fitted to the averaged signal of several time steps well before t_0 using the MATLAB curve fitting application. Subtraction of this linear background from the data restores the expected near-zero signal in the unoccupied region, ensuring that subsequent time-dependent changes are attributable to excitation dynamics.

Time-dependent spectral peak finder A built-in MATLAB peak-finding algorithm is utilised in a more complex preliminarily time-resolved tracing of the movements of prominent spectral peaks. The function TrHHG_findpeaks extracts rough peak positions from the dataset, as illustrated in Figure 2.13. Three clearly moving peaks and two regions with flat peaks (where the peak position cannot be reliably determined by a simple algorithm) are identified. These preliminary results are used to set constraints and starting parameters for the more complex TR-Spectrum-Fit routine.

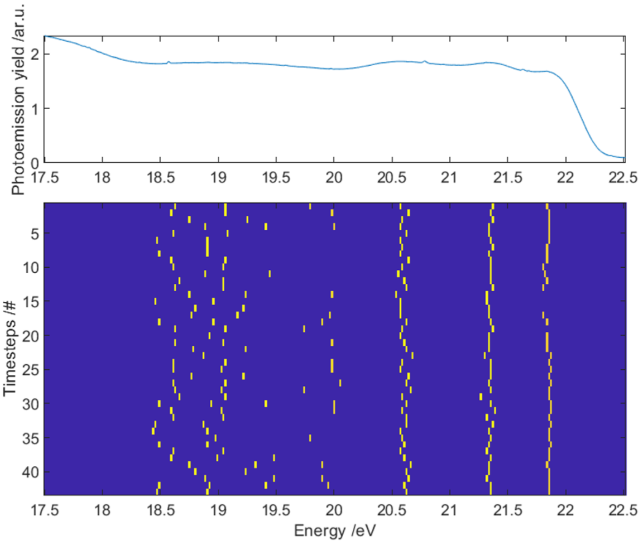

Figure (2.13) Time-resolved spectral peak finder for the graphene/Pb/Ni(111) sample. The upper panel shows the spectrum before t_0, and the lower panel displays the extracted peak positions for all 43 time steps. t_0 occurs at step 13. Three peaks exhibit clear movement, while two peaks remain flat such that their positions cannot be determined reliably by a simple algorithm.

Time-dependent constant-$E - E_F$ peak finder The peak finder is extended within the TrHHG_dispersion_fitting function to track peak positions not only in $k_{||}$ but also in constant-$E - E_F$ slices. Figure 3.14 shows the results for one exemplary time step (20fs after t_0) of the graphene/Pb/Ni(111) sample system. This method is most reliable close to t_0 where a sufficient electron population is present.

2.3.4.2. Time-dependent spectrum fit to extract Fermi function parameter and peak positions

One of the most frequently applied routines in this thesis is the time-resolved spectrum fit, which extracts the evolution of the Fermi function parameters and the spectral peak positions. Figure 2.14 schematically illustrates the process. As input data a Tr-spectrum is used. The routine begins with a pre-fit on several measurement points taken before excitation to determine a baseline, followed by a main fit that dynamically updates starting parameters and bounds based on the pre-fit results. Important constraints include: The number of peaks to describe it and the starting conditions (start parameter as well as upper and lower bounds) can be predetermined using the TrHHG_findpeaks function. The respective number of Gaussian or Voigt peaks multiplied with the Fermi distribution and a linear background form the first **Pre-Fit** function. The **Pre-Fit** is the first step within this fitting routine. Its goal is to fit the static spectrum before the excitation takes place. To achieve this a **pre-time-loop** is started. For a set number of measurement points far before t_0, normally I used four to six, the spectrum is fitted individually with the static-spectrum-representation (Pre-fit) function using the given starting parameters and bounds. The averaged result from this pre-loop together with additional or physical constrains are used to determine new starting conditions for the **Main-Fit**. The most important constrains are:

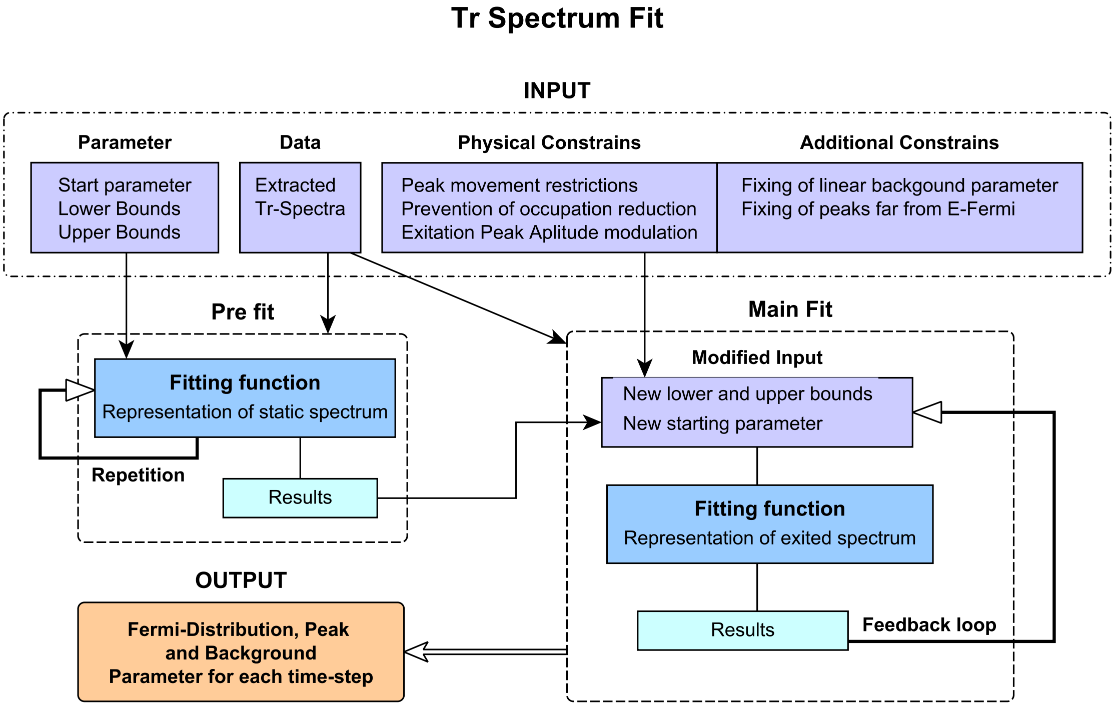

Figure (2.14) Schematic of the Tr-Spectrum Fit routine.

- Fixing of parameters to set values to reduce free parameter space, namely: linear background and if possible all peak parameter far from E_f. Very narrow upper and lower bounds can be chosen to allow for minimal movements.

- The fit is prohibited from fitting a Fermi function width smaller than in the pre-fit. Since this would indicate an unphysical cooling of the system.

- The peak population (amplitude) below E_f is not allowed to get bigger than in the pre-fit, since in the undisturbed system the amplitude represents the maximum population of the occupied region.

During the main fit, the fitting routine starts at the first taken measurement-point far before t_0. After each fit, the starting parameter and bounds are dynamically adjusted taking the results from the previous fit and the given constrains into account. This ensures that the fit can follow e.g. peak movements, but the peaks can not “jump” or move past each other. Additional Gaussian peaks may be incorporated during the main fit to represent the excitation above the Fermi energy. Equation 2.6 shows a typical fitting function that comprises n static Gaussian peaks multiplied by a Fermi distribution, augmented by an excitation peak and a linear background.

$$\begin{aligned}\mathrm{F}(E) = & \left[\frac{A_{\text{Excitation}}}{\sqrt{2\pi} * \sigma_{\text{Excitation}}} * \exp\left(-\left(\frac{E-E_{\text{Excitation}}}{\sigma_{\text{Excitation}}}\right)^2\right)\right] + \left[\frac{1}{2}\left(1-\text{erf}\left(\frac{E-E_{\text{Fermi}}}{\sqrt{2}\sigma_{\text{Fermi}}}\right)\right)\right] \\ & * \left[A_{\text{Fermi}} + \frac{A_1}{\sqrt{2\pi}\sigma_1} * \exp\left(-\left(\frac{E-E_1}{\sigma_1}\right)^2\right) + ... + \frac{A_n}{\sqrt{2\pi}\sigma_n} * \exp\left(-\left(\frac{E-E_n}{\sigma_n}\right)^2\right)\right] \\ & + LinBG\end{aligned} \tag{2.6}$$

were n represents the number of “static” peaks, A_i is the amplitude, E_i the peaks centre position and σ_i the width for the Gaussian-peak and Fermi-Distribution respectively. This static representation is augmented with the excitation peak and a linear background approximation $LinBG = x * E + \text{Offset}$. To suppress any unphysical excitation peak before t_0, the amplitude $A_{\text{Excitation}}$ is modulated by a nonlinear constraint as given in Equation 2.7

$$\mathrm{Mod}_{\mathrm{Excitation}}\left(\Delta \mathrm{t}\right) = \left[1 - \frac{1}{2}\left(1 - \mathrm{erf}\left(\frac{\Delta \mathrm{t} - \sigma_{\mathrm{Laser}}}{\sqrt{2} * \frac{\sigma_{\mathrm{Laser}}}{2}}\right)\right)\right] + 0.001 \tag{2.7}$$

where Δt is the time-delay for the current fitting step and σ_{Laser} is the pump laser pulse . This suppresses the onset of the excitation peak, by setting its amplitude close to 0, dependent on the used pump laser pulse width. While the routine stays the same, different functions were used depending on the number and type of peaks to be fitted.
A representative MATLAB code excerpt (algorithm setup and fit function) for the main fit using lsqnonlin is provided in Listings 2.3–2.5.

```
    % Function 2 - Main-Fit) with exitation Gaussian

    fit_ExiGaus_Modulated_5Gaus_Fermi_lin = @(p)...
        (p(1)./(sqrt(2*pi).*p(3)).*exp(-0.5.*((xdata-p(2))./p(3)).^2)  ... % Excit. G.
        + (p(4)./(sqrt(2*pi).*p(6)).*exp(-0.5.*((xdata-p(5))./p(6)).^2)  ... % Gaussian
        + p(7)./(sqrt(2*pi).*p(9)).*exp(-0.5.*((xdata-p(8))./p(9)).^2)  ... % Gaussian
        + p(10)./(sqrt(2*pi).*p(12)).*exp(-0.5.*((xdata-p(11))./p(12)).^2)  ... % Gaussian
        + p(13)./(sqrt(2*pi).*p(15)).*exp(-0.5.*((xdata-p(14))./p(15)).^2)  ... % Gaussian
        + p(16)./(sqrt(2*pi).*p(18)).*exp(-0.5.*((xdata-p(17))./p(18)).^2)  ... % Gaussian
        + p(19)) ...        % Fermi amplitude
        .* (0.5.*(1-erf((-p(20)+xdata)./(sqrt(2)*p(21))))) ...  % Fermi funktion
        + Steigung.*xdata ...               % Linear Funktion (From linBG is fixed here)
        + Offset);              % Offset (From lin fitBG is fixed here)
```

Listing (2.2) Exemplatory Main-Fit function

were $parameter \equiv p \equiv p(1)...p(21)$ are the given starting parameter.

```
    options = optimoptions(@lsqnonlin,'Algorithm','interior-point','SubproblemAlgorithm','cg','
         OptimalityTolerance',1e-6,'FunctionTolerance',1e-6,'MaxIterations',1000);
```

Listing (2.3) Settings for the lsqnonlin fitting algorithm

The amplitude modulation was implemented as a constraint by using

```

    % Calculate Exitation Amplitude Modulation depending on pump pulse temporal width:

    amplitudemodulation = zeros(1,size(xydatafile.channeldata(:,:,:),1));
    for timestep = 1:size(xydatafile.channeldata(:,:,:),1)
        amplitudemodulation(timestep) = 1-(0.5.*(1-erf((-(-LaserPulsWidth)+delaylist(timestep))
             ./(sqrt(2)*(LaserPulsWidth/2))))) + 0.0001; % so it does not resolve to 0
    end

    % set as constrains:
     A = [1, 0, -amplitudemodulation(timestep), 0 , 0, 0, 0, 0, 0, 0, 0, 0, 0, 0, 0, 0, 0, 0,
         0, 0 ];
     b = 0 ;
     Aeq = [];
     beq = [];
```

Listing (2.4) Excitation Peak Amplitude Modulation

resulting in the main fit

```

 [parameter,resnorm,residual,exitflag] = lsqnonlin(@(p) ...
        fit_ExiGaus_Modulated_5Gaus_Fermi_lin(p)-ydata , ...
        parameter_mod, parameter_mod_lb, parameter_mod_ub, ...
        A, b, Aeq, beq, @nonlincon, options);

    % Non-Linear constrain:
     function [c,ceq] = nonlincon(p)
     ceq = [];
     c = [];
     end
```

Listing (2.5) Main fit

where the parameter and bound are modulated according to the given constrains and no non-linear constrain is given. The extracted parameters can be used to track the evolution of the electron temperature and band structure.

Time-dependent constant-$k_{||}$-spectrum fit By selecting a specific ROI (region of interest) in momentum space, the time-resolved spectrum fit can be adapted to analyse constant-$k_{||}$ spectra. In this case, the time-resolved Fermi parameter results obtained from the full-spectrum fit are used as fixed inputs, thereby reducing the free parameter space and ensuring consistency across the dataset.

2.3.4.3. Time-resolved exchange splitting Fit

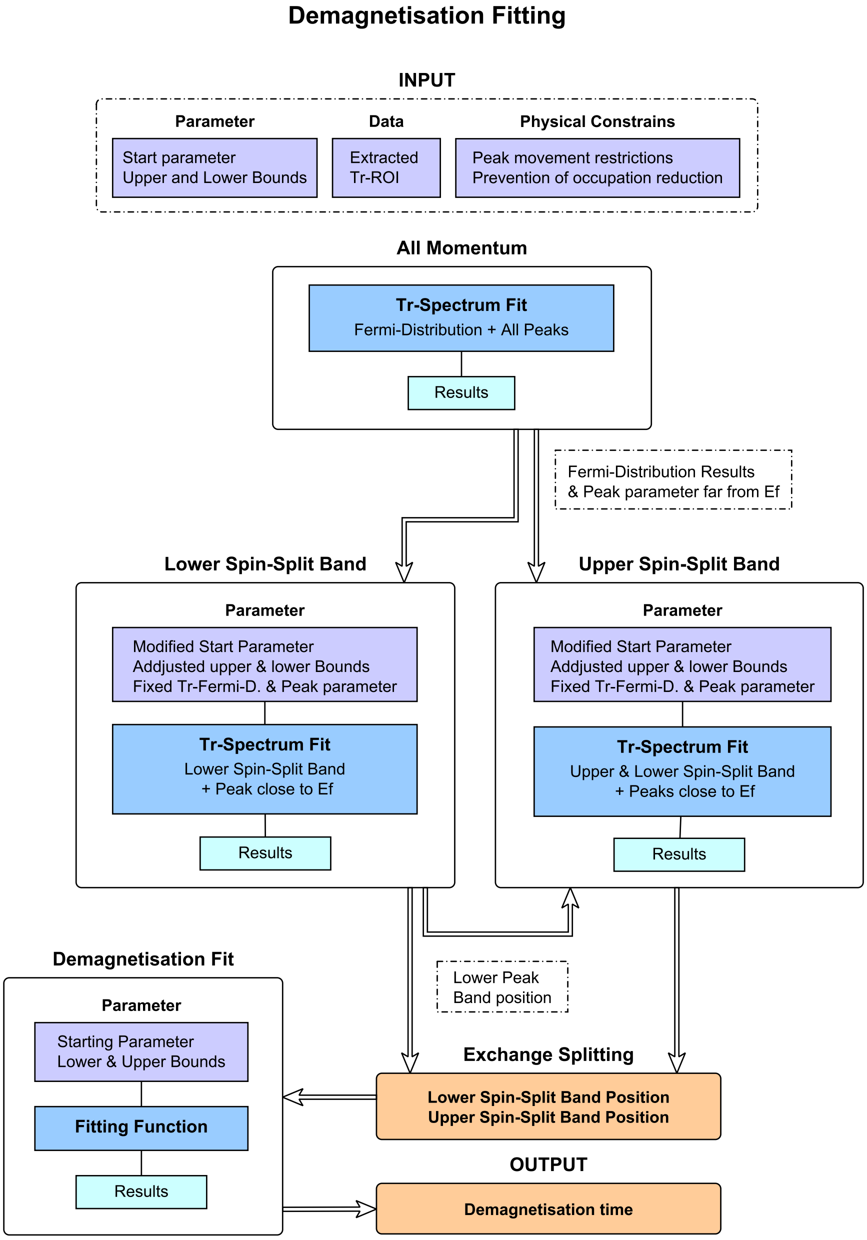

Figure (2.15) Schematic of the TR-DemagnetisationFitting routine.

This fitting routine was developed to extract the collapse of the exchange splitting from Tr-ARPES measurements on Ni(111), although it is also applicable to other cases. The goal of the routine is first to extract the signal and peak movement of the lower Ni spin-split band and then to use this information to fit the movement of the upper band. By tracing the movement of both bands, the difference (i.e., the exchange splitting dynamics) can be extracted. A schematic of this routine is presented in Figure 2.15. This routine makes heavy use of the Tr-Spectrum Fits described in Section 2.3.4.2. It is important to note that in this routine a single function is not sufficient to handle the fitting, user involvement is required to inspect the intermediate results and to input the correct parameters for the next steps. Full automation of this process may be achieved in future work. Initially, a spectral fitting is performed to determine the time-dependent evolution of the Fermi function, using Voigt functions (Equation 4.1) to represent the nickel peaks. In contrast to the standard spectral fitting, fitting weights are applied to emphasize the regions near the Fermi edge. For example, the weights are set as follows (see Listing 2.6):

```

    % All areas are equily importent, hence set to 1:
    weights = ones(1,size(NiPbGr_20211014_TrHHG_spol_NiBands_kpar_ROI.channeldata,3));

    % Choosing a wider range including the peaks close to Ef, here -1.2775eV to -0.4880eV
        ImportantEnergies = 103:180;
        weights(ImportantEnergies) = 5;
    % Chossing the area around the Fermi edge to have the biggest impakt on the fit, here -0.61eV bis 0.74eV ;
        EvenMoreImportantEnergies = 123:140;
        weights(EvenMoreImportantEnergies) = 10;
```

Listing (2.6) Fitting Weights

The calculated residual is multiplied by 1, 5 or 10, depending on the energy region. The lsqnonlin tries to minimise the residual which is multiplied by the set weights for the respective energy region. The weighted residual forces the fitting algorithm to emphasize the regions that are most critical for the fit. Explanatory fitting results are plotted in Figure 4.7. The extracted time-dependent results for the Fermi-Distribution will be used in the following fits to fix the Fermi-Distribution fitting parameter and thereby reduce the size of the free parameter space and more importantly ensure consistency between different fits on the same dataset.

In a first step, regions of interest are defined to represent the lower spin-split band. Depending on the chosen region, the number of fitted peaks must be adjusted. Here, the fitting function was modified to n=3 Voigt functions. Explanatory results are plotted in Figure 4.8. By extracting the peak parameter for the lower spin band peak its movements can be traced.

In a next step the movement of the upper spin band is fitted. Again an area representing the correct region in k-space is chosen. The peaks for the lower and the upper spin split band are easily to differentiate in the unexcited system. But when the system is driven out of equilibrium and the exchange splitting starts to collapse the peaks move towards each other. Additionally the band is very close to the Fermi edge and moves closely to its vicinity. The peak shape is therefore “cut” by the Fermi edge. Implementing the previous fitting results is an important step here to ensure reliable results. The time-resolved Fermi-Distribution as well as the lower spin band parameters are fed into the upper spin-split band fit. The same weights 4.2 were used, but the fitting function now consists of 4 Voigt peaks, to accommodate for addition of the upper Ni-band. Explanatory plotted in Figure 4.10.

The band positions can be analysed by themselves and they can be used to calculate the transient changes of the exchange splitting, as was done here. To enhance the reliability of the results multiple, closely neighboured regions for the upper and lower band were fitted and averaged. The difference between the peak positions equals the current exchange splitting. To extract the demagnetisation dynamics, in a next step the MATLAB curve fitting application was utilise to fit a double exponential decay function. From the exponential function parameter the respective demagnetisation timescales can be extracted. The results for the de- and re-magnetisation times are summarise in Table 4.4.

2.3.4.4. Time-dependent constant-$E - E_F$ fitting routine to trace Graphene π band

The goal of this method is to trace the graphene π movement over time and to determine if a band gap opened after the lead intercalation. While the Tr-spectrum fit could be used, it would require to fit five “initial” Gaussian-peak peaks as well as an excitation-peak, resulting in 21 fitting parameter - 19 for fixed Fermi-Distribution parameters and this for different regions in k-pace. Hence, the fits would be quite unstable and thereby their results unreliable. This was greatly reduced by implementing hard constrains, e.g. fixing the peak parameter for peaks far away from E_{Fermi} and others. But I found the constant energy fitting, meaning the tracing of the graphene features in the momentum dimension, more suitable. To do this I developed a multi-step fitting routine that fits a 2. degree polynomial to match the background and a Gaussian-peak for the graphene band, the graphene π band tracing: TrHHG_fit_1Gaus_Poly2_kpar. Figure 2.16 displays a schematic representation of this routine.

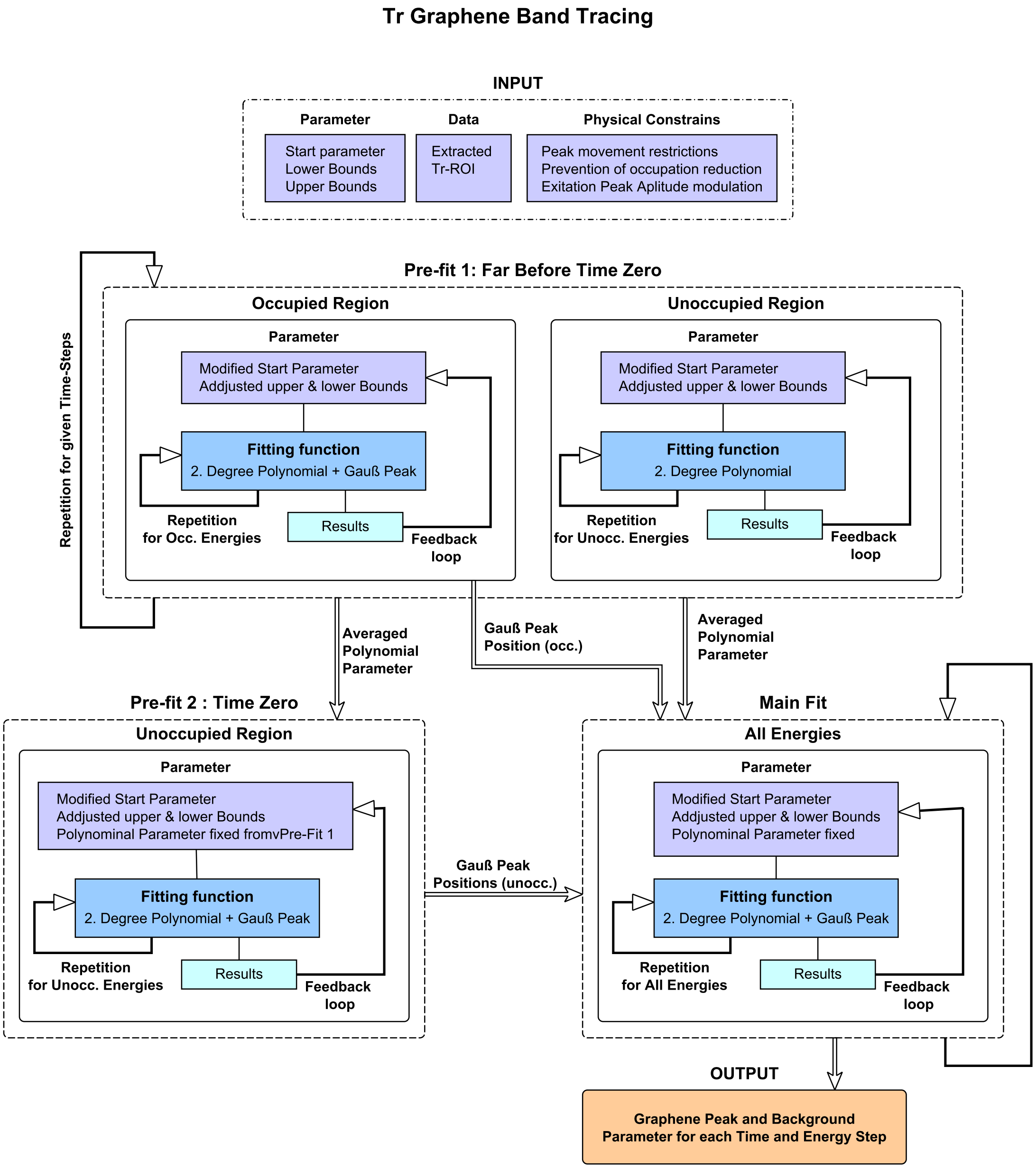

Figure (2.16) Schematic of the TR-GrapheneBand-Fit routine.

Only the dataset and starting parameters are needed for this fitting routing - no manual intervention required. Those starting conditions can be pre defined by the TrHHG_dispersion_fitting function 2.3.4.1. The fitted data must be restricted to an area were the graphene π band is clearly distinguishable from other features, ideally it should be the only prominent feature. Similar to the TrHHG_dispersion_fitting function, for every measured time-step and energy-channel in the ROI dataset a constant-$E - E_F$ cut is fitted. Since in the occupied region the graphene band is clearly visible throughout the measurement, fitting is designed to trace movements of the band in $k_{||}$. On the other hand, in the unoccupied region the graphene π^*-band features are only visible as long as they are populated by excited electrons. To accommodate for this the fitting routine differentiates between the unoccupied and the occupied region. It additionally has two **Pre-fits**.

Firstly, the **Pre-fit 1: far before Time Zero** is executed. Here a pre-time loop, including three to five time steps far before t_0 is executed. Starting with the lowest energy slice in the occupied region a 2. degree polynomial to match the background and a Gaussian-peak for the graphene band is fitted to the data. The peak position is used in a feedback loop to modify the starting parameter and the bounds for the next energy step, one energy slice upwards towards lower binding energies. This is repeated until the unoccupied region is reached. Here the fit is changed to only fit the poly-

nomial background approximation (the graphene band, represented through the Gaussian-peak is not occupied yet). When it is done with all energies, the process is repeated for the next time step. Again all results from the previous time step are used to modify the starting parameter.
Secondly the **Pre-fit 2: Time Zero** is executed. Shortly after t_0 the highest occupation is expected. Therefore the fitting of the unoccupied region is repeated, but this time using a 2. degree polynomial and Gaussian peak. The polynomial is not fitted, but its parameter are taken from the averaged results of the **Pre-fit 1**. Assuming that the polynomial background is the same for all time-steps and that changes in the data cut can be assigned to the changed graphene band population and position.
Lastly the **Main-Fit**. The complete dataset is fitted anew using a 2. degree polynomial and a Gaussian Peak. The starting parameter for the polynomial are given by the mean of the first fitting step - fit before t_0 - while the starting parameter for the Gaussian-peak **position** is given from the results of **Pre-fit 1** for the occupied region and from **Pre-fit 2** for the unoccupied region. This allows a more stable fitting of the Gaussian-peak in the unoccupied region even for small signals, again assuming that changes of the data in comparison to the data far away from t_0 are a result of the changes graphene band occupation and position. Explanatory fitting results for different delay-times, for the constant-$E - E_F$ cuts (marked in Figure 3.15) are shown in Figures 3.16, 3.17 and 3.18.

2.3.4.5. Time-dependent graphene band gap size fitting routine to trace graphene gap quenching

The last step is to give an estimation about the band gap size and its time-dependent behaviour. In this analysis the graphene band peak positions, extracted from extensive π-band tracing, were used while restricting the fitting region to exclude Ni-dominated features. The applied band-distribution fit used is assuming a simple model of gapped Dirac fermions and was automated to fit the upper and the lower half of the Dirac Cone for every measured time step. The employed fit function is

$$E_{\pm}(k_{II}) = E_D P \pm \sqrt{\hbar^2 v_F^2 (k - k_{DP})^2 + (\Delta E/2)^2} \tag{2.8}$$

where E_{DP} denotes the Dirac point energy (i.e. the mid-gap energy), k_{DP} is the wave vector at the Dirac point, v_F is the Fermi velocity, and ΔE is the energy gap between the conduction and valence bands. Exemplary fitting results for $\Delta t = 0\,\mathrm{fs}$ are shown in Figure 3.23 for both the upper and lower Dirac cone segments, which were fitted separately. When cutting along the $\overline{\Gamma}$ to $\overline{K}$ direction direction, as was done in the presented Tr-data set, only half of the Dirac cone is visible (dark corridor effect). Importantly, if visible, the Dirac cone does not form a perfect cross, rather the right (towards higher momentum values), visible arm has a flatter curvature (lower Fermi velocity) that the part to the left (lower momentum values) of the Dirac point. This can be seen when studying the curvature of the theoretical calculations presented in Figure 3.9. During the fitting of the unoccupied region, this will cause a systematic overestimation of the gap size (this will not influence the qualitative movements only their magnitude).
Additionally, the extracted gap sizes differ between the upper and lower Dirac cone fits. The extracted gap size for the upper Dirac point part was finally fitted using a double exponential fitting function to trace the time-dependent band gap quenching and its time scale. The results are presented in Figure 3.25.

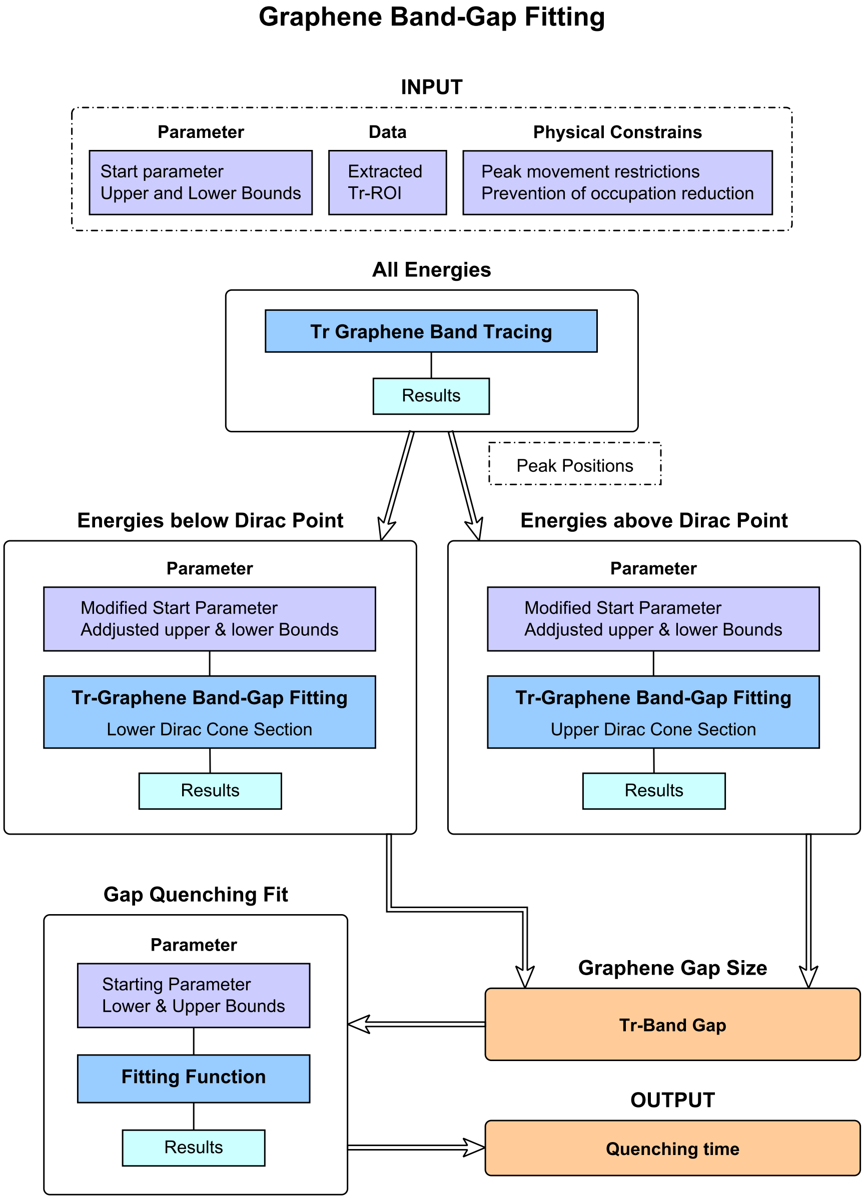

Figure (2.17) Schematic of the TR-GrapheneGap-Quenching-Fit routine.

2.3.5. Summary

The analytical framework developed for this thesis encompasses a wide range of data pre-processing, normalisation, and fitting routines, all implemented in MATLAB. Custom functions for handling raw ARPES data, performing flat-field corrections, stitching data from different measurement angles, and executing both static and time-resolved spectral fits have been described in detail. These methods enable robust extraction of physical parameters such as the Fermi level, electron temperature, band dispersion, exchange splitting, and graphene π band dynamics. Together, they provide a reliable pathway from raw experimental data to quantitative insights into ultrafast phenomena at surfaces.

3. Lead intercalated graphene on the nickel(111) surface - a material system for the future?

In this chapter I lay the groundwork for the thesis by showing how Pb intercalation transforms graphene/Ni(111) into a near–free-standing Dirac material. This band-structure decoupling not only realises a tunable band-gap, but also creates the well-defined electronic boundary conditions used in Chapter 4 to compare spin-relaxation on bare versus Pb-buffered graphene/Ni. Later in Chapter 5, that same decoupled graphene/Ni(111) interface — now understood in detail — will serve as the injector of optically excited, spin-polarised electrons into coronene.

Acknowledgement of collaborative efforts and individual work

The experimental work presented in this chapter would not have been possible without the valuable contributions of several colleagues, whose expertise and support I gratefully acknowledge.
This chapter is based on two sets of data.

Firstly, static and time-resolved measurements of a graphene/Pb/Ni(111) sample (gathered from 2021-10-11 to 2021-10-15).
Sample preparation: Katharina Hilgert, supported by Christina Schott; Data acquisition: Sebastian Hedwig, supported by Katharina Hilgert; Setup build-up and maintenance: Benito Arnoldi and Johannes Stöckl (ARPES), Eugen Nosenko and Sebastian Hedwig (Laser system and HHG-beamline); Data analysis: Myself.

Secondly, (Tr-) momentum microscopy was performed on the graphene/Ni(111) and graphene/Pb/Ni(111) system at a measurement campaign at the ELI-ALPS facility (2024-05-20 to 2024-06-20). Sample preparation: Martin Mitkov and myself, supported by Alexander Schmid; Data acquisition: Martin Mitkov, myself, Gyula Halasi, Nikolett Olah, Csaba Vass, supported by Alexander Schmid, Lu Lyu, Martin Anstett Laszlo Ovari; Beam-line- and Laser-operation staff: Zoltan Filu, Timea Timar-Grosz, Chinmoy Biswas, Peter Jojart, Balazs Major; Data analysis: Martin Mitkov, Alexander Schmid and myself.

Additional support regarding the sample system: Christina Schott. Scientific advisors throughout: Benjamin Stadtmüller, Martin Aeschlimann.

3.1. Introduction

In graphene the absence of a band gap or spin-polarisation poses a major hurdle for certain applications, notably logic devices and spin- and opto-electronics. A central challenge in graphene research has therefore been to **engineer a band gap** without sacrificing its excellent electronic properties. Both can be activated by changing graphene's surrounding. Numerous strategies have been explored, including sublattice symmetry breaking (e.g. via adsorbates), quantum confinement in nano-ribbons, and substrate-induced effects [13]. In particular, interfacing graphene with other materials has proven a powerful approach: for example, placing graphene on specific substrates or **intercalating** atomic layers underneath the graphene sheet can modify its electronic bands in desirable ways [13].
Another important aspect for spintronics is to integrate graphene with ferromagnets to inject or detect spin-polarised currents. Directly growing graphene on a ferromagnetic Ni(111) substrate yields a **lattice-matched interface**. Therefore, graphene on Ni(111) has emerged as a promising platform owing to the high-quality, large-area monolayer growth achievable via chemical vapour deposition (CVD). However, the strong interaction between graphene and the ferromagnetic Ni(111) substrate leads to significant hybridisation, dramatically altering graphene's band structure [14]. In other words, graphene on Ni(111) loses its signature linear dispersion and gap-less Dirac point due to this hybridisation. While the close contact with a ferromagnet can induce magnetism in graphene, it

comes at the expense of quenching graphene's high mobility and Dirac cone.
To overcome these limitations, the intercalation of heavy metal atoms, such as lead (Pb) or bismuth (Bi), between graphene and Ni(111) has been proposed as an effective strategy [46]. Theory has long predicted that if graphene's intrinsically weak spin-orbit interaction is boosted (for example, by proximity to heavy atoms), a band gap can open at the Dirac point, potentially realise a quantum spin Hall (QSHE) topological state with spin-polarised edge currents [47]. Indeed, a recent experimental study reported a $\sim 0.2\,\text{eV}$ gap induced by intercalating a monolayer of lead under graphene on Pt(111) [23]. This result sparked tremendous interest in graphene–heavy element systems as a platform for spin-orbit coupled Dirac physics. However, the interpretation remains under debate [24].

In this chapter, the focus is the investigation of lead (Pb)–intercalated graphene on Ni(111) as a means to induce a band gap at the Dirac point and control its size and energetic position. The choice of Pb aims to leverage its high atomic number (and thus strong spin-orbit potential) to open a gap, while using Ni(111) as the substrate provides a well-established growth template for epitaxial graphene and a route to eventually incorporate magnetic proximity effects. By introducing Pb, the spin-orbit coupling (SOC) is enhanced through the proximity effect effect, and the strong coupling between graphene and Ni(111) is substantially reduced (see Section 1.1). This decoupling in particular partially restores the linear dispersion of graphene's π bands and shifts the Dirac cone closer to the Fermi level E_F, as evidenced by static angle-resolved photoemission spectroscopy (ARPES) measurements on Au intercalated graphene/Ni(111) [48].
This study has two primary objectives, presented in Figure 3.1:

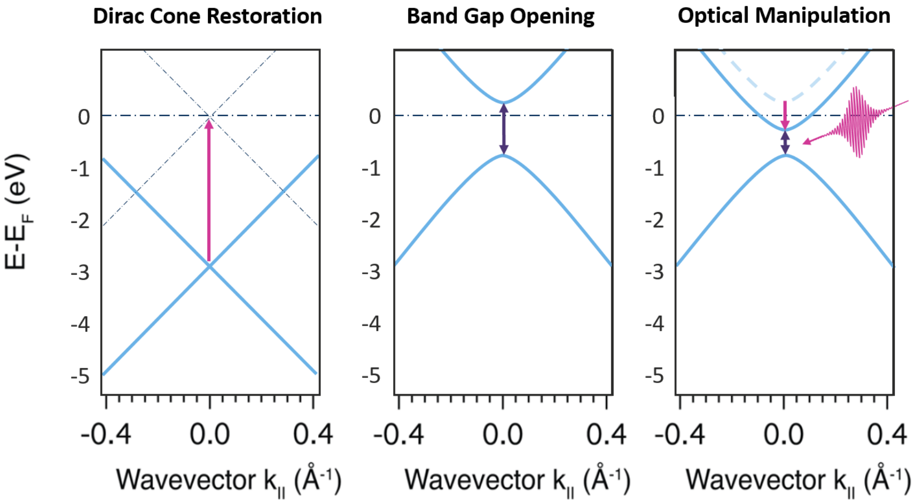

Figure (3.1) Research Objective - Band gap Engineering in Graphene: From restoring the Dirac Cone back to E_F over the introduction of a band gap to the optical manipulation of the gap.

Can intercalating a heavy element into the graphene/Ni(111) interface restore graphene's Dirac band structure and open a substantial band gap at the Dirac point?
If a band gap is present in graphene/Pb/Ni, how does it respond to ultrafast optical excitation?
Therefore I'll demonstrate and analyse the existence of a band gap at graphene's Dirac point induced by Pb intercalation and shed light on its origin. By exploring the ultrafast dynamics of this induced band gap under optical excitation, I aim to assess whether the gap (and more generally the electronic structure) can be modulated on femtosecond timescales. Achieving an ultrafast handle on the band gap would be a first step toward active, light-operated graphene devices, where one could switch graphene band gap magnitude between e.g semiconducting (gapped) and semi-metallic (gap-less) states with light.

This chapter starts with describing the static electronic structure of Pb-intercalated graphene/Ni(111) as revealed by angle-resolved photoemission spectroscopy (ARPES). A particular focus is placed on the section "**Band gap or no band gap?**" (3.3), which examines whether a Dirac point gap is present, how large it is if so, and what its implications are. In this section careful fitting of the Dirac

cone dispersion is employed. A consideration of various physical mechanisms (substrate hybridisation, sublattice symmetry breaking, spin-orbit coupling) that could contribute to any observed gap is attempted. Discrepancies with theoretical predictions (for example, whether the gap matches what a pure spin-orbit effect would suggest) are highlighted to provide context. In the subsequent section, "**Exploring the possibility for optical manipulation of the graphene band gap**", time-resolved ARPES measurements are presented that probe the graphene Dirac bands immediately after an ultrafast laser excitation. Experimental evidence for transient modifications of the band structure (such as changes in the gap or Dirac point energy), will be discussed as well as possible physical mechanisms, ranging from hot-carrier screening to lattice dynamics, that might explain the observations. I also assess the limitations of the data in drawing firm conclusions about optical gap control.
Lastly, I'll present the **key findings: the successful induction of a band gap in graphene via Pb intercalation and the initial demonstration of its ultrafast response**. The goal is to contextualise how Pb-intercalation in combination with a Ni(111) substrate fits into the broader landscape of graphene band-engineering. A short summary at the end highlights the essential results and their relevance—particularly emphasizing how a tunable graphene band gap could be leveraged in future spintronic applications.

3.2. The sample system

The upcoming section covers an introduction into the measured sample system is given, while for questions regarding the sample preparation I kindly refer to Section 2.1, .

3.2.1. Structural and geometric information

Graphene/Ni(111)

The geometric and electronic properties of the graphene/Ni(111) interface are well established through density functional theory (DFT) and a range of experimental techniques such as scanning tunnelling microscopy (STM), near-edge x-ray absorption fine structure (NEXAFS), photoemission spectroscopy, low-energy electron microscopy (LEEM), and low-energy electron diffraction (LEED). Reported adsorption heights for graphene on Ni(111) range from approximately 2.21 Å±0.04 Å [29] and 2.11 Å [49] down to 2.03 Å [50]. For a covalently bonded configuration, the minimum height is about 1.97 Å, while pure van-der-Waals interactions would yield 3.33 Å [51]. These values indicate a strong chemical bonding between graphene's π orbitals and Ni 3d electrons. Our own LEED, ARPES, and NIXSW studies [29] confirm that graphene adopts a flat, top-fcc adsorption geometry on the lattice-matched Ni(111) surface, ensuring homogeneous charge distribution. While the graphene is slightly stretched, relaxation after Pb intercalation into a wider Brillouin zone size was measured within this work (see Figure 3.6). It can be assumed, that no strong geometrical effects, like buckling influence the systems electronic structure.

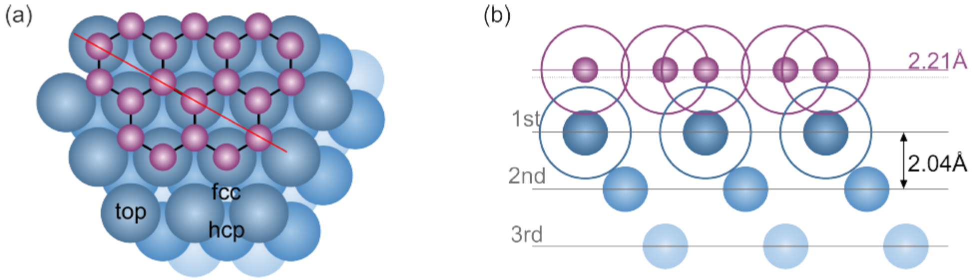

Figure (3.2) Graphene/Ni(111) interface: Adsorption height and geometry. (a) Top view and (b) vertical adsorption model of graphene on Ni(111), showing experimentally determined adsorption heights (purple) relative to the Ni(111) surface (blue). The dashed line indicates the covalent bonding distance. Reprinted with kind permission of the author from [29].

Graphene/Pb/Ni(111)

Intercalating lead beneath graphene serves to decouple the chemically bound graphene from the Ni(111) substrate and to introduce strong spin-orbit coupling (SOC) via the proximity effect [48]. normal incidence X-ray standing wave studies indicate that after complete intercalation, the Pb layer is flat, with an adsorption height of 2.38 Å ± 0.04 Å above Ni(111) and the graphene layer positioned at a distance of 6.08 Å ± 0.04 Å from the Ni layer [29] (see Figure 3.3). The graphene–Pb distance, corresponding closely to the sum of their van-der-Waals radii, confirms that the graphene is only weakly bound with the underlying Pb and exhibits quasi–free-standing behaviour.

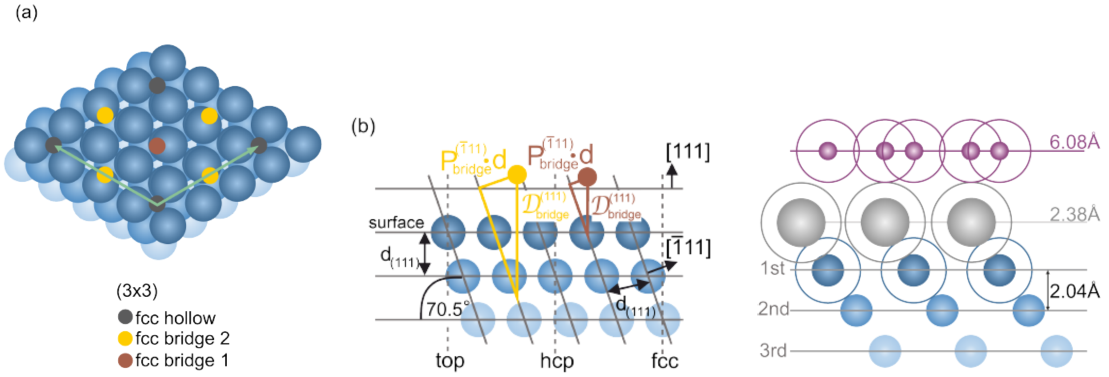

Figure (3.3) Graphene/Pb/Ni(111) Interface: Vertical and horizontal absorption. Illustration of the adsorption geometry for Pb atoms at the Ni(111) surface. Yellow and brown atoms illustrate both bridge sites, which were different in the NIXSW-analysis in [29]. (a) Adsorption model for (3x3) Pb superstructure with 4-atomic basis on Ni(111). (b) Horizontal-bridge sites arrangement. The coloured triangles illustrate the trigonometric relations with respect to the inclined Bragg planes. (c) Vertical adsorption model of graphene and Pb on Ni(111) showing the experimentally determined distances: Pb is 2.38 Å above Ni(111) and graphene is 6.08 Å above the Pb layer. Reprinted with kind permission of the author from [29].

Analysis of bonding distances (Ni–C ($d_{cov} \approx 1.97$ Å, $d_{vdW} \approx 3.33$ Å), Ni–Pb ($d_{cov} \approx 2.54$ Å, $d_{vdW} \approx 3.65$ Å), and Pb–C ($d_{cov} \approx 2.19$ Å, $d_{vdW} \approx 3.72$ Å) [51]) suggests that Ni and Pb form a metallic bond, enabling a closer interaction than expected for purely covalent or van-der-Waals bonds. The NIXSW results, combined with detailed analysis of Pb arrangement [29], support the formation of an ordered Pb intercalation layer in well-defined fcc-hollow and bridge configurations. The Pb-adsorption configuration is the fcc-hollow site, presented in Figure 3.3, in which the top atoms are located on top of an atom in the third nickel layer and the bridge atoms are situated vertically above the midpoint of two atoms in the third nickel layer. The same NIXSW studies by Schott *et al.* found, that the adsorption height and the occupied adsorption sides vary depending on the Pb coverage [29].

Moreover, NIXSW studies indicate that post–intercalation graphene is no longer aligned with the three-fold symmetry of Ni(111), likely due to a relaxation process that minimise interfacial strain.

3.2.2. Electronic structure

After successfully intercalating a monolayer of Pb at the graphene/Ni(111) interface (see experimental methods in Section 2.1), I used ARPES imaging to map out the band structure of the system near the graphene K-point (the corner of the Brillouin zone where the Dirac cone is located). Figure 3.4 shows a comparison of the ARPES spectra for graphene directly on Ni(111) ((a)-top) versus graphene with intercalated Pb ((a)-bottom). In the as-grown graphene/Ni case (prior to intercalation), the graphene-derived π bands are not readily discernible near the Fermi level (E_F) due to strong hybridisation with Ni states. Instead, one observes a broad spectral feature indicative of mixed Ni 3d–C 2p character, and the Dirac point is effectively obliterated (it is pushed far below E_F and smeared by interactions) [23].

In stark contrast, after Pb intercalation, the ARPES reveals a clear linear dispersion characteristic of graphene's Dirac bands. The π and π^* bands (valence and conduction bands of graphene) form an "X"-shaped dispersion, visible in Figure 3.5, that resembles that of quasi-free-standing graphene, demonstrating that the Pb layer has decoupled the graphene from the Ni substrate, as further illustrated by the zoomed-in view in Figure 3.4.

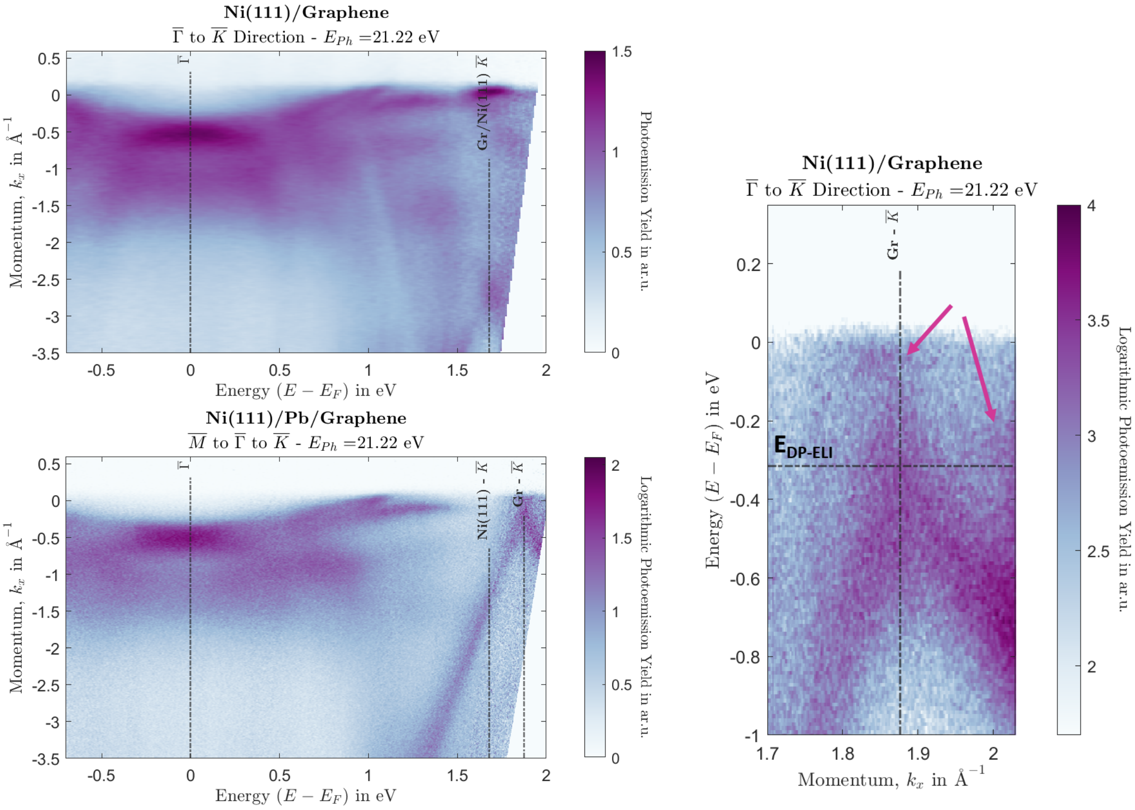

Figure (3.4) Electronic structure of the Graphene/Ni(111) and the Graphene/Pb/Ni(111) Interface. (a) Top: Monolayer Graphene on Ni(111) - Photoemission Yield. $\overline{\Gamma}$ to $\overline{K}$ direction. Measured with an VUV-lamp using a photon energy of $E_{ph} = 21.2182$ eV. Bottom: Static ARPES VUV(21.22 ev) - M to Γ to K - of lead intercalated Graphene on Ni(111). (b) lead intercalated Graphene on nickel - Dirac cone - Static ARPES data of graphene/Pb/Ni(111) around the K-Point, in Γ - K direction using E_{Ph} =21.22eV. A dashed line marks the extracted Dirac point position from the ELI-dataset shown in the next section. Two pink arrows indicate prominent Ni-features that obscure the graphene band gap.

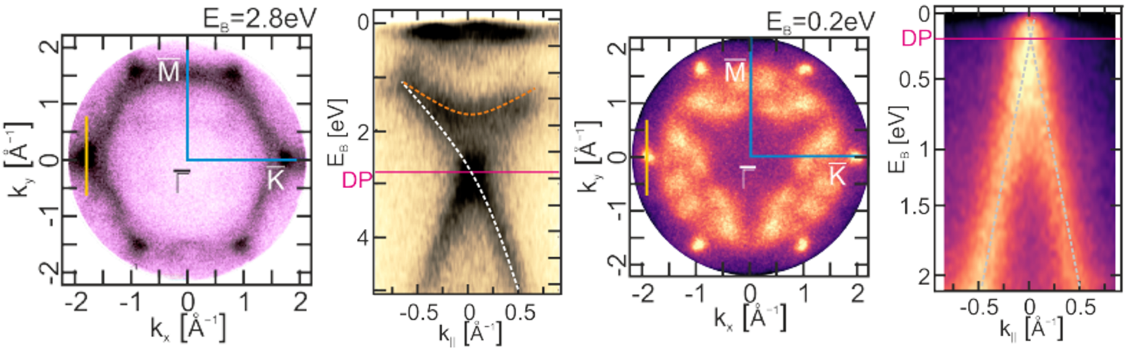

Figure (3.5) Comparison of nanoESCA constant energy map (CEM) and Dirac cone data of graphene/Ni(111) and graphene/Pb/Ni(111) depicted are momentum microscopy measurements of graphene/Ni(111) on the left and graphene/Pb/Ni(111) on the right. The orange and yellow line indicate the position of the energy momentum distribution map shown next to the respective CEM. Reprinted with kind permission from [29].

.

Weak electron doping shifts the Dirac cone towards $\sim E - E_F = 0.21\,\mathrm{eV}$ indicating, that Pb is acting as an electron donator.
The change of the electronic spectrum at the $\overline{\Gamma}$-point can be investigated using Figure 3.6, showing a dampening of the Ni-features near E_F, the shift of the work-function, and a secondary cut-off, resulting from incomplete intercalation of the sample.
The restoration of the sharp Dirac cone confirms the successful formation of a Pb buffer layer that electronically isolates graphene while preserving its lattice coherence with the substrate.

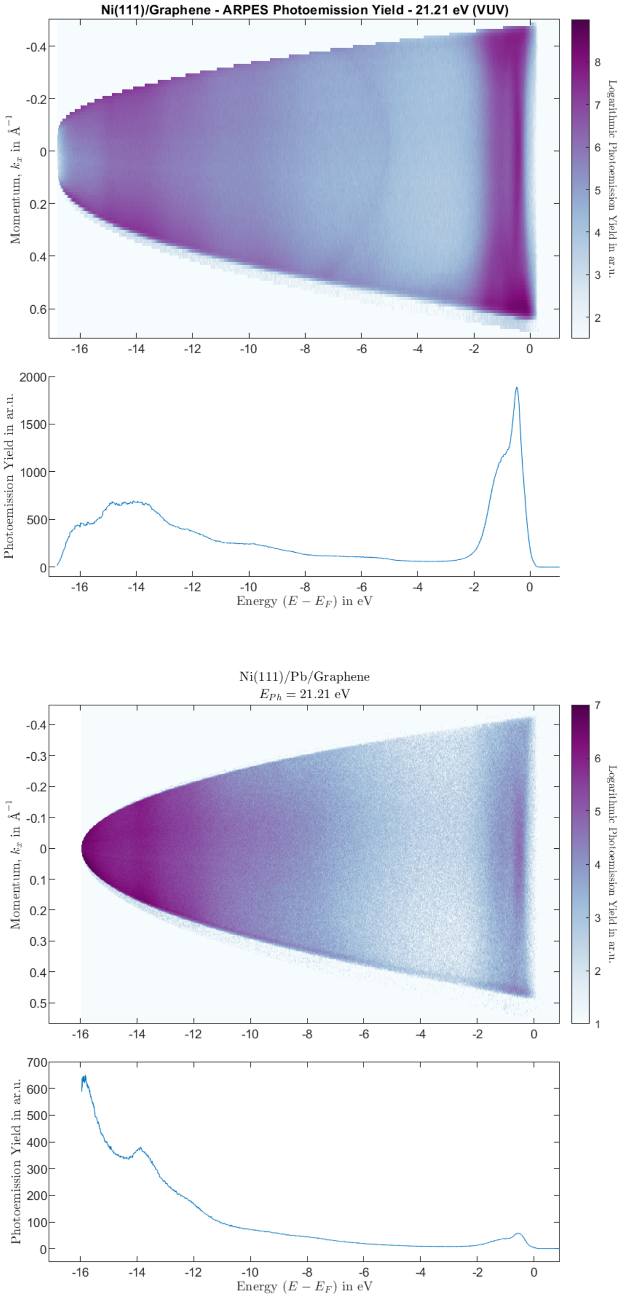

Figure (3.6) Static ARPES VUV $E_{ph} = 21.21\,\mathrm{eV}$ sweep around Γ-Point for Graphene on Ni(111) (a) and lead intercalated Graphene on Ni(111) (b)

3.3. Band gap or no band gap?

This section investigates whether lead intercalation induces a band gap at the Dirac point of graphene on Ni(111) (graphene/Pb/Ni(111)).
As discussed previously and evident in the ARPES data (e.g. Figure 3.15), no band gap is immediately apparent in the raw photoemission spectra collected using a VUV-light source at $E_{ph} = 21.21\,\text{eV}$ photon energy in our lap [1]. Specifically, in the time-resolved datasets, presented in the next section, collected using a HHG probing pulse at $E_{ph} = 22.25\,\text{eV}$ where no clear band gap is visible.
However, literature on analogous systems predicts a gap opening due to enhanced spin-orbit coupling (SOC) from the intercalated lead [20, 48]. Hence, it became clear that “finding” and analysing the band gap in static and rich in electron dynamic, time-resolved measurements would be challenging. Fortunately, I succeeded in doing so, hence in the next section two approaches, firstly for static measurements and secondly for the time-resolved dataset, will be presented.

During a measurement campaign at the **ELI-ALPS facility in Hungary**, we took high resolution images using the Helium-II-emission line of a VUV lamp light source ($E_{Ph-He2} = 40.57$eV. This photon energy is expected to yield a higher photoemission cross-section for the graphene and a lower for the nickel bands. The overlapping of these bands in the Dirac cone vicinity is thereby expected to be lower, offering the possibility to investigate the graphene bands with dampened Ni-influence. The results were analysed by Alexander Schmid. Figure 3.7 illustrates a clearly visible graphene band gap. All though the measured sample exhibited additional graphene rotational domains (due to imperfect graphene growth), visible as additional features next to the graphene spots, the data are comparable to other measurements from our lab. An EDM and the corresponding spectrum taken from the area surrounding the main graphene feature yield a clearly visible gap. The lower cone maximum is located at $E - E_{F,lower} = -450\,\text{meV}$ while the upper cone exhibits a minimum at $E - E_{F,lower} = -180\,\text{meV}$, resulting in a graphene band gap of $\Delta E = 270\,\text{meV}$.

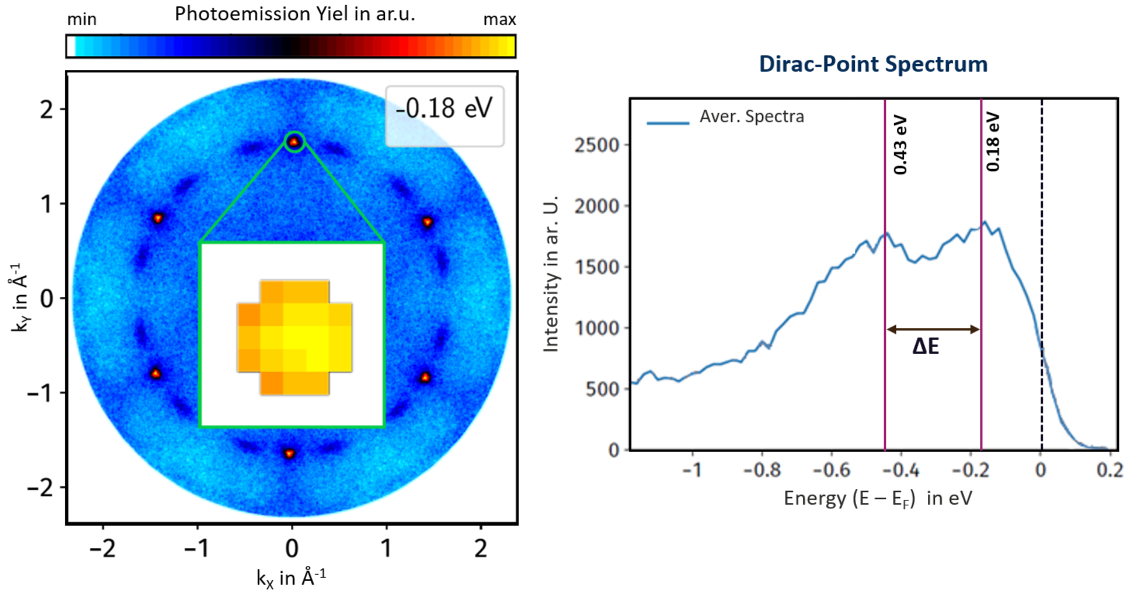

Figure (3.7) ARPES data showing the graphene/Pb/Ni(111) band gap. On the left a CEM at $E - E_F = -180\,\text{meV}$ of the graphene/Pb/Ni(111) heterostructure is shown. The upper graphene cone part close to its minimum is illustrated. Additional graphene rotation domains, originating from an imperfect graphene growth beforehand, are visible as additional features to the left and right of the main graphene Dirac cone. The to the Dirac points corresponding spectra were extracted and averaged. The results are shown on the right and yield a band gap of $\sim 270\,\text{meV}$. The data were taken at the ELI-ALPS facility in Hungary and presented at the DPG spring meeting 2025 by Alexander Schmid [52].

---

[1] Note: This specific dataset was collected without me being present, therefore I can not account for the accuracy of the sample alignment. It is generally possible, and a common issue for ARPES measurements, that the sample was not perfectly aligned towards the analyser sensitivity axis and the momentum cut captured therefore not perfectly centered at the K-Point. A misalignment would effect the band gaps visibility or its extracted size.

Importantly, the Dirac point energy E_D is found to lie below the Fermi level, indicating n-type doping of the graphene: E_D is about $-315\,\mathrm{meV}$ binding energy. This means the Fermi level cuts through the conduction band, placing the system in a moderately doped regime, shortly discussed in Section 3.2.2. Such doping likely arises from charge transfer between graphene, the Pb layer, and the underlying Ni. A similar magnitude of n-doping ($\sim 400\,\mathrm{meV}$) was reported for graphene intercalated with another heavy element (bismuth on Ir(111)) [13], suggesting that donation of electrons to the graphene is a common outcome in these heavy-intercalation systems. In our case, the Pb layer (which is metallic) and the Ni substrate (also metallic) establish a certain interface dipole and work function alignment that results in excess electrons in graphene. The exact doping level can be sensitive to details like Pb coverage and interface structure (hence different datasets might yield different results), but the observed E_D shift confirms a pronounced charge transfer.

The data taken at the ELI-ALPS nanoESCA endstation yield astonishingly clear results. Unfortunately, this is not the case for the data taken in our lab, and even less for the time-resolved HHG-probed datasets. To examine this in detail, the **Time-dependent constant-$E - E_F$ fitting routine**, described in Section 2.3.4.4, was applied to trace the evolution of the graphene π-band with high precision.

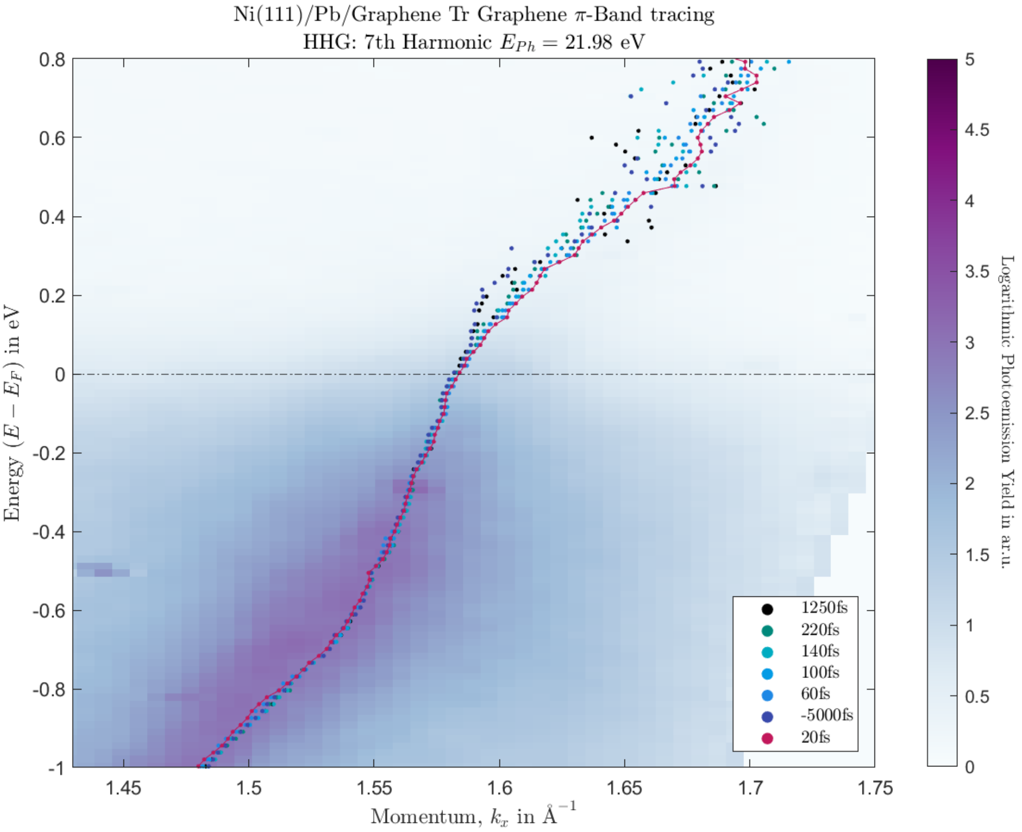

Figure (3.8) Graphene/Pb/Ni(111) ARPES Data for $\Delta t = 20\,\mathrm{fs}$ overlayed with the graphene π band positions for 7 different time-steps. The scatter plots show the fitted peak positions for $\Delta t = -5000\,\mathrm{fs},\ 20\,\mathrm{fs},\ 60\,\mathrm{fs},\ 100\,\mathrm{fs},\ 140\,\mathrm{fs},\ 220\,\mathrm{fs}$ and $1250\,\mathrm{fs}$. The red line plot additionally marks the results for $\Delta t = 20\,\mathrm{fs}$.

While the details of the time-resolved graphene-band tracing become relevant later, here the focus lies upon examination if a band gap can be detected in this dataset and if yes, to extract its size. One result from the fit is the peak position (momentum position for a fitted energy slice). By overlaying this fitted graphene-π-band positions onto a segment of the ARPES data, as shown in Figure 3.8, one can compare the results to the photoemission yield (in the unoccupied region, due to the only transient population, the fit-results are obtained shortly after t_0 are most reliable.). The figure presents **scatter plots** for different time delays ($-5000\,\mathrm{fs}$, $20\,\mathrm{fs}$, $60\,\mathrm{fs}$, $100\,\mathrm{fs}$, $140\,\mathrm{fs}$, $220\,\mathrm{fs}$ and

1250 fs). While the peak position represents the ARPES-image nicely (image was captured closely after t_0 it therefore represents the red data points), and an interesting dynamic change of the graphene band is apparent, it does not show a clear band gap.

This raises the question weather the data, or the sample are flawed or, if more complicated analysis is needed. To firstly validate the findings regarding the band position fitting and the band gap position, Figure 3.9 compares the fitted data at $\Delta t = 20\,\mathrm{fs}$ (dark blue) with static DFT calculations from Marius Weber (yellow), where the background represents the second derivative of the Tr-ARPES signal at $\Delta t = 20\,\mathrm{fs}$. Although the fitted peak positions largely coincide with the experimental data, discrepancies persist relative to the theoretical predictions. Assuming a band gap opening (as is confirmed by the static data in Figure 3.7), such discrepancies may stem from the well-known underestimation of the proximity effect in weakly bound systems by standard density functional theory (DFT), as observed in graphene/Au/Ni(111) [20], as well as lattice imperfections and sublattice symmetry breaking that is not accounted for within this calculations (a revision of the theoretical results may therefore be required).
It appears, contradicting the expectations and the experimental evidence, that no band is opened.

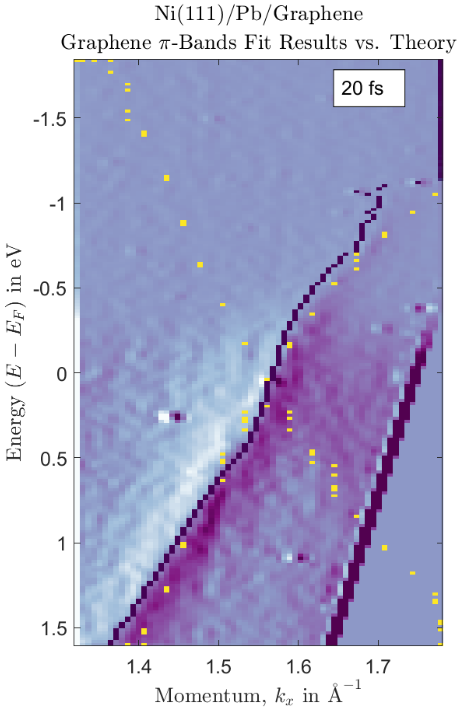

Figure (3.9) In the background the 2nd derivative of the Graphene/Pb/Ni(111) ARPES Data for $\Delta t = 20\,\mathrm{fs}$ are displayed overlayed with the graphene π band position from the fitting routine (dark blue) at $\Delta t = 20\,\mathrm{fs}$ and the static theoretical calculations (yellow) from Marius Weber.

To address the key question:
Can intercalating a heavy element into the graphene/Ni(111) interface restore graphene's Dirac band structure and open a substantial band gap at the Dirac point?
For the time-resolved dataset I analyse the fit results. The fitting itself is addressed in the next section and its quality and reliability is critically assessed on page 47, in the following only a short summary is needed: From the fit graphene peak position, width and occupation parameters are extracted for all measured timesteps. While the fitting routine robustly captures the π-band dynamics in the occupied region and near E_F, caution is warranted when interpreting results at higher energies, particularly far from t_0. This is due to the fact that in the unoccupied region the band can only be fitted as long a the light induced transient population is present. Conversely, within the occupied region and in the unoccupied region near E_F and close to t_0, the results are reliable for further analysis. Hence, for an initial band gap extraction, only the data close to t_0 are used.

From an analytical standpoint, the initial indication of a band gap in the time-resolved data was obtained via the constant-energy peak finder (Figure 3.14). Here a deviation from a linear dispersion of the graphene band, as can be found when a band gap is present, was extracted. Examination of Figures 3.8 and 3.10 supports this finding. I therefore affirm that a band gap is present, as evidenced by the clear deviation of the graphene π-band from linear dispersion, a deviation that can only be explained by a flattening of the graphene features. Notably, the fit still identifies a peak due to the superposition of graphene and nickel contributions, as best illustrated in Figure 3.4. Specifically, in Figure 3.4 a prominent nickel feature is observed around 1.55Å^{-1}, which coincides with the region where the graphene π-band shifts following intercalation (Figure 3.4). Thus, both the peak position and its width must be considered in the interpretation. Overlaying these parameters emphasises the region influenced by nickel, as shown in Figure 3.10.

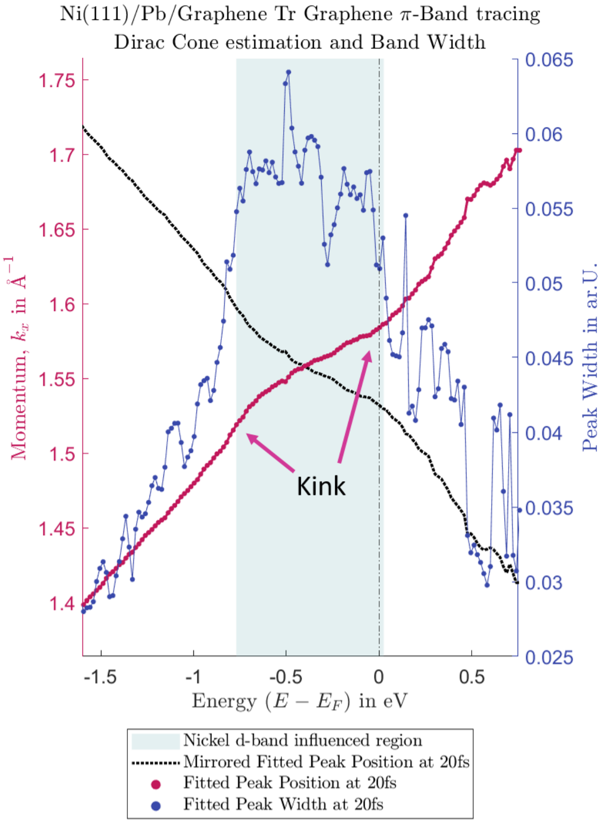

Figure (3.10) Graphene/Pb/Ni(111) graphene π band position and width from the fitting routine at $\Delta t = 20$fs. The red dotted line shows the fitted peak position and the black is a mirror of this results to illustrate the Dirac cone. The results for the graphene width are plotted in blue and the coloured area marks the region were the width strongly differs from the graphene band width in the occupied area. This is due to the influence of the nickel d-bands. The arrow highlights the gradient change and thereby the transition from a mostly graphene to the mostly Ni influenced parts.

For this analysis, data at $\Delta t = 20\,\text{fs}$ were used because the graphene π-band tracing in the unoccupied region is most reliable shortly after t_0. Furthermore, a mirrored peak position is included as guide to the eye to facilitate easier estimation of the Dirac cone. The pronounced discrepancy in the fitted peak width in addition to its observed step increase between the regions $-0.90\,\text{eV}$ to $-1.55\,\text{eV}$ and $-0.04\,\text{eV}$ to $-0.86\,\text{eV}$, is attributed to the relatively flat Ni-derived feature in that area. This superposition allows the detection and fitting of a nickel peak, even though it is not the target of the fitting routine, overshadowing the graphene bands gap development. The combined effect of graphene band flattening and superimposed nickel features produces a pronounced kink in the fitted peak position (see Figure 3.10). Although a similar band morphology was reported in potassium-doped graphene/SiC systems [53], where the kink was ascribed to many-body interactions renormalise the graphene π^*-band post-excitation without a gap opening, my data do not exhibit a nearly linear dispersion with a post-excitation kink. Thus, the many-body explanation can be rejected, and the question remains: what is the magnitude of the band gap? Definitive quantification requires further investigation, ideally incorporating spin-resolved measurements, here, only a preliminary estimate is provided. Considering that Ni features affect the fitting, regions dominated by nickel can be disregarded when estimating the gap. In Figure 3.10 an arrow indicates the change of the slope of the dispersion marking the transition from predominantly graphene-derived to Ni-influenced regions. The average graphene band width, determined from the fitted peak width in the occupied region (excluding Ni-dominated segments), is approximately 0.0335Å^{-1}. Figure 3.11 illustrates both the average graphene band width from the photoemission experiment and the estimated band gap. The figure shows a Dirac cone approximation (red: fitting results, black: their mirror). To estimate the graphene dispersion near the Dirac point, green-grey dashed lines are used as guidelines. A broad dashed line represents the band's mass centre (including linear segments and parabolic segment marking the band flattening at the gap extrema) and thin dotted lines represent

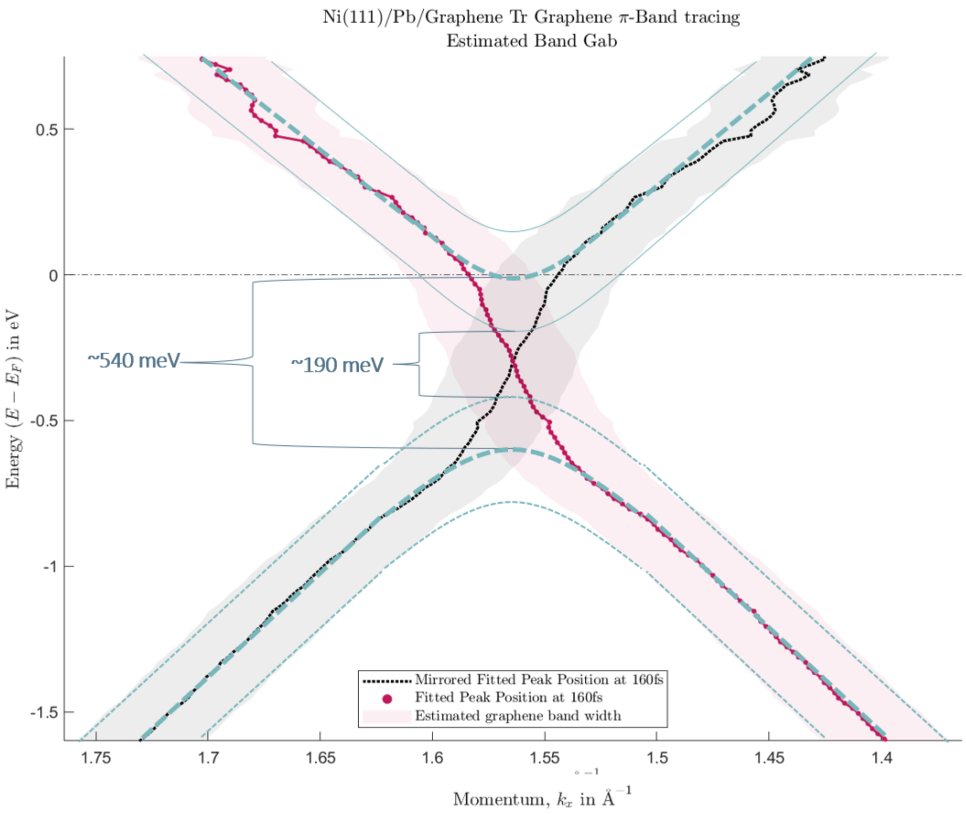

Figure (3.11) Graphene/Pb/Ni(111) graphene π-band position and broadening from the fitting routine at $\Delta t = 20\,\mathrm{fs}$. The red dotted line represents the fitted peak position with its mirror (black) to approximate the Dirac cone. The green-grey dashed lines are guidelines: linear segments represent the typical graphene dispersion near the Dirac point, while the parabolic segment marks the band flattening at the gap extrema. The broad dotted line indicates the band's mass centre and the thin lines its FWHM. Based on these, the band gap is estimated to be approximately $550\,\mathrm{meV}$ (mass-centre) and $190\,\mathrm{meV}$ (1/e width).

the estimated FWHM-width of the graphene band. Based on these, the band gap is estimated to be approximately between $190\,\mathrm{meV}$ (1/e width) and $550\,\mathrm{meV}$ (mass-centre width). These results are in agreement with the band gap size estimated of $\Delta E = 270\,\mathrm{meV}$ from static imaging presented in Figure 3.7. Deviations can be the result of different graphene layer quality (in the static measurements conducted at the ELI-ALPS facility multiple graphene rotational domains were present) and the exact amount of intercalated lead.

To qualify the results further a band-distribution fit was performed on the extracted peak positions. Assuming a simple model of gapped Dirac fermions, the dispersion can be described (in the vicinity of K) by:

$$E_{\pm}(k_{II}) = E_D P \pm \sqrt{\hbar^2 v_F^2 (k - k_{DP})^2 + (\Delta E/2)^2} \tag{3.1}$$

where $E_D P$ is the Dirac point energy (mid-gap energy), $k_D P$ is the wave vector at the Dirac point, v_F is the Fermi velocity (slope of bands), and ΔE is the energy gap between the conduction and valence band (i.e. the magnitude of the gap is ΔE). For a gap-less Dirac cone, $\Delta E = 0$ and the bands meet at a point, for a gapped spectrum, $\Delta E > 0$ and there is an avoided crossing with a gap $\Delta E < 0$ (bands move past each other while forming a gap to avoid crossing). The results yield different gap sizes depending if the upper or lower part of the graphene band is fitted, due to the not perfect X-shape of the graphene Dirac cone in the used cutting direction. Additionally, due to the "dark corridor" only one arm of the Dirac cone can be fitted. The best-fit to the dispersion yields a finite gap, supporting the previous analysis. Specifically, the fitting suggests a gap of approximately $\Delta E \sim 490\,\mathrm{meV} \;-\; 315\,\mathrm{meV}$, with an uncertainty on the order of $25\,\mathrm{meV}$ - $115\,\mathrm{meV}$. Fitting the lower part of the graphene band resulted in lower uncertainties, but higher band gap results. The results represent the **mass centre** fitting yielding lower values as the optical approximation shown

Table (3.1) Fit Results for graphene band gap at $\Delta t = 20\,\mathrm{fs}$

	$DeltaE$ **in meV**	**Error in meV**
$\Delta t = 20\,\mathrm{fs}$ upper part	315	110
$\Delta t = 20\,\mathrm{fs}$ lower part	470	25

before. To verify the trend, visible in Figure 3.8 of a **change in band gap magnitude** a more detailed fitting, including more time-steps is needed, see next section.
Compared to similar systems, **these values appear too large**, which may stem from the extraction methodology. In conventional photoemission analyses, the peak mass centre is often not rigorously fitted and the gap is estimated visually, typically yielding smaller values due to the persistent intensity at the 1/e width (the optical estimation for the 1/e width also yielded a smaller gap size). Moreover, the influence of initial conditions, fitting constraints, and overall fit quality must be considered. Although the fitting parameters were carefully chosen (see Section 2.3.4.4), the **Tr-HHG fitting results cannot substitute for high-resolution imaging**.

It is now established that a band gap ΔE exists (on the order of a few hundred meV, exact values depending on the extraction method), the origin and implications of this gap need some consideration. A gap at the Dirac point in graphene can originate from several possible mechanisms. While these mechanisms are not mutual exclusive, I will argue in the following, that the band gap observed here, originates mainly from a trivial (sublattice symmetry breaking) rather than a non trivial mechanism like Kane-Mele-type SOC. A distinction between different SOC mechanisms will be made, therefore Figure 3.12 illustrates three simplified examples of SOC induced spin-splitting that can cause a band gap. Depicted are the **Kane-Mele-type SOC** (left): opens a gap at the Dirac point with opposite spin polarisation at K and K',characteristic for topological insulators like Bi_2Se_3 and e.g. causes the quantum spin Hall effect; the **Rashba-type SOC** (centre): splits bands linearly with **momentum**, without a gap at the crossing point typical of non-centrosymmetric systems and can be observed e.g. in gold; and **Atomic SOC** (right): splits bands linearly with **energy**, in spin-degenerated bands.

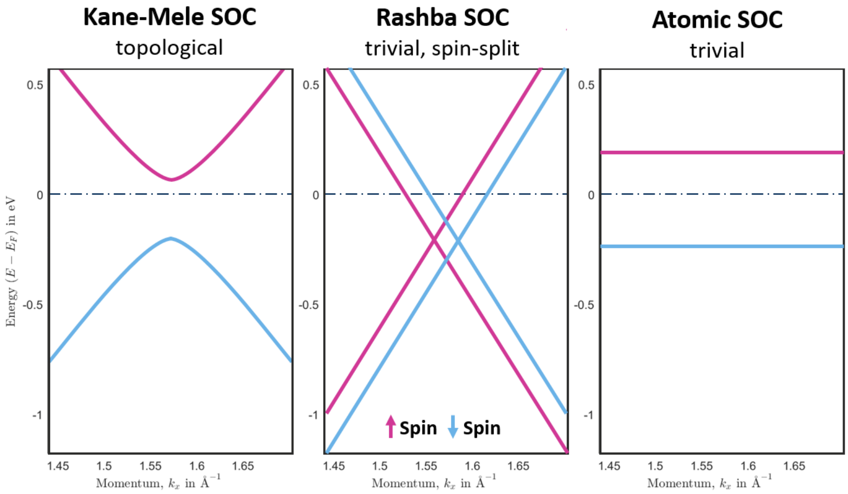

Figure (3.12) Comparison of different SOC induced band alternations. Kane-Mele SOC (left), Rashba SOC (centre) and Trivial (atomic) SOC.

The distinction between Kane-Mele-type and Rashba-type spin-orbit coupling (SOC) is clearly visible in ARPES experiments. In topological insulators like Bi_2Se_3, ARPES reveals a single Dirac cone surface state with spin-momentum locking, resulting from Kane-Mele-type SOC and band inversion. These states are topologically protected and persist despite non-magnetic disorder [54]. In contrast, materials like BiTeI display large Rashba-type spin splitting in the bulk conduction and valence bands due to broken inversion symmetry, as seen in ARPES spectra showing characteristic spin-split parabolic bands [55]. While both types of SOC lead to spin-polarised bands, only Kane-Mele-type SOC generates non-trivial topological surface states, distinguishing topological insulators from Rashba-split trivial systems. Let's adapt this additional knowledge to the graphene/Pb/Ni(111) system:

Spin-orbit Coupling (SOC) induced gap: Proximity to a heavy element can introduce a non trivial spin-orbit mass term in graphene's Hamiltonian (analogous to the intrinsic SOC that is very weak in pristine graphene). This can open a Kane-Mele type gap and is expected to preserve time-reversal symmetry, potentially leading to a topological insulator state. In such a scenario, the gap might come with a characteristic spin-splitting of bands and a helical spin texture around K [54, 56].

Hybridisation with Substrate States: If there is residual interaction between graphene and the substrate through the intercalant (for example, if the Pb layer is not perfectly continuous or if Pb itself hybridise with graphene π orbitals), a gap could appear due to an avoided crossing or band folding involving substrate bands. For hybridised bands the non-topological Rashba-type SOC would additionally cause spin-splitting of the bands due to symmetry braking at the graphene-Pb-interface, again a signature that is expected to be visible in ARPES [55, 57].

Sublattice Symmetry Breaking (A/B asymmetry): If the two carbon sublattices of graphene exist and experience different potentials, the degeneracy at the Dirac point is lifted, opening a gap. This can happen if an intercalant or substrate breaks the sublattice equivalence (for instance, one sublattice might be preferentially closer to an intercalant atom, or there is a $\sqrt(3)x\sqrt(3)$-type ordering that distinguishes sublattices). A prominent example for this effect can be found with the graphene-h-BN structure were the sublattice symmetry braking causes a band gap of $\sim 200\,\text{meV}$ [58].

Structural Corrugation or Strain: A slightly non-uniform strain or buckling in graphene could also break symmetry or cause mini-gaps at the Dirac point (though usually strain shifts or distorts Dirac cones rather than opening a gap at K unless it induces a pattern that breaks symmetry).

In the following I want to evaluate the likelihood for some of those mechanisms, based on the presented data and similar systems from the literature. First, the possibility of **direct graphene–Ni hybridisation** causing the gap is unlikely. Since the very purpose of intercalation is to decouple graphene from Ni and it was established before, that the intercalation was successful in doing so. The ARPES data in Figure 3.4 show no trace of the Ni d-band interactions that were present before intercalation. Most notably the restoration of the graphene Dirac cone, from its distorted hybridised state to an almost linear feature with the Dirac point close to E_F, indicating the Pb layer is continuous and effective as a spacer. Although, one can identify the secondary cut of in the graphene/Pb/-Ni(111) spectrum (Figure 3.6) as an indication of an incomplete intercalation, small remaining not intercalated graphene/Ni(111) patches are unlikely to cause a global band gap opening [59]. Thus, **hybridisation with Ni** can be safely excluded as a cause of the Dirac gap in the intercalated system.

Next, we consider **spin-orbit coupling**. The magnitude of the gap $\Delta E = 190\,\text{meV} - 270\,\text{meV}$-from (1/e) width approximation and high resolution imaging (Fit: $\Delta E \sim 490\,\text{meV} - 315\,\text{meV}$) is intriguingly similar to that reported for graphene/Pb on Pt(111) ($\Delta E \sim 200\,\text{meV}$)[23], which was attributed to enhanced SOC. If SOC were the primary cause here, one might expect to see signs of spin splitting or other SOC-related effects. For example, a strong Rashba effect (from inversion asymmetry and SOC) could split each band into two spin-polarised branches. In spin-resolved measurements on graphene/Pb/Pt, a $\sim 100\,\text{meV}$ splitting between spin-up and spin-down bands was noted for the upper Dirac cone [23]. The ARPES measurements presented in this thesis were spin-integrated, therefore I cannot directly observe spin polarisation. However, no clear doublet structure in the bands (e.g. visible as double or strongly flattened peak in the fitted constant energy cuts) were resolved. Considering the given momentum resolution a splitting in the order of $\sim 100\,\text{meV}$ would have been noted. The bands appear singly degenerate within experimental precision. This could mean that any spin splitting is smaller than our resolution (tens of meV). It's worth noting that if time-reversal symmetry is preserved (implicating that the graphene on Pb/Ni system as prepared is overall non-magnetic), a spin-orbit gap in graphene would still produce two spin-degenerate bands (each Kramers-degenerate, one primarily spin-up on one valley and spin-down on the other, and vice versa). In other words, a QSHE-type gap would not necessarily split the ARPES spectrum into two separate bands, it would manifest as a gap, but each state is two-fold degenerate (with opposite spins in opposite valleys). Thus, the mere presence of a gap could be consistent with an SOC-induced topological gap. However, a key signature of an SOC gap would be that it is not accompanied by a breaking of sublattice (inversion) symmetry – the gap comes purely from the spin-orbit coupling opening a gap in the Dirac spectrum. Additionally, it is well established in literature, that the proximity to a ferromagnet induces a magnetic moment into the graphene rendering the assumption of a "non-magnetic" sample system unlikely.

The remaining question is the role of **sublattice breaking**. In the case of Bi-intercalated graphene on Ir(111) (a system with many parallels to ours, substituting Bi for Pb and Ir for Ni), a small Dirac gap ($\sim 19\,\text{meV} - 44\,\text{meV}$ depending on Bi-coverage) was observed [46]. In this study the gap was attributed primarily to A/B sublattice asymmetry induced by the intercalated Bi layer. Krivenkov *et al.* systematically ruled out induced SOC (using SR-ARPES) and substrate hybridisation as dominant causes, and instead pointed to the breaking of sublattice equivalence. Caused by the intercalant atoms sitting in specific sites relative to the graphene lattice (e.g. favouring beneath either A or B sublattice sites or causing a local distortion that differentiates the two). In the Pb/Ni(111) system, Pb is expected to occupy two different fcc-hollow and fcc-bridge sites in a (3x3)-superstructure coinciding with the 3rd Ni-layer (see Section 3.2.1). An ordered Pb layer on nickel might break the sublattice symmetry relative to graphene (depending on coverage and strain). Depending on the configuration, one sublattice might e.g. have a Pb directly underneath every third carbon, an other sublattice might not. The detailed NIXSW studies in [29] do not resolve an exact graphene adsorption side in respect to the nickel surface but determine that the graphene is in a "free floating" state and no longer exhibits its previous top-fcc configuration. It is assumed, that graphene still occupies the three-fold symmetric adsorption sites. But, the results in combination with other ARPES measurements indicate a "relaxation" of the graphene. Even a commensurate (1×1) layer of Pb that is slightly buckled could cause one sublattice to be slightly closer to Pb atoms than the other. Therefore, an **imbalance between graphene sublattices** is plausible due to the different adsorption sides of the Pb on the nickel surface and the dependency on the intercalants coverage which sides are occupied and the Pb-Ni-bonding distance [29].

Lastly, in his calculations, Marius Weber was not able to resolve a band gap in graphene. While this might be due to the underestimation of the proximity effect introduced by Pb, the complete absence of an SOC induced band gap is noteworthy. Additionally, his simplified model did not account for coverage dependent Pb-adsorption height and occupation sides.

Leading to the conclusion that the observed band gap might primarily be due to sublattice symmetry breaking by the ordered Pb intercalant layer, rather than an intrinsic SOC gap. This interpretation is consistent with the fact that similar magnitude gaps have been seen in other intercalation systems and were attributed to symmetry breaking [46]. It does not preclude a contribution from SOC – indeed, Pb's heavy atoms certainly introduce significant SOC in graphene's electrons – **but the dominant gap-opening mechanism appears to be a straightforward breaking of graphene's sublattice (inversion) symmetry**, i.e. a trivial band gap. But, a "trivial" gap still yields a semiconducting graphene (a mass term in the Dirac equation), which is highly valuable for electronics, though its topological properties (like QSHE) would be absent unless a spin-orbit gap component is present. Renewed calculations and spin-resolved measurements are one way to further test the nature of the gap.

In summary, the answer to the primary research question of this section:
Can intercalating a heavy element into the graphene/Ni(111) interface restore graphene's Dirac band structure and open a substantial band gap at the Dirac point?
Yes, Pb intercalation on Ni(111) induces a band gap at graphene's Dirac point via a tailored interface.
But, as discussed in the previous section, the likelihood of the gap being a result of pure SOC induced by the proximity effect is small. While this effect certainly plays a role, it might be dominated by the lattice mismatched induced band gap.
However the existence of this gap is a pivotal result – it shows that graphene can be transformed into a semiconductor simply by interface engineering. The implications are: a $\Delta E = 190\,\text{meV}$ from (1/e) or $\Delta E \sim 470\,\text{meV} - 315\,\text{meV}$ (fit) gap is large enough to quench the conductivity at the Dirac point (since k_BT is only$\approx 25\,\text{meV}$ at room temperature). Thus, graphene in this state can, in principle, be turned "off" in a device configuration, unlike intrinsic graphene which always conducts. However, the graphene in the graphene/Pb/nickel(111) system is n-doped overlapping with intrinsic

Ni-States. To utilise the gap for a transistor-like device, one would ideally adjust the Fermi level into the gap so that at equilibrium the Fermi level lies in the gap, yielding a semi-insulating state until e.g. a gate voltage moves the Fermi level into a band.
In comparison, the magnitude of the gap is much larger than what the $\Delta E \sim 20\,\mu\text{eV} - 50\,\mu\text{eV}$ intrinsic spin-orbit in pristine graphene would produce. The approach presented here is comparable with other systems like graphene on SiC with hydrogen intercalation ($\Delta E = 250\,\text{meV}$) and if the true gap size is on the higher end of our estimations even in the same range as for the naturally semiconducting material InAs ($\Delta E_{InAs}(t = 300\,\text{K}) = 417\,\text{meV}$) or InSb ($\Delta E_{InSb}(t = 300\,\text{K}) = 235\,\text{meV}$) [60–62]. For topological considerations the observed gap is significant. If it were indeed a non-trivial spin-orbit (Kane-Mele) gap, it would make graphene a high-temperature quantum spin Hall insulator. I‘ve argued that the gap is largely trivial, however even a trivial gap in a two-dimensional Dirac system is valuable, and any admixture of SOC could manifest in spin Hall effects. The critical takeaway is that **lead intercalation has enabled a robust band gap in graphene**. With this static characterisation the following section moves on to examine whether this induced band gap (and the Dirac bands) can be manipulated on ultrafast timescales by optical excitation.

3.4. Time-dependent evolution of the Dirac cone in lead intercalated graphene on Ni(111)

Having established a sizeable band gap in the Pb-intercalated graphene, an intriguing question arises: **Can we modulate or control this band gap (or more generally the electronic structure of graphene) using light pulses on ultrafast time scales?**
If achievable, this would pave the way for ultrafast optical switches and novel photonics/spintronics applications where graphene's conductivity or topological state could be toggled by light. This question was experimentally approached using time-resolved ARPES (Tr-ARPES) in a pump-probe scheme, which allows us to observe transient changes in the band structure following an ultrafast optical excitation. To elucidate the dynamics of the graphene/Pb/Ni(111) interface, time-resolved pump-probe ARPES measurements were employed. In our experimental setup, the sample was excited with a s-polarised pump pulse of approximately 55 fs duration from the KM-Wyvern Ti:sapphire laser amplifier system laser system, with a photon energy of $E_{ph,red} = 1.58\,\text{eV}$ (corresponding to a wavelength of 783 nm). This pump was followed by an extreme ultraviolet (EUV) probe pulse generated by high-harmonic generation (HHG) with a photon energy of approximately 22.25 eV [63].
The pump penetration depth in nickel of 13 nm [43] is comparable to the EUV probing depth in nickel of roughly 10 nm [44], while the effective photoelectron escape depth for the maximum kinetic energy of about 16 eV is confined nearly to a monolayer [45]. Consequently, the time- and angle-resolved photoelectron spectroscopy signal predominantly reflects the electronic structure of the topmost surface layer, as schematically depicted in Figure 4.2. A comprehensive description of the measurement setup and sample preparation is provided in Section 2.2 and 2.1, respectively.
When interpreting graphene photoemission data acquired with polarised light sources, it is critical to consider the so-called “dark corridor”. This effect, first observed in graphite and explained theoretically by Shirley **et al.** [64], results in a pronounced modulation of the photoemission intensity along the Dirac cone. For instance, in constant energy maps (CEM) acquired on graphene/Ir(111) intercalated by gadolinium [59] (see Figure A.5), a marked intensity minimum is observed on one side of the Dirac cone due to matrix-element effects. In my measurements, this phenomenon limits the observable portion of the Dirac cone to a single arm, as evident in Figure 3.4.

The ARPES system combined with the pump-probe technique used in this study provides energy–distribution maps (EDMs) at each pump-probe delay, enabling the capture of a complete band structure snapshot at every measured time step. Figure 3.13 shows a series of snapshots of the graphene/Pb/Ni(111) band structure at the K-point in the $\overline{\Gamma} \rightarrow \overline{K}$ direction, together with corresponding differential maps (differential map) that highlight the changes relative to a reference spectrum recorded well before t_0. In these differential map images, an increase in photoemission yield is indicated in red and a decrease in blue, while unchanged intensity appears white. The presented data where analysed according to the standard raw-data handling explained in Section 2.3.1. Notably, the differential maps reveal a burst of population in the formerly unoccupied arm of the Dirac cone, best visible on the right side of the differential maps close to t_0. This transient increase of photoemission intensity is caused by the pump pulse.

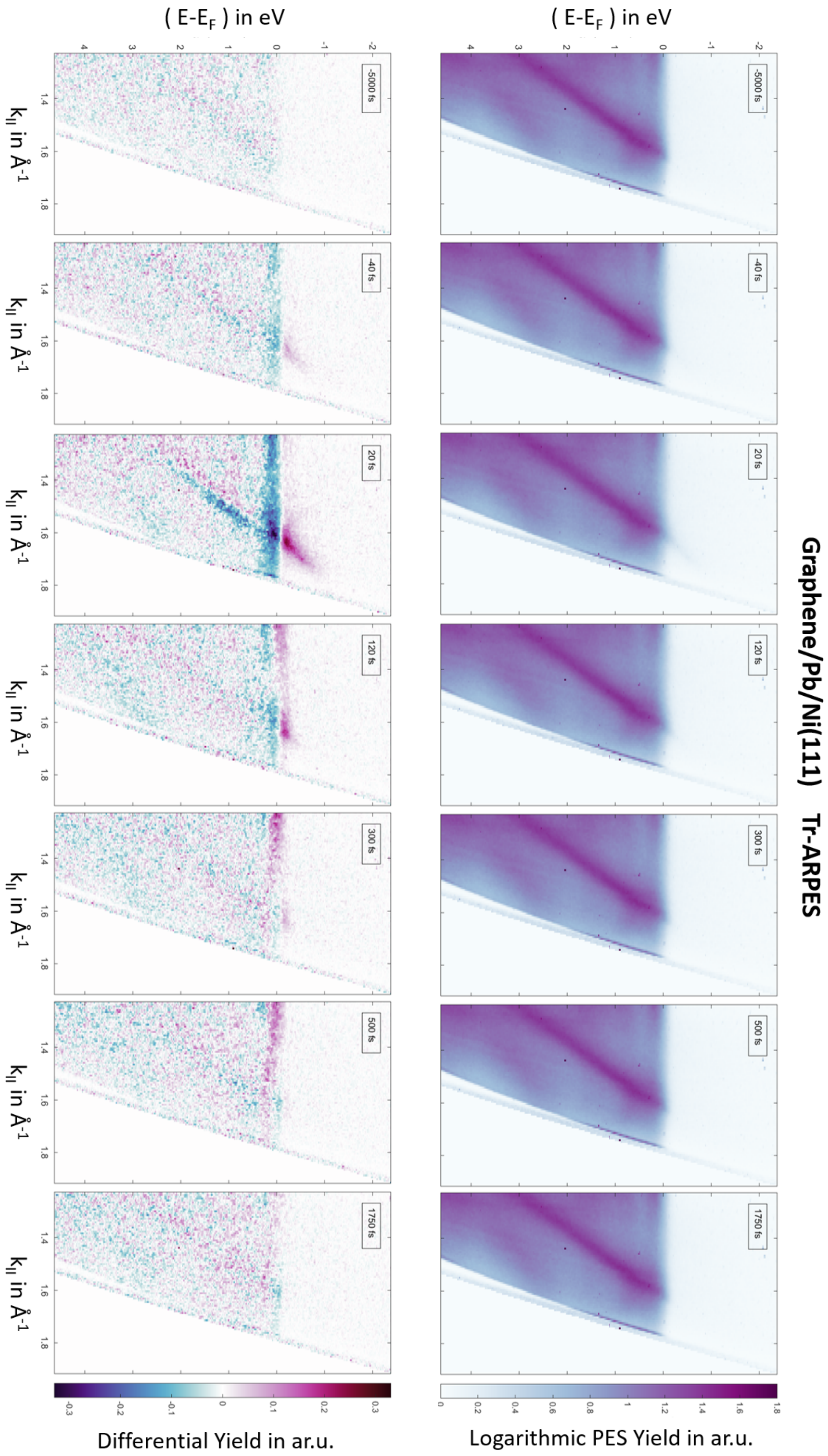

Figure (3.13) graphene/Pb/Ni(111) Tr-ARPES-data. The tops row shows Tr-ARPES data for different time-steps (as indicated in the inset). The bottom row shows differential map for the same time steps. Red indicates an increase of the photoemission signal in comparison to far before t_0 and blue a decrease. A clear excitation at t_0 into the unoccupied Dirac cone is visible (right side) as well as the excitation into the Ni bands at longer timescales ($\sim$ 120fs). The data were pumped with a red laser-pulse with $1.58\,\mathrm{eV}$ and probed using the 7th harmonic of the HHG beamline at $21.98\,\mathrm{eV}$

It excites electrons from below E_F into higher energy states, some of which are in the conduction band of graphene. These hot electrons can be photoemitted by the probe, allowing to observe states that are ordinarily unoccupied. In practice, at $\Delta t = 20\,\text{fs}$, we see that the upper Dirac cone (which was mostly not visible without pumping because it lay above E_F) is now clearly populated up to about$E - E_F = 1\,\text{eV}$. In other words, the conduction band of graphene becomes partially filled transiently. This is a common signature of photo excitation. Correspondingly, there is a depletion of electron population in the valence band just below E_F, as those electrons were excited upward.

A slight shift of the graphene π-band towards lower momentum values is also observed, suggesting a global band renormalisation. Indicated by the increase of photoemission signal in the differential data (red) to the left of the graphene π^*-band and a decrease (blue) on its original position. This renormalisation is most prominent near the Fermi level, yet remains detectable down to $-2.5\,\text{eV}$. Given the relatively low pump photon energy of 1.58 eV, the observed band shifts are likely attributable to renormalisation effects rather than direct transitions induced by the photon density of the pump pulse. Both, the excitation into the unoccupied region of the graphene band and the apparent band shift, are relatively short lived a no longer visible at 500fs after t_0.

Furthermore, while the graphene π-band dynamics are transient, diminishing after approximately 500 fs, the dynamics within the spin-split Ni bands (on the left of the depicted region) exhibit a delayed onset (around 100 fs) and persist over longer timescales.
The apparent changes of the graphene π^*-band position are slight and the expected band gap is not clearly visible, potentially due to the overlap of graphene and Ni(111) band-structure features close to E_F. To resolve the subtle time-dependent evolution of the graphene π-bands, a complex fitting routine was developed within this work. This routine allows to extract quantitative information on the band positions and widths as a function of pump-probe delay, thereby tracing the evolution of the Dirac cone following optical excitation.

3.4.1. Time- and angle-resolved photoelectron spectroscopy data fitting

This section provides an overview of the fitting routines applied to the time-resolved ARPES data, with further details provided in Section 2.3.4. In time-resolved pump-probe ARPES, overall band shifts arising from band renormalisation and space-charge effects must be considered. By tracking the time evolution of the Fermi function parameters — its energetic position, width, and amplitude — one can infer changes in the chemical potential and electron temperature. Thus, a sophisticated fitting approach is required.

Time-resolved pre-analysis tools: Prior to fitting, the Tr-Pre-Analysis Tools (Section 2.3.4.1) were employed. A linear background approximation, $f(E) = p_1 \cdot E + p_2$ (Section 2.3.4.1), corrects for HHG-specific background signals, excluding data points in the occupied region. Next, the Time-dependent Spectral Peak Finder (Section 2.3.4.1) was used to trace peak positions and movements over time (see Figure 2.13). Similarly, the Time-dependent Constant-$E - E_F$ Peak Finder (Section 2.3.4.1) extracts the approximate position of the graphene π-band and its $k_{||}$ shifts from constant-$E - E_F$ slices. An example at 20 fs after t_0 is shown in Figure 3.14. The chosen constant energy-cut was taken from the unoccupied region. Resulting from the exited electrons a clear peak marks the position of the graphene π-band. This peak in turn is recognised by the peak tracer algorithm.

Time-dependent spectrum fit: The Tr-Spectrum Fit (Section 2.3.4.2) was used to extract the transient spectral evolution of the graphene/Pb/Ni(111) system. Based on the peak positions determined by the Time-dependent spectral peak finder, the fit function therefore comprises five Gaussian peaks, is multiplied by a Fermi distribution and added to a linear background. To account for the excited-state population above E_F, an additional Gaussian term is included:

$$\begin{aligned}\mathrm{F}(E) = &\left[\frac{A_{\text{Excitation}}}{\sqrt{2\pi} * \sigma_{\text{Excitation}}} \exp\left(-\left(\frac{E - E_{\text{Excitation}}}{\sigma_{\text{Excitation}}}\right)^2\right)\right] + \left[\frac{1}{2}\left(1 - \operatorname{erf}\left(\frac{E - E_{\text{Fermi}}}{\sqrt{2}\sigma_{\text{Fermi}}}\right)\right)\right] \\ &* \left[A_{\text{Fermi}} + \frac{A_1}{\sqrt{2\pi}\sigma_1} * \exp\left(-\left(\frac{E - E_1}{\sigma_1}\right)^2\right) + ... + \frac{A_n}{\sqrt{2\pi}\sigma_n} * \exp\left(-\left(\frac{E - E_n}{\sigma_n}\right)^2\right)\right] \\ &+ LinBG\end{aligned} \tag{3.2}$$

were n represents the number of volume-band peaks - in this case $n = 5$, A is the amplitude, E_n the corresponding peak centre position and σ_n the width for the Gaussian-peak and Fermi distribution respectively. Lastly, $LinBG = x * E + \text{Offset}$ represents the linear background added from the previous analysis. To prevent premature fitting of the excitation peak (before t_0), its amplitude $A_{\text{Excitation}}$ is modulated by

$$\text{Mod}_{\text{Excitation}}(\Delta\text{t}) = \left[1 - \frac{1}{2}\left(1 - \text{erf}\left(\frac{\Delta\text{t} - \sigma_{\text{Laser}}}{\sqrt{2} * \frac{\sigma_{\text{Laser}}}{2}}\right)\right)\right] + 0.001 \tag{3.3}$$

were Δt is the time-delay for the current fitting step and σ_{Laser} is the pump laser pulse temporal full width half maximum (FWHM). Using starting parameters and constraints from the Time-dependent spectral peak finder the fitting routine extracts Fermi distribution parameters and peak positions - hence e.g. the electron system temperature or overall band structure movements. By restricting the input data to specific momentum regions, this fitting routine can be utilised to investigate only certain $k_{||}$ if required. This method was used to fit different $k_{||}$-slices through the graphene π^*-band and explore the band evolvement.

But, these results can not be used to answer the current question of the graphene *pi*-bands evolution over time in great detail.

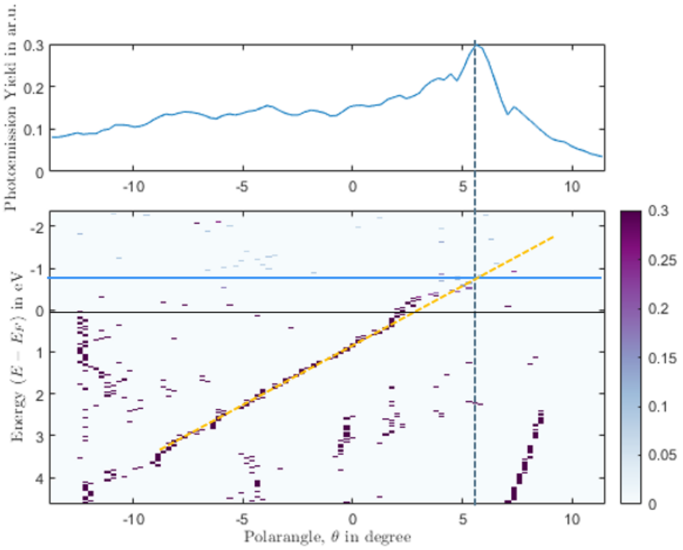

Figure (3.14) Graphene/Pb/Ni(111) time-resolved constant energy peak finder at $\Delta t = 20\,\text{fs}$. Dots represent peak positions in $E - E_F$ versus the measured polar angle θ, colour-coded by peak amplitude. The blue line marks the constant-$E - E_F$ cut presented in the top panel, and the black dashed line indicates the peak position found by the algorithm. The yellow line, representing an assumed linear dispersion, deviates near the Fermi level, suggesting a band gap at the Dirac point.

Time-dependent constant-$E - E_F$ fitting routine to trace graphene π band: To capture the evolution of the graphene π-band in the momentum dimension, a dedicated constant-$E - E_F$ fitting routine was developed. While previous constant-$k_{||}$ spectrum fits (requiring five "initial" Gaussian plus an excitation peak, totalling 23 parameters) were attempted — with hard constraints on peaks far from E_{Fermi} and fixation of presumed unchanging parameters like the time dependent Fermi distribution or the linear background results — this approach proved unstable. A simpler, more robust method was therefore implemented by tracing the graphene feature along constant-$E - E_F$ cuts.

For this purpose, the Time-dependent constant-$E - E_F$ fitting routine was established. Details and a graphical representation of the routine are provided in Section 2.3.4.4, here, the basics are summarise. In this multi-step routine, a second-degree polynomial is first fitted to model the background, and a Gaussian peak is used to represent the graphene π-band. The fitting is restricted to the region of interest (ROI) shown in Figure 3.15, where the graphene π band is clearly distinguishable from other features.

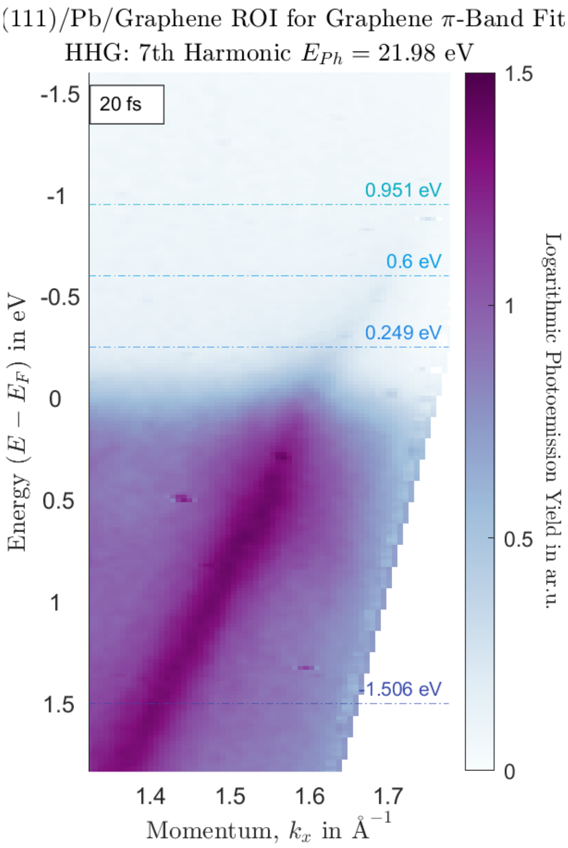

Figure (3.15) Graphene/Pb/Ni(111) ARPES Data for $\Delta t = 20$fs. The image shows the ROI of the Tr-ARPES dataset used for fitting at $\Delta t = 20$fs.

For each measured time-step (normally 43) and energy channel (up to 400) within the ROI, a constant-$E - E_F$ cut is extracted and fitted as follows:

1. **Fitting before t_0:** For a few time-steps (typically four) prior to t_0, the occupied region is fitted using both a second-degree polynomial and a Gaussian, while the unoccupied region is fitted solely with the polynomial (since the graphene band is not populated yet).

2. **Fitting shortly after t_0:** Immediately following t_0, when the excited electron population is highest, the unoccupied region is re-fitted using a second-degree polynomial and a Gaussian. In this step, the polynomial parameters are fixed to the mean values obtained in step (1), so that any variation is ascribed to changes in the graphene band's population and position.

3. **Fitting for all time-steps:** Finally, the entire dataset is re-fitted using the same polynomial-plus-Gaussian model. The initial parameters for the polynomial are taken from the mean values from step (1), while the starting parameter for the Gaussian peak position is taken from the occupied-region results (step (1)) and from the unoccupied-region results (step (2)), ensuring a stable fit even when the signal is weak.

This routine generally enables a robust tracking of the graphene π-band movement in $k_{||}$ as a function of time, attributing any changes in the data to variations in band population and energy shifts.
A detailed assessment of the fitting quality is provided by analysing constant-$E - E_F$ cuts at various energies, as presented in Figure 3.16,3.17 and 3.18. Exemplary fitting results for various constant-$E - E_F$ cuts (at energies $E = -1.506$eV, $E = 0.249$eV, $E = 0.600$eV, and $E = 0.951$eV, marked in Figure 3.15) across a range of delay times from -2500 fs to 3000 fs are shown. The presented data were chosen to represent different cases of data that need to be fitted and the respective issues and fit reliability:
In the occupied region (at -1.51 eV - at the edge of what can be addressed with the used pump pulse energy of 1.58eV) and in the unoccupied region (at 0.25 eV - close to E_{Fermi} were the graphene band has a small population even before pumping , 0.60 eV - a region were population can only be seen after optical excitation, and 0.95 eV - an area where the electron population upon pumping is so small that the fitting routine reaches its limitations).

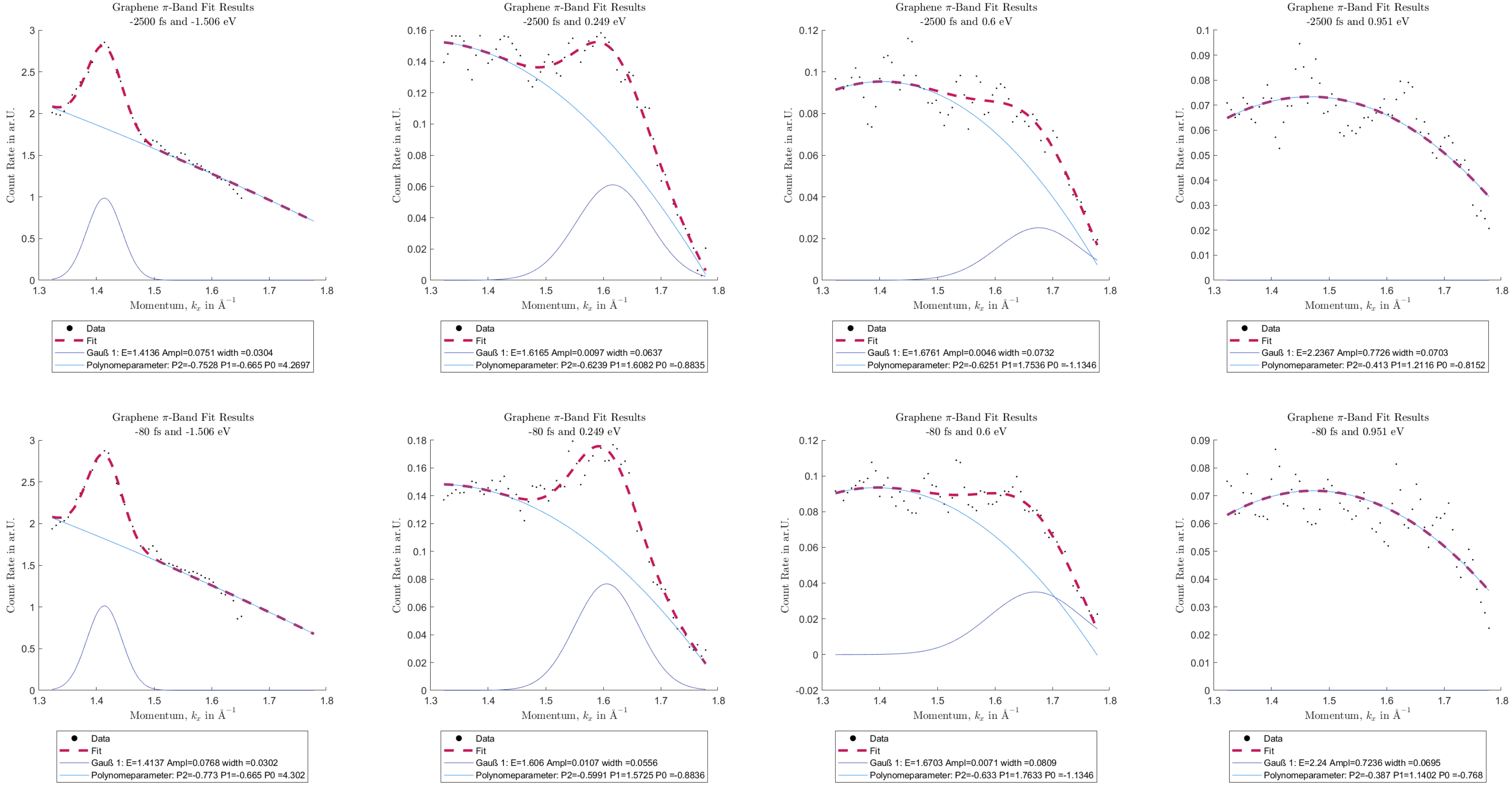

(a) Energy, $E = -1.506$eV.

(b) Energy, $E = 0.249$eV.

(c) Energy, $E = 0.600$eV.

(d) Energy, $E = 0.951$eV.

Figure (3.16) PART I: Explanatory Graphene π-band tracing results.

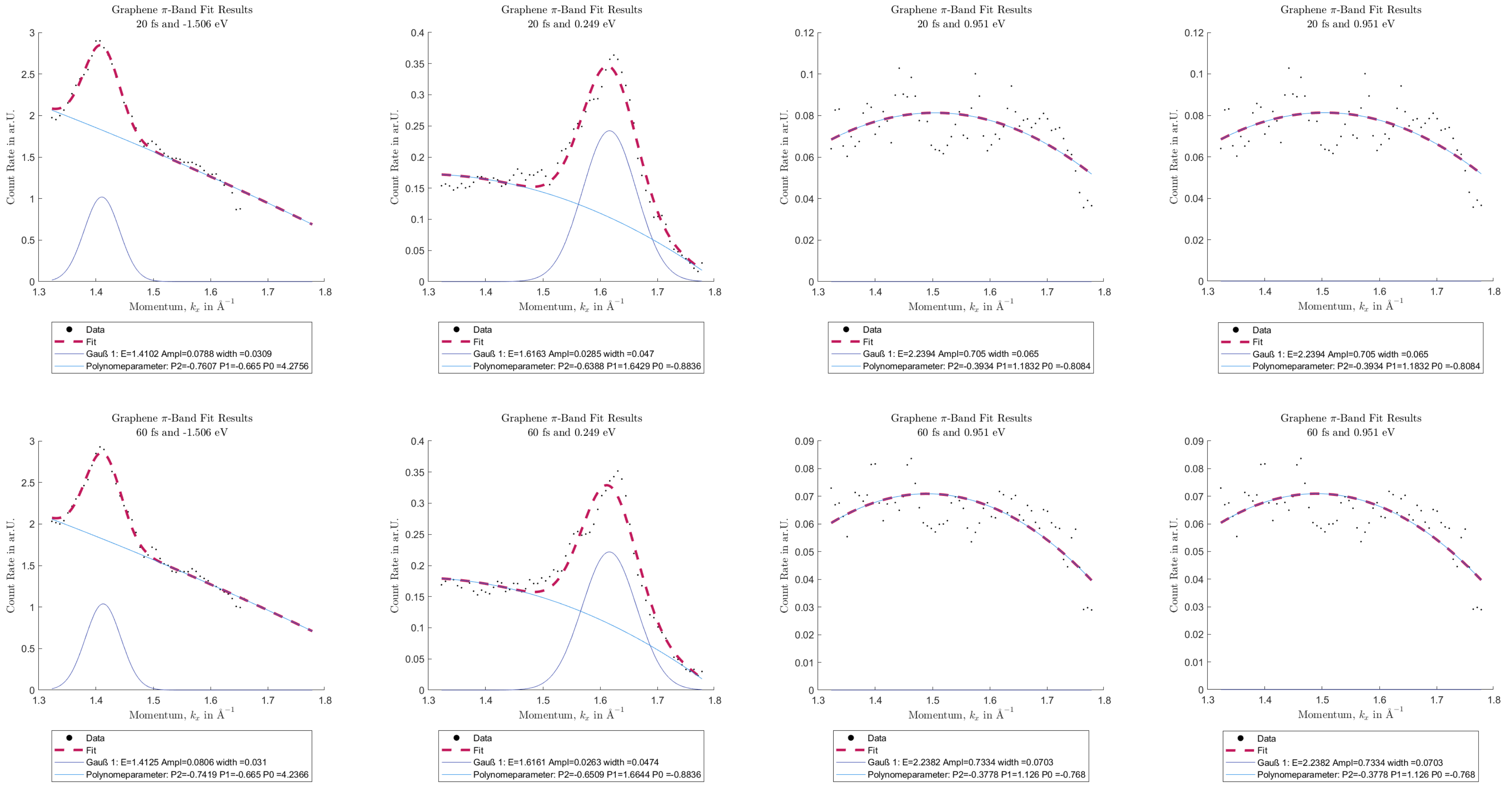

(a) Energy, $E = -1.506\text{eV}$.

(b) Energy, $E = 0.249\text{eV}$.

(c) Energy, $E = 0.600\text{eV}$.

(d) Energy, $E = 0.951\text{eV}$.

Figure (3.17) Part II: Explanatory Graphene π-band tracing results.

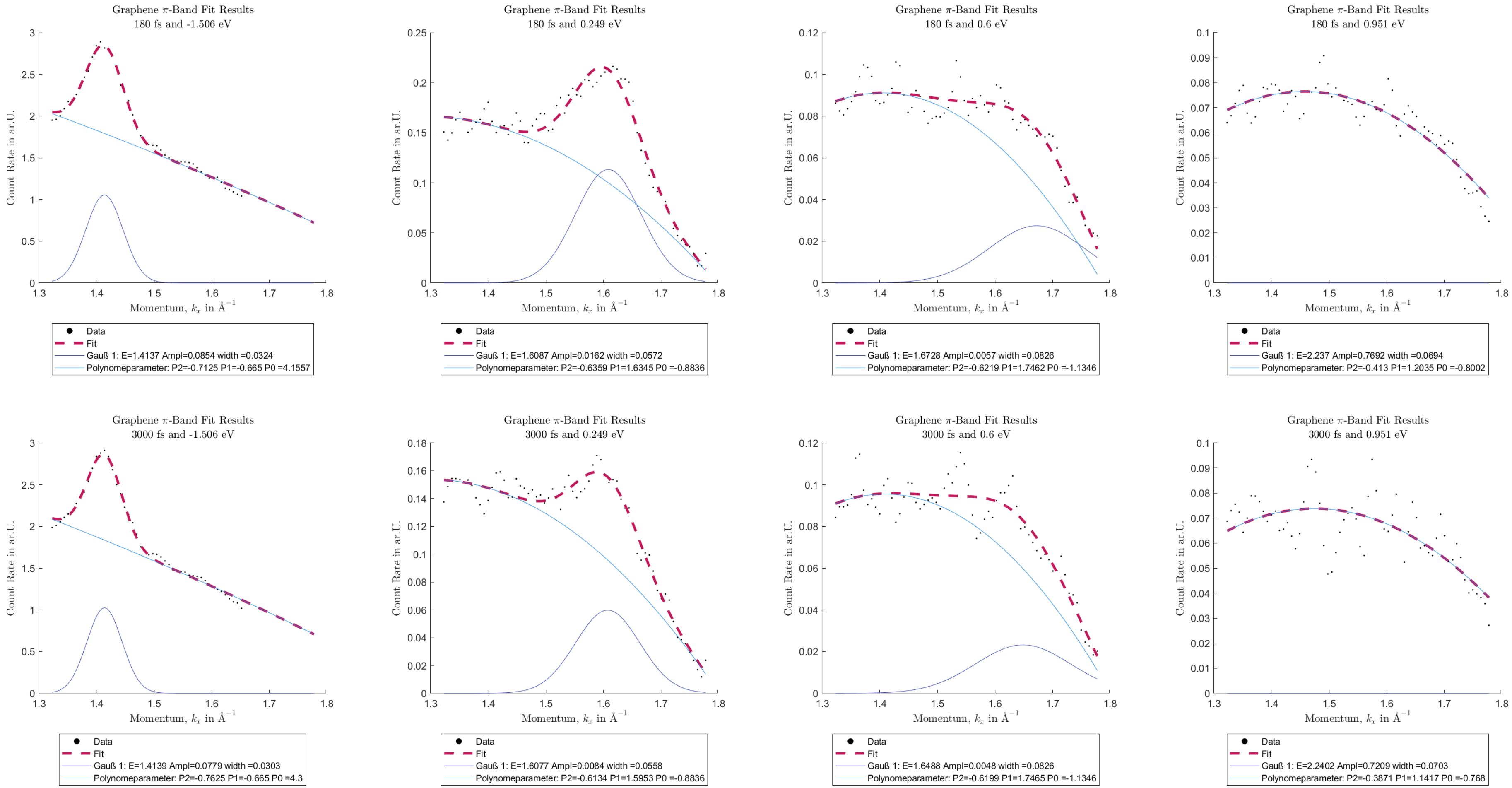

(a) Energy, $E = -1.506\text{eV}$.

(b) Energy, $E = 0.249\text{eV}$.

(c) Energy, $E = 0.600\text{eV}$.

(d) Energy, $E = 0.951\text{eV}$.

Figure (3.18) PART III: Explanatory Graphene π-band tracing results.

In the occupied region, the graphene π-band is clearly resolved, exhibiting an almost linear dispersion and background. Closer to E_F, overlapping Ni(111) bands cause the background to deviate. These deviations are effectively modelled by the second-degree polynomial. Figures 3.16b and 3.16c reveal a strong excitation near t_0, evidenced by an increase and subsequent decrease of the Gaussian peak amplitude - despite a slight shift toward lower $k_{||}$ values relative to visual inspection. At energies further into the unoccupied region, the excitation is too weak to yield a significant photoemission signal (Figure 3.16d). Hence, the fitting routine is unable to reliably extract a Gaussian peak and fits only the background.

In summary, while the routine robustly captures the π-band dynamics in the occupied region and near E_F, caution is warranted when interpreting results at higher energies, particularly far from t_0. Conversely, within the occupied region and near E_F, the results are reliable for further analysis.

3.5. Exploring the possibility for optical manipulation of the graphene band gap

Comparing the fit results for $\Delta t = 20\text{fs}$ in Figure 3.8 with other delay-times reveals a shift in the peak positions. This shift is apparent in the differential maps (Figure 3.13) and is corroborated by the close-up plots (full plot is shown in Figure 3.8 in the previous section) both the occupied and unoccupied regions shown in Figure 3.19.

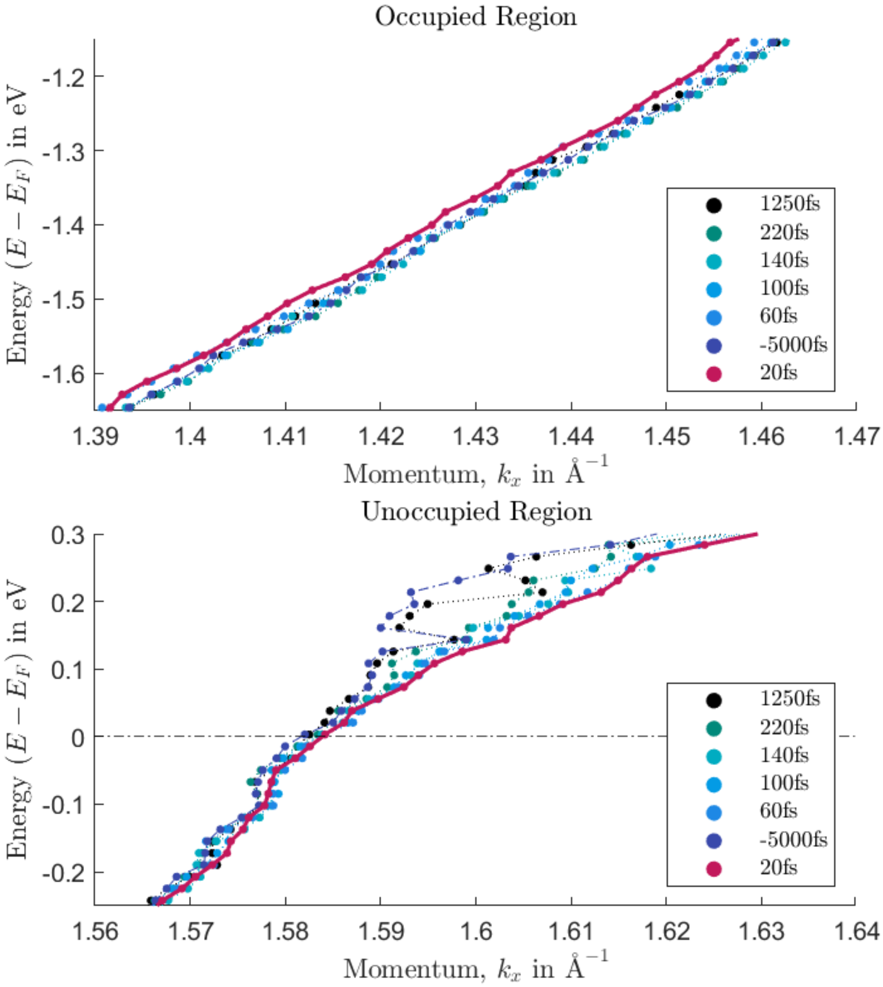

Figure (3.19) Graphene/Pb/Ni(111) graphene π band positions for different timesteps. The plots show the fitted peak positions for $\Delta t = -5000,\ 20,\ 60,\ 100,\ 140,\ 220$ and 1250fs. The red line plot additionally marks the results for $\Delta t = 20\text{fs}$.

In the occupied region the results for $\Delta t = 20\text{fs}$ (red) are moved slightly to lower momentum values, causing them to be on the left of all other time-steps. The opposite movement is observable in the unoccupied region, were the graphene π^*-band peak is on the right (higher momentum values) for $\Delta t = 20$fs compared time-steps. Importantly, the shifts are unequal: the upper Dirac cone part (unoccupied region) undergoes a significant bigger change than the lower Dirac cone area (occupied region). This movement is apparently caused by the optical excitation. The bands relax back to their original position within $\Delta t = 1250$fs (black).

Before any quantitative analysis of this apparent shift, it is essential to consider the experimental resolution, the stability of the fitting routine, and the imposed constraints. These factors prevent a rigorous quantitative evaluation of the shift at this stage. Consequently, we first assess the fit quality, as illustrated in Figure 3.20. The fits at selected energies — -0.979 eV and -1.330 eV in the occupied region, and 0.179 eV and 0.249 eV in the unoccupied region — demonstrate that the routine reliably reproduces the data. In the unoccupied region, a clear peak shift is observed. The fitted Gaussian even underestimates the shift compared to visual inspection. In the occupied region, the shift is minimal and may lie within the measurement uncertainty, suggesting that the apparent widening is systematic but requires cautious interpretation. Higher angular resolution measurements are needed to clarify this behaviour.

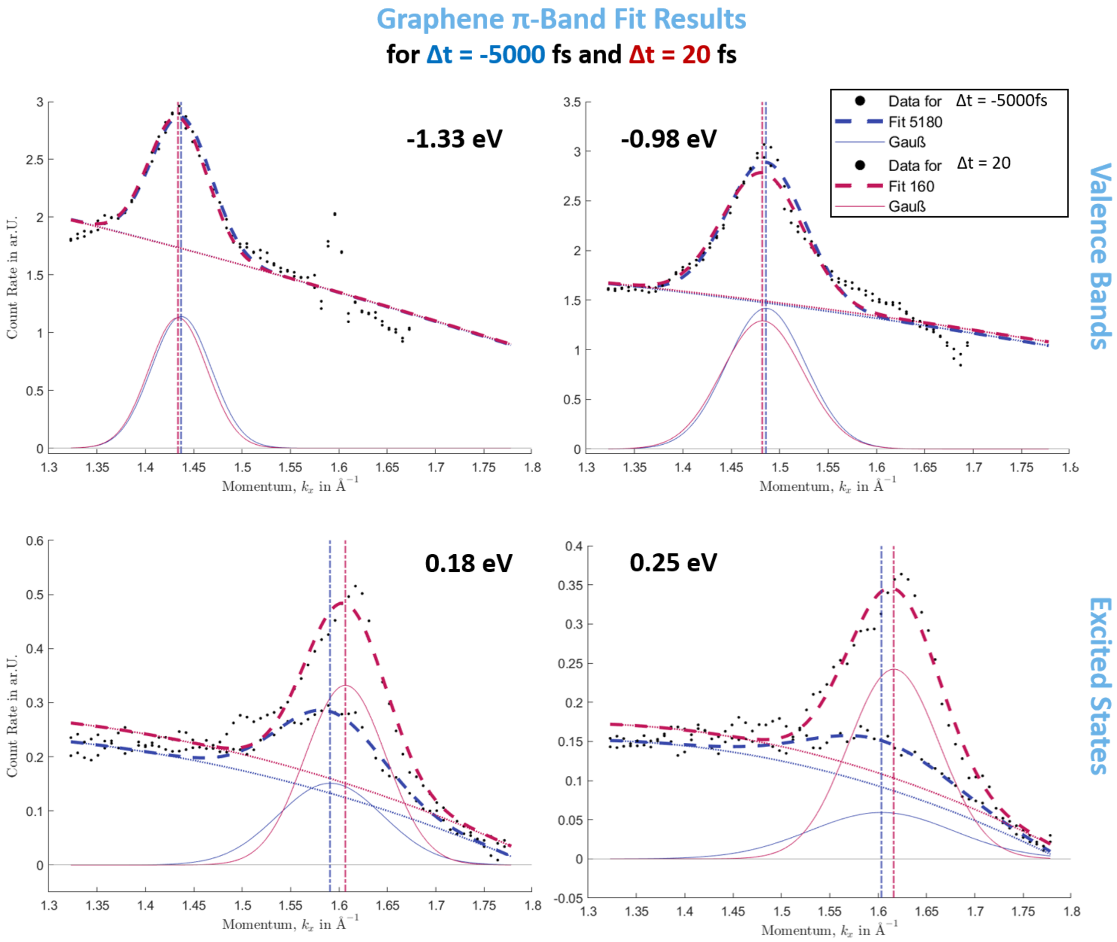

Figure (3.20) Graphene/Pb/Ni(111) graphene π band tracing results for $\Delta t = -5000$ and 20fs. The plots present the fitting results for 4 different energies, 2 from the occupied region -0.979eV and -1.330eV and two from the unoccupied region 0.179eV and 0.249eV. In both cases the depicted time-steps are far before t_0 at $\Delta t = -5000$fs and closely after t_0 at $\Delta t = 20$fs. Shown are the data points in black and the according fit in thick dotted lines, the subsequent parts of the fit, Gaussian peak and polynomial with thin lines, as well as the Gaussian peak position with thin dotted lines.

Several possible origins for the observed peak shift are discussed, depicted in Figure 3.21: A rigid band shift, spin-polarisation change or band gap magnitude quenching.

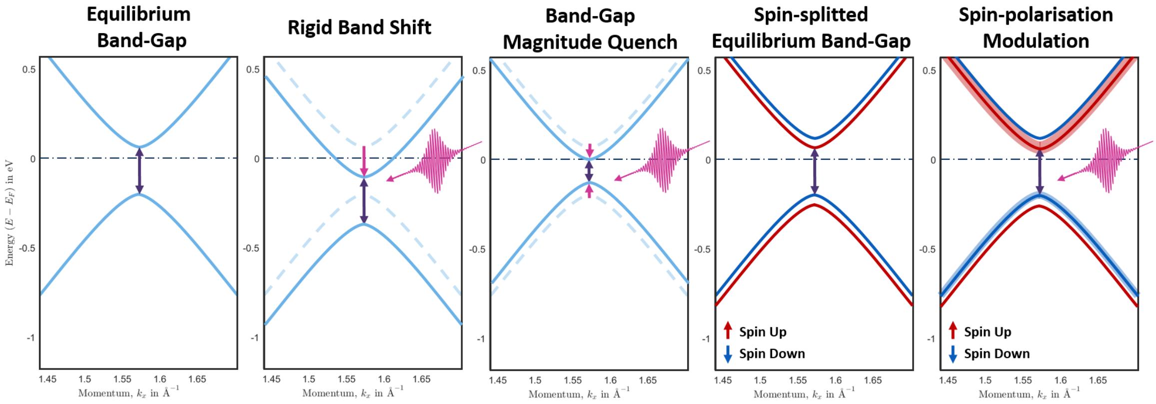

Figure (3.21) Possible origin of graphene π^*-band peak shift after optical excitation: A rigid band shift, a change of the spin-polarisation or band gap magnitude quenching.

A **rigid energy shift** (e.g. from space-charge effects or electronic doping) would displace the entire band uniformly, as displayed in the second panel of Figure 3.21. This is inconsistent with the non-parallel and unequal changes observed in the upper and lower parts of the Dirac cone and can therefore be disregarded.

Similarly, an **optical modulation of the spin polarisation** could affect the spin-integrated spectra. When considering the spin-polarisation of the graphene bands introduced by intercalated atoms, we firstly need to discuss its origin. From literature we can distinguish two intercalation material groups where a band gap can be opened: Heavy d- or sp-metal atoms such as the most significant examples apart from Pb being Au and Bi.
Those material influence the spin-structure of the graphene layer differently. While an experimental realisation of a large Rashba-effect introduced into the Dirac cone of epitaxial grown graphene was, among others [2], realise for gold intercalated graphene on nickel(111), this spin splitting was absent while using Bi as intercalation atom. It follows: in the case of gold the Au-d-band hybridisation with the graphene p_z-orbitals is the main mechanism for the introduces spin-orbit interaction (SOI) [65] and for Bi the proximity effect is dominant (bismuth misses the d-electrons at the Fermi energy) [59].
Both systems are similar to the graphene/Pb/Ni(111) interface used in this thesis.
In gold (atomic number 79 - [Xe]$4f^{14}5d^{10}6s^{1}$) the 5d subshell is fully filled and the valence band additionally has 1 electron from the 6th s shell, for lead (atomic number 82 - [Xe]$4f^{14}5d^{10}6s^{2}6p^{2}$) and bismuth (atomic number 83 - [Xe]$4f^{14}5d^{10}6s^{2}6p^{3}$) alike the valence electrons lack a contribution from the metal d-bands.
Due to the specifics of the respective electron configuration and according to the findings from Shikin *et al.*, we expect the graphene/Pb/Ni(111) system to act similar to a Bi intercalated sample. Resulting in a weak interaction of the graphene with the intercalated Pb atoms and therefore a weak hybridisation of their states.
However, considering the electronic configuration of Pb (and its similarity to Bi intercalation) and the associated weak hybridisation with the graphene p_z-orbitals, the induces SOC from the Pb is considered to be relatively small, as discussed in Section 3.3. Therefore, a dominant spin-splitting of the graphene states and following, an optically induced change in their spin splitting appears unlikely. Time-resolved ARPES experiments, probing at higher photon energies (e.g. 40–50eV) would enhance the yield of Pb states and allow for a more direct investigation of possible hybridisation changes [59, 65]. Unfortunately, a high photon energy source with sufficient photon flux suitable for ultrafast time-resolved measurements was not available during this thesis.

The most plausible explanation remaining at this point is an **optically induced modulation of the band gap magnitude**.

---

[2] graphene on Ir(111) and gold-intercalated graphene on SiC(0001)

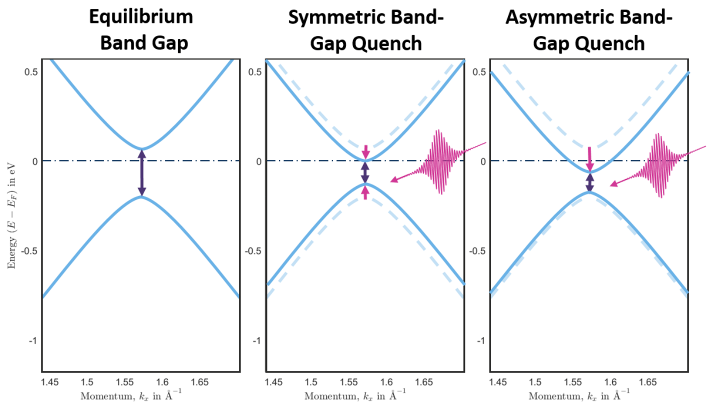

Figure (3.22) Comparison between symmetrical and asymmetrical graphene band gap quenching.

A transient quenching of the gap would cause the upper Dirac cone branch to shift downward and the lower branch upward (symmetric shift, depicted in Figure 3.22), resulting in the apparent widening observed in the photoemission data. Here, this band renormalisation caused by a band gap magnitude change, might be altered. The strong screening effects within (semi-) metallic systems could counteract the band-renormalisation leading to an uneven, or asymmetric shift (see Figure 3.22). In the following the movement, clearly visible in the time-resolved data analysis, will be characterised.

3.5.1. Optically induced modulation of the graphene band gap magnitude and dispersion

For a more comprehensive analysis of the time-resolved dataset, the band-distribution fit assuming a simple model of gapped Dirac fermions (used previously) was automated to fit the upper a the lower half of the Dirac Cone for every measured time step. The employed fit function is

$$E_{\pm}(k_{II}) = E_D P \pm \sqrt{\hbar^2 v_F^2 (k - k_{DP})^2 + (\Delta E/2)^2} \tag{3.4}$$

where E_{DP} denotes the Dirac point energy (i.e. the mid-gap energy), k_{DP} is the wave vector at the Dirac point, v_F is the Fermi velocity, and ΔE is the energy gap between the conduction and valence bands. A diagram showing the fitting workflow is presented in Section 2.3.4.5. In this analysis the graphene band peak positions, extracted from extensive π-band tracing, were used while restricting the fitting region to exclude Ni-dominated features. Exemplary fitting results for $\Delta t = 0\,\mathrm{fs}$ are shown

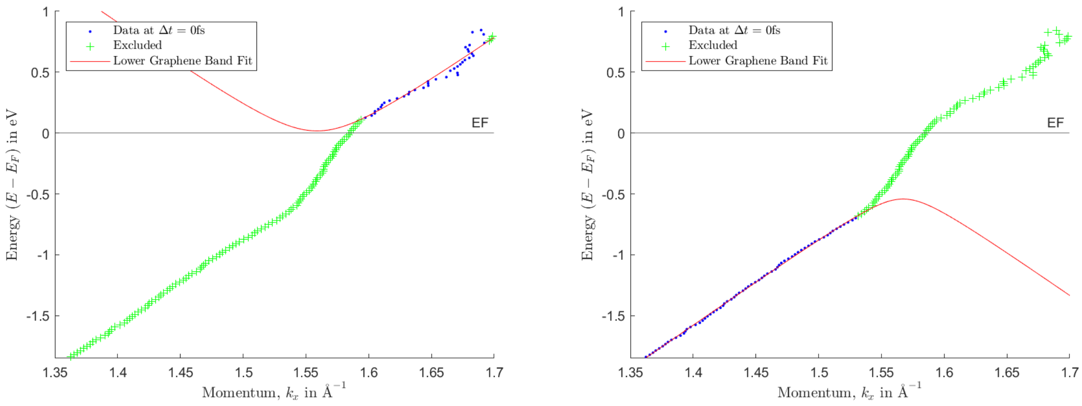

(a) Upper Dirac cone part

(b) Lower Dirac cone part

Figure (3.23) Explanatory Graphene/Pb/Ni(111) graphene π band dispersion fitting results for $\Delta t = 0\,\mathrm{fs}$, showing the upper (a) and lower (b) Dirac cone Fit. Presented are the graphene-peak positions extracted from the graphene-band tracing, the values used for fitting are (blue), the exuded data-points (green) and the resulting fit function (red).

in Figure 3.23 for both the upper and lower Dirac cone segments. When cutting along the $\overline{\Gamma}$ to $\overline{K}$ direction , as was done in the presented Tr-data set, only half of the Dirac cone is visible (dark corridor effect). Importantly, the Dirac cone does not form a perfect cross, rather the right (towards higher momentum values), visible arm has a flatter curvature (lower Fermi velocity) that the part to the left (lower momentum values) of the Dirac point. This can be seen when studying the curvature of the theoretical calculations presented in Figure 3.9. During the fitting of the unoccupied region, this will cause a systematic overestimation of the gap size (this will not influence the qualitative movements only their magnitude).

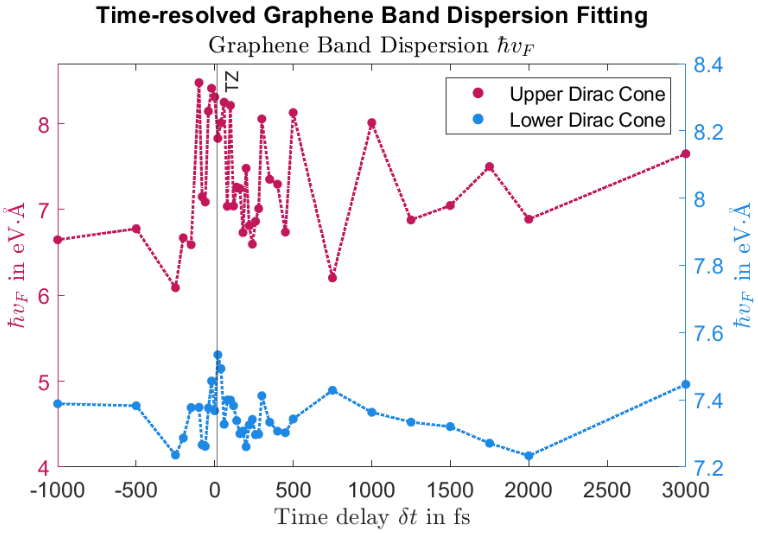

Figure (3.24) Time-resolved graphene π^*-band dispersion $\hbar v_F$ evolution after optical excitation, showing the results for the upper (green) and lower (blue) Dirac cone Fit.

Due to the stringent selection of data points, the use of previous fitting results, and the low signal-to-noise ratio in the unoccupied region, these outcomes must be considered as approximation rather than absolute values (to verify the extracted magnitude of the gap and its change thorough theoretical calculations are needed). Taking these limitations into account, Figure A.8 presents the evolution of the graphene band gap magnitude over time, while Figure 3.24 shows the corresponding evolution of the band dispersion, $\hbar v_F$. The following constraints were applied during the fitting procedure:

Table (3.2) Upper and lower fit-parameter constrains for graphene π^*-band gap fitting

	k_{II}	k_{DP}	E_{DP}	$\hbar v_F$
Upper Cone	$1.595\,\text{Å} - 1.690\,\text{Å}^{-1}$	$1.557\,\text{Å} - 1.570\,\text{Å}^{-1}$	$-0.31\,\text{eV} - -0.32\,\text{eV}$	$4\,\text{eV Å} - 10\,\text{eV Å}$
Lower Cone	$1.350\,\text{Å} - 1.530\,\text{Å}^{-1}$	$1.557\,\text{Å} - 1.570\,\text{Å}^{-1}$	$-0.31\,\text{eV} - -0.32\,\text{eV}$	$4\,\text{eV Å} - 10\,\text{eV Å}$

The extracted gap sizes differ between the upper and lower Dirac cone fits. In the upper cone, ΔE ranges between approximately 0.577 eV - 1.110 eV, while in the lower cone it varies between 0.381 eV - 0.544 eV (see Figure A.8). Both sets of values exceed the equilibrium gap of 0.270 eV determined from static high-resolution imaging. More importantly, the band dispersion $\hbar v_F$ increases upon optical excitation, reaching maximum values of 8.48 eV Å for the upper cone and 7.53 eV Å for the lower cone. This fitting result is surprising and need due consideration.

3.5.2. Discussion

3.5.2.1. The Fermi velocity

Graphene's low-energy band structure features conical Dirac bands near the K points, described by $E(\mathbf{k}) \approx \hbar v_F|\mathbf{k}|$. The product of the reduced Planck's constant and Fermi velocity, $\hbar v_F$, is widely cited as roughly 6.3 eV Å - 6.6 eV Å for pristine monolayer graphene [66]. This corresponds to a Fermi velocity v_F on the order of $1 \times 10^6\,\frac{\mathrm{m}}{\mathrm{s}}$ (about 1/300 the speed of light). Comparing this to established literature, experimental values from angle-resolved photoemission spectroscopy (ARPES) and other measurements confirm graphene's $\hbar v_F$ is on the order of $6\,\mathrm{eV\,Å} - 7\,\mathrm{eV\,Å}$. One ARPES-based fit reports $\hbar v_F \approx 7.3\,\mathrm{eV\,Å}$ ($v_F = 1.1 \times 10^6\,\frac{\mathrm{m}}{\mathrm{s}}$) when graphene is doped slightly [67]. Notably is the finding on the higher end of $\hbar v_F \approx 8.3\,\mathrm{eV\,Å}$ ($v_F = 1.26 \times 10^6\,\frac{\mathrm{m}}{\mathrm{s}}$) from scanning tunnelling spectroscopy investigations, slightly above the free-standing value (the reduction of charge carrier, e.g. though doping, leads to an increase in the Fermi velocity). This was attributed to reduced dielectric screening on the $\mathrm{MoS_2}$/vacuum interface) [68]. On the lower end, graphene on metallic substrates or within graphite can exhibit slight reductions in slope, e.g. effective v_F nearer $0.86 \times 10^6\,\frac{\mathrm{m}}{\mathrm{s}}$, $\hbar v_F \approx 5.3\,\mathrm{eV\,Å}$, in some highly screened cases. Factors causing the Fermi velocity to change, like application of a gate voltage, or heavy doping can not be explained by pure optical excitation of the band structure. While a change in the graphene band gap, yields a change in the exact band curvature and thereby influence the $\hbar v_F$ fit results, the **observed change is highly questionable**. It follows, while the general range of the fitted $\hbar v_F$ results are generally reasonable, the drastic change observed within the fit can not plausible be explained by optical excitation of the graphene. Especially, the increase above $\hbar v_F \approx 8.3\,\mathrm{eV\,Å}$ appears unphysical.

This behaviour can be explained by the chosen fitting function. The influence of the results for $\hbar v_F$ on ΔE within the fitting is very strong and an independent fitting is not possible. Therefore, the fitting was repeated using the previous results to restrict $\hbar v_F$ to a range of $6.98\,\mathrm{eV\,Å} - 7.18\,\mathrm{eV\,Å}$. The values were chosen to represent an average between the values of the upper and lower cone in the previous fit and to represent values extracted from ARPES from the literature. This can cause unwanted effects. The band dispersion for the upper and lower part is different (no perfect X-shape), therefore it can not be the same value, forcing it into a certain range could cause the band gap to be overestimated for the upper Dirac cone fit and underestimated for the lower part. Best practice at this point would be to use results from theoretical calculations as a basis for the fitting, unfortunately I do not have such values for my sample system [3]. The renewed results are presented in Figure 3.25, representing a more reasonable outcome.

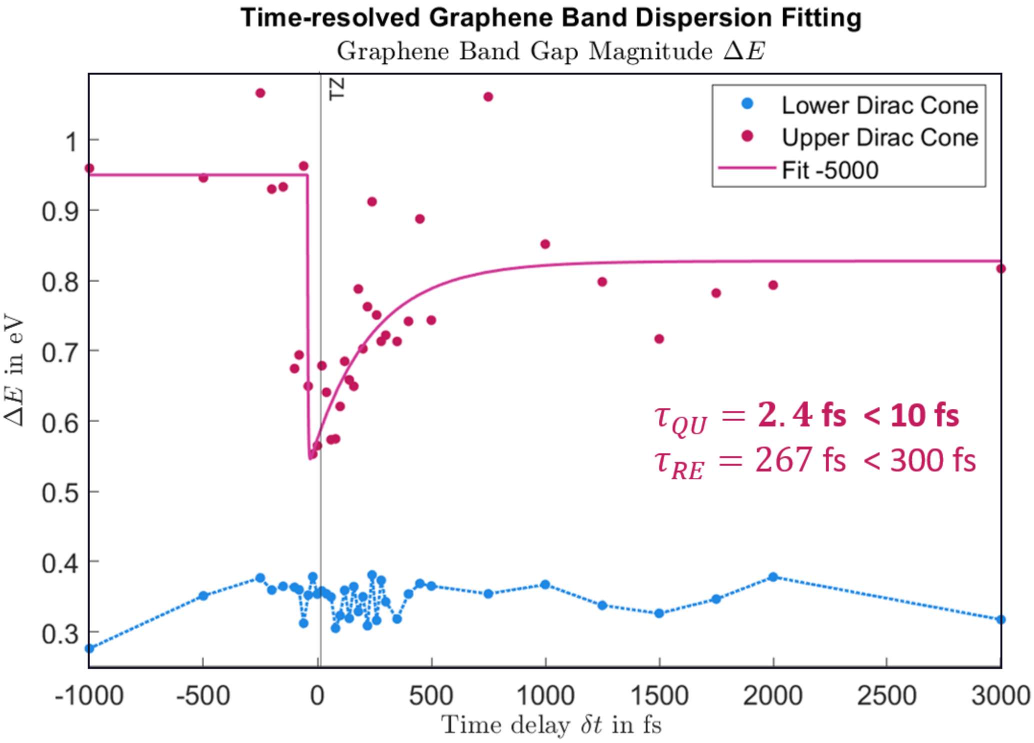

Figure (3.25) Time-resolved graphene π^*-band gap magnitude evolution after optical excitation, showing the results for the extracted band gap evolution for the upper (red) and lower (blue) Dirac cone Fit.

---

[3] the theoretical calculations from our theoretical support, Marius Weber, did not yield a band gap and are therefore not applicable for this analysis

3.5.2.2. The band gap

The new fit results are in good agreement with the visible movements in Figure 3.19. While the lower Dirac cone section stays relatively constant - ΔE ranging from 270 meV to 350 meV - and in an area with good agreement to the high resolution datasets, the results for upper Dirac cone suggests a possible transient band gap quenching of 42 %. To set this into reference with the lower cone results, the effective band gap is calculated (the energetic position of the respective cone minimum or maximum is calculated using the fit results, the difference forms the effective band gap). Within the fit, the effective band gap magnitude far before t_0 is $\Delta E_{eff} = 660\,\text{meV}$ and is quenched to t_0 is $\Delta E_{eff} = 540\,\text{meV}$ (witch is in excellent agreement with the band gap size extracted in Section 3.3 taking the respective band width into account), equivalent to an effective **transient band gap quenching of** 18 %. The effective band gap size is illustrated in Figure 3.28b. The uncertainty around t_0 is such (depicted in Figure 3.26 are the values together with their 90% confidentiality intervals from the fit as error-bars) that this results can be considered a good indication but renewed fitting after some theoretical input is needed to verify the depicted behaviour. However, the results confirm the expected asymmetric band gap magnitude quenching (Figure 3.22). The main shift, causing the band gap to shrink in size is initiated from the upper Dirac cone part. Therefore using a double exponential approach the quenching and its recovery time were fitted. The results are presented in Figure 3.25. Due to the uncertainty of the double exponential fit itself, but more importantly the used data (exacted band gap size), as illustrated in Figure 3.26, the extracted values must be viewed as an indication not as absolute values. Nevertheless, the results are impressive. The band gap is quenched within a few femtoseconds, likely less than 10 fs. This is followed by a fast recovery within a few 100 femtoseconds.

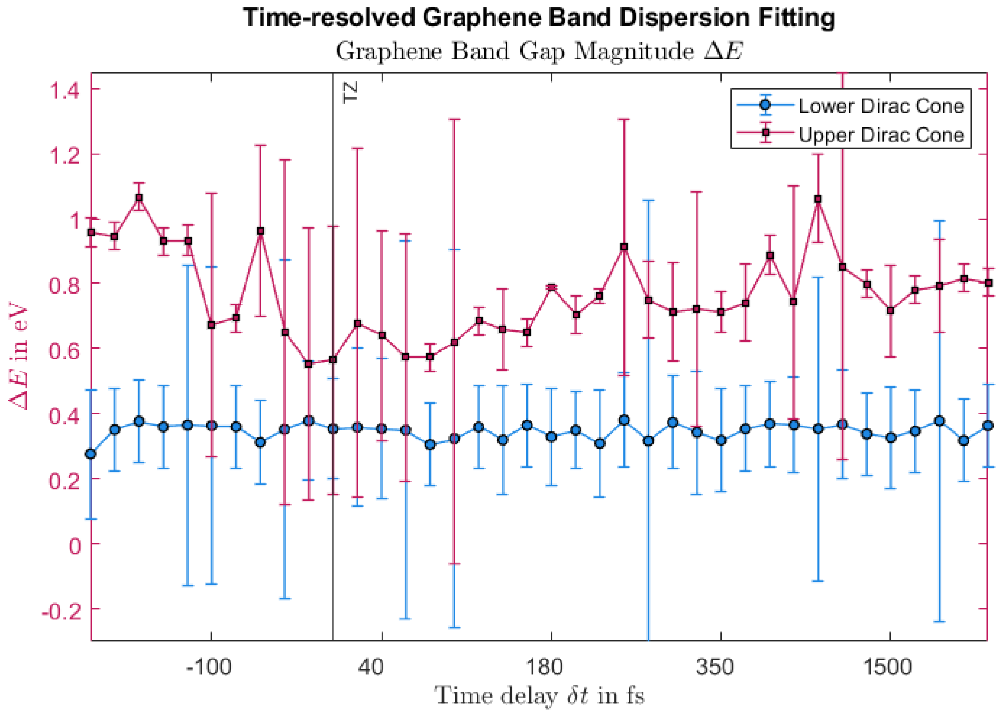

Figure (3.26) Time-resolved graphene π^*-band gap magnitude evolution after optical excitation, showing the results for the extracted band gap evolution for the upper (red) and lower (blue) Dirac cone Fit. Depicts are the results with the 90% confidentiality interval as error bars.

Discussion

From the data-analysis presented in the previous section, I conclude that an asymmetric band gap magnitude quenching of 18 % (Figure 3.22 and Figure 3.28b) is initiated by optical excitation with a fs laser pulse. If this is caused by filling of the conduction band on a short timescale and further intra-band scattering and continuous filling of the band minimum or through truly quenching the gap (caused by demagnetisation and potential screening) is a matter of interpretation at this point.

The following will therefore address different physical mechanisms that could drive a transient band gap changes and their respective likelihood.

One likely factor is **photo-induced screening**. In equilibrium, the band gap is maintained by the symmetry-breaking potential (and any intrinsic SOC). By inject a high density of electron-hole pairs with the pump pulse, these carriers can screen electronic potentials in the material. If the gap is due to, say, a potential difference between A and B sublattices (coming from Pb's presence), the photoexcited carriers might alter that potential, effectively weakening the sublattice asymmetry and thus reducing the gap on ultra short timescales. The ultrafast quenching-time - estimated to < 10fs - is likely due to electronic screening of the sublattice breaking. But, if this would be the sole cause, this effect would likely only be observable within a few tens of fs around t_0, since carriers can be screened efficiently in the metal substrate. Therefore, for the **longer timescale band gap quenching** (as is observed here) this effect might not be the main cause.

Long lifetime potential contributors to the gap reduction are **phonons**. The sudden deposition of energy from the pump will heat the lattice on a picosecond timescale. Phonons, including those at the interface, might cause transient structural changes. For example, if the graphene and Pb layer thermally expand even a tiny amount. This appears reasonable, knowing that around 2.3% of the optical energy is deposited in the graphene layer [6]. This mechanism would relies heavily on the electron-phonon coupling. It is known that electron-phonon coupling is strong ($\lambda \approx 0.6$ to 0.9) in graphene-σ-bands even causing kinks in the electronic band structure, visible in ARPES [69]. This effect is reported to be quite fast (few fs to sub-100 fs), but the σ-bands are $\sim$3 eV to 4 eV below E_F. For quasi-free standing graphene π^*-band (H-intercalated graphene on SiC and O-intercalated graphene on Ir), the electron-phonon coupling was found to be considerable weaker with λ only reaching 0.05 ± 0.03 [70, 71]. Nevertheless, the distance or respective orientation between Pb and graphene could change, perhaps reducing the asymmetry that causes the gap. Due to the low electron-phonon coupling for excited electrons in the graphene π^*-band , this would be a relatively slow effect (hundreds of femtoseconds to picoseconds as the lattice heats), and indeed the data show that any gap reduction is most pronounced at delays of a few hundred femtoseconds and begins to recover by 1–2 ps (maybe when the lattice is equilibrating). This recovery suggests that once the carriers cool and recombine and the lattice settles, the gap returns to its original value, meaning the effect is reversible and not due to any permanent change like desorption of Pb (the experiment consist out of over 60 runs, all showing similar effects, confirming the sample was not optically damaged or altered in a lasting way).

A more exotic mechanism is the generation of **Floquet–Bloch states**. If a strong coherent laser field is applied to graphene, theory predicts the opening of a dynamical band gap at K due to photon dressing of the electronic states (the so-called Floquet topological insulator scenario) [72]. In the experiment, however, the pump pulse is short-lived and does not continuously drive the system while measuring. More important, we used s-polarised light for pump and probe as well, removing the out-of-plane component needed for Floquet physics. Indeed, I do not see any band replica - the essence of Floquet-physics - in the ARPES signal, a band gap manipulation as predicted in [72] can be safely disregarded as driving mechanism behind the observed transient band gap changes.

One more important point: **Ultrafast demagnetisation of Ni**. The highest band gap quenching temporally coincides with the ultrafast nickel demagnetisation timescale (discussed in great detail in the next chapter 4). Two effects might alter the graphene band structure. Firstly, during ultrafast demagnetisation the exchange splitting of the nickel collapses causing the spin-splitted bands to move towards each other. By employing the time-resolved spectral fitting routine for different k_{II} (see Section 2.3.4.2 and 2.3.4.2) the evolution of the nickel bands at different positions in k-space was traced. The movement is depicted in Figure 3.27. Especially at t_0 one band former mainly located in the unoccupied region moves towards E_F. This might enable hot electrons excited into the unoccupied Ni-bands to flow or diffuse into the Pb/graphene layer, transiently filling the unoccupied region of the graphene Dirac cone, changing the local electron population thereby influencing the fitted band gap size. Secondly, the demagnetisation of the nickel itself might cause changes in the graphene gap. If Ni demagnetises, the magnetic fringe fields or any exchange coupling to graphene would diminish. All though I established before that the graphene band gap might not originate from SOC, it was discussed, that it is still quite likely that a descent amount of SOC and thereby some spin-

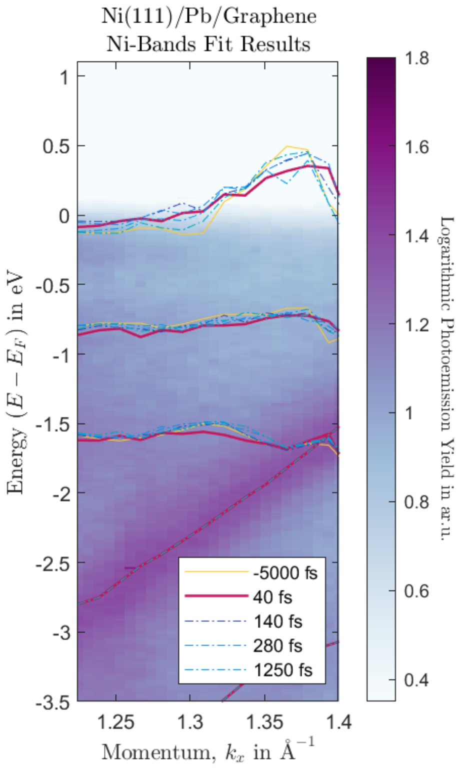

Figure (3.27) Time-resolved nickel band position tracing. The photoemission yield of the graphene/Pb/Ni(111) data taken at $\Delta t = 120\,\text{fs}$ is overlayed with the band peak position fitting results for constant k_{II} spectrum fits at different delay times. Due to signal overlapping a fitting directly in the vicinity of the $\overline{K}$-point was not possible.

polarisation might be introduced by the lead. A change in the substrates magnetisation might direly influence this component. While, a direct optical influence of the spin-polarisation of the graphene band gap can be disregarded, a change of the spin polarisation as a result of the demagnetisation might alter the system drastically. This theory is supported by the timescales coinciding with extreme fast demagnetisation dynamics of the graphene/Pb/Ni(111) system (discussed in detail in Section 4.4). Time- and spin-resolved experiments on this system, using a pump-pulse sufficient to demagnetise the nickel substrate are highly interesting to further investigate this question.

Conclusion

From the presented observations, I gathered experimental evidence for an ultrafast modulation of the graphene band structure. The evidence is primarily the temporary filling of the unoccupied graphene band with excited electrons and an apparent reduction in the energy separation of the valence and conduction band, presented in Figure 3.28.

However, given the experimental and analytical uncertainties, this interpretation is approached cautiously. The data strongly confirm that optical excitation transiently manipulates the band gap. If this is caused by filling of the conduction band on a short timescale and further intra-band scattering and continuous filling of the band minimum or through truly quenching the gap (caused by demagnetisation and potential screening) is a matter of interpretation at this point.
Even within the limitations of our data, **the principle of ultrafast optical modulation is demonstrated**: it was shown that the electronic state of graphene can be markedly changed within tens of femtoseconds by a light pulse and that it relaxes back in a few ps. Most remarkable is the size and energetic position of the band gap. The equilibrium band gap size is estimated to be $\Delta E_{eff} = 340\,\text{meV}$. This paces the equilibrium Dirac point in the fitted dataset at $E_{D,equ} = -196\,\text{meV}$, this would place the upper graphene cone minimum within the unoccupied region, roughly $140\,\text{meV}$ above E_F (band centre position, band minimum for the 1/e-width: $E_{1/e-min,up} = 43\,\text{meV}$), illustrated in Figure 3.28. After optical excitation the gaps magnitude is reduced to $\Delta E_{eff} = 280\,\text{meV}$ and the Dirac point shifted accordingly (to $E_{D,t_0} = -262\,\text{meV}$). This reported optical induced quenching of 18% would breach the gap to the Fermi level making this system a truly optical tunable material ($E_{min,up} = 18\,\text{meV}$ and $E_{1/e-min,up} = -80\,\text{meV}$).

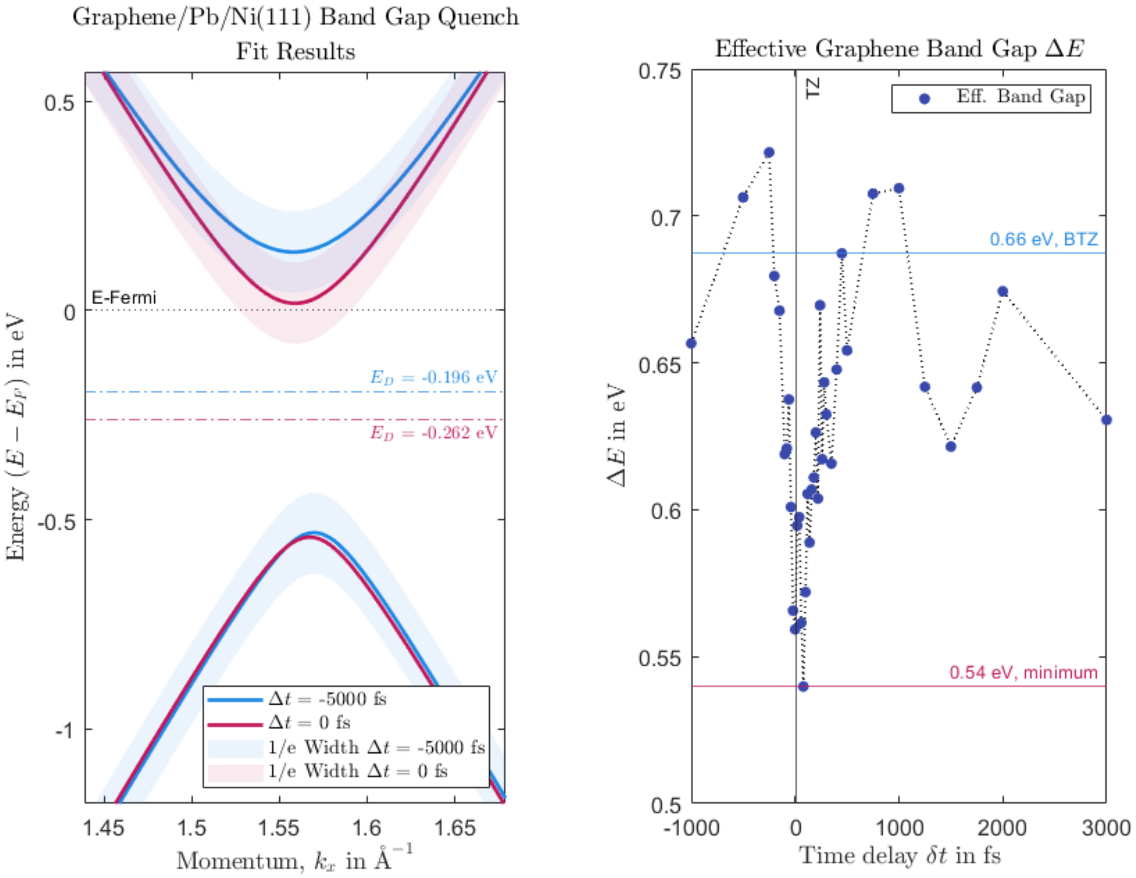

(a) Dirac cone fits

(b) Tr-Band gap size

Figure (3.28) Magnitude of optically induced graphene band gap quenching. (a) Depicted are the equilibrium Dirac cone centre position and its 1/e-width (extracted from fitting, blue) compared to its position and 1/e-width at t_0 (red). The respective Dirac point energies E_D and the Fermi energy E_F are marked with horizontal lines. (b) Corresponding Tr-Band gap size development. Shown is the normalised gap size, taking the upper and lower fitting results into account. The gap reduces in size by approx. 18%, from 0.66 electronvolts to 0.54 electronvolts at its minimum.

Even for the smallest reported gap, the size - if correct - as discussed in the previous section is notable. If one's goal was to use this in a device, one challenge would be to make the effect more controllable and pronounced. One important step would be to lift the Dirac Point above E_F. After this for instance, using a mid-IR pump tuned to half the gap energy (i.e. far-infrared) could resonantly drive direct transitions between valence and conduction band at K, which might yield a more selective and possibly coherent modulation of the Dirac gap (perhaps even a transient population inversion or a more uniform filling of the Dirac point), if not obscured by the simultaneous excitation of the metal substrate. Another strategy could be to apply a strong DC bias or gate while pumping, to see if the gap can be permanently changed (e.g. any structural change triggered by the pump). In this reversible pump-probe experiments we did not observe any permanent change, which is actually desirable for repeatability and demonstrates the robustness of the Pb-intercalated structure: the intercalated layer stayed intact through many hours of pump-probe cycles.

Summary

To summarise this section: I explored the possibility of optical manipulation of the graphene band gap and found suggestive evidence that the band gap can be dynamically influenced on ultrafast timescales. Answering the key question for this section:
Can we modulate or control this band gap (or more generally the electronic structure of graphene) using light pulses on ultrafast time scales?
Yes, the primary effect observed is a transient filling of the gap by photo-excited carri-

ers and a slight narrowing of the gap right after excitation. This suggests that, at least in principle, one can switch the electronic state of graphene/Pb/Ni on a sub-picosecond timescale.
While this is not yet a controlled "on-off" switch for the gap itself, and the Dirac point being to far below E_F, it provides a foundation for future studies to build on. With improved experimental resolution and setup, one could aim to measure the gap size more precisely as a function of pump fluence, time and spin, to see if it indeed collapses at higher excitation densities or increased demagnetisation. Moreover, applying this technique to graphene with various intercalates coverage or different magnetic substrates, could reveal how general the phenomenon is. Taking the experimental restrictions, working with an ARPES setup not a momentum microscope (only measuring one energy-momentum cut at a time), signal-to-noise ratio while using the HHG-light source, low probe pulse energy and lake of spin-resolution into account, a renewed systematic study might lift the presented analysis from interpretation an indication of effects towards truly convincing results.

In closing, the ultrafast ARPES results complement the static findings by adding a dynamic dimension: not only is a band gap present, but it is also tunable (even if in a limited, transient way) by optical stimuli. This dynamic tun ability is a key aspect of the main project objective, as it touches on the ability to actively control graphene's electronic structure in time – an important step toward ultrafast electronic and spintronic devices.

3.6. Summary: lead intercalated graphene on the nickel(111) surface

The static electronic properties of graphene/Pb/Ni(111) turned out to be highly encouraging: a quasi-free-standing Dirac cone (meaning linear dispersion and high Fermi velocity close to that of pristine graphene, in the of range of $6.977\,\mathrm{eV\,Å} - 7.177\,\mathrm{eV\,Å}$ from our fits) with a band gap was achieved. The statically extracted band gap of 270 meV is, in practical terms, sufficiently large to affect transport at room temperature and is one of the largest band gaps induced in graphene via proximity effects (most other methods, like placing graphene on HBN or slight hydrogenation, induce gaps of only tens of meV or less). This demonstrates the effectiveness of heavy-element intercalation as a band gap engineering tool. By comparison, intercalating noble metals like Au/Ni(111) yields no gap [13], and intercalating light elements like oxygen can decouple graphene but tends to form insulating oxides (e.g., O/Ni(111) forms NiO. This work adds to the growing evidence that the combination of a heavy element and graphene can produce new gaps and spin phenomena: for example, prior studies found that intercalating a Bi–Au alloy under graphene on Ni led to a spin-splitting of the Dirac cone [25], and Eu intercalation (which forms an europium oxide layer) under graphene/Ni induced a spin-dependent gap of 100 meV with potential topological character [26]. Those systems differ in that the former (Bi–Au) is non-magnetic but heavy (emphasizing SOC), whereas the latter (EuO) is magnetic (emphasizing exchange splitting). Our Pb/Ni system is in between: Pb is heavy (SOC) and Ni is magnetic, but Pb potentially cuts of or dampens the magnetic interaction.

Looking at expectations versus the results, my finding of a band gap aligns qualitatively with the idea that heavy ad-layers can open a gap [23]. However, the precise mechanism appears to be structural symmetry breaking rather than purely a Kane-Mele SOC gap [59]. This is a subtle but important point: a Kane-Mele type gap (intrinsic SOC) in graphene would be accompanied by edge states and a spin Hall effect, whereas a trivial gap (sublattice potential) would not. Nonetheless, even a trivial gap solves the problem of graphene's lack of a band gap for device applications. Considering the controversy around the Klimovskikh *et al.* Pt/Pb results published by Dedkov and Voloshina [24], this work adds another data point. It suggests that indeed a gap opens with Pb, but careful analysis (and possibly spin-resolved ARPES or other probes) is required to identify its nature.

The time-resolved findings add a dynamic perspective. The observation that the gap can be modulated by ultrafast optical excitation is particularly relevant for envisaging active devices. In a spintronic context, one could imagine a device where graphene is kept in proximity to a ferromagnet (for spin injection) and a heavy element (for SOC and gap) – not unlike the investigated system. If we instead had a ferromagnetic insulator plus a heavy intercalant, graphene might have both spin splitting and a gap. Optical excitation could then be used to control spin currents or turn on/off a spin Hall effect. For example, if the gap can be reduced by a laser, one might induce a transition from an insulating state (no spin-current) to a quantum spin Hall state (edge currents) momentarily. There is a long way to go to realise that, but the demonstration of any optical tunability is a step in that direction.

Finally, let's consider the broader implications and next steps. The results underscore that ultrafast dynamics can reveal aspects of the band structure not visible in static experiments (such as the gap modulation). It would be highly interesting to extend these measurements to, time-resolved spin ARPES, to see if any spin polarisation emerges transiently (e.g., does the upper Dirac band acquire a net spin-polarisation under certain conditions?).

In summary, the time-resolved measurements presented in this section offer critical insights into the ultrafast evolution of the electronic structure in lead-intercalated graphene on Ni(111). They reveal both a transient population of unoccupied states within the Dirac cone and a subtle band renormalisation effect, which together underscore the potential of this material system for future spintronic and optoelectronic applications.

By decoupling graphene's π-bands from Ni(111) via Pb intercalation, a precise electronic platform employed in Chapter 4 to modulate femtosecond magnetisation and in Chapter 5 to inject hot carriers into an organic overlayer is established. Thus, this first study is not an endpoint but the bedrock for the spin- and charge-dynamics experiments that follow.

4. Modulation of Nickel Magnetisation Dynamics at the Graphene/Nickel(111) and Graphene/Lead/Nickel(111) Interface

Building on Chapter 3's band-structure tuning, here I probe how that same Pb-mediated decoupling alters ultrafast spin dynamics. By directly comparing graphene/Ni(111) and Pb/graphene/Ni(111), I reveal how interface coupling controls sub-100 fs demagnetisation. These insights into spin–electron scattering then feed into Chapter 5, where the rate of those hot carriers determine their injection and recombination efficiency with a coronene overlayer.

Acknowledgement of collaborative efforts and individual work

I gratefully recognise the contributions of colleagues whose input was vital to the experimental work discussed in this chapter.
This chapter is based on two sets of data.

Firstly, static and time-resolved measurements of a graphene/Pb/Ni(111) sample (gathered from 2021-10-11 to 2021-10-15).
Sample preparation: Katharina Hilgert, supported by Christina Schott; Data acquisition: Sebastian Hedwig, supported by Katharina Hilgert; Setup build-up and maintenance: Benito Arnoldi and Johannes Stöckel (ARPES), Eugen Nosenko and Sebastian Hedwig (Lasersystem and HHG-beamline); Data analysis: Myself.

Secondly, static and time-resolved measurements of a graphene/Ni(111) sample (gathered at between 2023-01-24 and 2023-07-18).
Sample preparation: Myself; Data acquisition: Myself supported by Gregor Zinke; Setup build-up and maintenance: Benito Arnoldi and Gregor Zinke (ARPES), Eugen Nosenko, Gregor Zinke and Sebastian Hedwig (Lasersystem and HHG-beamline); Data analysis: Myself supported by Paul Herrgen.

Additional support regarding magnetisation dynamics: Paul Herrgen and Sebastian Weber. Scientific advisors throughout: Benjamin Stadtmüller, Martin Aeschlimann.

4.1. Introduction

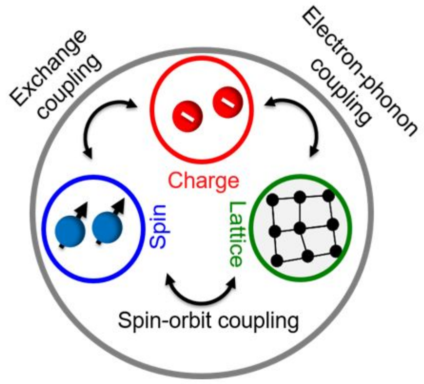

Figure (4.1) Schematic of solid state sub systems and their interaction

Generating a deeper understanding of the mechanisms driving demagnetisation and the corresponding recovery channels is crucial for the design of next-generation data storage devices. Graphene serves not only as a functional element but also as an electrode material to connect ferromagnets with organic or other materials. As Herbert Kromer famously stated, "The interface is the device" [1], a sentiment that underscores the critical importance of interfaces in determining overall device performance. Accordingly, it is essential to investigate the influence of the graphene/ferromagnet interface on magnetisation dynamics.
Previous studies have demonstrated that the presence of a monolayer of graphene on Ni(111) significantly influences the magnetic properties of the interface [18, 73]. For instance, modifications in domain wall movement [18], spin polarisation, and magnetic

anisotropy have been observed at the graphene/Ni(111) interface. Such interactions can be further modulated by atomic adsorption, intercalation, or chemical modifications such as hydrogenation [74], each leading to a variety of magnetic behaviours including ferromagnetic [75] or antiferromagnetic coupling [76]. These findings underscore the complexity and tunability of graphene's influence on the de- and re-magnetisation dynamics of Ni(111) at the nanoscale.

My research focuses specifically on the impact of lead atom intercalation into the graphene/Ni(111) interface. As discussed in Chapter 1, the hybridisation between the graphene π states and Ni 3d valence-band states induces partial charge transfer of spin-polarised electrons into the graphene π^* unoccupied states, thereby generating a magnetic moment in the carbon atoms [16, 17]. This effect has been confirmed by spectroscopic investigations, including X-ray absorption spectroscopy (XAS), X-ray magnetic circular dichroism (XMCD), angle-resolved photoemission spectroscopy and S-ARPES studies, which revealed strong modifications of the valence-band states of both Ni and graphene. Moreover, it is well documented that the presence of graphene on Ni(111) enhances the atomic corrugation and leads to an inversion of spin polarisation relative to the bare Ni surface due to the quenching of Ni surface states [18]. Such modifications not only expose the nickel surface and its image potential state but also provide a potential source for spin-polarised electrons, supporting the concept of spin filtering at the graphene/Ni(111) interface [16].

The general consensus in the literature is that the influence of graphene on the magnetic properties of nickel is predominantly due to the hybridisation between the two materials. An intriguing research question then arises: what is the outcome if this hybridisation is reduced or completely lifted by means of intercalation? Earlier studies have indicated that intercalation of atoms can significantly enhance the complexity of the system, with the specific effects depending on the d-band position and the SOC strength of the intercalant [65]. For example, research by Weser *et al.* [77] demonstrated that intercalating iron (Fe) between graphene and Ni(111) drastically alters the magnetic response of the graphene layer, an effect attributed to the formation of a highly spin-polarised 3d(z^2) quantum-well state in the thin iron layer. To the best of my knowledge, no studies have yet examined the outcome when using a non-magnetic heavy metal such as lead.

In the following, I present my research on the effect of lead intercalation at the graphene/Ni(111) interface, focusing on the following objective:

How does the presence of graphene, and an intercalated heavy metal layer, influence the femtosecond demagnetisation of a ferromagnetic substrate?

4.2. How to measure ultrafast magnetisation dynamics at metallic interfaces?

The influence of graphene on nickel's magnetic properties is complex. In the literature, the typical approaches employed to specifically determine **magnetic** properties include methods like time-resolved magneto-optical Kerr effect (Tr-MOKE) and XMCD. While each technique offers unique insights, both exhibit limitations when probing the magnetic behaviour of surfaces or interfaces. Although the high element sensitive of XMCD is needed to disentangle magnetic contribution in multi-component sampes, the photon energies in the x-ray regime (used to probe core-level states) lack surface sensitivity, resulting in a bulk signal that can overshadow the surface response. Furthermore, to study the de- and re-magnetisation processes, the system must be driven out of equilibrium. Conventional XMCD setups however, are static experiments and therefore not configured for time-dependent studies employing pump-probe schemes. The alternative approach is Tr-MOKE, which allows for the measurement of ultrafast demagnetisation using femtosecond laser irradiation. In such experiments, the material's magnetisation is quenched within a range of 100 fs - 500 fs and subsequently recovers on the order of tens of ps [44, 78–80]. In contrast to XMCD, a typical Tr-MOKE setup utilises visible or near-IR to EUV lasers for both excitation and probing, thereby enhancing surface sensitivity.

However, both XMCD and Tr-MOKE can be used for spectral analysis to identify phenomenons such as OISTER (optically induced intersite spin transfer) [81–83], but they share a common limitation: they cannot readily distinguish between the coupled spin, electron, and lattice subsystems 4.1. To disentangle the contributions from these subsystems, it is necessary to employ a technique that not only extracts the demagnetisation dynamics but also resolves distinct band structure features. This requirement motivates the use of the Tr-ARPES method. An investigation comparing Tr-ARPES

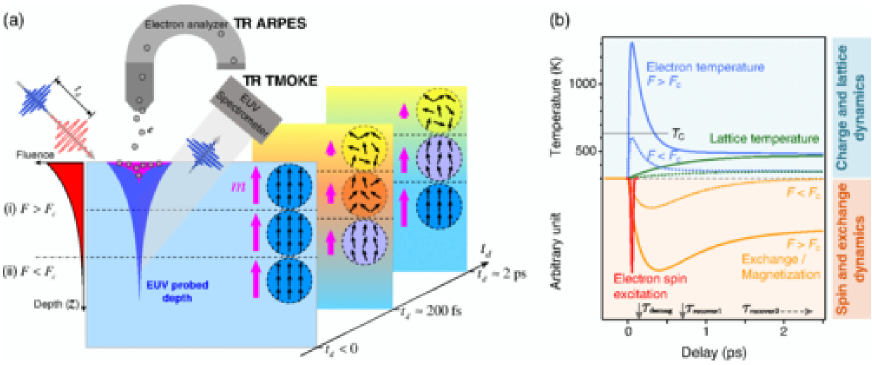

Figure (4.2) (a) Schematic representation of extreme ultraviolet angle-resolved photoemission spectroscopy (EUV-ARPES) and Tr-MOKE measurements on Ni(111). The depth dependent laser excitation fluence profile beneath the sample surface delineates areas with different magnetisation response, depending on whether the in situ fluence exceeds the critical fluence F_c needed for demagnetisation. (b) Schematic depiction of the laser-induced phase transition in Ni. When the laser fluence surpasses F_c, the electron temperature exceeds T_c, and the sample undergoes a rapid magnetic phase transition. Reprinted from [44], ©IEEE.

and Tr-MOKE was performed on a 400 nm Ni(111) film by the group of M. Murnane [44, 84]. As illustrated in Figure 4.2, the experiment was designed to analyse depth-dependent physical effects while accounting for differences in absorbed energy that drive demagnetisation. Although You et al. focused on the fluence dependence of the magnetisation dynamics to uncover fundamental mechanisms, the findings relevant to the present work concern the application of Tr-ARPES in extracting de- and re-magnetisation dynamics on surfaces, particularly on Ni(111). Figure 4.2 emphasises that Tr-ARPES probes only a few monolayers, whereas Tr-MOKE encompasses the entire laser-heated

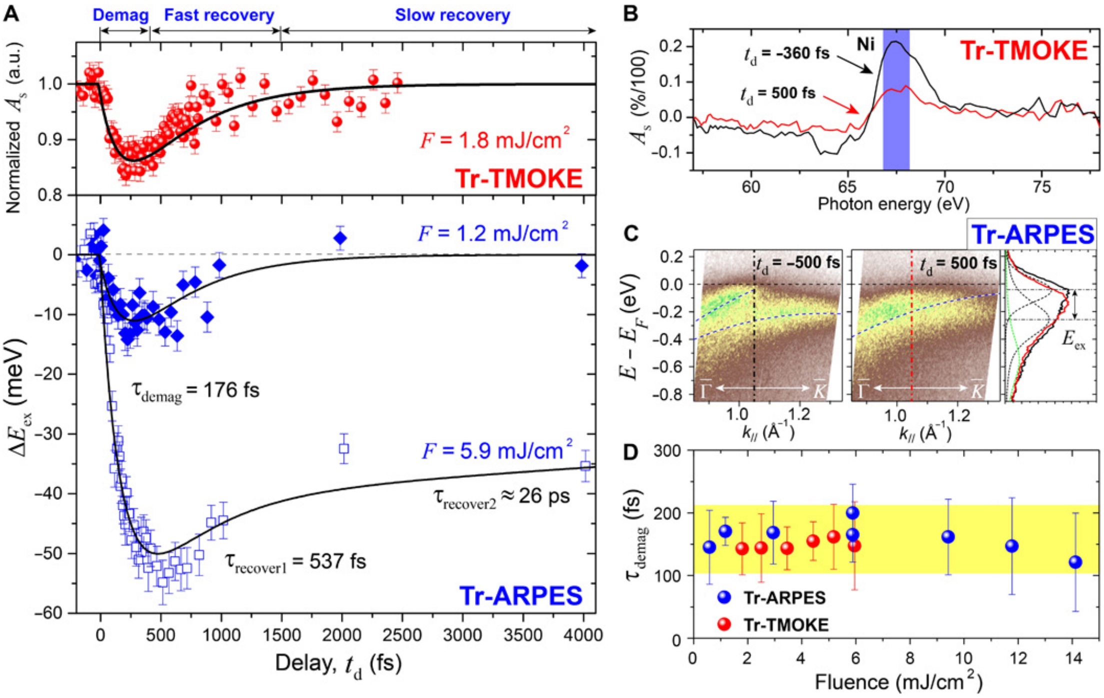

Figure (4.3) Comparison of magnetisation dynamics in Ni(111) measured via Tr-MOKE and Tr-ARPES. (a) Tr-MOKE and Tr-ARPES asymmetry change and exchange splitting reduction ΔE_{ex} as functions of time delay for two laser fluences. The solid lines represent demagnetisation fit results from which characteristic times for demagnetisation (e.g. τ_{demag} and recovery $\tau_{recover}$ were extracted. (b) Tr-MOKE asymmetry before ($t_d = -300\,\text{fs}$) and after ($t_d = 500\,\text{fs}$) excitation. (c) Tr-ARPES of Ni(111) along the designated direction before ($t_d = -500\,\text{fs}$) and after ($t_d = 500\,\text{fs}$) laser excitation, displaying the collapse of the exchange splitting E_{ex} (blue dashed lines). The exchange splitting was extracted from a Voigt function fit, shown to the right. (d) Fluence-independent demagnetisation time for Tr-MOKE and Tr-ARPES measurements. Reprinted from [84], ©IEEE.

depth of approximately 10 nm (13 nm penetration depth for the EUV-probe). Figure 4.3 further illustrates their results: although the spectroscopic signature of demagnetisation — as observed in the collapse of the exchange splitting via Tr-ARPES and the demagnetisation observed in Tr-MOKE — depends on the laser fluence, the characteristic timescale (176 fs) remains essentially invariant (the spin-system does not react significantly slower). This observation suggests that Tr-ARPES is an effective method for probing the spin system's response when the material is driven out of equilibrium: The results obtained via Tr-ARPES are comparable to those from Tr-MOKE. However, the limited probing depth of only a few monolayers permits a detailed investigation of surface dynamics without interference from the bulk signal. Therefore, to study the magnetisation dynamics of the graphene/Ni(111) and graphene/Pb/Ni(111) interfaces while preserving electronic band structure information, Tr-ARPES was employed. The subsequent section provides an overview of the methodological approach.

4.3. Extracting the influence of interfacing a ferromagnet with graphene by time-resolved exchange splitting collapse tracing

Illumination of a magnetic sample with a strong laser field, analogous to the Tr-MOKE technique, drives the sample system out of equilibrium, enabling the extraction of demagnetisation dynamics. Conventional Tr-ARPES setups do not directly address the overall magnetisation. However, they provide access to the evolution of the spin system following optical excitation. As established by the M. Murnane group [44, 84], the band normalisation following demagnetisation can be monitored by

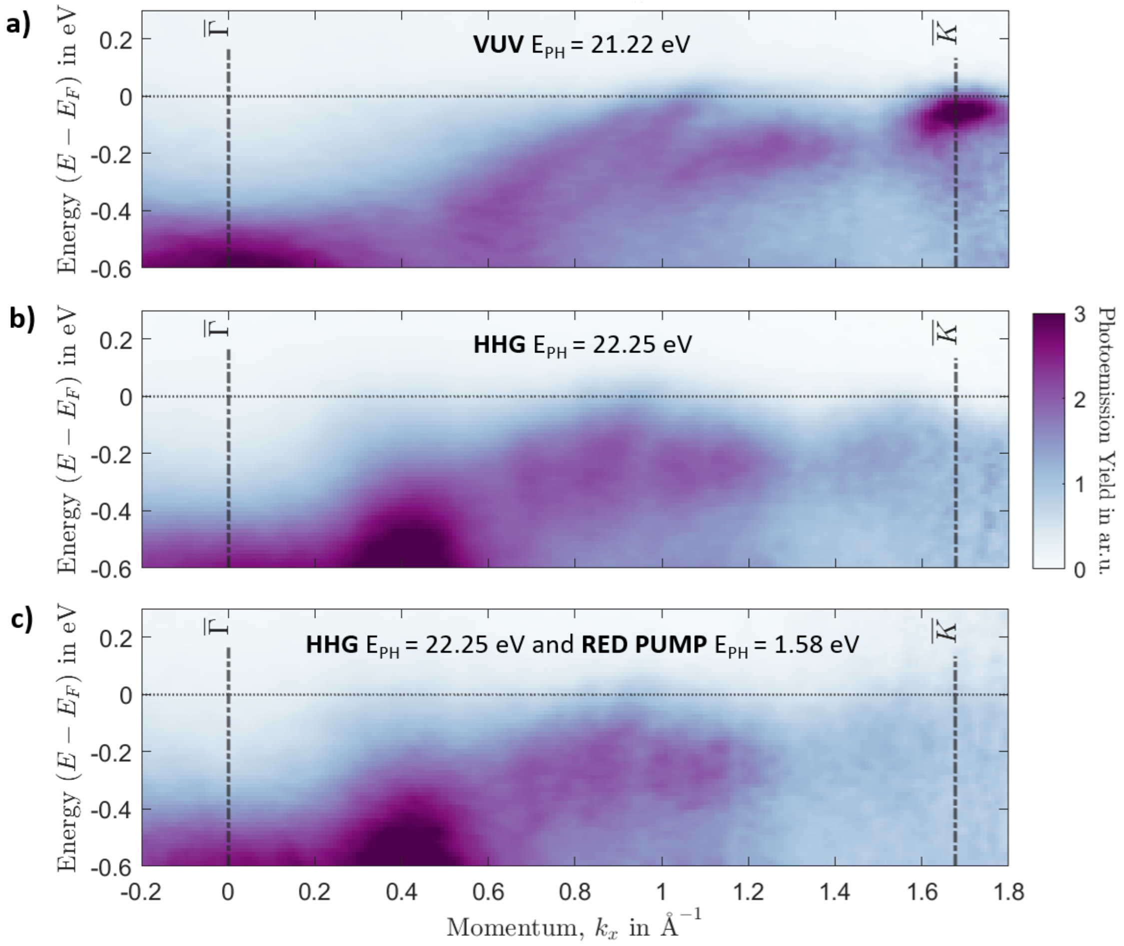

Figure (4.4) Comparison of static ARPES image of the graphene/Ni(111) sample surface taken with the VUV (a), HHG (b) or HHG + red pump (c) as light source.

tracing the collapse of the exchange splitting. In the present work, a similar approach is adopted. It is crucial to use a probing beam in the EUV range to probe the spin-split nickel bands, as demonstrated by the close-up ARPES image in Figure 4.4 obtained with VUV lamp radiation. An measurement taken with an VUV lamp is showing a close up image of the Ni(111) spin-splitted bands is depicted in Figure 4.4. To evaluate the exchange splitting collapse, the time-dependent positions of the upper and lower spin-split bands must be traced. High-harmonic generation (high harmonic generation) radiation was therefore employed to perform extreme ultraviolet time- and angle-resolved photoemission spectroscopy (EUV-Tr-ARPES) experiments. Comparison of the static measurement using a VUV lamp light source (Figure 4.4) with that obtained using high harmonic generation radiation (Figure 4.4) immediately reveals differences in overall sharpness and resolution of the spectral features. Both measurements were taken at the same sample in short succession. The relevant bands become more difficult to distinguish when using HHG radiation. However, this approach is essential to access the high momentum regime ($k_x = 0.8\,\text{Å}^{-1}$ to $k_x = 1.4\,\text{Å}^{-1}$) in the time-resolved measurements. The slight differences in the photoemission yield for different time-steps that need to be examined can be investigated in Figure 4.5. This challenge is illustrated by the spectral cuts taken from the Tr-ARPES-measurement shown in Figure 4.6. This challenge is illustrated by the spectral cuts taken from the Tr-ARPES-measurement shown in Figure 4.6. A slight difference near E_F between cut 3 and the combined cuts 1 and 2 is attributed to the additional contribution from the upper Ni bands. Close examination of the temporal evolution of these spectral features reveals the shift of the peaks, which constitutes the spectral trace of the collapsing upper and lower spin-split bands as the sample magnetisation is quenched. Accordingly, an advanced analysis routine was developed to extract the band shifts. The following a short description will be given, a more detailed explanation on this evaluation routine can be found in Section 2.3.4.3.

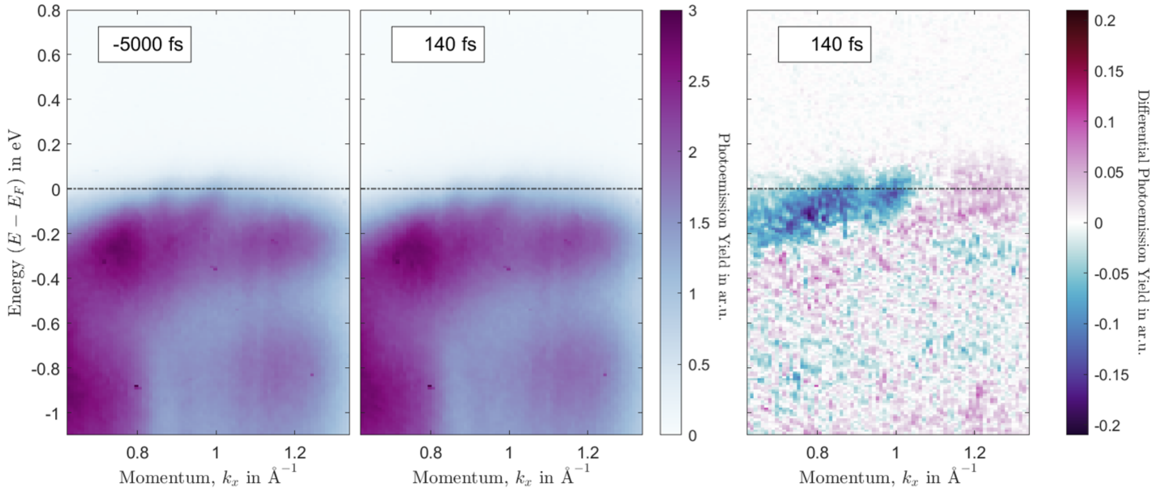

Figure (4.5) Tr-HHG ARPES of the spin-splitted Ni(111) bands in graphene/Ni(111) for $\Delta t = -5000\,\text{fs}$, $\Delta t = 140\,\text{fs}$ and the differential Map at $\Delta t = 140\,\text{fs}$

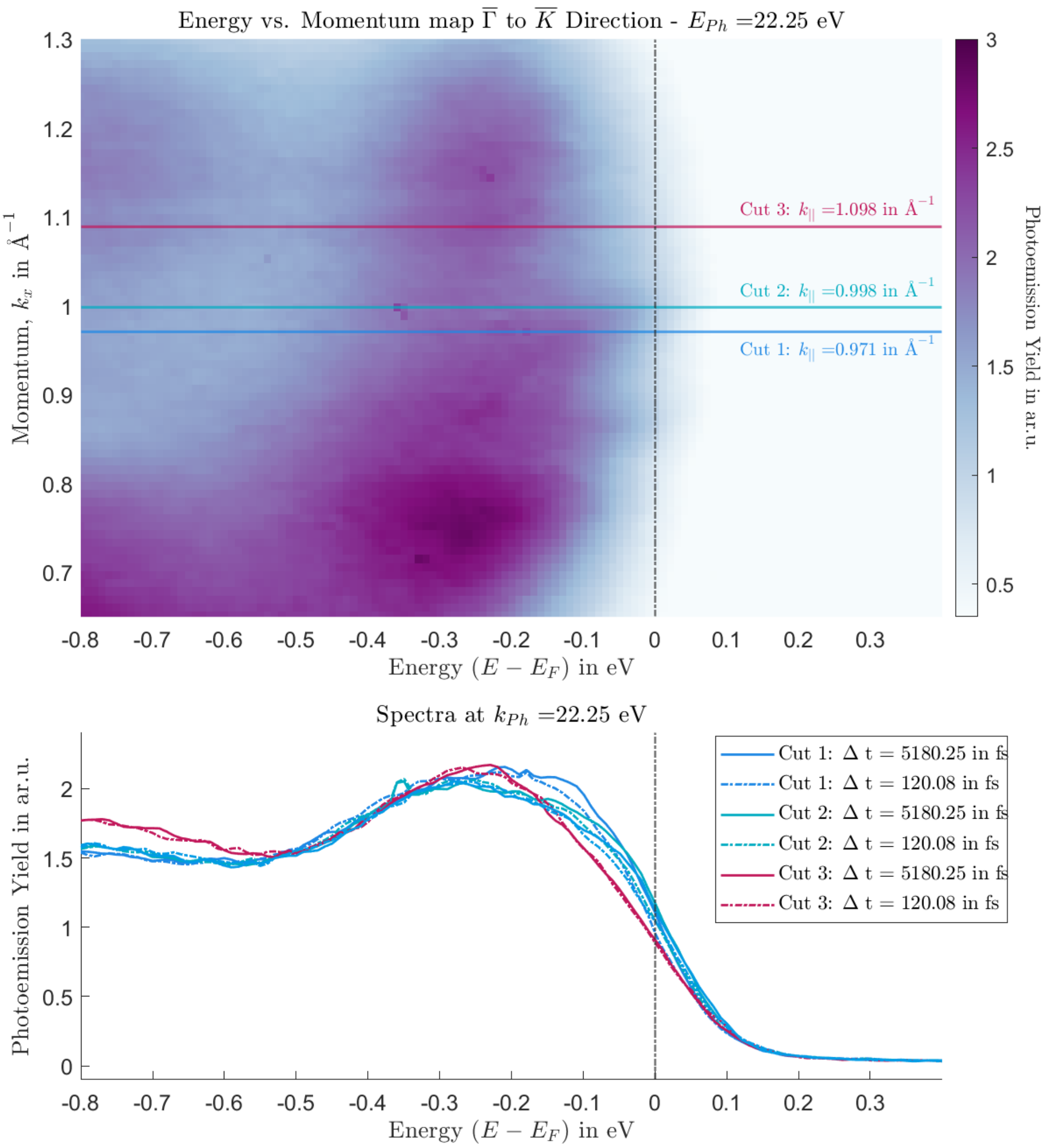

Figure (4.6) ARPES image of the spin-split nickel bands in graphene/Ni(111) along with spectra from several k-space cuts before and at t_0 and $\Delta t = 20\,\mathrm{fs}$. Cut 3 (red) at $k_x = 1.098\,\text{Å}^{-1}$ represents the lower Ni-band, while cuts 1 and 2 (blue and cyan) at $k_x = 0.971\,\text{Å}^{-1}$ and $k_x = 0.998\,\text{Å}^{-1}$, respectively, reflect a mixture of the lower and upper Ni bands. The dotted lines denote the corresponding cuts at $\Delta t = 20\,\mathrm{fs}$, demonstrating the band shift as the upper and lower Ni bands close their band gap.

Spectral fitting For both the graphene/Ni(111) and graphene/Pb/Ni(111) datasets, a spectral fitting procedure was first applied to determine the time-dependent evolution of the Fermi function parameter (see Section 2.3.4.2). The k-integrated datasets were fitted using a composite function comprising four Voigt functions (for graphene/Ni(111)) or two Voigt functions (for graphene/Pb/Ni(111)) (see Equ. 4.1) multiplied by a Fermi distribution and augmented by a linear background (Equ. 4.2).

$$Voigt_1(E) = \left[m_1 \cdot \frac{\sigma_1}{2\pi(E - E_1)^2 + \left(\frac{\sigma_1}{2}\right)^2} + (1 - m_1) \cdot \left(\frac{1}{\sigma_1\sqrt{2\pi}}\right) \cdot \exp\left[-\frac{1}{2}\left(\frac{E - E_1}{\sigma_1}\right)^2\right] \cdot A_1 \right] \tag{4.1}$$

$$Fit(E) = (\mathrm{Voigt}_1(E) + \cdots + \mathrm{Voigt}_n(E) + A_{Fermi}) \cdot \mathrm{Fermi}(E) + E_{off} + mE \tag{4.2}$$

Explanatory results are depicted in Figure 4.7. Notably, the results for the Fermi function parameter are critical and are subsequently used to fix this parameter in later fits, thereby reducing the number of free parameters and enhancing the stability of the fits.

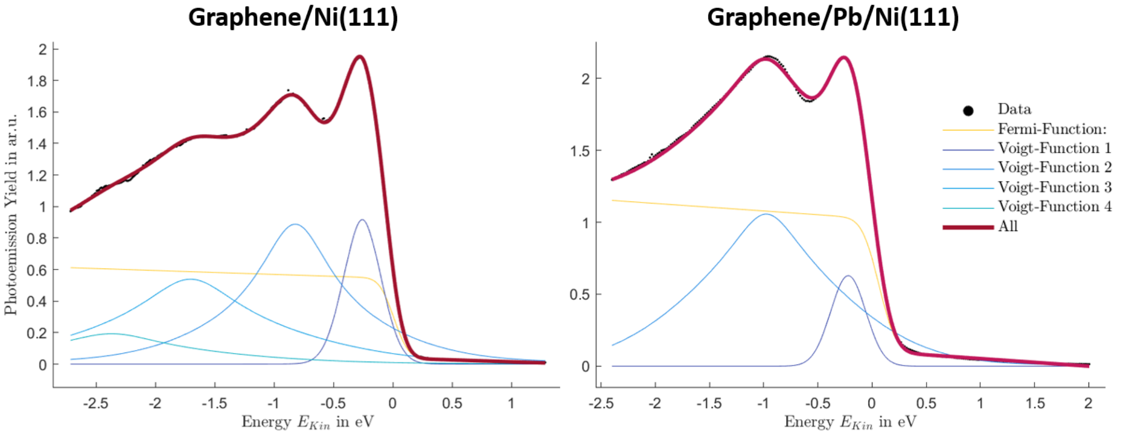

Figure (4.7) Explanatory fitting result plots for graphene/Ni(111) (top) and graphene/Pb/Ni(111) (bottom) at t_0. The applied fitting function (red, Equ. 4.2) consists of 4 (for graphene/Ni(111)) or 2 (for graphene/Pb/Ni(111)) Voigt functions (blue shaded peaks, Equ. 4.1) multiplied by the Fermi distribution and a linear background (yellow line).

Lower spin split band fitting Different k-space regions were defined to represent the lower spin-split band. Three representative cuts are analysed (see Table 4.1). Fitting weights, as listed in Table 4.2 were applied according to the method explained in Section 2.3.4.3, to emphasise the region near the Fermi.

Table (4.1) Fit results: lower spin split band

	graphene/Ni(111)	graphene/Pb/Ni(111)
Cut 3a	$k_x = 1.080\,\text{Å}^{-1}$ to $k_x = 1.098\,\text{Å}^{-1}$	$k_x = 1.080\,\text{Å}^{-1}$ to $k_x = 1.097\,\text{Å}^{-1}$
Cut 3b	$k_x = 1.117\,\text{Å}^{-1}$ to $k_x = 1.135\,\text{Å}^{-1}$	$k_x = 1.1066\,\text{Å}^{-1}$ to $k_x = 1.1159\,\text{Å}^{-1}$
Cut 3c	$k_x = 1.162\,\text{Å}^{-1}$ to $k_x = 1.180\,\text{Å}^{-1}$	$k_x = 1.125\,\text{Å}^{-1}$ to $k_x = 1.134\,\text{Å}^{-1}$

Table (4.2) Fit results: lower spin split band

	weights	Energies $E - E_F$
graphene/Ni(111)	5	0.242 eV to −0.761 eV
graphene/Ni(111)	6	0.039 eV to −0.059 eV
graphene/Pb/Ni(111)	10	−0.489 eV to −1.278 eV
graphene/Pb/Ni(111)	20	0.740 eV to −0.576 eV

In this case, a region with a smaller energy window was used, and the fitting function was modified to include 3 Voigt functions. Explanatory results are provided in Figure 4.8. The peak positions extracted from these fits trace the evolution of the lower Ni-band, as compared in Figure 4.9. The red plot illustrates the mean of the 3 different cuts. One can see that the general shape is the same

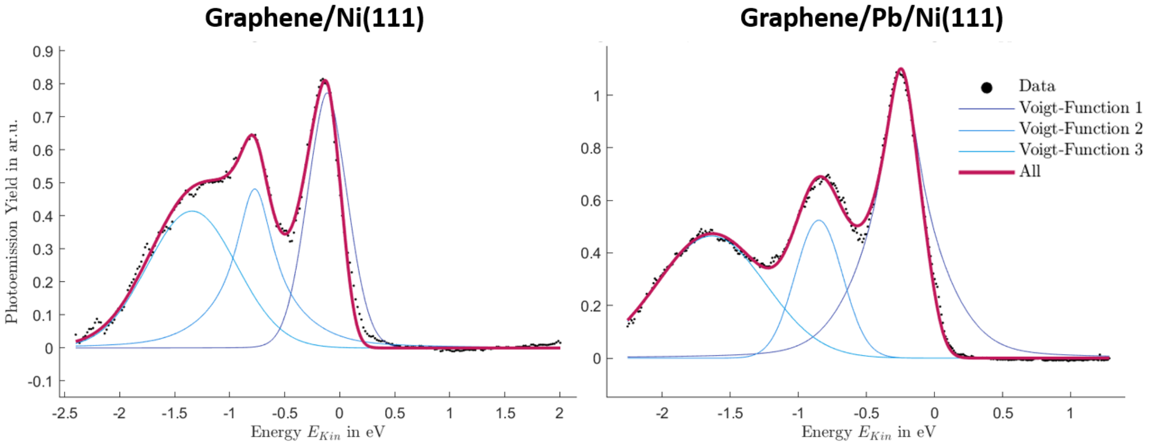

Figure (4.8) Explanatory fitting result plot for graphene/Ni(111) at $\Delta t = -1000\,\text{fs}$ for the lower spin-split Ni-band. graphene/Ni(111) dataset (left) and graphene/Pb/Ni(111) dataset (right). The fitting function (red; Equ. 4.2) comprises 3 Voigt functions (blue shaded; Equ. 4.1) multiplied by the Fermi distribution.

for all 3 cuts. The dip at t_0 can be explained by an overall band shift after the strong laser excitation. After the initial dip the lower Ni-band moves towards lower binding energies within the first 200 f sec and slowly recovers to its initial position, marked by dotted lines for the different cuts.

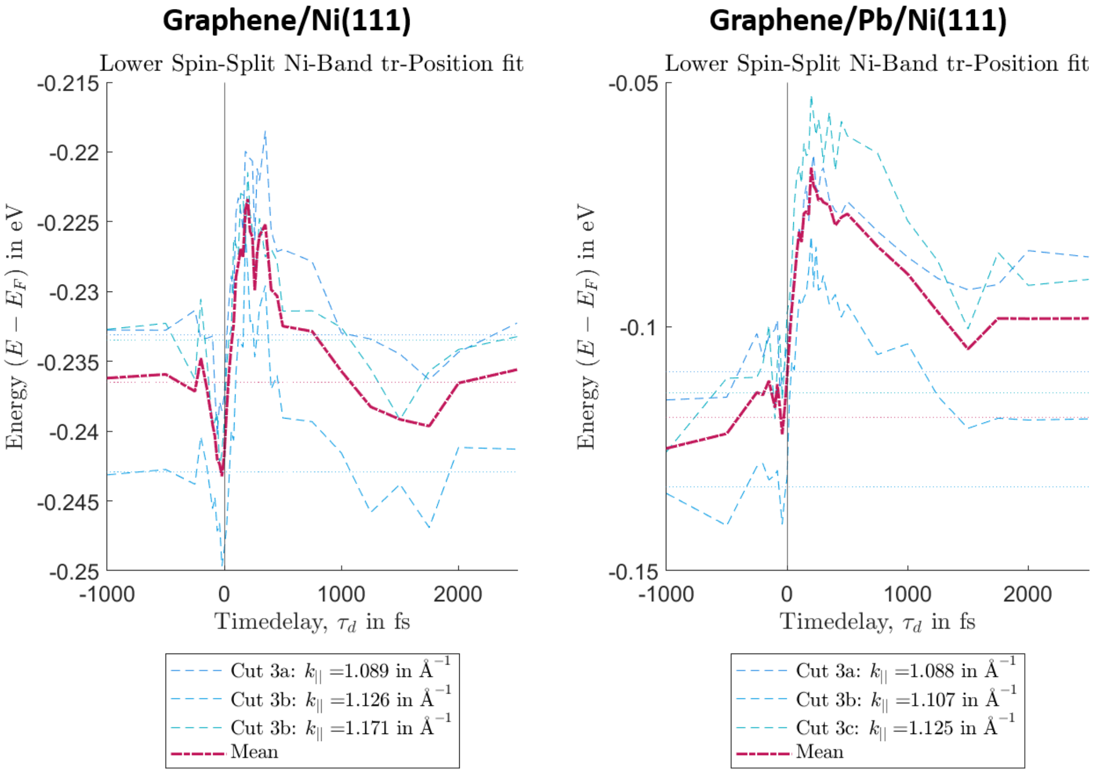

Figure (4.9) Comparison of time-resolved lower Ni-band peak positions for cuts 3a, 3b, and 3c (blue shaded curves) in graphene/Ni(111). The red curve indicates the mean of the three cuts. The dip at t_0 is attributed to a collective band shift following strong laser excitation, after which the lower Ni-band shifts toward lower binding energies within the first 200 fs and gradually recovers.

Upper spin split band fitting Next, the shift of the upper spin band is fitted. This task is more challenging because the signal is overlapped by the lower band and is close to the Fermi edge, leading to a truncated peak shape. The results from the lower spin band fits and the time-resolved Fermi function are incorporated as constraints, with the lower spin band cut nearest to the upper band

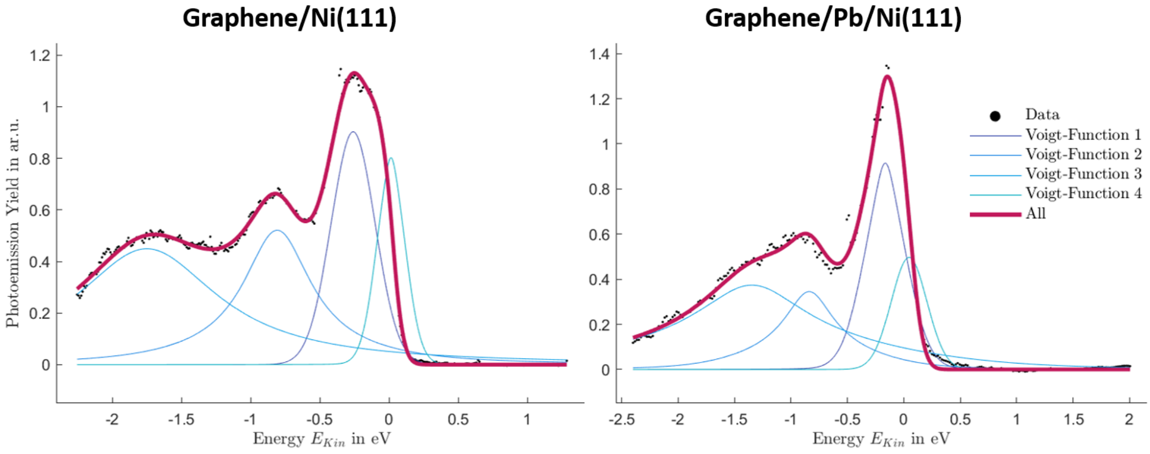

Figure (4.10) Explanatory fitting result plot for graphene/Ni(111) at $\Delta t = -1000$ fs for the upper spin-split Ni-band. The fitting function (red; Equ. 4.2) comprises 4 Voigt functions (blue shaded; Equ. 4.1) multiplied by the Fermi distribution and a linear background.

serving as a reference. Three cuts are analysed (see Table 4.3). The same weighting as in Table 4.2 is applied, while the fitting function now comprises 4 Voigt peaks to capture the upper Ni-band. Explanatory results are shown in Figure 4.10. Comparison of the peak positions from the upper band fits is shown in Figure 4.11. The results indicate that, despite a less reliable fit due to the overlapping structure, the upper spin band follows a similar temporal trend in all cuts.

Table (4.3) Fit results: upper spin split band

	graphene/Ni(111)	graphene/Pb/Ni(111)
Cut 1	$k_x = 0.961\,\text{Å}^{-1}$ to $k_x = 0.980\,\text{Å}^{-1}$	$k_x = 0.885\,\text{Å}^{-1}$ to $k_x = 0.894\,\text{Å}^{-1}$
Cut 2	$k_x = 0.989\,\text{Å}^{-1}$ to $k_x = 1.007\,\text{Å}^{-1}$	$k_x = 0.903\,\text{Å}^{-1}$ to $k_x = 0.912\,\text{Å}^{-1}$
Cut 4	$k_x = 1.007\,\text{Å}^{-1}$ to $k_x = 1.016\,\text{Å}^{-1}$	$k_x = 0.885\,\text{Å}^{-1}$ to $k_x = 0.912\,\text{Å}^{-1}$

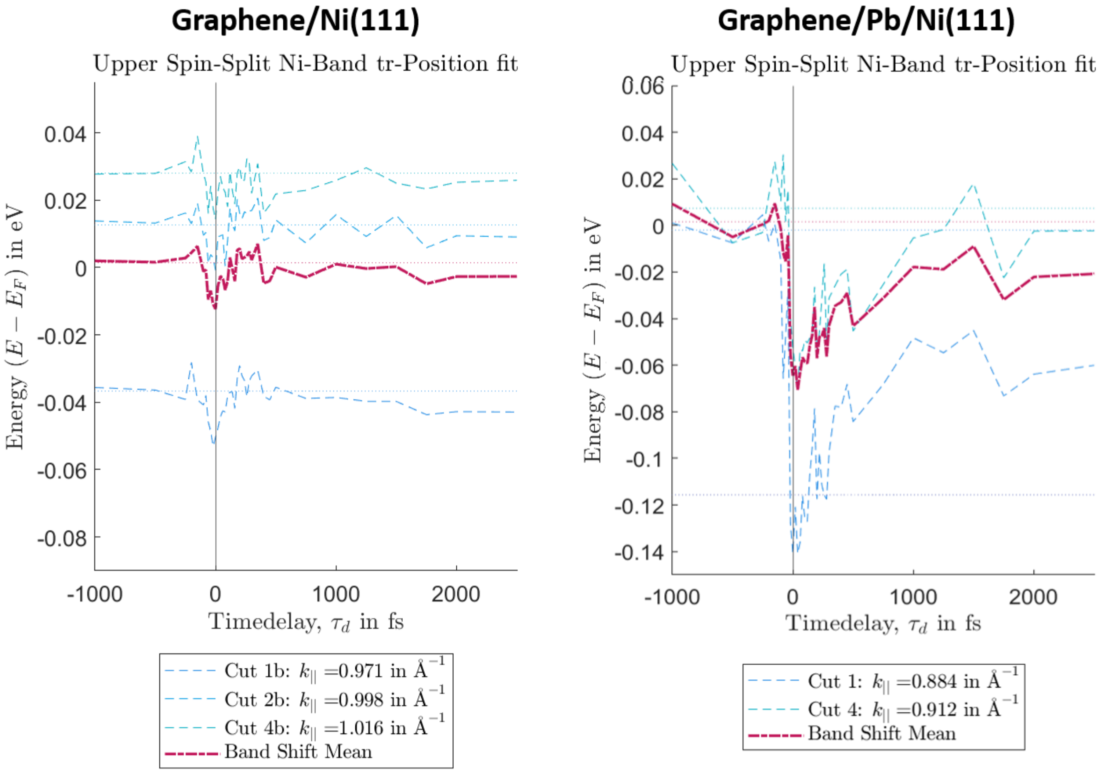

Figure (4.11) Comparison of time-resolved upper Ni-band peak positions for selected cuts in graphene/Ni(111) and graphene/Pb/Ni(111) (blue curves) with the mean indicated by the red curve. The upper band remains below its baseline and recovers slowly.

Extraction of the exchange splitting collapse In agreement with the expected band renormalisation, the upper and lower Ni bands start to converge after optical excitation. In both cases (figures: 4.11 and 4.9) the peaks move from their original position within 200 f sec. The recovery on the other hand appears to be comparatively slow. The subsequent analysis subtracts the mean values of the upper and lower Ni bands to yield the change in exchange splitting over time, as shown in figures 4.12 (for graphene/Ni(111)) and 4.13 (for graphene/Pb/Ni(111)).

The illustration in Figure 4.12 and 4.13 conveys, not only the possibility to extract the exchange splitting from the upper and lower band position fitting routine, but also the similarity to the data (black) taken on pristine Ni(111) at the transverse momentum $k_{||} \approx 1.05\,\text{Å}^{-1}$ along the $\overline{\Gamma} - \overline{K}$ direction by KM et al [44]. The original data plot from the paper is separately shown in Figure 4.12. Unfortunately, the experiments for graphene/Ni(111) and graphene/Pb/Ni(111) could not be performed with the exact same driving laser conditions. The result is a higher applied fluency (after taking the reflectivity of nickel of 64% [44] into account) in the graphene/Pb/Ni(111) - $F_{NiPbGr} \approx 1.432\,\text{mJ/cm}^2$ - experiments compared to graphene/Ni(111) - $F_{NiGr} \approx 0.895\,\text{mJ/cm}^2$ (for details on the calculation see Section 2.2.3). Of this, approximately $0.034\,\frac{\text{mJ}}{\text{cm}^2}$ and $0.021\,\frac{\text{mJ}}{\text{cm}^2}$ (around 2.3%

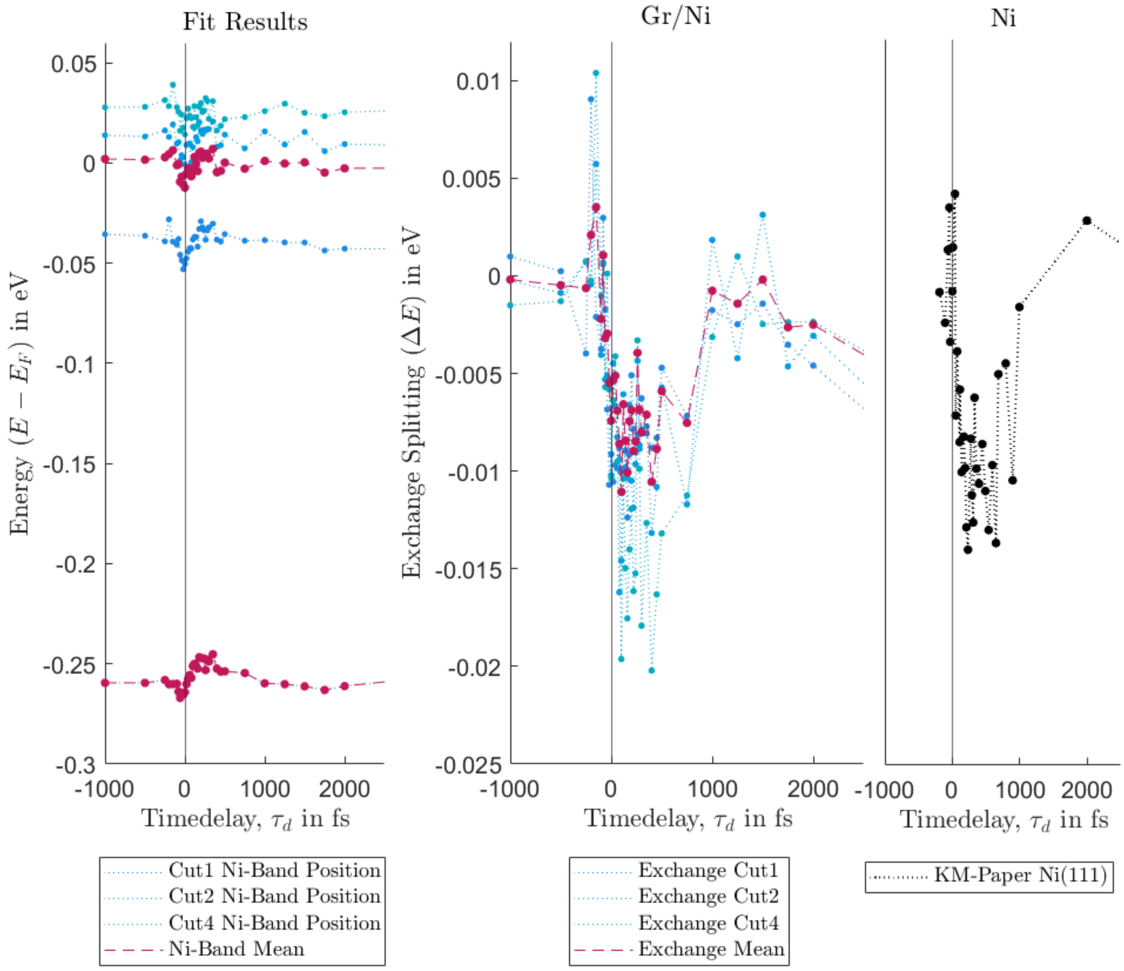

Figure (4.12) Upper and lower Ni-band peak positions from all fitted cuts and the resulting exchange splitting in graphene/Ni(111). For comparison, data from pristine Ni(111) at $k_{||} \sim 1.05\,\text{Å}^{-1}$ along the $\overline{\Gamma}$–$\overline{K}$ direction from [44] are plotted in black.

[11]) is absorbed by the graphene layer respectively. Lead on the other hand is almost transparent in the visible spectral range resulting, based on findings in [85] the absorption of one monolayer lead is assumed to be in the range of $\sim 0.5\,\% - 1\,\%$, hence $0.007\,\frac{\text{mJ}}{\text{cm}^2}$ - $0.014\,\frac{\text{mJ}}{\text{cm}^2}$ (potentially on the lower end). Measurements on a 1 nm nickel film found absorption efficiencies of $\sim 10\,\% - 15\,\%$ [86] resulting in an absorbed fluence of $F_{NiGr}(1nm) \approx 0.089\,\frac{\text{mJ}}{\text{cm}^2} - 0.134\,\frac{\text{mJ}}{\text{cm}^2}$ and $F_{NiPbGr}(1nm) \approx 0.142\,\frac{\text{mJ}}{\text{cm}^2} - 0.213\,\frac{\text{mJ}}{\text{cm}^2}$ (1nm is roughly the relevant depth for this surface sensitive measurement, since only electrons from the first few layers contribute to the measured signal). Approximation of these values to one ML ($\sim 2.04\,\text{Å}$ [29]) yields an $\sim 2.5\,\% - 3\,\%$ absorption rate, hence $F_{NiGr}(1stML) \approx 0.022\,\frac{\text{mJ}}{\text{cm}^2} - 0.027\,\frac{\text{mJ}}{\text{cm}^2}$ and $F_{NiPbGr}(1stML) \approx 0.036\,\frac{\text{mJ}}{\text{cm}^2} - 0.043\,\frac{\text{mJ}}{\text{cm}^2}$ for the first Ni layer (i.e. in the same regime or slightly higher than the graphene sheet). Therefore, a lead monolayer is likely to absorb less laser power compared to the first few Ni layers or the graphene, with the first few nickel layer absorbing the bulk of the introduced energy in the ARPES-probed surface area. Additionally, due to the differences in absolute applied laser fluence, the magnetisation quenching in the graphene/-Ni(111) system is expected to be weaker (lower exchange splitting collapsing rate). Comparing Figure 4.12 and 4.13 the clearly smaller shift of the spin-splitted bands is visible. Although the absolute quenching rate (exchange splitting collapse in percent, depicted in Figure 4.15) is different, the timescales still can be extracted and compared, as demonstrated by the Murnane group, who had a similar absolute exchange splitting quenching in there low fluency experiments (see Figure 4.12). Since my experiments are both within the low fluency range as defined in [84], I do not expect any additional effects to take place as they have seen in the higher fluency graphene/Pb/Ni(111) measurement, namely a two-time components remagnetisation dynamic.

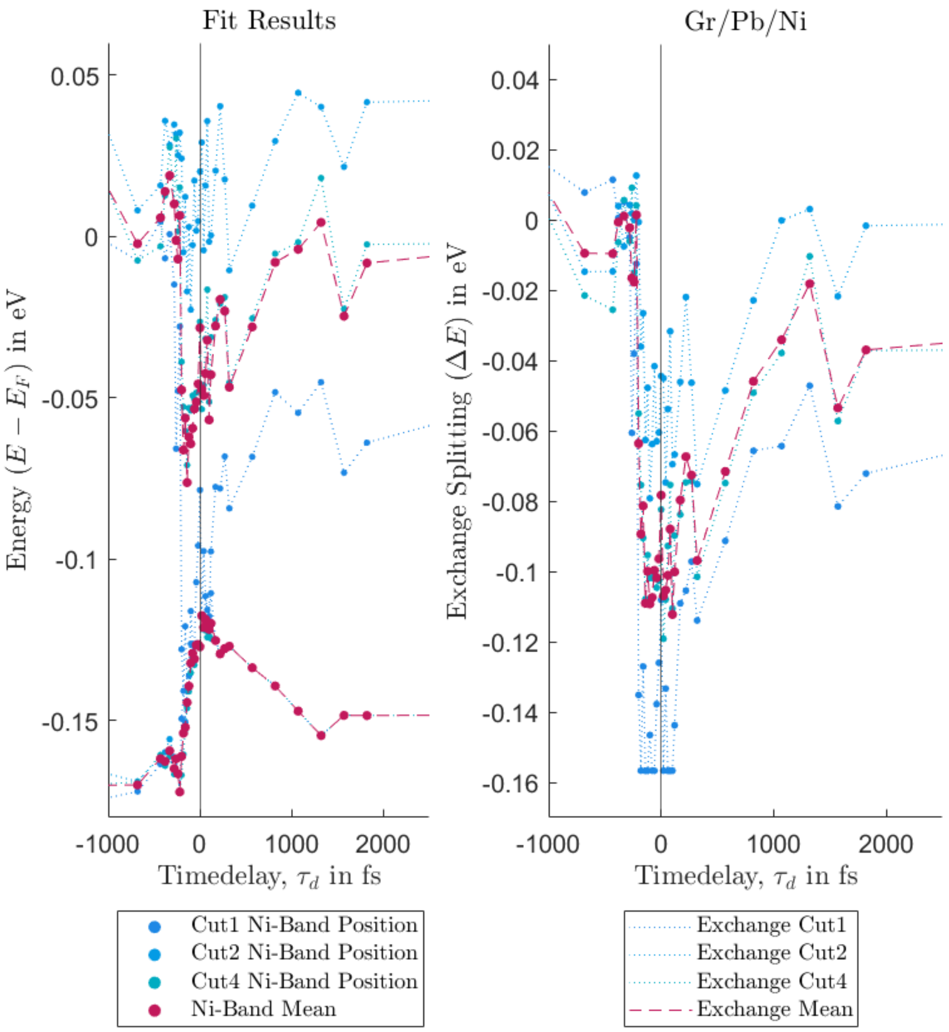

Figure (4.13) Upper and lower Ni-band peak position for all fitted cuts and the resulting exchange splitting in graphene/Pb/Ni(111).

De- and remagnetisation in graphene/Ni(111) and graphene/Pb/Ni(111) While there is agreement on the different mechanisms driving ultrafast demagnetisation, their relative importance within different material systems is debated. Among other parameter, how the processes show themselves in the materials band structure may varies. In the context of this work, as established in the beginning of this chapter, it is known from previous studies [44, 84] that the demagnetisation of nickel has a band structure fingerprint: the exchange splitting collapse. The overall shape of the extracted exchange splitting curves indicates a fast demagnetisation process followed by a slower remagnetisation. This is in accordance with the general trace of demagnetisation dynamics after optical excitation [78]. One indicator of the general processes is the electron system temperature. Demagnetisation is driven by the rapid heating of the electronic degree of freedom out of equilibrium. In the absence of equilibrium, the electron system may no longer adhere to a Fermi distribution. However, it is important to note that the results obtained from the fitted Fermi function width can serve as a valuable indicator of the electron system temperature. Figure 4.14 shows that in both graphene/Ni(111) and graphene/Pb/Ni(111) the electron system reaches the maximum of the absorbed pump energy (determined by the Fermi distribution width) within 20 fs following the pump pulse peak. Although the electron system absorbs the pump energy rapidly, the magnetic response (spin-system) observed in the angle-resolved photoemission spectroscopy signal evolves on a longer timescale, similar to observations in Tr-MOKE experiments. One can fit the same double exponential decay function to the extracted exchange spitting data as one would use in Tr-MOKE to extract the

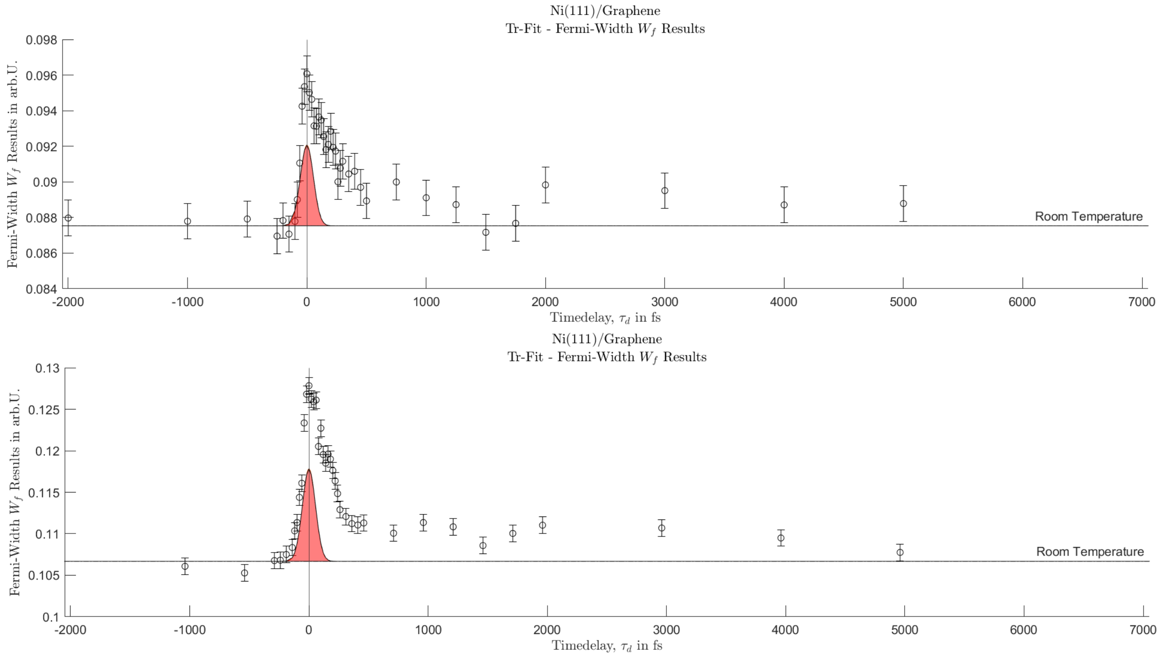

Figure (4.14) Fermi function width fitting results for graphene/Ni(111) (top) and graphene/Pb/Ni(111) (bottom), which reflect the electron temperature. The pump pulse is indicated in the background, and the baseline (black line) represents the pre-excitation (room) temperature. The electron system absorbs the pump energy within 20 fs, followed by a fast (∼200 fs - 500 fs) and a slow (multiple ps) recovery.

de- and remagnetisation timescales [44, 84].

$$m(t_{delay}, z) = \begin{cases} 1 & \text{if } t_d < 0 \\ 1 + a_1(z)\mathrm{e}^{\frac{t_d}{\tau_{demag}}} - a_2(z)\mathrm{e}^{\frac{t_d}{\tau_{recover1}}} - a_3(z)\mathrm{e}^{\frac{t_d}{\tau_{recover2}}} & \text{if } t_d \geq 0 \end{cases} \tag{4.3}$$

where m is the normalised magnetisation (with full magnetisation corresponding to an exchange splitting of 1 and a closing of the band gap$\Delta E = 0$, yields complete demagnetisation), t_d is the pump-probe delay, and a_1, a_2, and a_3 are amplitudes corresponding to the underlying physical processes [44].

For the low-fluence regime investigated here, the slow recovery amplitude a_3 was found to be negligible, and a double-exponential fit suffices (this is in accordance with the conclusion from the Murnane group, that the long timescale recovery only applies for high fluency excitations). Additional fits involving a convolution with a Gaussian (performed by Paul Herrgen) are presented in Figure A.9 in the Appendix. The goal was to control whether accommodating the pump laser peak width of 55fs changes the results. The results for the demagnetisation and remagnetisation times are summarised in Table 4.4 and compared with literature values from the Murnane group. For our fits the 90% confidentiality interval is given as well. Figure 4.15 displays the extracted exchange splitting curves,

Table (4.4) Comparison of magnetisation dynamic fit-results for graphene/Ni(111) and graphene/Pb/Ni(111)

	Gr/Ni mean	Cut1	Cut2	Cut4	Gr/Pb/Ni mean	Cut1	Cut2	Cut4	Ni(111) [44]
Convoluted: $\tau_{demag} =$	120 ± 61fs	30 ± 26fs	259 ± 2342fs	185 ± 126fs	38 ± 29fs	21 ± 38fs	19 ± 56fs	21 ± 39fs	176 ± 27fs
Convoluted.: $\tau_{recover1} =$	491 ± 253fs	401 ± 123fs	281 ± 255fs	587 ± 501fs	678 ± 279fs	991 ± 468fs	1083 ± 499fs	776 ± 285fs	$\tau_{re1} = 537 \pm 173$fs
double exp.: $\tau_{demag} =$	112 ± 57fs	55 ± 36fs	148 ± 88fs	168 ± 107fs	56 ± 15fs	40 ± 11fs	38 ± 20fs	45 ± 18fs	176 ± 27fs
double exp.: $\tau_{recover1} =$	540 ± 312fs	349 ± 190fs	482 ± 325fs	687 ± 501fs	597 ± 167fs	682 ± 166fs	902 ± 223fs	665 ± 222fs	$\tau_{re1} = 537 \pm 173$fs

the corresponding fit double exponential function, and the deduced demagnetisation time τ_d for both the graphene/Ni(111) and graphene/Pb/Ni(111) samples. For the graphene/Ni(111) system, the demagnetisation results (except for one cut) closely resemble those reported for pristine Ni(111) [44, 84], with a tendency toward a slightly shorter demagnetisation time for the graphene/Ni(111) interface. As expected, one monolayer of carbon does not influence the nickel magnetisation strongly. In particular as is is in contrast to the graphene/Pb/Ni(111) data exhibiting **exceptionally short**

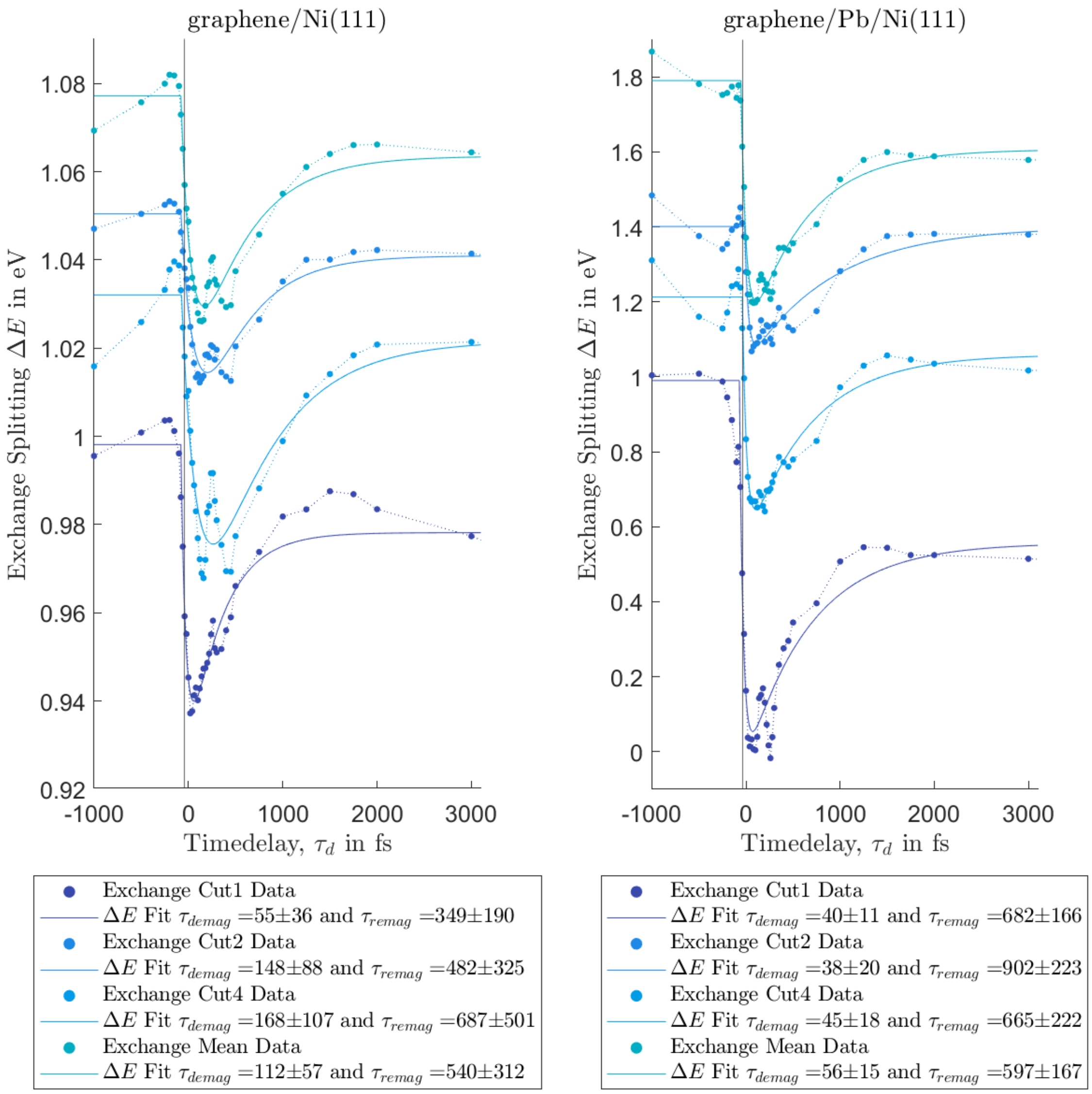

Figure (4.15) Double-exponential fitting results for the demagnetisation curves of graphene/Ni(111) (left) and graphene/Pb/Ni(111) (right), showing the extracted exchange splitting and corresponding fit function. A peak near 1.5ps is evident in all curves, which does not appear in pristine Ni(111) data. The curves were moved transversal to ensure better visibility in the plot.

demagnetisation times of approximately 20 to 40 fs, which almost approach the timescale of electron systems maximal pump energy absorption (see Figure 4.14). The remagnetisation times are similar (within the 90% confidence interval) for all three systems, suggesting a common underlying mechanism. These findings indicate a strong tendency, although further measurements are required to confirm their reliability. The subsequent discussion addresses potential effects influencing the magnetisation dynamics at interfaces.

4.4. Towards "high speed" demagnetisation of nickel through graphene/lead interfacing

The respective importance of the driving mechanisms behind ultrafast optical demagnetisation remain a topic of debate, with a number of models proposed, such as light-induced spin currents, Elliott–Yafet spin-flip scattering [87], dynamic reduction of the exchange splitting via spin-orbit coupling [88], coherent optical excitation [89], and incoherent magnon excitation [90, 91]. The contributing factors are complex and multifaceted.

The time-resolved ARPES measurements show that, for all samples, the exchange-split Ni 3*d* bands converge in energy after optical excitation, signalling an ultrafast loss of magnetisation. This femtosecond collapse of exchange splitting is attributed to the well-known laser-induced demagnetisation effect in Ni [92]. Table 4.5 compares demagnetisation and recovery times obtained from different nickel-based sample systems. The table shows data for the nickel surface from literature, and the results from this thesis. As a note: results for the magnetisation dynamics in a bulk system vary over a wast range, this is mainly due to the respective methods used. It is anticipated that magnetisation dynamics in bulk and surface will differ (for example, due to the significantly stronger influence of spin transport effects on the surface). Consequently, they are only presented to provide a comprehensive overview. Two fitting approaches are distinguished: the **mean** value refers to fits where the exchange gap size was first averaged over all cuts and then fitted, while the **Cut mean** value refers to the averaged values for the individual cuts after fitting. Noteworthy is the differences between all these timescales.

Table (4.5) Comparison of demagnetisation and recovery times obtained from different nickel-based sample systems

		τ_{demag}	$\tau_{recover}$
Ni Bulk [80, 93–96]		300 fs over 500 fs up to 1000 fs	-
Ni(111) surface [44]		176±27fs	537±173fs
graphene/Ni(111)	Average conv.	158±129fs	423±258fs
	Average doubl.exp.	124±77fs	506±339fs
	Mean conv.	120±61fs	491±253fs
	Mean doubl.exp.	112±57fs	540±312fs
graphene/Pb/Ni(111)	Average conv.	20±44fs	919±418fs
	Average doubl.exp.	56±15fs	750±204fs
	Mean conv.	38±29fs	920±418fs
	Mean doubl.exp.	56±15fs	597±167fs

Focussing first on the reference Ni(111) surface (no overlayer) from [44, 84] [1]. The initial demagnetisation of Ni(111) is governed by two key processes: (1) **local spin-flip scattering** driven by electron–phonon interactions (Elliott–Yafet mechanism) [92], and (2) non-local spin transport (superdiffusive spin currents) that transport spin angular momentum out of the probed nickel regime [30]. Ni is known to demagnetise on a $\tau_{\mathrm{Ni}} \sim 100\,\mathrm{fs} - 200\,\mathrm{fs}$ timescale in both theory and previous experiments [78, 79]. In good agreement with this findings, a demagnetisation time of 170 fs was reported. The experiments were done under UHV-conditions using Tr-ARPES, therefore no capping layers were present (in contrast to Tr-MOKE studies normally conducted in air). Here the Ni film's hot electrons can still escape to the vacuum or the bulk substrate, but there is **no specific spin sink layer**. Thus, τ_{demag} for bare Ni is primarily dictated by **intrinsic spin-flip scattering** rates and transport from the surface to non-probed regions in the bulk. The measured $\tau^{\mathrm{Ni}}_{\mathrm{demag}}$ (approximately 170 ± 20 fs from a fit to the exchange splitting vs. time) is in excellent agreement with the Elliott–Yafet predictions for Ni's material parameters [92]. This consistency validates that the Ni(111) reference can serves as a reliable baseline for my ultrafast magnetisation dynamics analysis.

The presence of a graphene monolayer on Ni(111) notably alters the demagnetisation behaviour (see Figure 4.16). The Tr-ARPES data presented in this chapter show that graphene-capped Ni still undergoes ultrafast demagnetisation, but the effective demagnetisation amplitude is slightly reduced (due to the low applied fluence) compared with other findings in this thesis. Notably, the graphene layer appears to enhance the demagnetisation process, shortening the overall demagnetisation time to $\sim 116\,\mathrm{fs} \pm 59\,\mathrm{fs}$ (mean, see Table 4.5).

These observations can be explained by considering graphene's dual role at the interface. First, graphene passivates the Ni surface, possibly suppressing surface-specific magnon generation or preventing Ni surface atom rearrangements during laser heating, which could otherwise slightly enhance demagnetisation.

Second, and more importantly, laser-induced demagnetisation experiments on thin nickel films have revealed that **surface-enhanced spin currents** significantly accelerate the demagnetisation process compared to bulk nickel, where spin-orbit coupling predominantly drives spin-flip transitions [97, 98]. It follows that graphene potentially provides an additional pathway for spin-polarised electrons to delocalise: as a one-atom-thick semimetal with high conductivity, graphene can accept hot

---

[1] The used Nickel film was 400 nm thick while the signal observed is from maximal 13 nm due to the probing depth in the used Tr-HHG setup shown in Figure 4.2

electrons from Ni and allow them to propagate out of the probed surface region. While pristine graphene has weak intrinsic SOC, when it is in contact with Ni the proximity effect and the strong hybridisation (see Section 3.2.1) can induce moderate SOC and exchange splitting in graphene's π bands [16]. This means graphene can act as a **spin current sink**, as confirmed by Mondal et al. who found faster demagnetisation in graphene-covered ferrimagnetic layers than in uncovered ones [99].

Despite the novelty of these findings and the speculative nature of their applicability to the graphene/-Ni(111) system, it is important to note a recent study by Bobowski et al. on gadolinium [83]. They found, using Tr-ARPES techniques, that the **OISTR-effect** strongly facilitates the spin-transport between surface and bulk-aiding ultrafast demagnetisation. As gadolinium is a 4f-ferromagnetic system with localised 4f and 5d stated transferring the spin-polarised charge into the bulks delocalised bands, this is not true for pristine nickel. However, it is known from previous studies in this group [19] that the strong hybridisation between graphene and nickel causes "new" hybrid states at the interface and influences the nickel surface states and spin-polarisation at the interface. Just like in Gd, where surface-localised electrons transfer spin to bulk states, here the graphene/Ni hybridised bands may act as interfacial channels with modified spin character and optical excitation could induce spin-polarised charge transfer from Ni into hybridise interface states or vice versa. This would enable a form of intersite spin transfer, not between atoms of the same kind (like in Gd), but across a hetero-interface. Bobowski et al. state that in Gd: "**Spin-polarised electrons transition across chemically distinct, spin-active orbitals in real space during optical excitation**", thereby strongly hybridised graphene/Ni(111) could create OISTR-like conditions, aiding the demagnetisation.

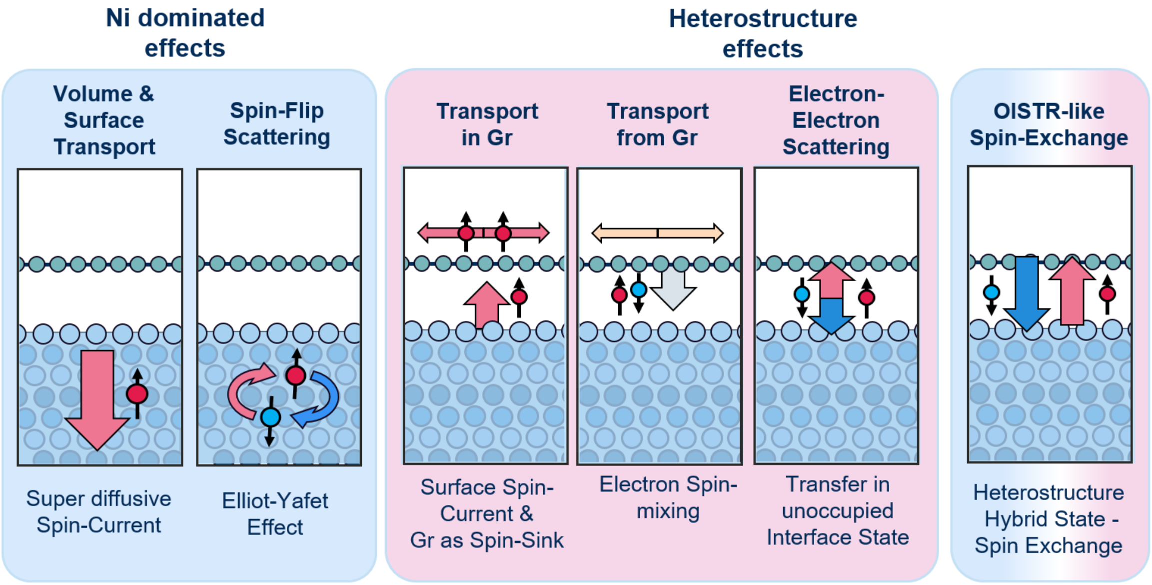

Figure (4.16) Different processes contributing to ultrafast energy and magnetisation dissipation in graphene/Ni(111).

Therefore, the presence of graphene opens an additional channel for **ultrafast energy and spin-polarised electron flow** out of the Ni layer. Furthermore, its high thermal conductivity in combination with its adsorption of 2.3% of the applied lacer fluence, could lead to spin-mixed electrons flowing from the graphene into the topmost (probed) nickel layer facilitating the spin-depolarisation. Graphene's high in-plane thermal conductivity may also rapidly spread the deposited energy, aiding quicker recovery. The re-magnetisation generally is on a similar timescale as the pure nickel, but, not considering the uncertainties, a tendency for a slightly faster recovery is visible. A faster re-magnetisation in Ni/Gr (Ni/graphene) could be a result of graphene conducting heat away, cooling the Ni electrons faster and thus shortening the magnetisation recovery time. The data quality (hence the resulting uncertainties) and used pumping fluency for the graphene/Ni(111) measurements, however, remains insufficient for definitive comparative conclusions at this stage.

In summary, the Ni/Gr interface exhibits an ultrafast demagnetisation with a kinetics that is consistent with partial spin-current emission into graphene. Including graphene in device designs could therefore be a way to tune demagnetisation time τ_m.

Finally, the graphene/Pb/Ni(111) tri-layer demonstrates the most rapid and extensive demagnetisation of the three cases discussed here (Table 4.5)). The observed high-speed demagnetisation time in the range of 20 fs ± 44 fs to 56 fs ± 15 fs is astonishing. Empirically, I recorded the largest collapse of exchange splitting (up to 160 meV), and a complete quenching of Ni's spin polarisation at the peak of the response for cut1 (see Figure 4.13).

This result is fully consistent with the role of the intercalated Pb monolayer as a **highly efficient spin sink**. As discussed earlier, the expectations for this system regarding adsorbed pump laser power are different for each layer, the respective absorption rates are depicted in Figure 4.17. The graphene is expected to absorb 2.3% of the applied laser fluence, the lead only ∼0.5 % - 1 % and the first nm nickel ∼ 10 % − 15 % (∼ 2.5 % − 3 % in the first ML).

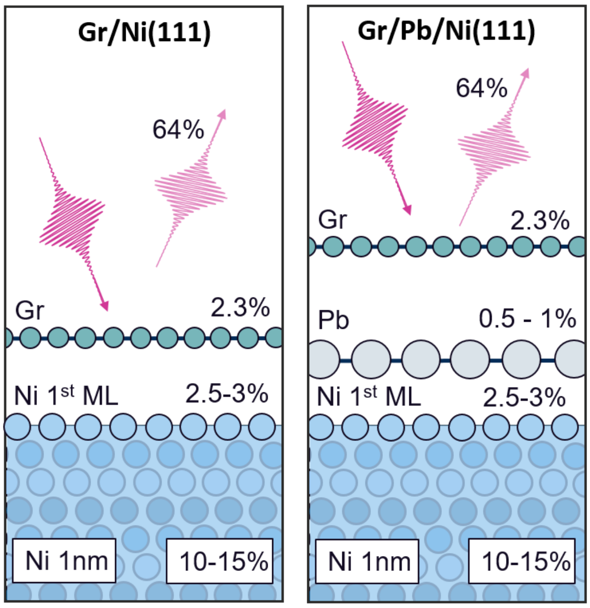

Figure (4.17) Layer depended laser energy absorption scheme

Therefore, when the pump laser excites Ni's electrons, a substantial fraction of majority-spin electrons will traverse into the adjacent heavy-metal layer before they can scatter or thermalise in Ni (a net electron transfer from Ni to Pb). Pb has a low magnetic moment (non-magnetic) and a large atomic number (high SOC), which means it can absorb spin-polarised electrons from Ni and rapidly randomise their spins via spin-orbit scattering (see below). The process can be viewed as an ultrafast version of spin pumping, where Ni's transient magnetisation injects a spin current into Pb on the timescale of Ni's electron thermalisation (tens of femtoseconds). The theoretical framework by Battiato et al. predicts exactly this: a ferromagnet in contact with a heavy metal will lose magnetisation faster because majority spins leave the ferromagnet [30]. The experimental observation backs this model.

Several studies have examined lead-doped nickel, where an **alloy-like band structure** is often emphasised [100, 101]. Nickel and lead form a strong bond at their interface [29], but no alloy. However, even though the Pb layer is atomically thin, it is enough to markedly increase the interfacial spin conductance. This can be attributed to the surface sensitivity of the employed measurement methods (Tr-ARPES) as discussed previously. Furthermore, it aligns with element-specific studies, such as Eschenlohr et al.'s XMCD experiment, where Ni demagnetises more in the presence of an Au capping [31]. The function of the graphene layer in this transportation scheme may be realised in two distinct ways. It has the capacity to adsorb a significant quantity of laser fluency, which could result in the transportation of spin-mixed electrons into the nickel. On the other hand, its high in-plane conductivity could facilitate the spin-polarised transportation from nickel out of the probed surface region. The question at hand cannot be answered with the extant experimental data; theoretical spin-transport calculations for the presented systems are required.

Another primary mechanism regarding ultrafast demagnetisation is **spin–lattice scattering**. Lattice disorder enhances spin–lattice scattering [102], suggesting that the faster demagnetisation in the graphene/Pb/Ni(111) system may be promoted by the higher disorder in the graphene/Pb/nickel(111) interface layer compared to pristine nickel and the graphene/Ni(111) system (potentially due to imperfect intercalation or Pb concentration fluctuations within the surface). This might provide additional phononic scattering partners. Bonetti et al. propose that scattering from atomic disorder facilitates a more efficient transfer of spin angular momentum to the lattice, strongly influencing demagnetisation [102].

Intercalation of lead between graphene and nickel also alters the interfacial electronic structure. Being a heavy element, lead introduces enhanced spin-orbit coupling at the interface, which may promote more efficient **spin-flip scattering** processes and lead to faster demagnetisation [103]. Aligning with this findings, S. Acharya et al. [104] have reported that rapid demagnetisation around 50 fs is mainly due to electron correlations and memory effects that trigger spin-flip transitions from occupied to unoccupied orbitals, dynamically reducing the exchange splitting. Enhancing this further is the restoration of the graphene band structure which not only increases the density of states at the Fermi level (more scattering partners). And it is affecting the electron-phonon coupling and thus the dynamics of energy dissipation from the electronic system to the lattice.

Since the Pb layer directly contacts Ni, and its high density of states at E_F provides an immediate sink for Ni's spin-polarised electrons which then might be migrated to the graphene. The graphene might additionally assist by stabilising the Pb layer and preserving a clean interface.

Lastly, if potentially less important, **structural dynamics**, including strain induced by high-intensity laser irradiation, such as strain waves, may also differ in systems with an intercalation layer. It was found that especially systems, were the mechanical properties are strongly altered (like intercalating lead underneath the graphene), this can have an impact on magnetisation dynamics [105].

Interestingly, while for the graphene/Ni(111) system the remagnetisation appears to be slightly faster, in the graphene/Pb/Ni(111) sample the recovery time is drastically increased. This might be an indication on the prominent effect facilitating the demagnetisation. Comparing the timescale of 597 fs ± 167 fs to 920 fs ± 418 fs to the more rapid thematisation of the electron temperature (Fermi width, depicted in Figure 4.14) indicates a slower thematisation of the spin-systems temperature compared to the electron system. While ultrafast majority spin-transport to the Pb and graphene and the consequent spin-mixing through spin-flip-scattering processes within this layers facilitates the demagnetisation, recovery and consequently back scattering of the spins appears to be much slower. Several factors can contribute to the significantly slower magnetisation recovery in the graphene/Pb/Ni(111) system compared to the graphene/Ni(111) system:

Pb acting as a spin sink or spin diffusion layer: The intercalated Pb layer is not magnetic, but due to its high atomic number, introduces strong SOC at the interface. This increased SOC facilitates efficient spin-flip scattering, which can lead to a deeper and more prolonged quenching of the Ni magnetisation. The enhanced spin-orbit interactions can trap spin angular momentum in the Pb layer. Additionally, Pb intercalation alters the interfacial spin-mixing conductance and the efficiency of spin current transfer. In the graphene/Ni(111) system, spin-polarised electrons can rapidly re-equilibrate via efficient spin transport through graphene. However, in the presence of Pb, the heavy-metal layer may act as a **spin reservoir** that absorbs and retains spin angular momentum. This reduces the effective spin current backflow into Ni, thereby prolonging the recovery process.

Graphene as a heat bath: The graphene layer and its high thermal conductivity might act as a heat bath. Since the graphene is considered quasi-free standing, the heat transfer from graphene to the substrate might be inefficient and thereby prolonged. The ARPES data obtained support the instant electronic excitation in the graphene layer. As discussed in the previous section, the graphene band gap collapse might be facilitated through nickel electrons filling the graphene conduction band during demagnetisation. If so, it is possible that the graphene returns (hot) spin-mixed electrons over an extended period of time to the up most-probed nickel layer prolonging the measured exchange-splitting recovery.

Consequently, the extremely fast and efficient heterostructure-supported "transformation" of majority-spin-electron to minority-spin-electron and their subsequent transport within the heterostructure might cause a spin-mixing as long as the electron-system temperature is high enough for strong transport effects. At the same time, electron-phonon interaction will cool the electron system. The

system might therefore be still in a highly spin-mixed state when this cooling of the general electron temperature (within 500 fs) starts reducing the overall spin-scattering rate. The, at this point, much lower electron temperature - compared to the point where spin-equilibration dominates the spin system in pristine nickel or graphene/Ni - might lead to a generally slower recovery time.
This theory remains speculative and theoretical calculations are needed to address the question of slow re-magnetisation in the tri-layer system.

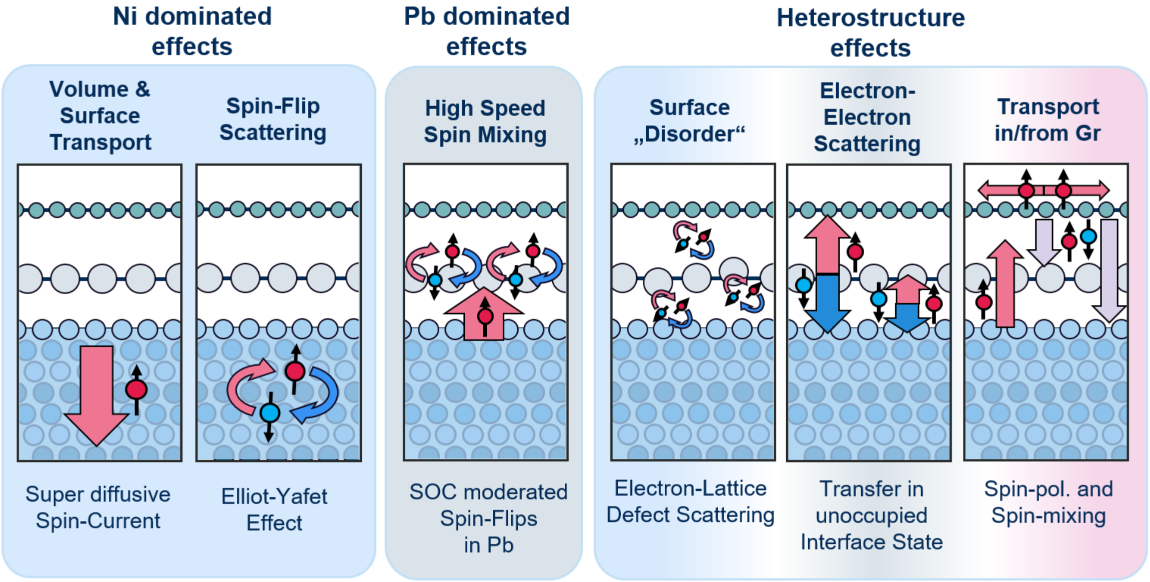

Figure (4.18) Different processes contributing to ultrafast energy and magnetisation dissipation in graphene/Ni(111).

In conclusion, the Ni/Pb interface effectively shortcuts the spin angular momentum out of the Ni film, leading to a faster and more complete demagnetisation. After the initial drop, the recovery of magnetisation in Ni/Pb/Gr is slower than in Ni/Gr, presumably because the spin and energy that flowed into the heavy Pb layer take longer to diffuse back or dissipate. The Ni layer is relatively cooler (magnetically) after demag, and the re-magnetisation must await either spin currents returning or repopulation of majority spins via equilibration with the lattice. This is consistent with a two-step demagnetisation scenario: an ultrafast drop (fs) followed by a slower re-magnetisation (ps), where the second step is prolonged when a sink layer is present (since the Ni layer is effectively more decoupled from its own spin reservoir).

Conclusion

I have performed a comprehensive study of ultrafast magnetisation dynamics in Ni(111) modified by two types of interfacing layers: a graphene monolayer and a Pb intercalation layer beneath graphene. Using time- and angle-resolved photoemission to directly monitor Ni's exchange-split band structure, the following key research objective was answered:

How does the presence of graphene, and an intercalated heavy metal layer, influence the femtosecond demagnetisation of a ferromagnetic substrate?
A single layer of graphene on Ni(111) does change the ultrafast demagnetisation.
Extensive peak position fitting and analysis of the exchange gap collapse indicate a tendency toward shorter demagnetisation times at the graphene/Ni(111) interface compared to pristine Ni(111) surfaces, providing strong evidence for an interfacial influence on surface magnetisation dynamics. I conclude that graphene influences Ni in two ways: it preserves Ni's magnetic order (no quenching of equilibrium magnetisation) while also providing an extra channel for spin and heat transport. The net result in my samples was a minor reduction in demagnetisation to roughly 120 fs (faster than the 176 fs observed at the bare surface [44]) while the remagnetisation remains unchanged, suggesting that in this specific interface, graphene acts as a spin sink, potentially further facilitated

through a hetero-interface OISTR-like effect [83]. In principle, with an atomically clean interface, graphene's enhanced spin-orbit coupling (when proximate to Ni) can absorb spin angular momentum more efficiently, potentially accelerating demagnetisation as reported in other systems. However, it remains unclear whether this effect arises from magnetic moment transfer to graphene, an increased number of scattering partners, or graphene acting as a heat sink. The findings still highlight that the graphene/Ni(111) interface can be tuned – through interface quality or multilayer graphene stacks – to slightly enhance ultrafast demagnetisation while additionally passivating the highly reactive Ni(11) surface. This tunability and passivation is of interest for ultrafast spintronic device engineering.

Introducing a single layer of Pb between graphene and Ni yields a markedly faster and more complete demagnetisation of Ni.
Thus, intercalating lead does not diminish graphene's effect on nickel, rather, the graphene/Pb/-Ni(111) system exhibits an extraordinarily fast demagnetisation time that approaches the intrinsic timescale of the hot electron system. I attribute this to the Pb layer acting as a powerful spin sink, siphoning off excited spin-up electrons from Ni and facilitating spin-flip scattering at the interface. The graphene/Pb/Ni(111) sample reached a lower minimum magnetisation (nearly zero residual exchange splitting) than graphene/Ni(111) (potentially mitigated by lower pump fluenies), indicating that Pb enabled Ni to achieve a transient paramagnetic state more fully (or at least faster). This result is a clear experimental demonstration of the enhancement of ultrafast demagnetisation by a heavy metal contact, in line with theoretical predictions [30] and previous studies on Ni/Au and Co/Pt interfaces. It underscores the importance of spin-current transmission in dictating demagnetisation dynamics: even a single-atom interlayer can dramatically change the flow of angular momentum. Since the analysis traces the peak centre positions (indicative of exchange gap collapse) rather than the absolute magnetisation, it is evident that the fast dynamics observed are not solely due to band mirroring. Element-sensitive, time-resolved magnetisation dynamic measurements are needed to verify this effect. The exact role of the graphene in this interface is debatable. The intercalant prevents some of the mechanisms discussed for the graphene/Ni(111) system (e.g. a potential OISTR-like effect due to the prevention of hybrid state formation), but the free floating graphene layer might act as a source for (hot) spin-mixed electrons over an extended period of time, influencing the magnetisation recovery. At this point, it can be concluded that the intercalated system represents a promising candidate for optically induced ultrafast demagnetisation in thin films.
For applications, this means one can control the speed and extent of magnetisation loss with tailored interface layers (e.g. inserting high-Z materials to speed up spin dissipation) on device interfaces. The optical dynamic quenching of the exchange splitting on timescales approaching that of the hot electron system is highly promising for future applications in data storage, transistors, and other electronic devices.

In conclusion, the chapter demonstrates that coupling Ni(111) with two-dimensional or heavy-metal materials can modulate Ni's femtosecond magnetisation dynamics in a controllable way. This advances the fundamental understanding of ultrafast spin exchanges at interfaces and could be valuable for the design of future magnetic heterostructures where ultrafast control of magnetism is desired. For instance, graphene could be used as a protective capping that still permits fast spin dissipation, and heavy metal interlayers could be engineered to achieve extremely rapid quenching of magnetisation for all-optical magnetic switching schemes. These findings bridge the knowledge gap between traditional ultrafast magnetism in pure metals and the emerging arena of 2D material/ferromagnet interfaces, highlighting the rich physics that occurs when spins, interfaces, and femtosecond dynamics converge.

Summary

Overall, this chapter reconciles the ultrafast magnetisation dynamics at graphene/Ni(111) and graphene/Pb/Ni(111) interfaces using Tr-ARPES with established physical mechanisms. By comparing the different scenarios, direct evidence is provided that the efficiency of angular momentum evacuation from the ferromagnet is the decisive factor governing the demagnetisation rate. Graphene, a light element, offers a moderate enhancement (or at least no hindrance) of demagnetisation via spin-pumping into its delocalise π-electron system. Pb, a heavy element, provides a much stronger enhancement via spin-orbit scattering and high spin conductance. These conclusions are supported by a range of literature, from classical Ni experiments [78] to modern interface-specific studies [31, 95, 99], solidifying the interpretations.

This chapter has shown that the very interface engineered in Chapter 3 governs femtosecond demagnetisation, enhancing it dramatically when Pb decouples graphene from Ni. This spin-dynamics control is the critical link to Chapter 5, where I will exploit precisely these hot-carrier lifetimes to drive charge transfer into a molecular semiconductor.

5. Light Driven Charge Carrier Injection From Graphene/Nickel(111) Interface Into Organic Molecular Systems

In the final result chapter, I complete the thesis by using the interfaces characterised in Chapters 3 and 4 as active injectors. The graphene/Ni(111) stack delivers spin-polarised hot electrons whose demagnetisation dynamics I quantified in Chapter 4. Here, I track how those same carriers populate coronene's unoccupied orbitals on dual timescales, tying together band engineering and spin dynamics into an unified picture of hybrid charge transfer.

Acknowledgement of collaborative efforts and individual work

I sincerely appreciate the expert support of several colleagues, whose valuable contributions were crucial to making the experimental work in this chapter possible.
This chapter is based on two sets of data:

Firstly, static measurements of a coronene/Ni(111) sample (gathered at the 2024-04-12 and from 2024-05-07 to 2024-05-08).
Sample preparation: Aaron Gebert and myself; Data acquisition: Aaron Gebert and myself; Setup build-up and maintenance: Benito Arnoldi and Johannes Stöckel (ARPES); Data analysis: Myself, separate, more detailed analysis of this sample system was done by Aaron Gebert and published in his master thesis.

Secondly, static and time-resolved measurements of a coronene/graphene/Ni(111) sample (gathered at between 2023-07-24 and 2023-07-30).
Sample preparation: Myself; Data acquisition: Myself supported by Gregor Zinke; Setup build-up and maintenance: Benito Arnoldi and Johannes Stöckel (ARPES), Eugen Nosenko, Gregor Zinke and Sebastian Hedwig (Lasersystem and HHG-beamline); Data analysis: Myself.

Additional support regarding the sample system: Christina Schott. Scientific advisors throughout: Benjamin Stadtmüller and Martin Aeschlimann.

Scientific objectives

This chapter addresses the ultrafast, optically induced injection of charge carriers across the Ni(111)-graphene (graphene/Ni(111)) interface into an organic molecular system, using coronene as the representative molecular component. The motivation behind this study lies in the growing interest in controlling interfacial charge transfer in hybrid organic–inorganic systems, a topic of significant relevance for next-generation electronic and optoelectronic devices.

The studied heterostructure exemplifies a prototypical **Spinterface**. Spinterfaces, as defined by Cinchetti *et al.* [106], are interfaces formed between ferromagnetic materials and organic molecules where spin-dependent interactions occur. Such interfaces play a crucial role in the realisation of molecular spintronic devices due to their intrinsic spin-selective properties. The hybridisation between molecular orbitals and electronic states of the ferromagnetic substrate generates a spin-dependent electronic structure at the interface, pivotal for effective spin injection and detection in molecular spintronics. Moreover, the alignment and interplay of molecular orbitals with substrate electronic states profoundly influence the interfacial spin polarisation. Controlled tuning of these interactions thus holds significant potential for enhancing spintronic functionalities. However, precise control and reproducibility of spinterfaces remain challenging, primarily due to interface disorder and variability inherent in molecular adsorption processes.

By leveraging time-resolved photoemission (TR-ARPES) techniques, I explore how optical excitation can modulate the electronic structure at the (sp-)interface, leading to transient band renormalisation and enabling the injection of charge carriers into the molecular orbitals of coronene, visualise in Figure 5.1.

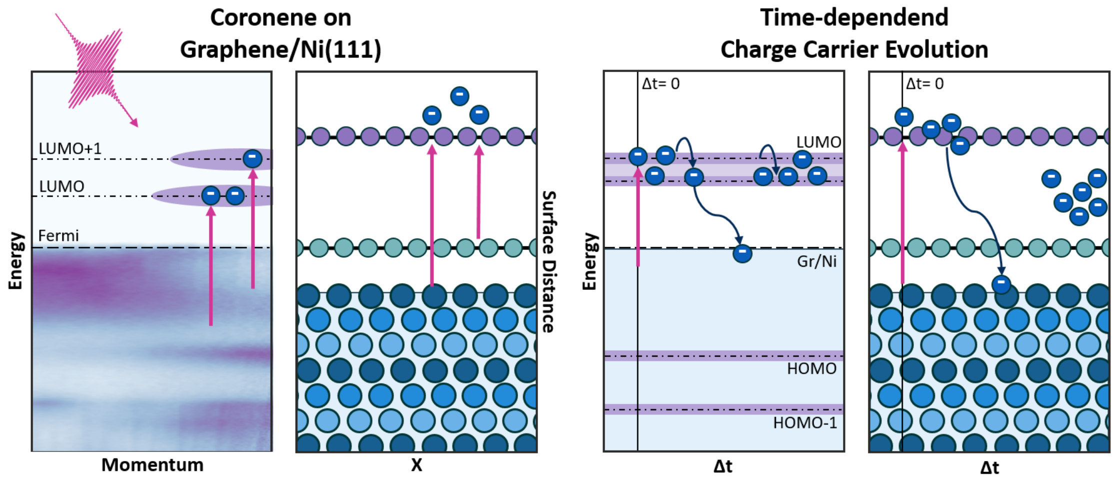

Figure (5.1) Research Objective: Light induced charge carrier injection from the graphene/Ni interface into a molecular system and their time-resolved evolution.

Coronene, a well-defined polycyclic aromatic hydrocarbon (PAH) with a fully conjugated π-electron system, is frequently employed as a model system for studying π–π interactions and charge delocalisation. When deposited on reactive substrates such as Ni(111), coronene exhibits strong hybridisation with the underlying metal, resulting in geometric distortions and modifications to its electronic properties. In contrast, the incorporation of a graphene buffer layer decouples coronene from the substrate, preserving its intrinsic molecular orbital structure. This chapter details the **static** and **Stationary-delay configuration** (excited state spectroscopy for one time delay step at t_0) investigations that elucidate these effects, and it further presents time-resolved measurements that capture the transient dynamics following optical excitation.

By combining static structural characterisation with time-resolved spectroscopic measurements and advanced data analysis, this work aims to provide a comprehensive understanding of light-induced charge transfer processes in complex hybrid interfaces. The insights gained here are expected to inform the design of future organic–inorganic heterostructures for applications in nano-electronics and spintronics. Furthermore, I aim to answer the prime question addressed in this chapter:
Can a graphene monolayer facilitate the injection of photo-excited charge carriers from a metal into an adsorbed molecular semiconductor, and what are the ultrafast dynamics of such charge-transfer processes?

5.1. Introduction into coronene and its application

Coronene ($C_{24}H_{12}$) is a polycyclic aromatic hydrocarbon (polycyclic aromatic hydrocarbon molecules) comprising six benzene rings arranged in a highly symmetric, planar hexagonal configuration, depicted in Figure 5.2. This molecular architecture gives rise to a fully conjugated π-electron system, rendering coronene a prototypical model for exploring π-π interactions and charge delocalisation. The extensive π-conjugation and electron delocalisation, underpins its relatively high electron affinity and its propensity for strong π-π stacking interactions with other aromatic systems. Owing to its well-defined geometric and electronic structure, coronene is extensively utilised as a reference material in surface science to benchmark the adsorption behaviour of more complex two-dimensional (2D) organic systems, particularly graphene. Due to its structural similarity to graphene, coronene is frequently referred to as “nano-graphene” in the literature.

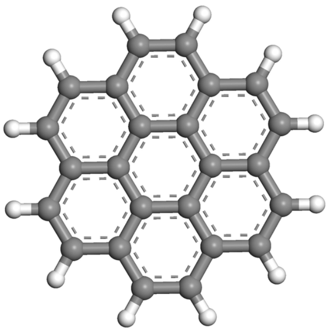

Figure (5.2) The Molecular structure of coronene. Reprinted from [32]

Coronene has been rigorously investigated on various metallic substrates. On highly reactive surfaces, most molecular adsorbate fail to establish ordered arrangements. An ordered molecular arrangement is crucial because it leads to reproducible and well-defined interfacial electronic structures. This ordering allows for better control of the spin-dependent hybridisation between the molecules and the ferromagnetic surface, which is key to achieving consistent and effective spintronic functionality. Disordered arrangements can introduce variability and unpredictability, which negatively affects device performance [106].

However, on Ni(111), the structural congruence with graphene induces a well-ordered adsorption pattern. In the case of coronene/Ni(111), this epitaxial ordering enables precise electronic and geometric characterisations. Notably, when deposited on Ni(111), coronene undergoes a slight bending deformation, as illustrated in Figure 5.4, while preserving its overall ordered configuration. This deformation facilitates stronger hybridisation between the nickel d-bands and the inner carbon atoms of coronene, allowing an analogous interaction as observed for graphene on Ni(111) (the deformation compensates for the repulsive potential of the hydrogen atoms on coronene, those are not present in pristine graphene, hence a buckling to achieve strong hybridisation does not occur). Such strong interfacial interactions may perturb the intrinsic π-bonding, thereby hindering the goal to utilise the unique π-bonding properties of coronene. The ensuing structural modifications and concomitant electronic band structure alterations are discussed comprehensively in Section 5.1.1.1 and in the dissertation by Christina Schott [29].

In addition to studies on metal surfaces, previous investigations have demonstrated that coronene can actively modulate the electronic properties of 2D materials through mechanisms such as charge transfer and local density of states modification. These effects are pivotal for elucidating molecule–substrate interactions and for the design of organic–2D material heterostructures in advanced electronic and optoelectronic devices [107]. For instance, coronene adsorption on graphene has been shown to preserve the π-conjugation in both the adsorbate and the substrate, thus enabling the study of π-π stacking interactions in a low-dimensional framework. Such comparative analyses provide critical insights into the delicate balance between physisorption and chemisorption, highlighting the influence of substrate selection on molecular orientation, binding energy, and the emergent electronic structure. These investigations further establish coronene as a sensitive probe for fundamental interactions at organic/inorganic interfaces, particularly in systems where the interfacial electronic structure is governed by the interplay between molecular orbitals and substrate states.

A resent theoretical study by Darían *et al.* [108] found that coronene can not only serve as a model system for π-π stacking, but also to study ultrafast dynamics in polycyclic aromatic hydrocarbon molecules and graphene nano flakes. Through their in-depth computational analysis of the ultrafast excited-state dynamics of coronene and circumcoronene they found that decay of electronic states is largely size independent and predominantly driven by “breathing” and “tilting” vibrational motions, facilitating relaxation away from the **Franck–Condon region** - the “initial position” in an excited state of a molecule with unchanged nuclear configuration. The study further highlights, that the energy distribution via molecule breathing and tilting happens on a sub-100 fs to a few hundred fs timescale.

The combination of this coronene behaviour, together with the graphene/nickel(111) substrate as a potential source of spin-polarised electrons naturally leads to the central research question of this chapter.

5.1.1. Geometrical properties

5.1.1.1. Coronene/Ni(111)

As noted above, coronene has been extensively investigated on various metallic substrates. Despite the highly reactive surface of Ni(111), coronene molecules form a long range ordered superstructure [109, 110]. Importantly, in the context of this study, coronene molecules on Ni(111) form a single molecular unit cell, ensuring that all molecules experience an identical chemical environment and contribute uniformly to the photoemission signature. Enables precise electronic and structural characterisation (most methods average over a certain region and thereby over a multitude of molecules, on an ordered structure, these signals still reveal precise information about individual molecules). In contrast to graphene, the peripheral hydrogen atoms in coronene induce a repulsive interaction between adjacent molecules, thereby establishing a well-defined minimal intermolecular distance. Two dominant commensurate adsorption configurations are observed, namely the condensed and relaxed structures [29], as depicted in real-space models and low-energy electron diffraction images presented in Figure 5.3 (depending on the exact preparation and nickel surface conditions other structures might be favoured by the molecules [29]).
For the condensed structure, the unit cell dimensions reach the lower limit for molecular proximity with $b_1 = b_2 = 10.85\,\text{Å}$. This structure is distinguishable by a characteristic double-feature in the LEED pattern (Figure 5.3(b)).

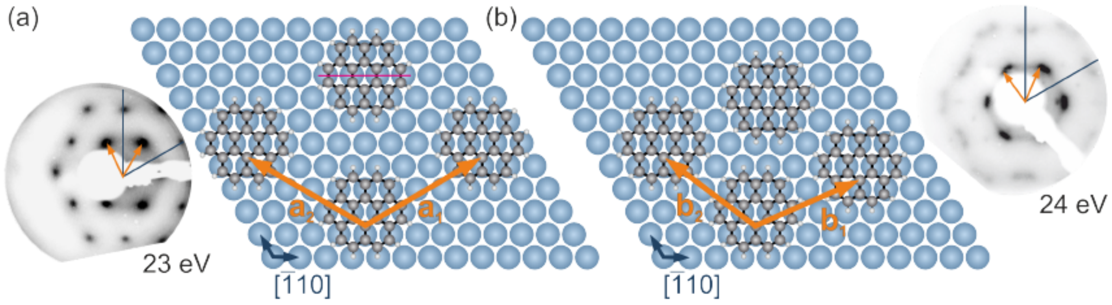

Figure (5.3) LEED pattern and lateral adsorption sketch of (a) relaxed and (b) condensed coronene structure. $a_1 = a_2 = 12.94\,\text{Å}$ and $b_1 = b_2 = 10.85\,\text{Å}$. Reprinted from [29].

normal incidence X-ray standing wave (NIXSW) studies conducted within our group indicate that on the highly reactive Ni(111) surface, coronene exhibits a bending deformation while maintaining its ordered arrangement [29], as shown in Figure 5.4. This is in contrast to adsorption on noble metals such as Au(111), Ag(111), and Cu(111), where coronene adsorbs nearly flat. This "nickel-induced" bending is indicative of hybridisation between the inner carbon atoms of coronene and the Ni(111) d-bands. The local bonding configuration favours this hybridisation over a homogeneous π-bonding network, leading to a stronger orbital overlap and enhanced hybridisation at the interface.

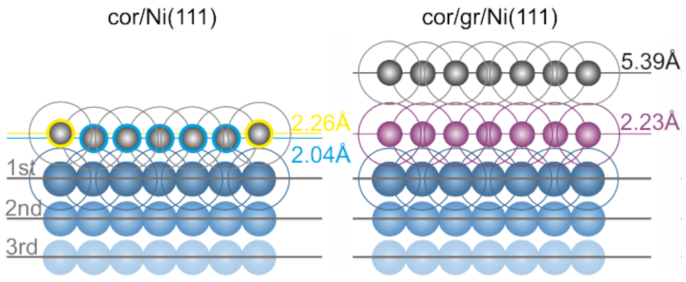

Figure (5.4) Vertical adsorption scheme of the relaxed coronene/Ni(111) structure and the coronene/graphene/Ni(111) heterostructure. Reprinted with kind permission of the author from [29].

5.1.1.2. Coronene/Graphene/Ni(111)

While coronene is strongly bound to the Ni(111) surface, it is critical to assess whether the introduction of a graphene buffer layer alters the adsorption geometry. This issue was addressed using NIXSW measurements. The results indicate an average distance of 5.46(4) Å between the coronene layer and the Ni(111) surface, and a distance of 3.20(4) Å between the coronene molecules and the graphene buffer layer [29]. A schematic comparison of these distances with the graphene/Ni(111) system is provided in Figure 5.4. The measured coronene–graphene distance corresponds to approximately 94% of the van-der-Waals distance between two carbon atoms, which is comparable to the interlayer spacing observed in π-bonded molecular heterostructures such as graphite [111]. For comparison, stacking multiple graphene layers in graphite yields an interlayer spacing of approximately 3.3 Å [112, 113]. Thus, the coronene–graphene stack exhibits a similar interlayer distance and bonding strength, indicating that the graphene buffer layer effectively decouples coronene from the Ni(111) substrate. Consequently, the chemical environment of graphene - in the case presented here, referring to the strong hybridisation with the nickel surface - remains largely unaltered by the additional coronene layer.

Schott *et al.* further investigated the lateral geometry of the coronene/graphene/Ni(111) system. They found that the coronene superstructure is rotated by approximately 11 degree relative to the graphene/Ni(111) substrate. This rotation optimises the π-orbital overlap between the graphene sheet and the coronene layer and may be observable in ARPES measurements. The corresponding LEED pattern and lateral adsorption model are illustrated in Figure 5.5.

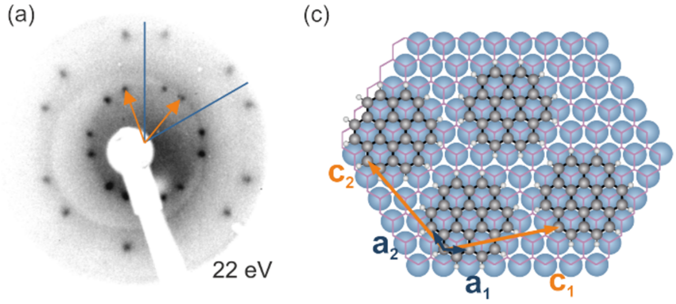

Figure (5.5) (a) LEED pattern for coronene/graphene/Ni(111); (c) lateral adsorption model of the coronene/graphene/Ni(111) heterostructure. C_1 and C_2 denote the coronene unit cell vectors with a length of 11.41 Å, while a_1 and a_2 represent the graphene unit cell. The coronene layer is rotated by 11 degree relative to the substrate. Reprinted with kind permission of the author from [29].

5.1.2. Decoupling coronene from highly reactive surfaces

While strong bonding to reactive surfaces such as Ni(111) can be advantageous for certain applications, the lost of specific molecular functionalities needed by many modern organic electronic devices requires suppression of such interactions. Previous chapters have demonstrated the high utility of the graphene/Ni(111) interface for charge transfer studies, within the study presented in this chapter graphene is additionaly used as a passivation or buffer layer between nickel and coronene. It is therefore essential to verify that the coronene layer is sufficiently decoupled from the Ni(111) substrate.

When a pristine Ni(111) surface is measured using ultraviolet photoemission, the Ni d-bands dominate the spectrum. After deposition of coronene, distinct molecular orbital features appear in the otherwise featureless photoemission yield, as illustrated in Figure 5.6. Figure 5.6 presents a comparison of ARPES measurements for Ni(111), graphene/Ni(111), coronene/Ni(111), and the coronene/graphene/Ni(111) sample system. The momentum-resolved photoemission spectroscopy (PES) maps (top panels) and the corresponding energy distribution spectra (bottom panels) reveal that increasing coronene coverage leads to a dampening of the Ni(111) d-bands photoemission signal, concomitant with the emergence of molecular orbital signatures. Additional low-coverage measurements (shown in the next section) further substantiate this trend. In Figure 5.7 a zoomed in depiction of the coronene/graphene/Ni(111) band structure measurement is shown. Noteworthy for the following analysis is the broad range in momentum space that is occupied by the molecular features. Especially, the HOMO is visible almost from the $\overline{K}$-point to the $\overline{\Gamma}$-point with its spectral weight being centered at higher momentum values.

The ability of graphene to decouple a coronene molecular layer from Ni(111) was investigated using NIXSW and XPS experiments, as detailed in [29] and Section 5.1.1.2. These studies show that when adsorbed directly on Ni(111), coronene forms strong bonds with the nickel d-bands. This bonds result in tetrahedral localise electronic states, disrupting the π-conjugation and thereby breaking the planarity and aromaticity at the bonding site (hence a re-hybridisation from sp^2 to sp^3). The result is the bending deformation of the coronene molecules on the Ni(111) surface, depicted in 5.4. This bending reflects significant hybridisation, which not only alters the molecular geometry but also induces electron doping and shifts the molecular orbital energies toward higher binding energies. Notably, the first Ni(111) d-band peak is more strongly attenuated than the second, suggesting a

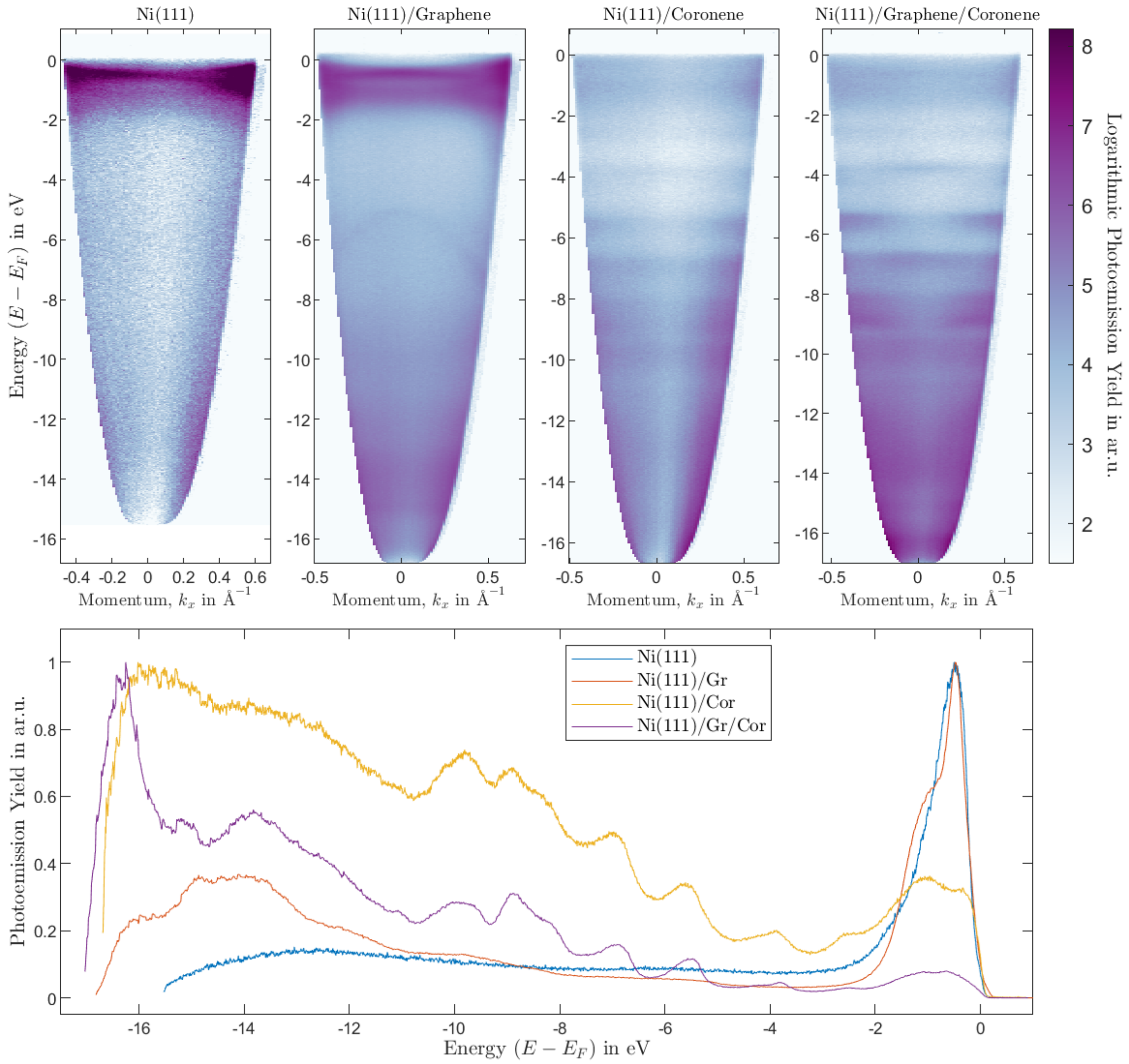

Figure (5.6) Comparison of ARPES measurements at the $\overline{\Gamma}$-point for Ni(111), graphene/Ni(111), coronene/Ni(111) and the coronene/graphene/Ni(111) sample system. On the top momentum vs energy maps are shown and the graph on the bottom depicts the respective spectra for the four sample systems. With rising coverage a dampening of the Ni(111) d-bands can be observed as well as the emerging of the molecular orbital signature.

non-uniform hybridisation with the coronene across the d-bands energy range.
Momentum microscopy measurements published in [29] confirm the strong hybridisation between coronene and the nickel surface. Studies on similar systems (e.g. coronene on Ag(111)) have shown that ordered coronene monolayers can exhibit distinct π-derived bands in ARPES [114]. On Ag(111), coronene's π-orbitals hybridise slightly with the metal's sp-bands, yielding a "graphene-like" band structure in the low binding energy-region [114]. In analogy, when coronene is adsorbed on a graphene buffer layer (i.e., in the coronene/graphene/Ni(111) system), a nearly free-standing character of coronene is restored. The ARPES data indicate that the coronene–graphene interface exhibits a pure π-π-stacking (non-covalent) character, which is consistent with weak van-der-Waals bonding. This observation is corroborated by NIXSW and XPS results, which yield an interlayer distance of $3.20\,\text{Å} \pm 0.04\,\text{Å}$ between the graphene and the coronene superstructure. For comparison, the interlayer spacing in graphite is approximately $3.3\,\text{Å}$ [29, 112, 113]. These findings support the conclusion that, in the context of this thesis, the coronene layer can be treated as a quasi-free-standing molecular layer when decoupled by a graphene buffer sheet.

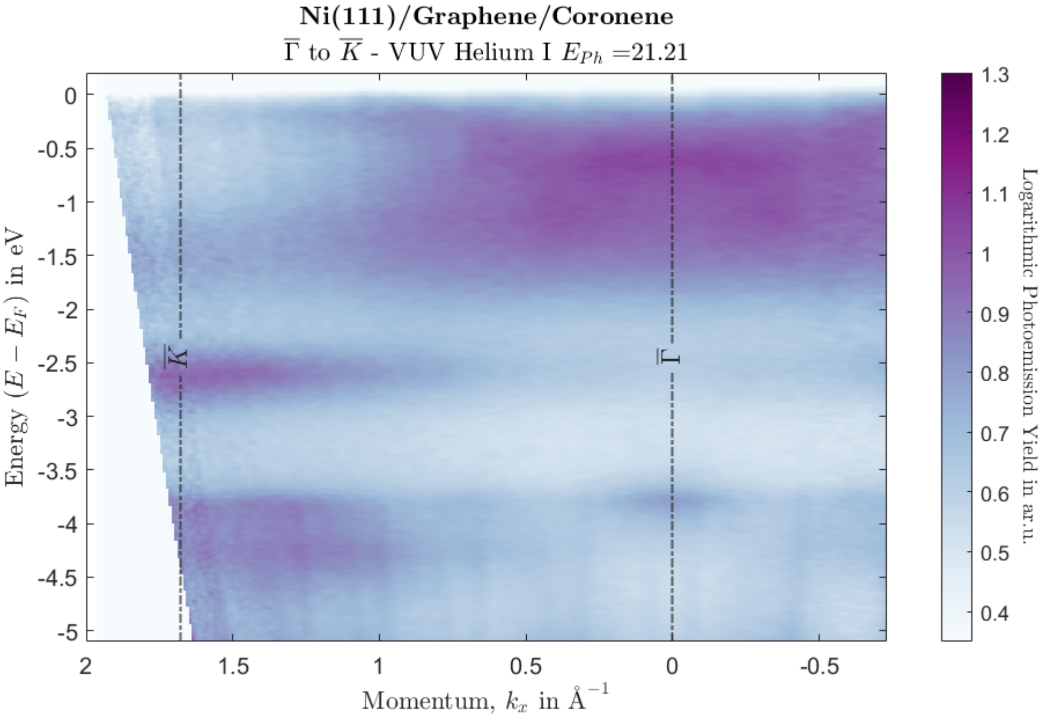

Figure (5.7) coronene/graphene/Ni(111) - Photoemission Yield. $\overline{\Gamma}$ to $\overline{K}$ direction. Measured with an VUV-lamp using a photon energy of $E_{ph} = 21.22$ eV.

5.2. Investigation of ultrafast charge carrier injection through molecular excited state photoemission orbital tomography

5.2.1. Static investigation of the coronene/Ni(111) and the coronene/graphene/Ni(111) sample system

The aim of this study is to elucidate optically excited charge transfer into the prototypical molecular system coronene. To this end, an initial extraction of the molecular orbital signature in momentum space was essential. The molecular features were identified based on the energetic positions in the ARPES spectra. Figure 5.8 shows a comparison between ARPES data from pristine Ni(111), coronene/Ni(111), and coronene/graphene/Ni(111) surfaces. In the first panel, the spectra extracted from the measurements are displayed, integrated over the full momentum range and normalised to the maximum intensity. Panels two to five present energy–distribution maps (energy momentum distribution map) extracted from the data. Only the k_x direction averaged over $k_y = -0.2\,\text{Å}^{-1}$ to $0.2\,\text{Å}^{-1}$ is shown. As a guide to the eye, the dominant molecular features are marked by black dashed lines at energies of $-1.10\,\text{eV}$, $-1.31\,\text{eV}$, $-2.56\,\text{eV}$, $-3.92\,\text{eV}$, $-4.28\,\text{eV}$ and $-5.61\,\text{eV}$.

In a subsequent step, constant energy maps (CEM) were extracted at the energy positions of these dominant molecular features. For this extraction, it was crucial to account for the fact that the coronene/Ni(111) and coronene/graphene/Ni(111) datasets were acquired on different Ni(111) crystals. Therefore, the extracted CEMs were rotated to align the high-symmetry axes of the nickel substrate. The respective rotation angles are detailed in Section 2.3.2.1 and illustrated in Figure 2.10. Moreover, the optimisation of the π-orbital overlap between the graphene sheet and the coronene layer induces an intrinsic rotation of 11 degree of the coronene layer relative to the graphene/Ni(111) substrate [29]. Figures 5.9 and 5.10 compare the extracted CEMs for Ni(111), coronene/Ni(111) (with both higher and lower coronene coverages), and the coronene/graphene/Ni(111) system. The data were extracted around the dominant molecular features using an energy window of 0.25 eV. The CEMs were then calculated by averaging over the selected energy range.

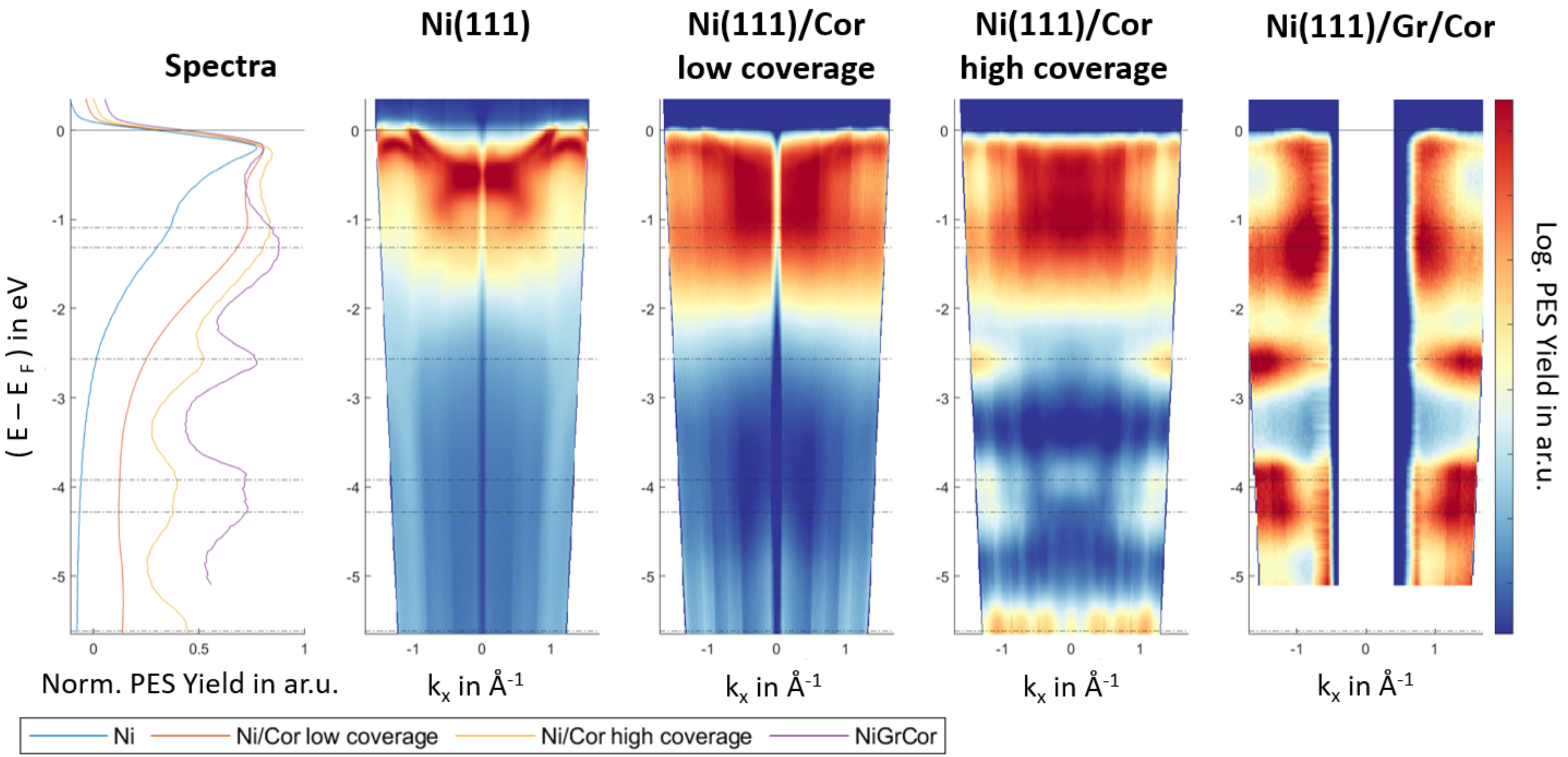

Figure (5.8) Comparison between **Azimuthal** ARPES data from Ni(111), the coronene/Ni(111) and the coronene/graphene/Ni(111) surface, ranging from the $\overline{K}$ to the $\overline{K}'$ point. From the left: The first panel shows the spectra extracted from the measurements. The data were integrated over all k and normalised to the maximal value. Panel two to five show energy momentum distribution map extracted from the given data. for the calculations the maps along the k_x and the k_y direction are given while for the measurements only the k_x direction, averaged from $k_y = -0.2\,\text{Å} \ - \ 0.2\,\text{Å}^{-1}$ is displayed. As a guide to the eye, the energy position of the dominant molecular features are marked by black dashed lines. The positions are at: $-1.10\,\text{eV}$, $-1.31\,\text{eV}$, $-2.56\,\text{eV}$, $-3.92\,\text{eV}$, $-4.28\,\text{eV}$ and $-5.61\,\text{eV}$.

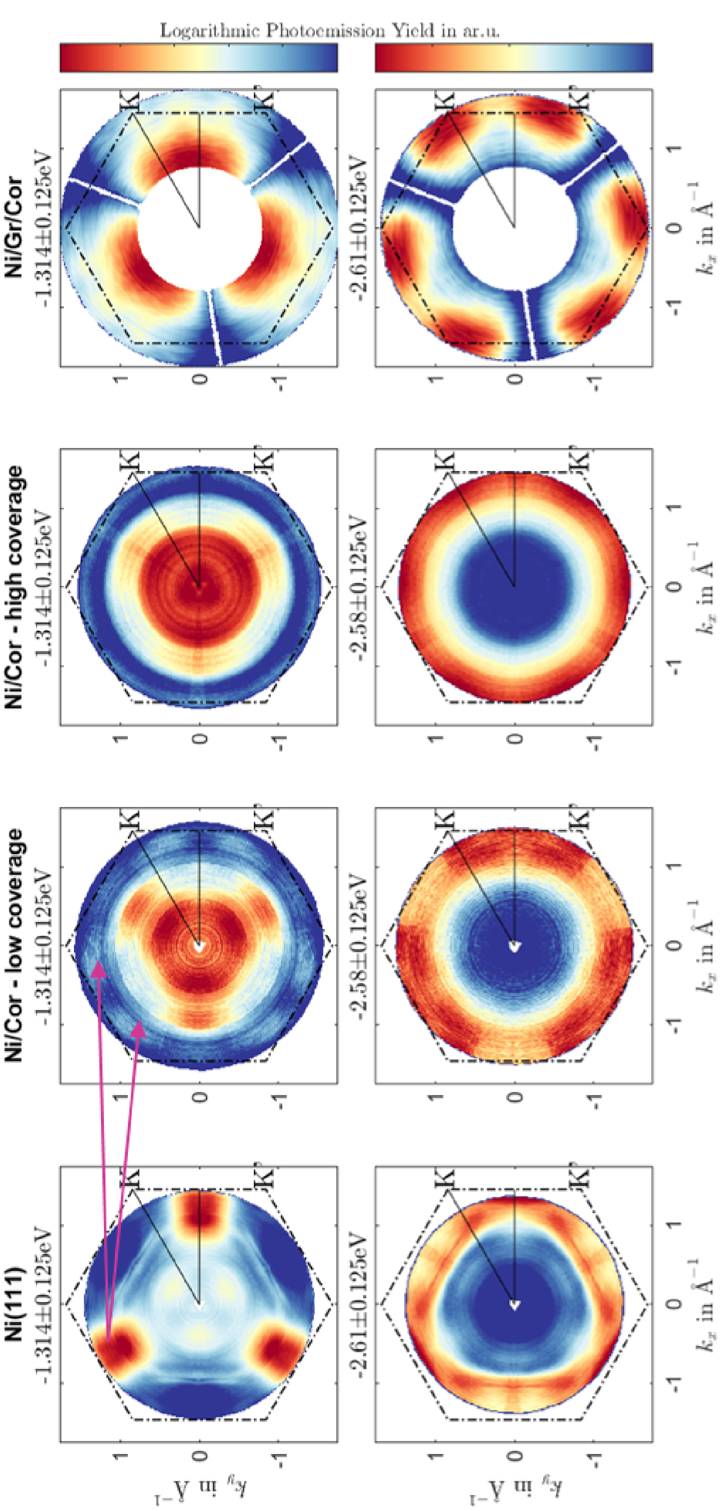

Figure (5.9) Photoemission yield of Ni(111), coronene/Ni(111) (with both higher and lower coronene coverages), and coronene/graphene/Ni(111) from VUV azimuth-sweep measurements. Pink arrows indicate a signature in the coronene/Ni(111) (low coverage) data originating from back-folding of Ni(111)-features at the coronene The maps are centered at the specified energy and averaged over an energy width of 0.25 eV. In black, the Ni(111) Brillouin zone and the $\overline{\Gamma} \to \overline{K}$ and $\overline{\Gamma} \to \overline{M}$ directions are marked.

The dominant molecular orbitals discernible at these energies are the LUMO (only for coronene/-Ni(111)), the HOMO, and the HOMO-1. A detailed analysis of these features can be found in the dissertation of Christina Schott [29]. Although the measurements presented here differ slightly from those in [29] due to variations in coronene coverage, they underscore the fundamental process of decoupling coronene from the Ni(111) surface. For this investigation, two coronene coverages were considered: low coverage (less than one monolayer) and high coverage (exceeding one monolayer).

At low coverage, strong hybridisation between the molecules and the substrate is anticipated. In the low-coverage coronene/Ni(111) system, the spectrum (see Figure 5.8) closely resembles that of pristine Ni(111), with only subtle molecular peaks visible in the spectrum. However, at the lowest

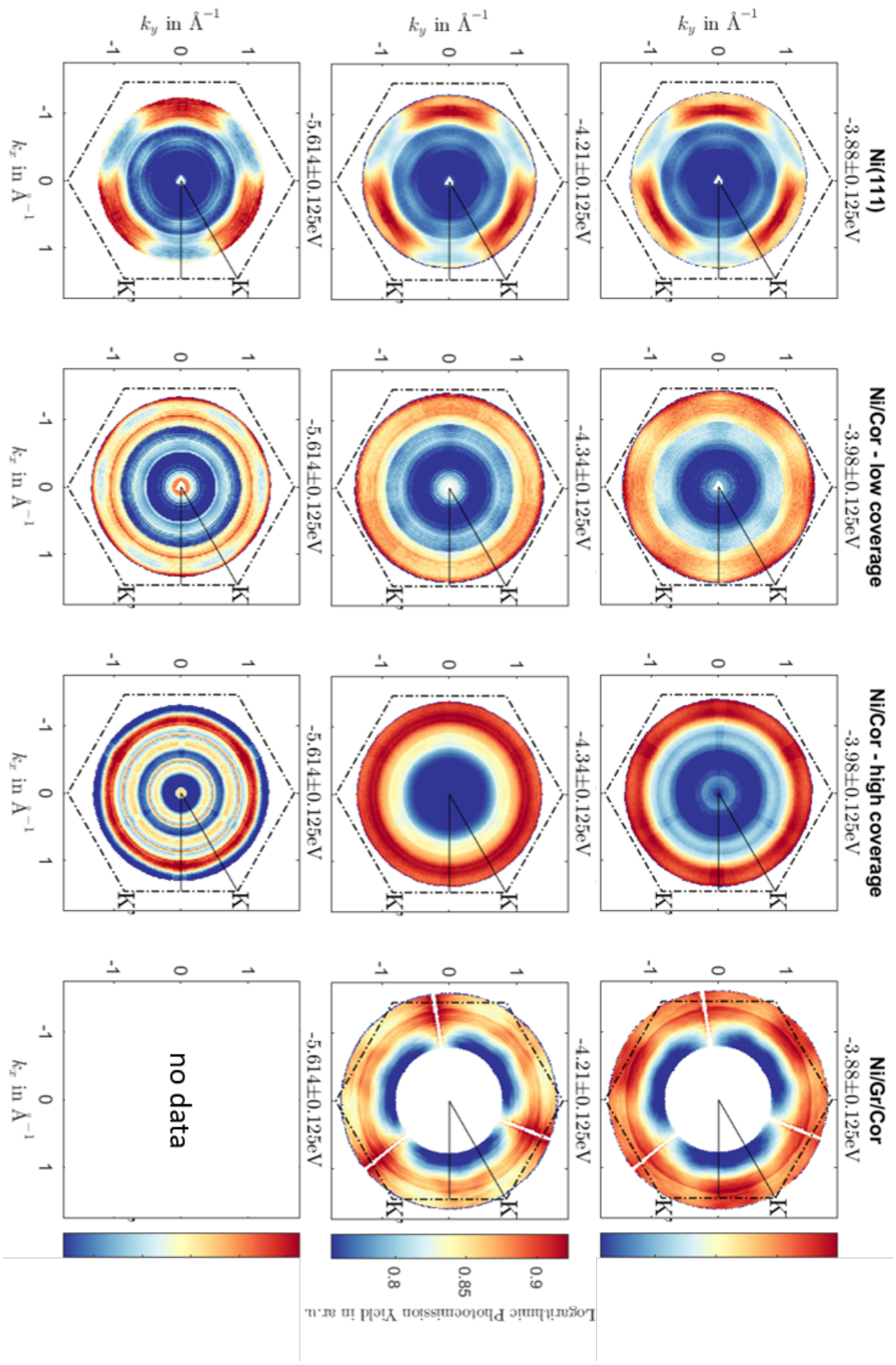

Figure (5.10) Photoemission yield of Ni(111), coronene/Ni(111) (with both higher and lower coronene coverages), and coronene/graphene/Ni(111) from VUV azimuth-sweep measurements. The maps are centered at the specified energy and averaged over an energy width of 0.25 eV. In black, the Ni(111) Brillouin zone and the $\overline{\Gamma} \rightarrow \overline{K}$ and $\overline{\Gamma} \rightarrow \overline{M}$ directions are marked.

unoccupied molecular orbital (LUMO), highest occupied molecular orbital (HOMO) and HOMO-1 positions for the coronene/Ni(111) system — located at approximately −2.58 eV, −3.98 eV, and −5.62 eV, respectively — the molecular orbitals are clearly discernible as six distinct features arranged on a circle approximately 60° apart. In the region of the nickel d-bands, one can observe a doubling (back folding, marked with pink arrows) of the Ni bands, attributable to back-reflections from the molecular Brillouin zone boundaries.

In contrast, for coverages exceeding 1 ML, a second coronene layer forms that is not hybridise with the Ni(111) substrate. Since the 1.layer-LUMO and 2.layer-HOMO energies in the strongly bound (1.layer) and decoupled (2.layer) systems are similar, the spectral contributions from both layers become mixed, leading to a blurring of the molecular features in the CEMs, illustrated in Figure 5.11. Here, the superiority of the coronene/graphene/Ni(111) system becomes evident. Not only does the coronene/graphene/Ni(111) spectrum closely resemble that of the high-coverage coronene/Ni(111) system (with signals originating from a decoupled 2. molecular layer), but the graphene buffer

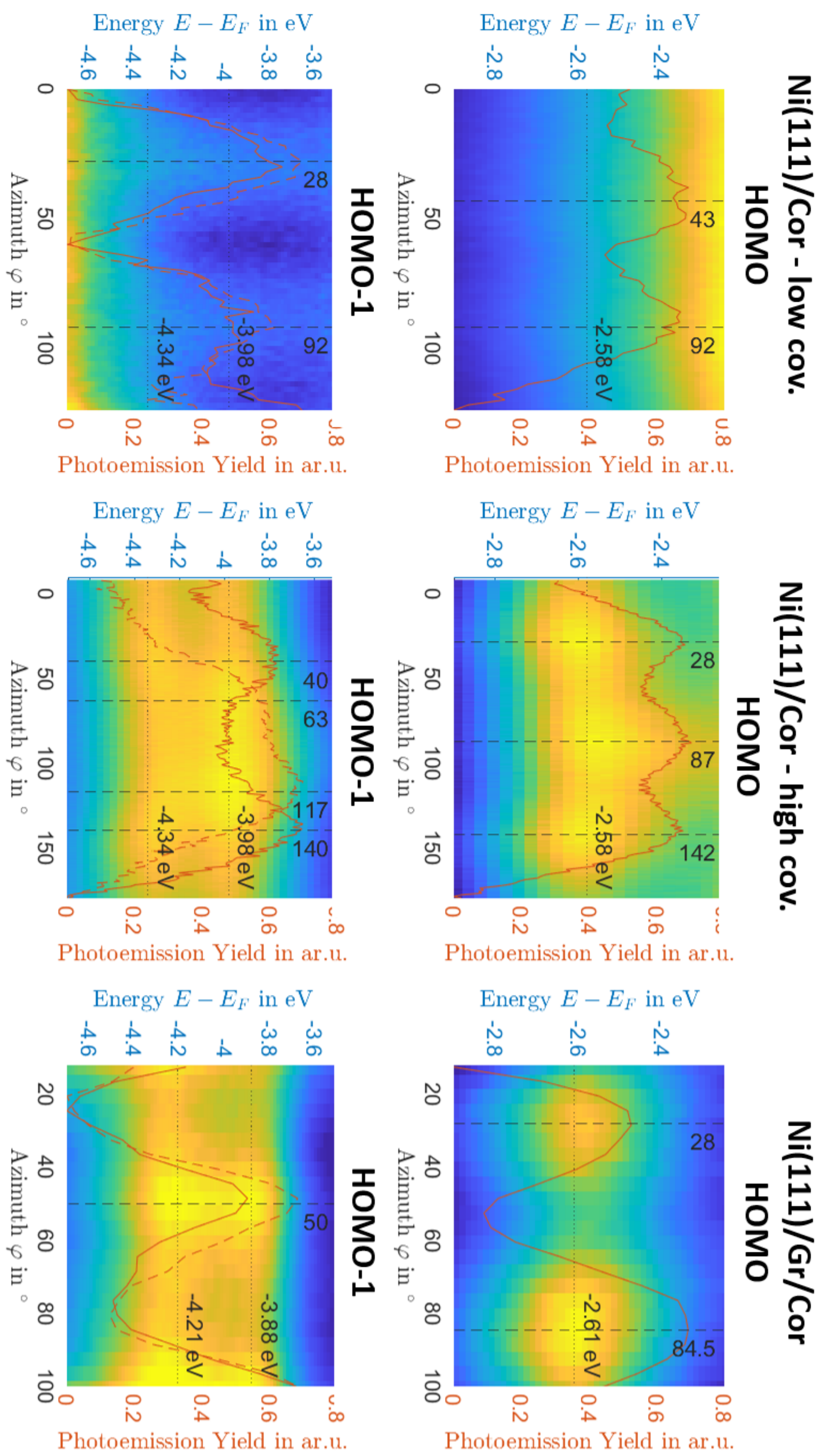

Figure (5.11) Photoemission yield of Ni(111), coronene/Ni(111) (with both higher and lower coronene coverages), and coronene/graphene/Ni(111) from VUV azimuth-sweep measurements. The maps depict the energy vs angle maps along the measured azimuthal angles and are overlayed by the extracted photoemission intensity extracted at the corresponding LUMO, HOMO and HOMO-1 positions. While the low coverage coronene/Ni(111) and the coronene/graphene/Ni(111) sample show two district peaks, for the high coverage coronene/Ni(111) a mixing of signals from the decoupled second layer and the strongly bound 1. layer are visible.

layer also facilitates decoupling without compromising the clarity of the molecular features. In the decoupled coronene/graphene/Ni(111) system, the HOMO is observed at $-2.61\,\mathrm{eV}$ and the HOMO-1 appears at $-3.88\,\mathrm{eV}$ and $-4.21\,\mathrm{eV}$, with the coronene layer rotated by 11 degree relative to the graphene/Ni(111) substrate. The corresponding LUMO is expected to exhibit a similar rotational signature, with sharp, rounded maxima at approximately $1.40\,\mathrm{eV}$ above E_F.
Additionally, while the low-coverage, strongly hybridise coronene/Ni(111) system exhibits a distinct inner circle composed of six spots (e.g., at $E - E_F = -3.92\,\mathrm{eV}$ as shown in Figure 5.10), this feature is absent in both the pristine Ni(111) and the coronene/graphene/Ni(111) systems. These observations strongly suggest that such features are a direct consequence of hybridisation between coronene and the nickel substrate. The absence of these hybridisation-induced features in the coronene/graphene/-Ni(111) system confirms the successful decoupling of coronene from the Ni(111) substrate via the graphene buffer layer. The well-resolved molecular features for the HOMO and HOMO-1 in the decoupled system, and the therefore expected similarly clear unoccupied molecular features (e.g. LUMO and LUMO+1) provide a robust foundation for detailed time-resolved investigations aimed at probing transient, light-induced charge carrier injection into the unoccupied molecular orbitals.

5.2.2. Excited State Imaging of Charge Carrier Transfer in a Stationary-Delay Configuration

To investigate the light-driven charge-carrier dynamics in organic–molecular systems via photoemission, it is helpful to employ photon energies in the EUV range. This requirement arises from the molecule-specific enhancement of the photoemission yield at higher momentum values, which renders these regions accessible only with probing light outside the optical spectrum. [115]. During this thesis, a momentum microscope combined with an EUV light source was not available. Therefore, the organic–metal heterostructure was investigated using an EUV-Tr-ARPES setup. In this configuration only a specific momentum direction can be measured at any given time. To maximise the signal over a wide range of azimuthal angles and to map an extended portion of the surface-projected Brillouin zone, the light-driven charge carrier injection was performed in a stationary-delay configuration ARPES acquisition. This involved illuminating the sample with both a red- and a blue-pump pulse while conducting an azimuthal sweep, with the sample probed by EUV light. All measurements were conducted at time-zero (t_0, corresponding to a pump-probe delay of $0\,\mathrm{fs}$), where the highest light-induced occupation in the excited states is expected.

The idea is to attribute spectral features observed in time-resolved ARPES (TR-ARPES) data to coronene's molecular orbitals (e.g. the HOMO and LUMO) of a quasi-free-standing monolayer of coronene on graphene/Ni(111). This explanation is based on the coronene being only weakly bound to the substrate. This was extensively shown in the dissertation of Christina Schott [29] and was analysed in detail in Section 5.1.2. Therefore, for coronene on graphene/Ni(111) one would expect the coronene-derived features in the unoccupied region to be present, though their exact energies may be shifted by interface interactions. The correct identification of molecular features vs. substrate features in the unoccupied region is crucial for the interpretation of the presented measurements.
Therefore, the molecular features in the occupied region were initially extracted from the pumped-HHG-measurements to determine their respective orientations and positioning. While this can also be done in the static measurements above, this process is repeated for the occupied molecular orbitals using the pumped measurement to exclude influences of e.g. the changed excitation scheme (excited states might cause band renormalisation shifting the band positions in the occupied region) or sample degeneration (extraction happens at the exact same measurement instead of two different acquisitions) on the exact energetic positioning. The CEM for the HOMO and the HOMO+1 are presented in Figure 5.12. The measurements clearly reproduce the expected molecular features and the theoretical positions of the orbitals. Slight differences between the blue-pumped and red-pumped maps are observed, which can be attributed to variations in band-renormalisation processes following optical excitation [63]. From Figure A.2, the energetic distances from the HOMO to the unoccupied molecular orbitals can be deduced. According to the numbering from the theoretical calculations, the energy difference from the HOMO to the LUMO and LUMO+1 is approximately $4.0\,\mathrm{eV}$ (experimentally labelled as the LUMO), and from the HOMO to the LUMO+2 and LUMO+3 is approximately $5.1\,\mathrm{eV}$ (experimentally labelled as the LUMO+1). Given that the HOMO is positioned at $-2.62\,\mathrm{eV}$ below E_F, the LUMO is expected near $1.45\,\mathrm{eV}$ and the LUMO+1 around $2.60\,\mathrm{eV}$. Both regions exhibit a broad energetic width of approximately $0.5\,\mathrm{eV}$, with small energetic deviations and additional

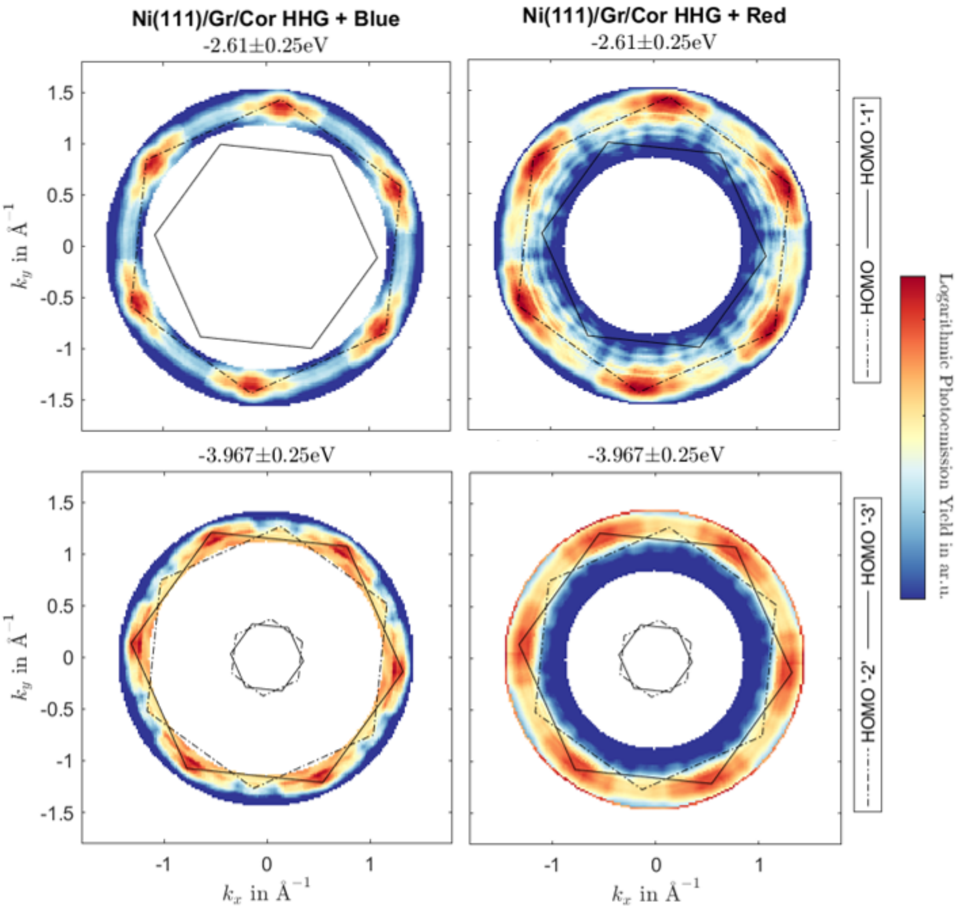

Figure (5.12) Constant energy maps (CEM) of stationary-delay configuration ARPES acquisition at t_0 of the coronene/graphene/Ni(111) surface using a red-laser pulse (right) and a blue-laser pulse (left) as the pump, with the HHG pulse as the probe. The maps are centered at the specified energetic positions (corresponding emission maxima) and averaged over an energy window of $0.25\,\text{eV}$. Top panels show the HOMO-emission map while the bottom panels display the HOMO-1-emission map. Hexagons overlay the maps to indicate the theoretical positions of the HOMO orbitals emission maximum of gas-phase coronene, as depicted in Figure A.2. According to theoretical calculations, the experimental HOMO comprises contributions from "HOMO" and "HOMO-1", while the experimental HOMO-1 corresponds to "HOMO-2" and "HOMO-3".

broadening anticipated due to substrate-induced effects.

Subsequently, CEMs were extracted at the energetic positions corresponding to the LUMO and LUMO+1. Using these images, the area in which an excitation into molecular features is visible was determined, and the corresponding spectra were extracted using an extraction mask. The resulting spectra are shown in Figure 5.13. Explanatory CEMs of the blue-pumped data (labelled as **blue data**) and the extraction mask corresponding to the **"Blue Feature"** spectrum in Figure 5.13 (labelled as are **blue signal**) are shown on the right of Figure 5.13. While the extraction mask was used to determine the shown spectra - from an area with molecular feature (labelled **Red Feature** and **Blue Feature**) and an area without visible molecular features in the CEMs (labelled **Red No Feature** and **Blue No Feature**) - the residual data were used as a background-spectrum and subtracted from the extraction-mask-spectrum. The extraction method is described in more detail in Section 2.3.3.1. The extraction mask had a radius of $0.39\,\text{Å}^{-1}$ and was centred at ($k_x = 1.37\,\text{Å}^{-1}$, $k_y = 0.39\,\text{Å}^{-1}$) and ($k_x = 1.41\,\text{Å}^{-1}$, $k_y = -0.39\,\text{Å}^{-1}$) respectively. Additionally, Figure A.10 (shown in the appendix) presents the spectra extracted from a smaller region using an extraction radius of $0.18\,\text{Å}^{-1}$. Within the graph areas either corresponding to the substrate or the molecule are marked. The reasoning behind this attributions to the different origins and molecular orbitals is explained in the following.

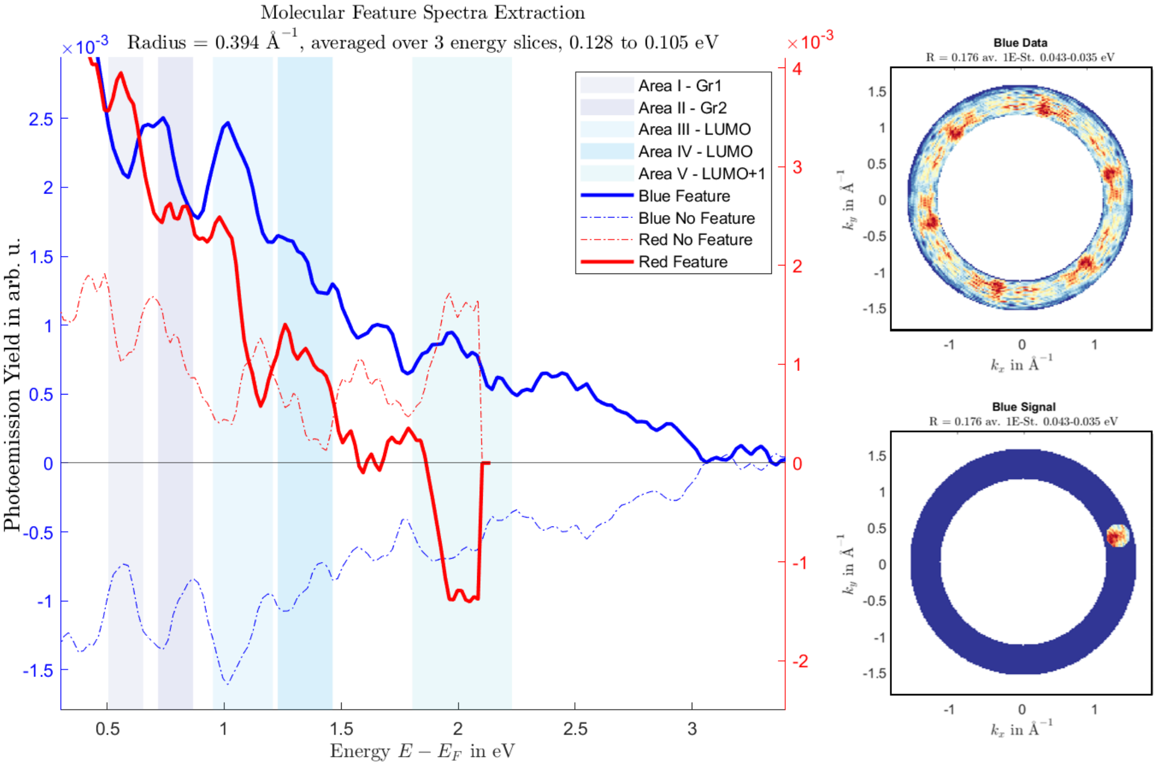

Figure (5.13) Extracted spectra from stationary-delay configuration ARPES measurements at t_0. The spectra were extracted from CEMs using an extraction mask (on the right) from areas exhibiting prominent molecular signatures (**feature**), additionally results from regions with no expected molecular signal (no-feature), are shown for both blue- and red-pumped measurements. The extraction mask had a radius of $0.39\,\text{Å}^{-1}$ and was centered at ($k_x = 1.37\,\text{Å}^{-1}$, $k_y = 0.39\,\text{Å}^{-1}$) and ($k_x = 1.41\,\text{Å}^{-1}$, $k_y = -0.39\,\text{Å}^{-1}$), respectively. The corresponding residual spectra (spectra generated from data outside the extraction mask and its rotations according to the sample symmetry) were used as a background and subtracted from the "feature" and "no feature" spectra. Areas corresponding to either the graphene/Ni substrate, or the coronene are marked within the graph.

Naively, one might expect to observe two distinct photoemission signals corresponding to the LUMO and LUMO+1. However, as evidenced in Figure 5.13, multiple peaks are observed, with clear differences between the red- and blue-pumped measurements. To further resolve the spectral features, spectra were extracted from both regions where molecular signals are expected and from regions where no molecular signal is anticipated. By comparing the results with calculations and the respective energetic positions, the attribution to either the substrate or the molecule is possible.
For example, graphene/Ni(111) alone has a strongly shifted graphene Dirac cone ($\sim 2.8\,\text{eV}$ below E_F) compared to free standing graphene due to hybridisation with nickel [116], so any dispersive bands far below E_F likely arise from graphene-Ni hybrid states rather than the coronene monolayer or the pristine nickel(111). Analogously, in the coronene/Ni(111) system the LUMO is shifted far below E_F. The question is: is the LUMO in the coronene/graphene/Ni(111) system above E_F and can therefore be a target for charge transfer or e.g. at the same energetic position as the Ni(111) d-bands and thereby not clearly visible in the ARPES signals. In the neutral molecule, coronene's HOMO is localised a few eV below E_F and the LUMO is normally above E_F (unoccupied). Photoemission studies on comparable, not strongly hybridise polycyclic aromatic hydrocarbon molecules-based sample systems like C_{60}-molecule on Cu(111) can provide a reference: For C_{60}-molecule on Cu(111) the HOMO appears at $E - E_F = 2.2\,\text{eV}$ and the LUMO-derived affinity level at $E - E_F = 1.8\,\text{eV}$ [33]. I expect coronene (a smaller PAH) to have a larger gap, but still the Fermi level of the substrate will likely lie between its HOMO and LUMO. Thus, any occupied-state peak near E_F in the spectra would not be coronene's LUMO (since LUMO is initially empty), it could be the coronene HOMO or a graphene/Ni state.
Additionally, signals originating from real unoccupied intermediate states within the selected extraction radius should appear as distinct peaks in the "feature" spectra and likely as dips in the

"no-feature" spectra.
In typical multi-photon photoemission experiments, electrons are excited by the pump pulse from occupied states into a real (or virtual) intermediate state and are subsequently photoemitted by the probe pulse [63]. Due to the homogeneously broadened energetic distribution and the delocalisation in momentum-space of the coronene molecular orbitals, the orbitals in the unoccupied region provide a wide range of possible **intermediate** states. In contrast, the **initial** (occupied) states in the Ni(111)/graphene substrate are more confined to specific momentum and energy areas, as illustrated in Figure 5.14. Here the calculated spin-resolved band structure of graphene/Ni(111) is presented. The images was adapted from [117], to only show the area interesting in this experiment and augmented by violet features roughly representing the coronene molecular orbitals.

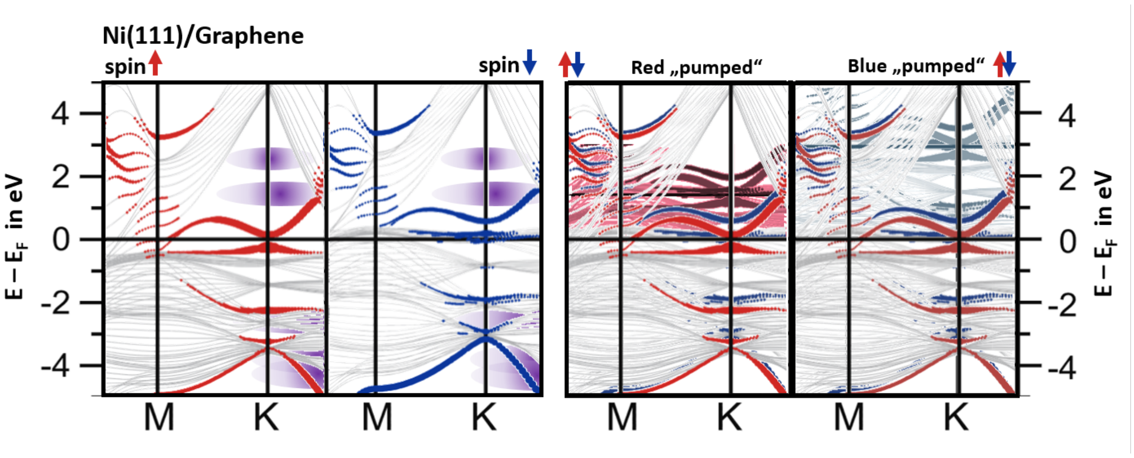

Figure (5.14) Adapted spin-resolved electronic band structure calculation of graphene/Ni(111), augmented with representations of the coronene molecular orbitals (left) and an illustration of the projection of initial states into the unoccupied region after light-induced electron excitation (right), corresponding to red and blue pumping. Adapted from [117].

For a clearer understanding of the spectral peak positions in Figure 5.13, Figure 5.14 additionally illustrates the projection of initial states into the unoccupied region after light-induced excitation (a shift of the features by the used photon energy).

In this figure, the possible intermediate points for electrons from the graphene/Ni(111) band structure are shown for red pumping (left) and blue pumping (right). When considering this graph, it is important to note that it shows the band structure of the graphene/Ni(111) substrate. Since the coronene is rotated by 11° towards the substrate structure (see Section 5.1.1.2) the molecular features spectral weight centre is not aligned with the nickel K-direction but moves towards the M-Point. The projections, adapted from [117], align well with the peaks observed in the extracted spectra, thereby underlining the influence of the initial state on the final photoemission signal for measurements taken at t_0. In the given spectra we can clearly identify two peaks aligning with the unoccupied graphene states at roughly 0.55 eV and 0.75 eV (area I and area II) and identify a peak in the red-feature-spectrum ranging from roughly 1.23 eV - 1.45 eV as the coronene LUMO (area IV). It is neighboured by an additional peak, best visible in the blue spectrum, ranging from 0.95 eV - 1.21 eV (area III) that is attributed to an excited coronene state corresponding with the LUMO. The LUMO+1 is assumed to be in the area of 1.80 eV - 2.23 eV (blue spectrum, area V). Again, an additional peak is visible, potentially corresponding to the LUMO+1 but this can not be confirmed by the presented measurements.

These additional excited states might correspond to excitonic excitation or other phenomena. Since in metals the electrons response to shield perturbations in the electric field (screening effect) - e.g. holes after optical excitation - takes place almost instantaneously ($t \sim 1$ fs) the formation of excitons after off-resonant optical excitation is very unlikely. Although the screening effect is expected to shield an exciton hole from its corresponding electron within a few fs, causing their rapid de-phasing, conducting the measurement at t_0 allows the probing of the excited states, before fast scattering effects reduce their population.

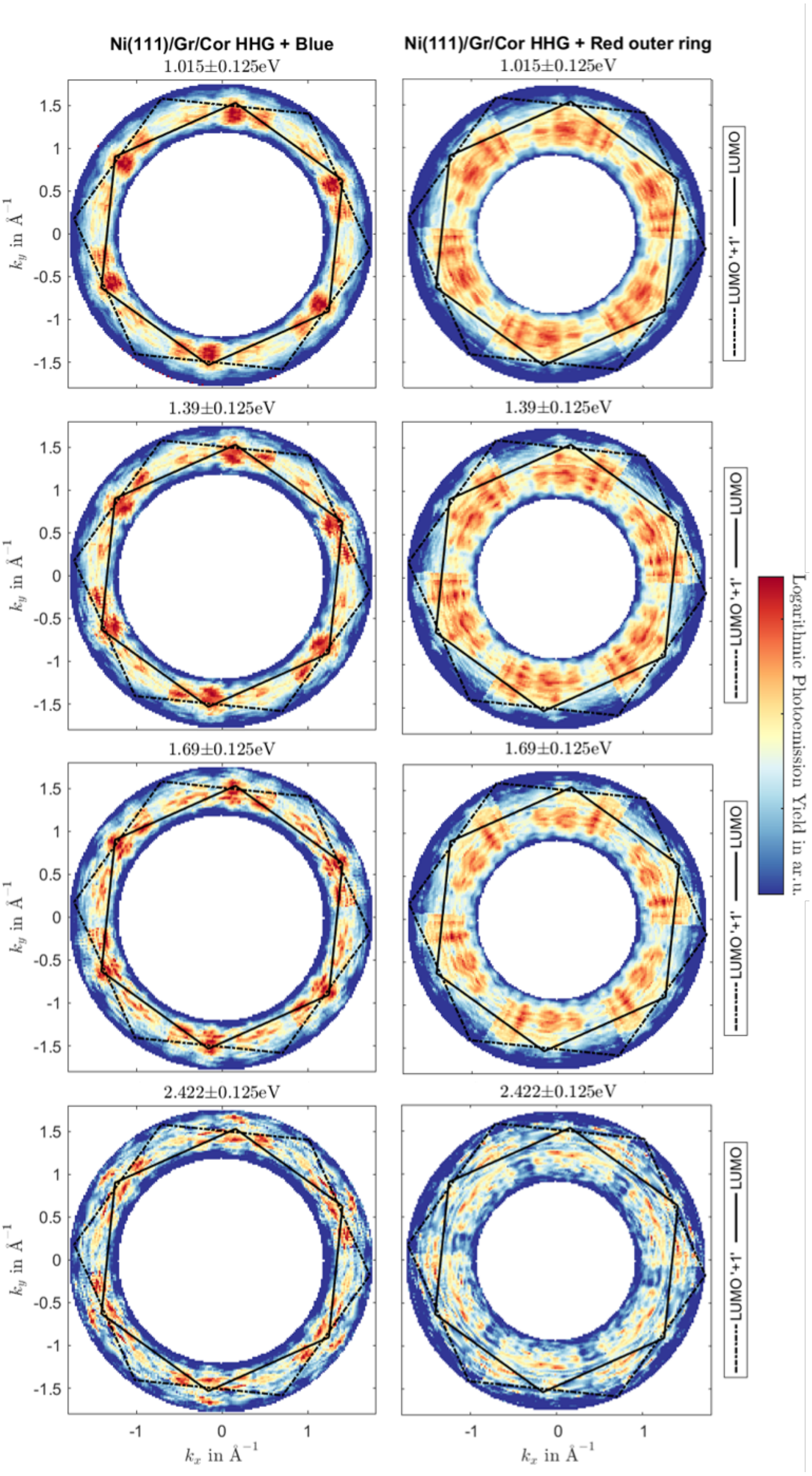

Figure (5.15) CEM of semi-static ARPES measurements at t_0 using a red-laser pulse (right) and a blue-laser pulse (left) as the pump and the HHG pulse as the probe. The maps are centered at the specified energetic positions and averaged over an energy window of $0.125\,\mathrm{eV}$. The top two rows display the LUMO and the bottom two rows show the LUMO-1. Hexagons overlay the maps to indicate the theoretical positions of the LUMO and LUMO+2 (solid line) and the LUMO+1 (dashed line) for gas-phase coronene, as depicted in Figure A.2. According to theoretical calculations, the experimental LUMO consists of contributions from "LUMO" and "LUMO+1", while the experimental LUMO+1 corresponds to "LUMO+2" and "LUMO+3".

Taking C_{60}-molecule as a reference, it is known that the momentum signature of (in this case) excitons resembles the signature of the molecular orbital in correspondence to this exciton. The energy of the exciton states is expected to be lower - 0.3 eV to 0.5 eV for C_{60}-molecule [118] - than the original unoccupied molecular orbital position. Effects like exciton formation would lead to additional peaks in the given coronene/graphene/Ni(111) spectrum, occurring a few hundred electron volts below the associated unoccupied molecular orbital. The occurrence of excitonic states would additionally explain the visible molecular signature in the CEMs over a wide range of energies. But, for the given sample and the used pump-laser photo-energies excitons **can not** result from an excitation between HOMO and LUMO or LUMO+1, because the energetic distance of 4 eV far exceeds the photon energy. Therefore, excitons can only form between the nickel or more likely the graphene sheet and the molecular layer. As dicussed before, due to the strong hybridisation between nickel and graphene, and therefore the very strong screening effects, it is unlikely, that “true” excitonic states form. While excitons will allow an interpretation of the extracted spectral peaks as well as the features in the momentum maps, their existence within the coronene/graphene/Ni(111) sample system remains highly speculative and very unlikely at this point. Here, I can only state that additional excited states of unclear nature, likely corresponding to the LUMO, form upon light driven electron excitation.

Unfortunately, due to the strong imprint of the substrate's band structure, the unclear effects of possible excited states as well as the low signal-to-noise ratio, it is not possible to directly extract the energetic positions of the LUMO and LUMO+1 for this quasi-free-standing coronene layer beyond doubts. Nevertheless, Figure 5.15 shows the CEMs extracted in the excited state regions. The chosen energies correspond to the calculated positions of the LUMO and LUMO+1, as well as to peaks observed in the extracted spectra.
One might argue that, since these measurements were conducted at t_0, the observed substrate band structure imprint is merely a signature of simultaneous two-photon photoemission, where an electron is initially pumped into a virtual intermediate state and then photoexcited by the XUV probe. However, two key arguments counter this interpretation. Firstly, the two-step process, in which an electron is excited into a real intermediate state and subsequently photoemitted, is more probable than simultaneous absorption of pump and probe photons, because the intermediate state allows a finite residence time before the probe pulse is absorbed [63]. Secondly, the momentum maps in Figure 5.15, particularly for the blue-pumped measurement, reveal distinct, rounded features that align well with the expected positions of the molecular orbitals, rather than merely reflecting the occupied substrate band structure. Furthermore, if direct transitions where solely responsible, one would expect regions were no corresponding occupied state can be found and therefore, no specific features but only background signal would be visible. Instead, the molecular orbital imprints persist across a broad energetic range of the momentum maps. Although the spectral features vary in intensity and shape, this variation indicates that the signal originates from real intermediate states. Given the wide energetic and momentum distribution of the LUMO and LUMO+1, an electron excited into these orbitals can undergo partial thermalisation within the intermediate state. With a pump pulse width of 55 fs at t_0, complete thermalisation is unlikely, yet some redistribution might occur, while the majority of electrons retain the imprint of the initial state.
Therefore, I conclude that it is indeed possible to generate a significant charge carrier population, originating from the substrate, within the molecular orbitals. This finding is especially intriguing in light of the spin-splitting inherent in nickel, since the electrons transferred into the molecular orbitals originate from the substrate, it may be feasible to inject a spin-polarised electron current into the molecular system. Moreover, the effective decoupling of coronene from the substrate via the graphene buffer layer may lead to extended lifetimes and enhanced stability of the injected current. Although these aspects lie beyond the scope of the current thesis, they offer promising avenues for future research into the application of coronene in spintronic devices.

5.3. Interface carrier dynamics after light induced charge carrier injection into coronene

When evaluating materials for electronic applications, understanding the temporal evolution of charge carriers is crucial. In the preceding section, I demonstrated electron injection from the substrate into the coronene layer. In Section 3.5, a similar system (graphene/Pb/Ni(111)) was investigated, where instead of a decoupled coronene layer, a quasi-free-standing graphene layer was optically excited, revealing indications of optical band gap renormalisation. Electron injection into the coronene layer may induce analogous effects on the band structure of the coronene/graphene/-Ni(111) system.

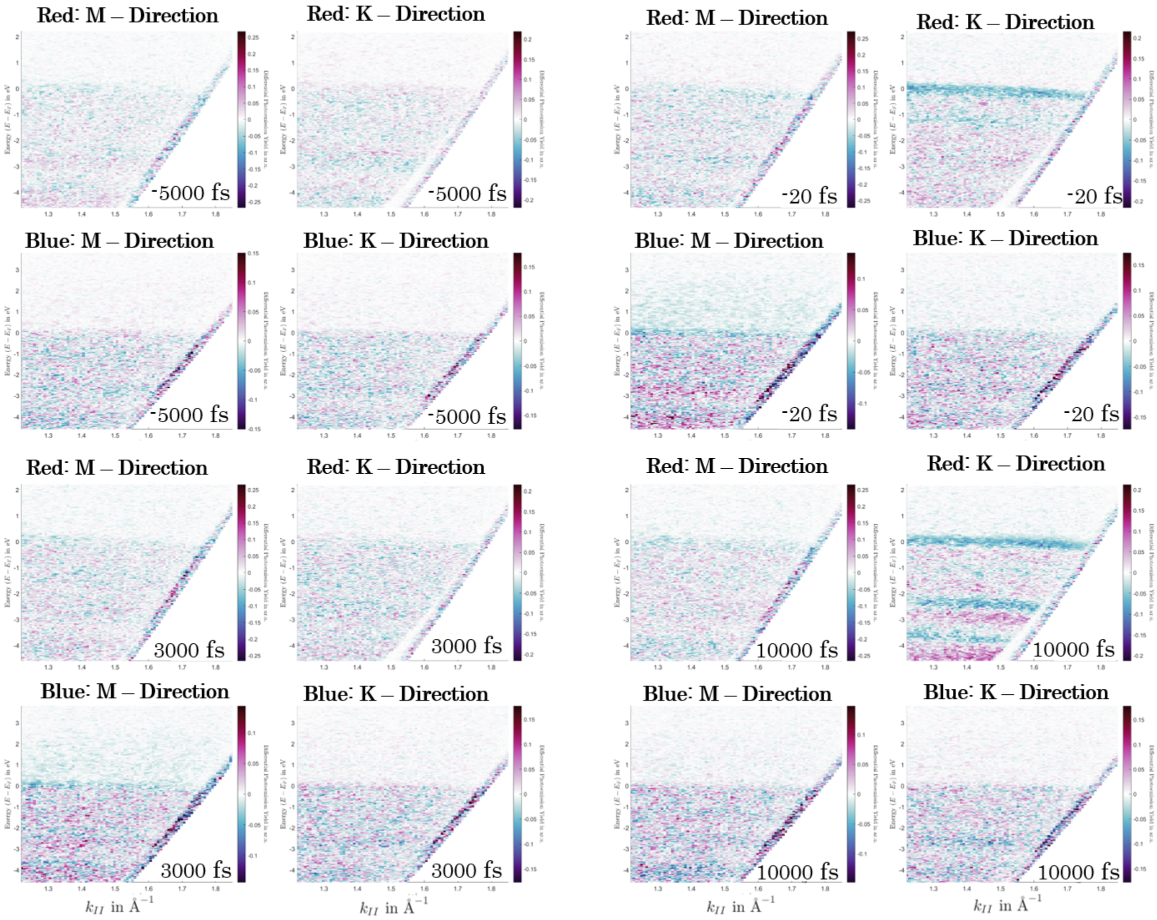

Figure (5.16) Differential Tr-ARPES data for the coronene/graphene/Ni(111) system. The differential map illustrates regions of increased (red) and decreased (blue) photoemission yield, with unchanged intensity indicated in white. Differences are calculated for the shown time step relative to measurements acquired significantly before t_0.

To examine transient modifications in the band structure of the coronene/graphene/Ni(111) system, the angle-resolved photoemission spectroscopy setup (see Section 2.2.1) was integrated with the time-resolved laser system (see Section 2.2.2). As described previously, the sample was excited using a p-polarised laser pulse generated by the KM-Wyvern Ti:sapphire laser amplifier system. The pump pulse has a temporal duration of 55 fs and photon energies corresponding to its fundamental at $E_{ph,red} = 1.58\,\text{eV}$ and second harmonic at $E_{ph,blue} = 3.17\,\text{eV}$. Measurements were conducted on the identical sample utilised in the stationary-delay configuration investigations described earlier. By aligning the sample relative to the electron analysers sensitivity direction, photo-excited electrons originating from the coronene Brillouin zone high-symmetry axes were captured, allowing direct observation of carrier dynamics at the molecular orbital spectral weight centres. Measurements were taken along directions corresponding to the HOMO and the HOMO-1, which are separated by an azimuthal rotation of 30°. To emphasise dynamic variations in the electronic band structure's photoemission yield, difference maps (differential map) were generated, as depicted in Figure 5.16. The differential map indicates an increased photoemission yield in red and a decreased yield in blue, with unchanged intensity displayed in white, relative to a reference acquired significantly before time zero. The differential map does not exhibit clear excitation features in the unoccupied region. For comparison, one may refer to the pronounced excitation observed in the graphene/Pb/Ni(111) system (see Figure 3.13). However, shifts in the band positions are detected. Differential Tr-ARPES data for the coronene/graphene/Ni(111) system, plotted as time delays versus energy $E - E_F$, are

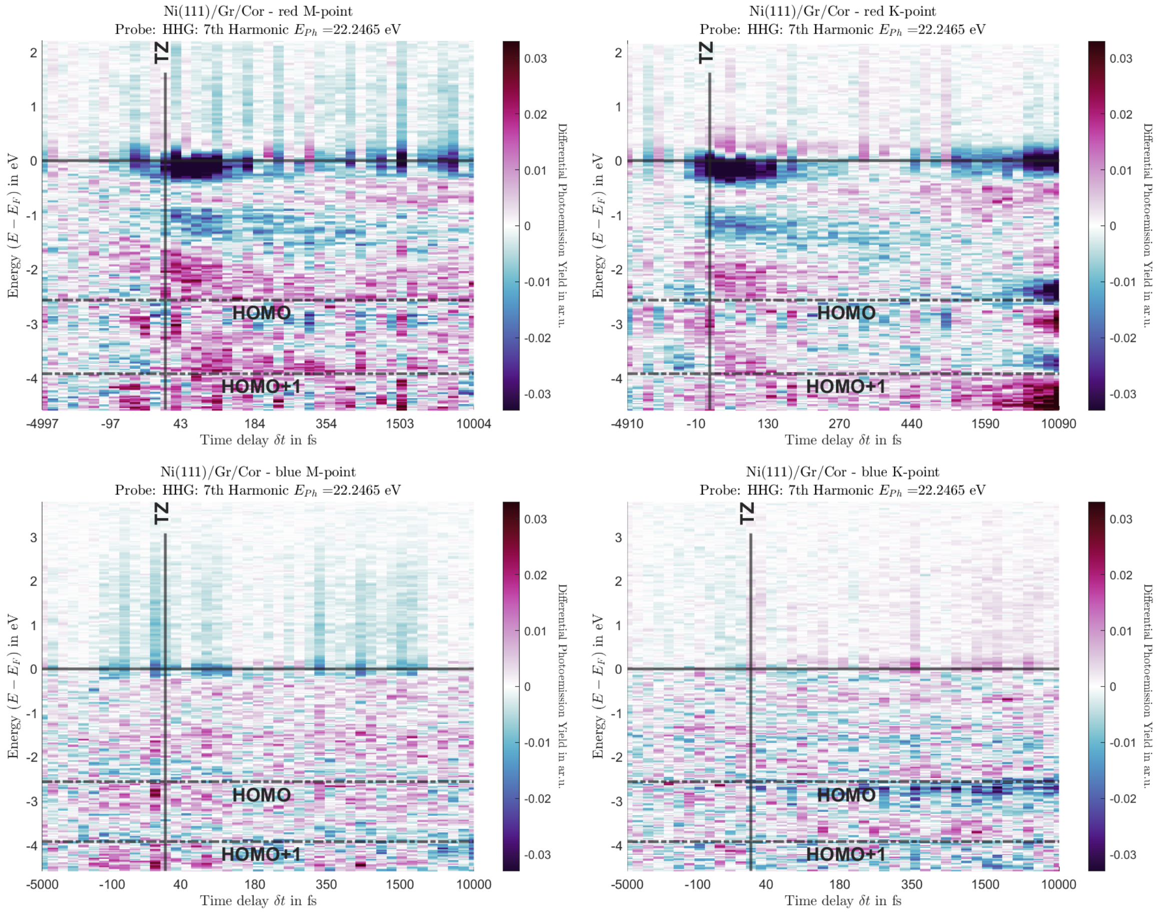

Figure (5.17) Differential Tr-ARPES data for the coronene/graphene/Ni(111) system, displaying time delays versus energy $E - E_F$. The momentum integration range is $k_{\parallel} = 1.3\,\text{Å} \; - \; 1.7\,\text{Å}^{-1}$. The differential map shows increased photoemission yield (red) and decreased yield (blue) compared to long before t_0, with unchanged intensity in white. The time delays are acquired in non-equidistant steps: finer intervals (20 fs) near t_0 (black line) and coarser intervals (2500 fs) at greater delays. Black lines indicate molecular peak positions (before time zero (BTZ)) and the Fermi energy, while a vertical line denotes t_0.

presented in Figure 5.17. While a simple excitation from an initial state below the Fermi level into unoccupied states would typically manifest as distinct red features at intermediate energies and, for semiconductors, corresponding blue features at initial state energies, the data here exhibit broad structures across extensive momentum (Figure 5.16) and temporal (Figure 5.17) ranges. These broad features suggest a global shift of the electronic band structure in momentum space rather than localised, discrete excitations. This effect is particularly pronounced in datasets obtained with red-pump excitation. Although stationary-delay configuration measurements with blue excitation revealed clear excitations into molecular orbitals, comparable features are not evident in the time-resolved data. This discrepancy likely arises from the significantly lower fluence of the blue pump (average $W_{blue} = 14\,\text{mW}$, $F_{blue} \approx 0.03\frac{\text{mJ}}{\text{cm}^2}$) compared to the red pump (average $W_{red} = 250\,\text{mW}$, $F_{red} \approx 0.56\frac{\text{mJ}}{\text{cm}^2}$). Instrumental constraints prevented the achievement of higher blue-pump fluences in the current experimental configuration [1]. Consequently, the subsequent analysis predominantly addresses results from the red-pump measurements, though selected blue-pump results will be included for comparative purposes.

The overall shifts in band structure extend over a wide energy range. Considering the relatively low photon energy of the red laser pulse ($E_{ph,red} = 1.58\,\text{eV}$), the observed shifts likely result from band renormalisation effects induced indirectly by excited charge carriers rather than direct interactions with the electromagnetic field. The initial band shift is transient, dissipating after approximately 400 fs. Notably, a secondary band shift emerges at longer delays exceeding 1.0 ps, presenting a most

---

[1] In this experimental setup, most of the available laser power is consumed for HHG generation (see Figure 2.6). Only a fraction, converted via SHG, is available for sample excitation, this conversion significantly reducing fluence compared to excitation at the fundamental wavelength.

intriguing phenomenon.

Although differential maps offer a clear visualisation of global effects, quantitative analysis necessitates time-dependent spectral fitting to precisely determine changes in the photoemission spectra. A time-resolved fitting routine was implemented to extract parameters related to the Fermi distribution and band positions. Detailed descriptions of the fitting procedure are provided in Section 2.3.4.2. Prior to fitting, pre-analysis data processing (outlined in Section 2.3.1) was executed. Each dataset underwent momentum integration and was fitted using a function composed of four Voigt profiles:

$$Voigt_1(E) = \left[m_1 \cdot \frac{\sigma_1}{2\pi(E-E_1)^2 + \left(\frac{\sigma_1}{2}\right)^2} + (1-m_1) \cdot \left(\frac{1}{\sigma_1\sqrt{2\pi}}\right) \cdot \exp\left[-\frac{1}{2}\left(\frac{E-E_1}{\sigma_1}\right)^2\right] \cdot A_1 \right] \tag{5.1}$$

The final fitting function is a sum of four such Voigt functions multiplied by a Fermi distribution and modulated by a linear background:

$$F(E) = (\mathrm{Voigt}_1(E) + \cdots + \mathrm{Voigt}_4(E) + A_{Fermi}) \cdot \mathrm{Fermi}(E) + E_{off} + mE. \tag{5.2}$$

This function incorporates weighting factors m_n, determining the relative contributions of Lorentzian and Gaussian components, peak widths σ_n, peak centre positions E_n, and amplitudes A_n. Representative fitting results at t_0 for the time-resolved coronene/graphene/Ni(111) data are presented in Figure 5.18. The fitting outcomes closely align with experimental data. However, due to the limited photon flux from the employed HHG source, the signal-to-noise ratio within the unoccupied states remains insufficient, precluding reliable peak fitting of the LUMO feature. Therefore, while the subsequent analysis offers meaningful insights into electron dynamics, future measurements utilise higher - flux HHG sources — potentially in conjunction with a momentum microscope—could facilitate excited-state orbital tomography.

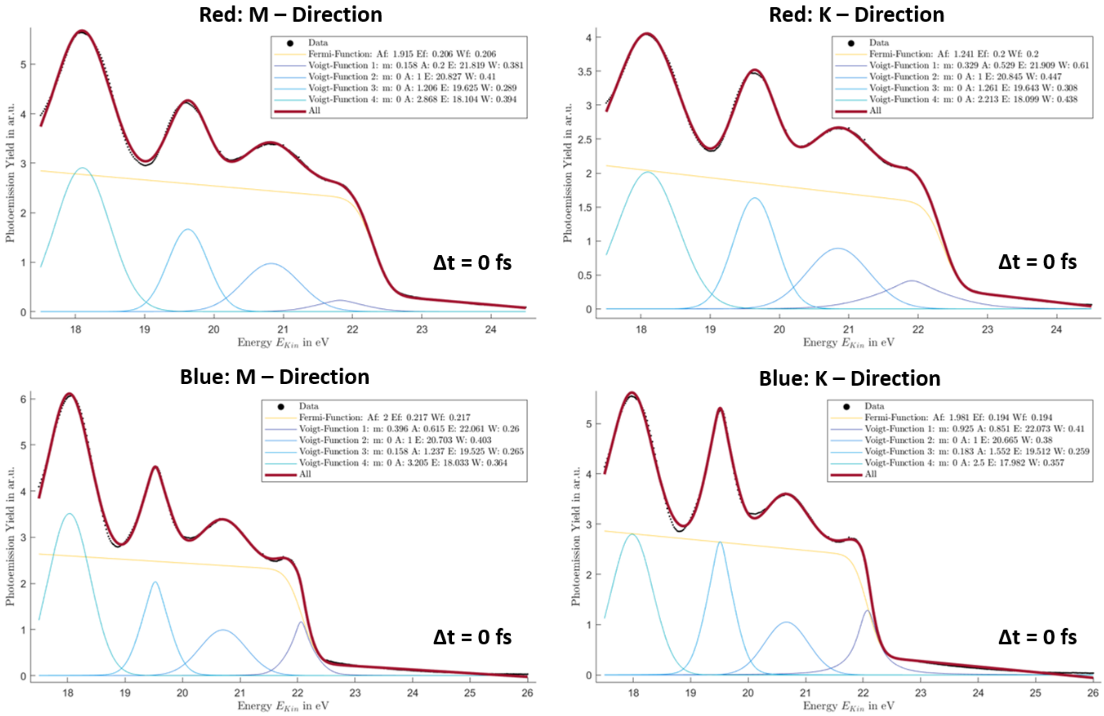

Figure (5.18) Exemplary fitting results for time-resolved coronene/graphene/Ni(111) data at t_0. The top panel corresponds to red-pumped data, while the bottom panel represents blue-pumped measurements. The overall fitting function (Equation 5.2) is depicted in red, the Fermi function with linear background in yellow, and individual Voigt peaks (Equation 5.1) are shown as blue shaded curves.

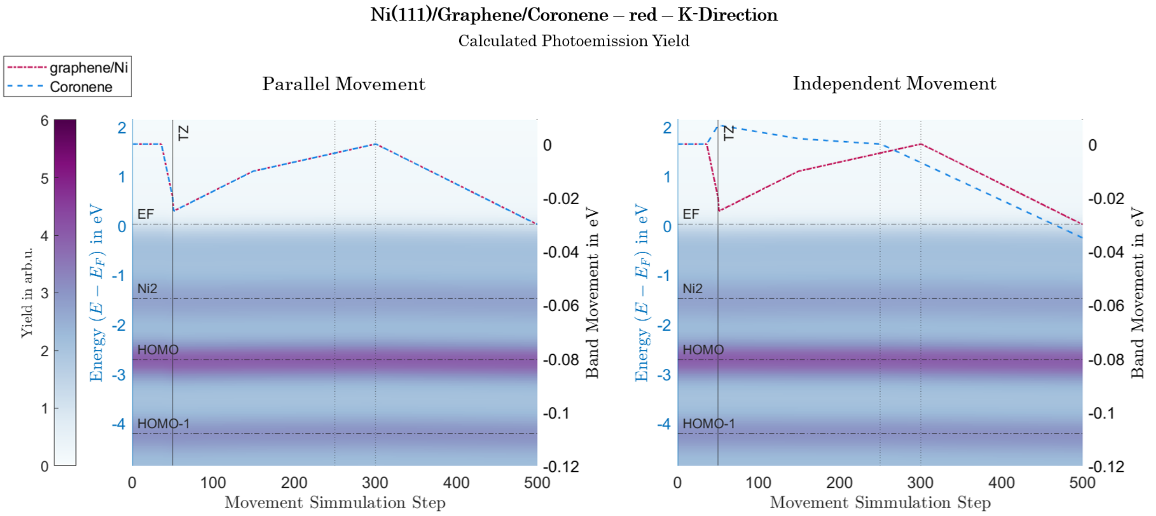

Figure (5.19) Simulated photoemission yield for artificial band shifts in the coronene/graphene/Ni(111) system. Depicted are simultaneous substrate-molecule shifts (left) and independent shifts (right). 500 shift increments were considered, with molecular shifts marked in blue and substrate shifts in red (upper panel). Due to the modest magnitude (tens of meV), shifts are not visually distinguishable.

With these limitations in mind, attention now returns to the observed band shifts in the differential maps. To further test the band renormalisation hypothesis, artificial band structure dynamics were computed based on the equilibrium fitting results obtained well before t_0. Calculated band evolution results for the red-pumped data along the HOMO direction are displayed in Figure 5.19.

For this calculation a separation between the substrate and the molecule was implemented. The substrate (Fermi Energy and nickel bands) follows the red line, while the molecular feature shift (HOMO and HOMO-1) are represented by the blue plot. Two shift pattern were chosen. Firstly, a parallel shift of all features and secondly independent shift of the molecular features vs. the graphene/nickel substrate. The shift amplitude is in the range of 7 meV to −35 meV and can therefore not be discerned by visual examination of the calculated photoemission yield. Differential maps derived from these calculations (Figure 5.20) are promising and support distinct interpretations: initial dynamics shortly after t_0 align more closely with independent molecular and substrate shifts, whereas longer-delay phenomena are consistent with uniform substrate-molecule shifts. It follows,

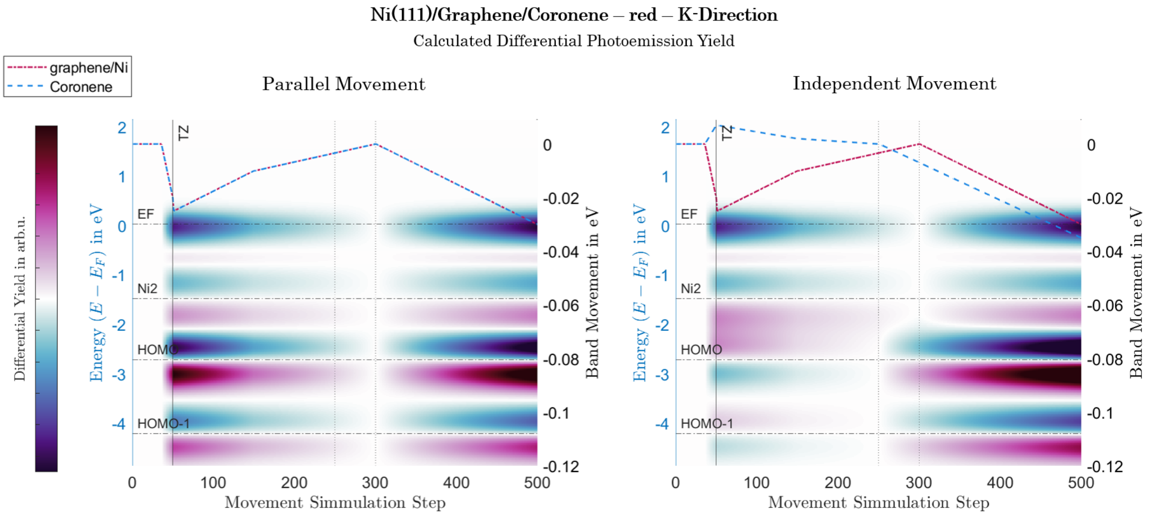

Figure (5.20) Calculated differential photoemission yield for artificial created band shifts of the coronene/graphene/Ni(111) system. Parallel shift of the substrate and the molecular features (left) as well as calculations for an independent shift (right) are presented.

that the band renormalisation upon laser excitation affects molecule and substrate differently, while the secondary shifting at higher delay times is perfectly in line with a band shift inflicted upon the complete sample system. Interestingly, this analysis procedure replicated for the HOMO-1 (M-direction) yields similar calculated differential maps (Figure A.11), yet diverges from experimental observations. While in the differential maps a similar behaviour for the HOMO-1(M)- and HOMO-(K)-direction right after the optical excitation is visible, the same is not true for the secondary band shifts at later delay times. This appears to be restricted mostly to the HOMO-direction. Since, the data were obtained in a row, without changing the sample or the setup, this can not be explained by a measurement artefact (an artefact would appear in both datasets), and is thereby an indication for a localised effect in momentum space.

5.3.1. Transient band renormalisation after charge carrier injection

The analysis based on computation of artificial band shifts using the spectral fitting of the earliest delay steps yields initial insights into interfacial charge dynamics. It reveals transient band shifts on two characteristic time scales: an ultrafast component ($< 100\,\mathrm{fs}$) associated with optically excited electrons, and a slower component ($\sim 1\,\mathrm{ps}$). Similar dynamics were reported by Benito Arnoldi in the C_{60}-molecule/WSe_2 heterostructure [41], where evolving interfacial potential gradients were attributed to exciton formation. To investigate analogous behaviour in the used graphene/ferromagnetic metal–organic heterostructure, I present below the time-resolved spectral fitting results, employing, among others, the same parameters analysed in [41].

I employed four Voigt profiles to decompose each TR-ARPES spectral signature: 1st: the N 1 band near the Fermi level (E_F), 2nd: a Ni 2 band approximately 1.4 eV below E_F, 3rd: the highest occupied molecular orbital (HOMO), 4th: the HOMO–1.
I first consider the primary excitation immediately following laser illumination. The most pronounced dynamic is the transient shift of the chemical potential, μ_F (E_F), shown in Figure 5.21. All panels display the normalised, time-dependent fit parameters: E_F at the top and the Fermi-distribution width, σ_F, at the bottom. Normalisation was achieved by subtracting the mean of the first five delay steps (measured well before t_0) from each subsequent value; this baseline is indicated by dashed lines and t_0 by a solid black vertical line. In the red-pumped measurements, μ_F (i.e. E_F) exhibits a transient decrease that is temporally correlated with a broadening of the Fermi-Dirac distribution, σ_F, following excitation. This effect is absent in the blue-pumped data, consistent with the lower applied laser fluency. The red pump's higher incident fluence induces significant electronic heating, which broadens σ_F. The observed reduction in μ_F cannot be attributed to particle conservation alone; in nickel, a decrease in chemical potential under non-equilibrium conditions is expected due to the steep energy dependence of the density of states near E_F. A high DOS slope at the equilibrium chemical potential amplifies this shift. Importantly, this shift reflects a redistribution of electronic occupation and does not imply a modification of the intrinsic band dispersions or positions in respect to E_F. However, the optical excitation also transiently renormalised the band structure itself. This becomes evident upon comparing the chemical potential shift to the peak energy shift of the Ni 2 band, $E_{Ni,2}$, as shown in Figure 5.22. All panels display normalised peak energies $E_{Ni,2}$ (top) and widths $\sigma_{Ni,2}$ (bottom). The red-pumped measurements exhibit a pronounced decrease in $E_{Ni,2}$ that mirrors the transient drop in μ_F (E_F) after laser excitation. The blue-pumped data show a similar trend, although the corresponding shift in μ_F is less distinct due to lower signal magnitude. This shift cannot be attributed solely to a rigid chemical potential displacement due to particle conservation, instead, it reflects genuine band renormalisation induced by e.g. an excited-state population or transient demagnetisation of the ferromagnetic substrate (see Chapter 4). In contrast, the Ni 1 band (Figure A.12) shows negligible shift, likely because its proximity to E_F constrains the fitting parameter space and complicates separation of band and chemical potential contributions. However, the similarity between simulated and experimental differential data suggests that the nickel 1 band indeed shifts alongside other substrate features. Overall, these time-resolved substrate dynamics corroborate the proposed ultrafast graphene/Ni(111) band renormalisation initiated at t_0, which, despite non-linear relaxation, follows a consistent temporal trend. This observation motivates the next question: how do the adsorbed molecules respond to the ultrafast modulation of the substrate electronic structure?

To elucidate molecular responses, I analysed the temporal evolution of the occupied molecular

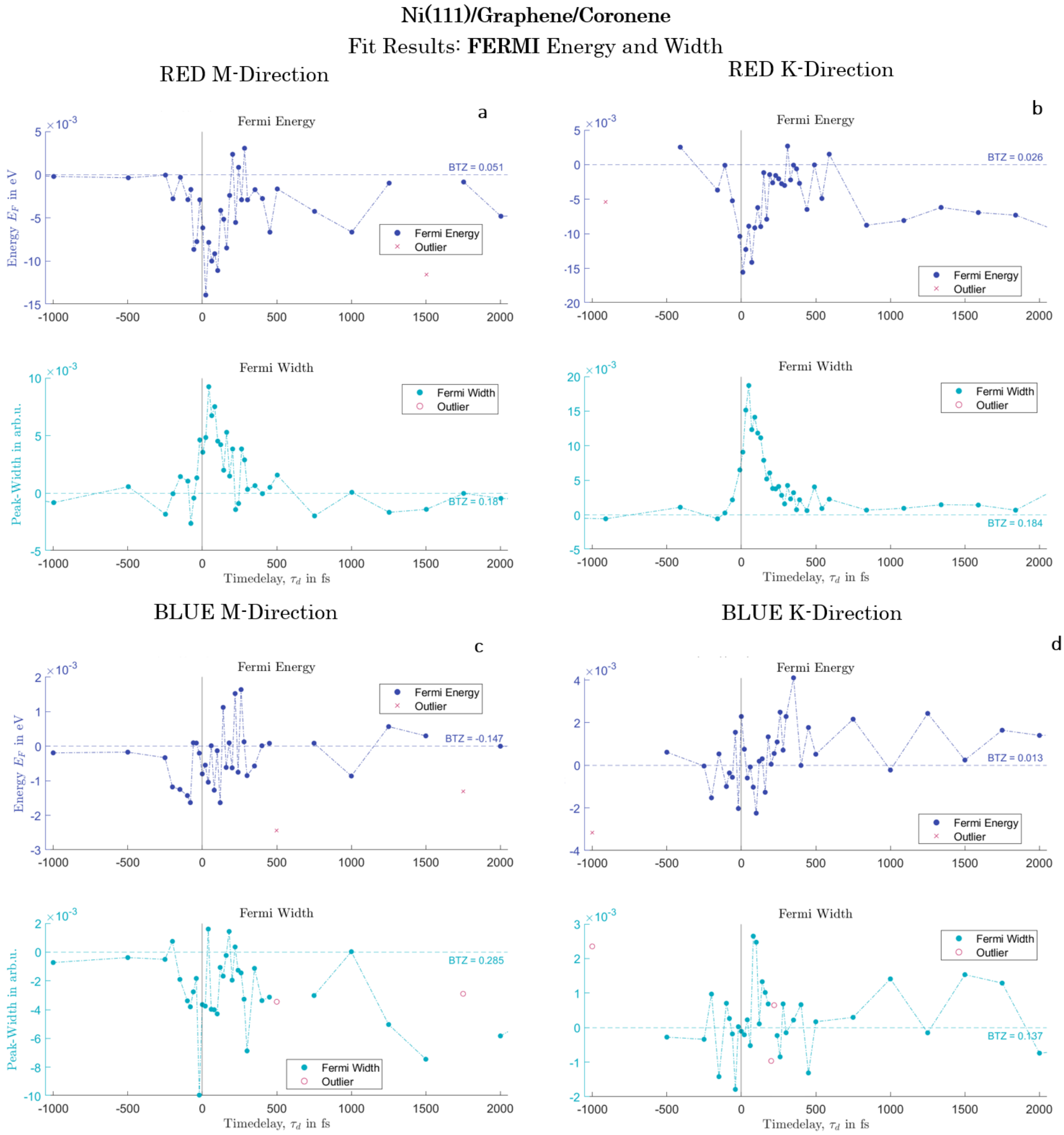

Figure (5.21) Time-resolved spectral fit results for the Fermi energy E_F (top) and the Fermi width σ_F (bottom) for both red- and blue-pumped measurements. The data are normalised to the average of the first five time steps acquired well before t_0, by subtracting the far-before-time-zero value (dashed lines) from the fit results. For red pumping, a clear transient decrease in E_F is observed concurrently with an increase in σ_F. No similar behaviour is seen for the blue-pumped data.

orbitals, as shown in Figure 5.23. Only the red-pumped data are presented due to insufficient signal-to-noise in the blue-pumped measurements. The blue-pumped datasets may suggest an increase in HOMO and HOMO-1 peak energies after laser excitation along the K-direction, but this interpretation must be approached cautiously (see Figure A.13). All panels display the time-resolved spectral fit results for the HOMO peak energies (E_{HOMO}, E_{HOMO-1}) and corresponding HOMO bandwidths (σ_{HOMO}, σ_{HOMO-1}) for the red-pumped data. The data are normalised to the average of the first five time steps far before t_0, by subtracting the far-before-time-zero value from the fit results, with a dashed lines representing this average and t_0 marked by a solid black vertical line. Measurements aligned along the HOMO's primary emission direction (K-direction) are shown on the right, whereas those along the HOMO-1's primary emission direction (M-direction) are shown on the left. The normalised fits reveal an increase in molecular bandwidths at t_0 characterised by a sharp rise and a subsequent gradual decrease, especially pronounced for the HOMO-1 bands along the M-direction. Meanwhile, the peak energies remain stable, with only slight shifts toward lower

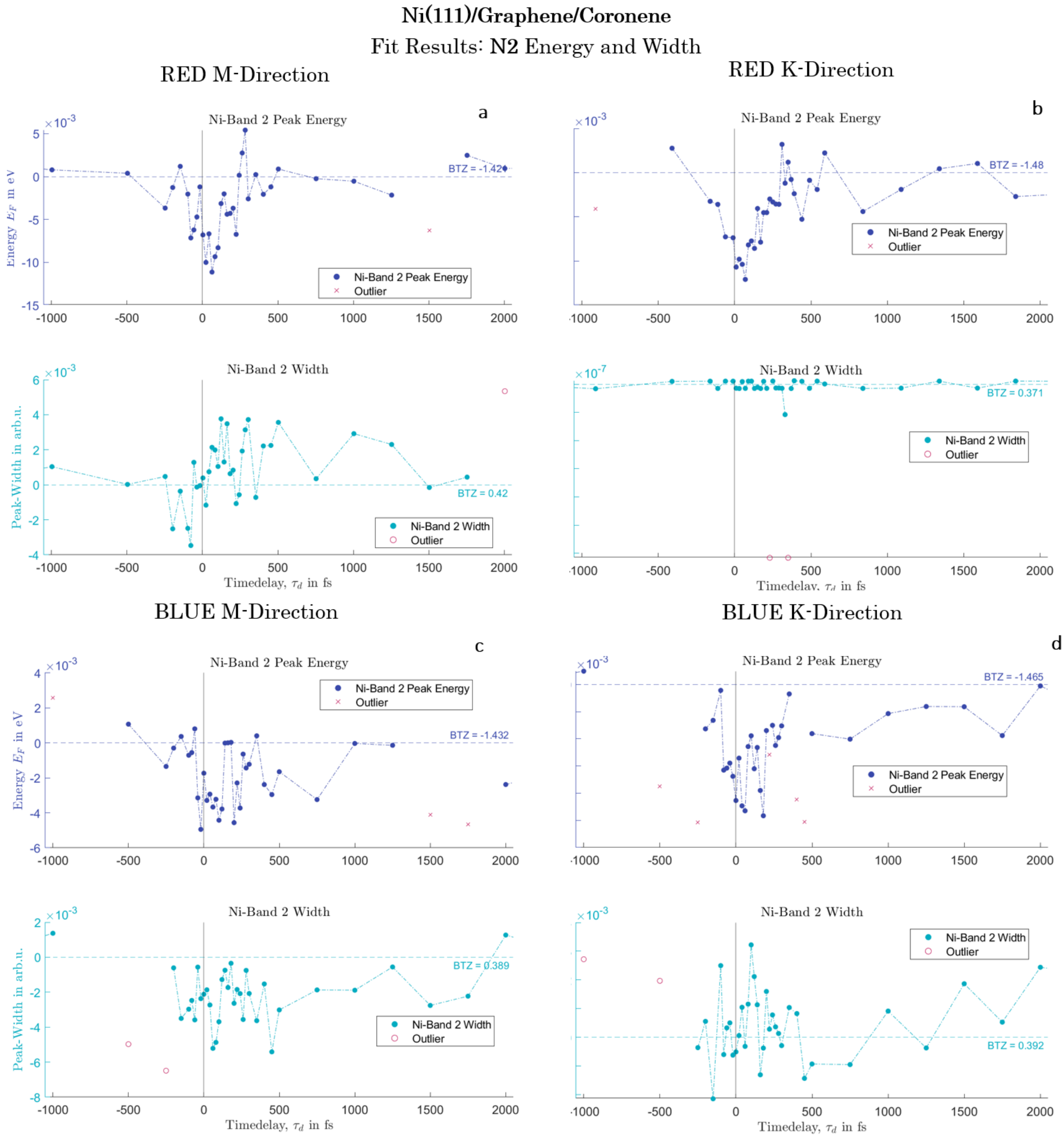

Figure (5.22) Time-resolved spectral fit results for the Ni 2 band peak energy $E_{Ni,2}$ (top) and width $\sigma_{Ni,2}$ (bottom) for red- and blue-pumped measurements. The data are normalised by subtracting the mean of the first five delay steps (dashed lines), with t_0 marked by a vertical line. A clear transient decrease in $E_{Ni,2}$ closely follows the decrease in μ_F. The Ni 1 band (Figure A.12) shows a weaker shift, likely due to its proximity to μ_F. Neither band exhibits a systematic, time-dependent change in width, $\sigma_{Ni,n}$.

binding energy.

Accounting for the 25 meV downward shift of the chemical potential and Ni bands the analysis yields an effective 30 meV upward shift of the molecular orbitals relative to the graphene/Ni(111) substrate. By contrast, Arnoldi observed a 90 meV downward shift of the conduction band and a concurrent 40 meV upward shift of the HOMO at the C_{60}/WSe_2 interface, resulting in a net convergence of 130 meV—four times larger than my measurement [41]. This difference arises from substrate properties: my metallic Ni substrate, with its higher electron density and Fermi velocity, exhibits significantly reduced interfacial charge redistribution (due to strong electrical screening) compared to the semiconducting WSe_2. The low photon energy of the red pump precludes direct excitation of the HOMO and HOMO-1 orbitals. Two scenarios are possible: either the substrate changes while the coronene layer is unaffected, e.g. changes of the surface dipole only effecting electrons origi-

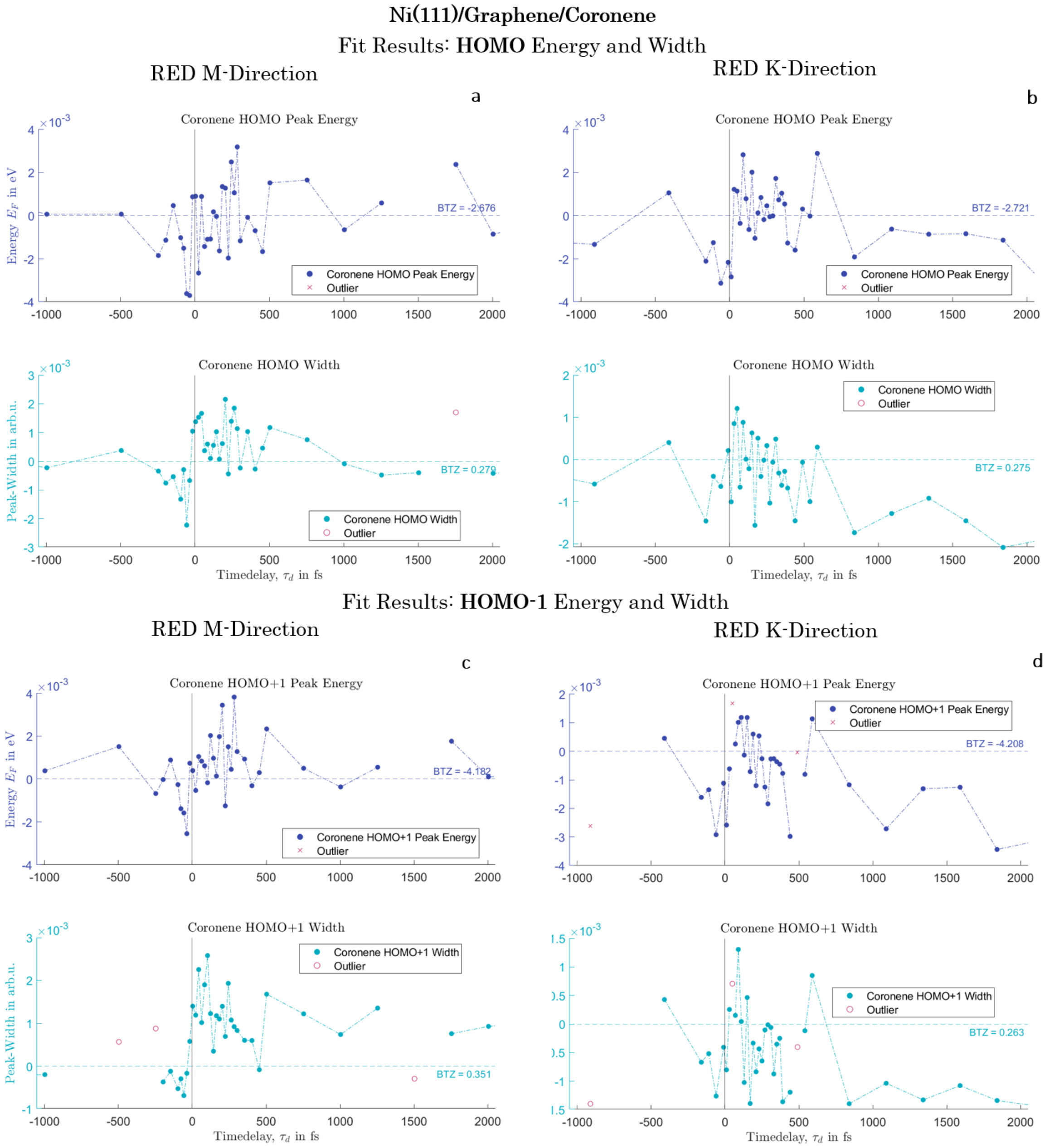

Figure (5.23) Time-resolved spectral fit results for the HOMO and HOMO-1 peak energies (E_{HOMO}, E_{HOMO-1}) and widths (σ_{HOMO}, σ_{HOMO-1}) for red-pumped data. The data are normalised by subtracting the mean of the first five delay steps measured well before t_0 (dashed lines), t_0 is marked by a vertical line. Measurements along the HOMO emission centre (K-direction) are shown in the left panels, and those along the HOMO-1 emission centre (M-direction) in the right panels. The results show transient broadening of both molecular bands at t_0, more pronounced for the HOMO-1 feature, while peak energies remain stable with minor shifts to lower binding energy.

nating from the substrate, or the molecular peaks themselves broaden and shift to lower binding energy. The observed shift towards lower binding energies of the HOMO-1 peak in the K-direction, independent of the shift of μ_F (i.e. E_F), supports the latter interpretation. Simultaneous peak broadening suggests a non-coherent Stark-like effect. The Stark shift refers to a coherent change in energy level alignment of molecules after optical excitation, similar effects if not coherent, might be caused by image-charge forces, dipole-layer formation, or static interfacial fields "build in" when connecting two materials. This mechanism is consistent with the blue-pumped results (see Figure A.13).

In conclusion, immediately after excitation the substrate bands shift to higher binding energy while molecular orbitals remain essentially stable or display slight upward shifts with increased broadening. Since the both materials shift in opposite directions, towards each other, space charge and other measurement artefacts, can be excluded as they would cause a shift in the same direction.

As a last step the long-time dynamics are analysed. Figure 5.24 shows that the laser deposits energy into the electronic system, causing a rapid increase in the Fermi-edge width followed by thermalisation within approximately 500 fs. Notably, the long-time shift of the Ni 2 band toward higher binding energy in the K-direction is independent of electronic temperature and onsets with thermalisation. The shift reaches approximately 20 meV by the end of the 10 ps measurement window, preventing determination of its maximum or recovery time. The absence of a comparable long-term shift in the M-direction (the bands follow the initial sharp degrease after laser excitation) supports a k-space localise mechanism and thereby implies real-space delocalisation. Figure 5.24 also compares the

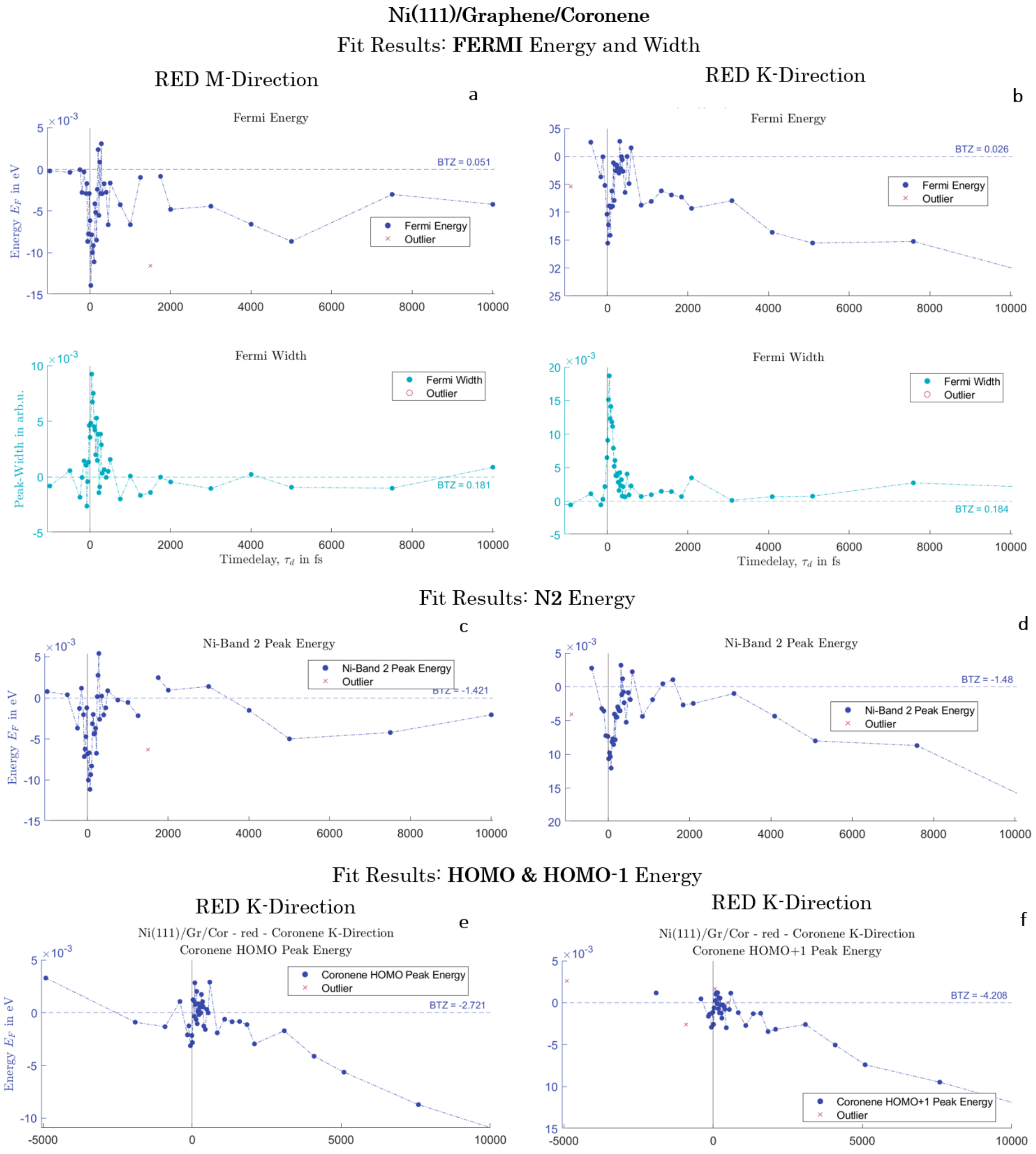

Figure (5.24) TR-Spectral Fit Results for the Fermi and nickel 2 Band Energies $E_{Ni,2}$ and the Fermi width σ_F for long time delays for the red-pumped measurement. The Fermi width, indicating the electron system temperature, rises steeply after t_0 and decreases within the first 500 fs. The Fermi energy on the other hand, exhibits a fast dynamic after the laser excitation, a recovery back to its original value and a long time scale degrease, similar to the shift of the Ni2 band.

HOMO and HOMO-1 peak shifts, which follow the substrate trend and match the decay gradient. Finally, the HOMO occupation parameter, A_{HOMO}, and the Ni 2 band occupation, $A_{Ni,2}$, are shown in Figure 5.25, revealing a clear decrease in A_{HOMO} concurrent with the global band-shift onset.

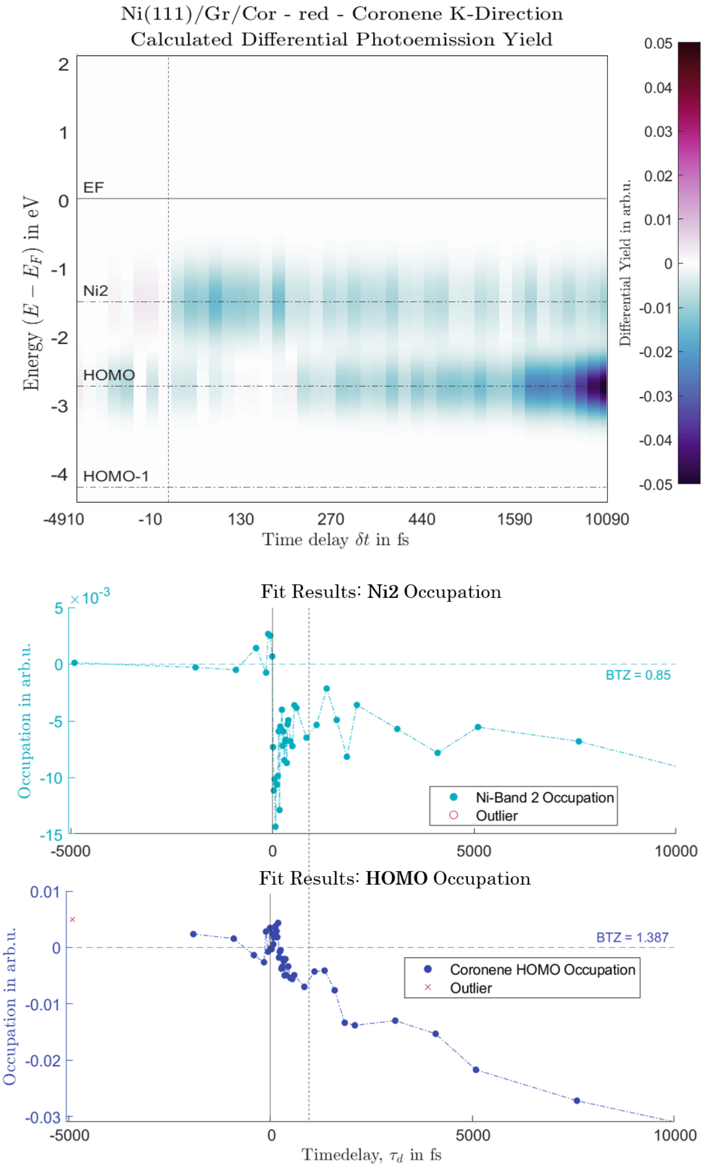

Figure (5.25) Top: Differential map of band occupation change, ΔA_n, for red-pumped data. Only A_{HOMO} and $A_{Ni,2}$ are shown, as changes in Ni 1 and HOMO-1 occupations are negligible. Blue indicates decreased occupation and red indicates increased occupation relative to the pre-t_0 baseline (dashed line). Middle: fit results for $A_{Ni,2}$. Bottom: fit results for A_{HOMO}

The fit results were used to calculate a differential map, showing a degrease in blue and an increase in red in comparison to the occupation before t_0. Only A_{HOMO} and $A_{Ni,2}$ are shown, as changes in Ni 1 and HOMO-1 occupations are negligible. While the Ni2-band energetic position allows for a direct electron excitation and thereby a population reduction after optical excitation, decrease in A_{HOMO} is astonishing. The exact mechanism behind this observation is elusive. Possible, not mutually exclusive, effects are:

A **slow electron transfer** occurs between the molecule and substrate with holes accumulating in the molecule. This would also cause a localised increase of the negative surface potential, consistent with the observed energetic downward shift. The delayed onset can be explained, if the process is assisted by thermal phonons, or the transfer is mediated through trap or hybrid states, as well as a cascaded carrier relaxation.

A **transience interface dipole formation** were excited electrons might get trapped at the interface leading to an increased surface dipole and thereby a shift of the electronic band structure (akin to the surface photovoltage effect) in combination with a **screening driven orbital reorganisation**. This orbital reorganisation could follow a charge redistribution at the interface, causing the slight redistribution of the spectral weight of the molecular signature in k-space and potentially alter the photoemission cross-section. In this case the apparent decrease in the HOMO occupation would only be an artificial fitting result due to these not observable changes with the used measurement setup. To verify this behaviours next steps, which exceed the scope of this thesis, would be to probe the system fluence and temperature dependency, e.g. cooling the system during the measurements helps to determine the roll of phonons. Additionally, by monitoring the cut-off region during the laser excitation in future experiments changes of the work function could be visualised.

5.3.2. Indication of long lifetime charge carrier in the coronene LUMO on coronene - graphene/nickel interfaces

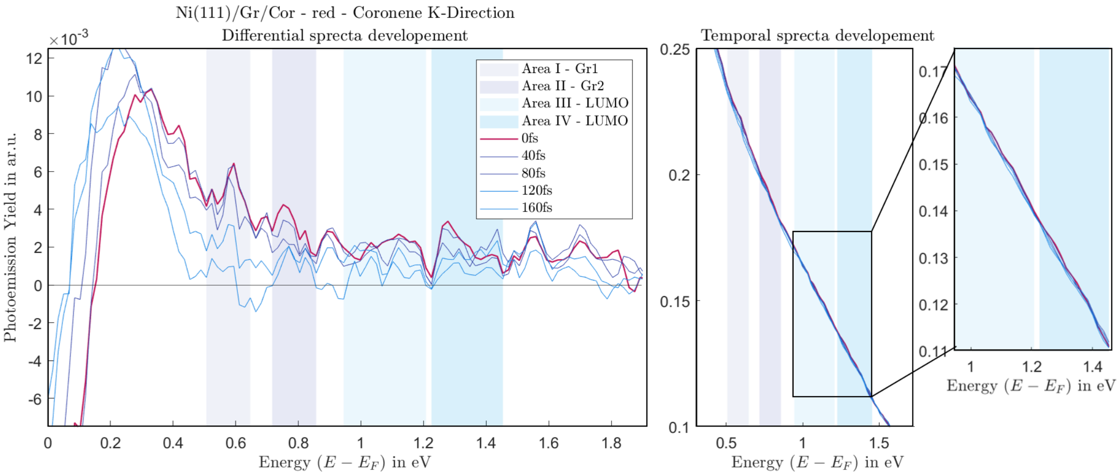

Figure (5.26) Shown are the differential spectra extracted from the Tr-ARPES measurements on the coronene/graphene/Ni(111) system along the coronene-K-Direction, ranging from 0 fs - 160 fs. The reference spectrum for differential normalisation was constructed by averaging data from early delay steps (steps 1 to 5), following the procedure used in the differential intensity maps discussed earlier (see method Section 2.3.1). t_0 is depicted in red. Areas corresponding to specific excited states are marked and the temporal development of the corresponding spectra shown on the right.

Both the transient line width broadening and the upward shift (toward lower binding energy) of the occupied molecular orbitals strongly indicate light-induced charge–carrier dynamics involving unoccupied substrate states and molecular orbitals. Analogous behaviour is observed when exciton formation induces a Stark shift of molecular bands toward each other. Although this heterostructure does not support bound excitons, a Stark-like effect may still occur (see previous section). Within the light-induced Stark framework, both occupied and unoccupied molecular orbitals undergo transient energy shifts. This observation raises the question of whether the unoccupied LUMO becomes transiently populated by optical excitation and whether such population produces a measurable modification of its spectral signature.

Direct analysis of the raw photoemission signal above the Fermi level is hampered by low signal-to-noise ratio and inherently low transition probability in multi-photon photoemission experiments. Only weakly resolved features are observed in the unoccupied region, complicating direct interpretation. Therefore, I employ differential spectra, subtracting a reference spectrum recorded well before t_0, to enhance contrast and reliably identify time-dependent changes (see Section 2.3.1). The resulting differential spectra, extracted from a sequence of time delays, are presented in Figure 5.26, with the right panel illustrating the temporal evolution of the signal. The analysed energy–momentum window ($\sim 1.35\,\text{Å}^{-1}$ to $\sim 1.65\,\text{Å}^{-1}$) matches that studied under stationary-delay configuration in Section 5.2.2. The differential reference spectrum was obtained by averaging the first five delay steps, following the procedure used for the intensity maps. Figure 5.26 shows photoemission spectra at selected delays from t_0 to 160 fs. At t_0 (red curve), a pronounced transient intensity increase appears just above the Fermi level, consistent with population of optically excited hot electrons. These carriers occupy two distinct features at 0.58 eV and 0.77 eV, corresponding to graphene-derived π^* bands in the graphene/Ni(111) substrate band structure (see Figure A.1). The rapid decay of these features reflects ultrafast relaxation and scattering of photoexcited carriers into lower-lying states or the substrate continuum. Simultaneously, the substrate-derived peaks on the low-energy side shift slightly toward lower binding energy over time. This shift follows the general trend observed for occupied substrate states and matches the chemical potential displacement of approximately 20 meV. As shown by the overlaid spectral plots in Figure 5.26, these spectral changes are subtle and warrant cautious interpretation. Moreover, the apparent shift toward lower kinetic energy may partially arise from background changes due to modification of the Fermi-Dirac distribution.

In contrast, the spectral region corresponding to the molecular LUMO, nominally between 1.1 eV - 1.45 eV above the Fermi level, displays markedly different behaviour. Two peaks appear at t_0: one at 1.15 eV and another at 1.35 eV. Either overlayed by the initial state structure, discussed in Section 5.2.2, or given the energetic positions the lower peak might be an additional excited state corresponding to the LUMO. The LUMO-related signal decays more slowly than the graphene-derived features. The dynamical behaviour becomes even more intriguing at longer time scales. Figure 5.27 shows differential spectra from 350 fs - 3500 fs, with the t_0 spectrum in red for reference.

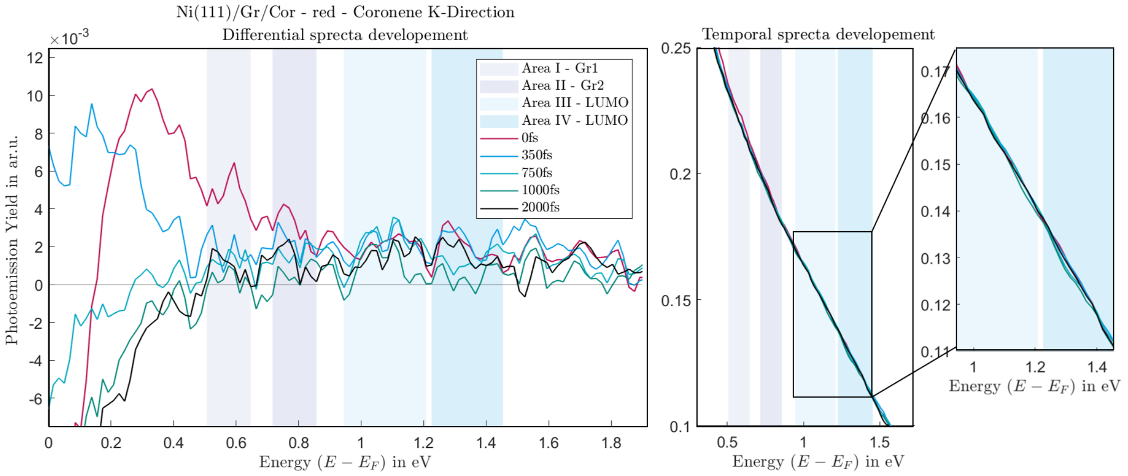

Figure (5.27) Shown are the differential spectra extracted from the Tr-ARPES measurements on the coronene/graphene/Ni(111) system along the coronene-K-Direction, ranging from 350 fs - 3500 fs. The reference spectrum for differential normalisation was constructed by averaging data from early delay steps (steps 1 to 5), following the procedure used in the differential intensity maps discussed earlier (see method Section 2.3.1). t_0 is depicted in red.

Notably, the LUMO signal nearly vanishes by 160 fs (see Figure 5.26) but reemerges near 750 fs and strengthens over the following picoseconds. This initial decay followed by a delayed build-up of spectral weight suggests a secondary population mechanism distinct from the prompt excitation dynamics observed near time zero or a charge carrier redistribution within the LUMO. A closer view indicates that the higher-energy feature is depleted around 1000 fs and partially recovers at longer delays, whereas the lower-energy feature gains population relative to t_0 and decays only slowly. The persistence (counting possible repopulation) of the LUMO-associated signal up to a few ps indicates a long-lived excited state. Other unoccupied features, such as the graphene-derived bands, do not exhibit comparable delayed re-population dynamics. As the experimental window terminates at 10 ps, the full relaxation dynamics of the long-lived LUMO occupation remain unresolved. Nevertheless, even at the end of the measurement period, clear signatures of spectral redistribution and band shifts are evident in the differential spectra and differential energy-vs-time-maps in Figure 5.17.

Interestingly, the magnitude of the delayed band shifts, visible in Figure 5.17, exceeds that of the initial response. Although the blue-pumped data have insufficient signal-to-noise for definitive analysis, in the energy-vs-time-maps (Figure 5.17) a slight change at high delay times is visible, indicating a similar process as can be measured in the red-pumped data.

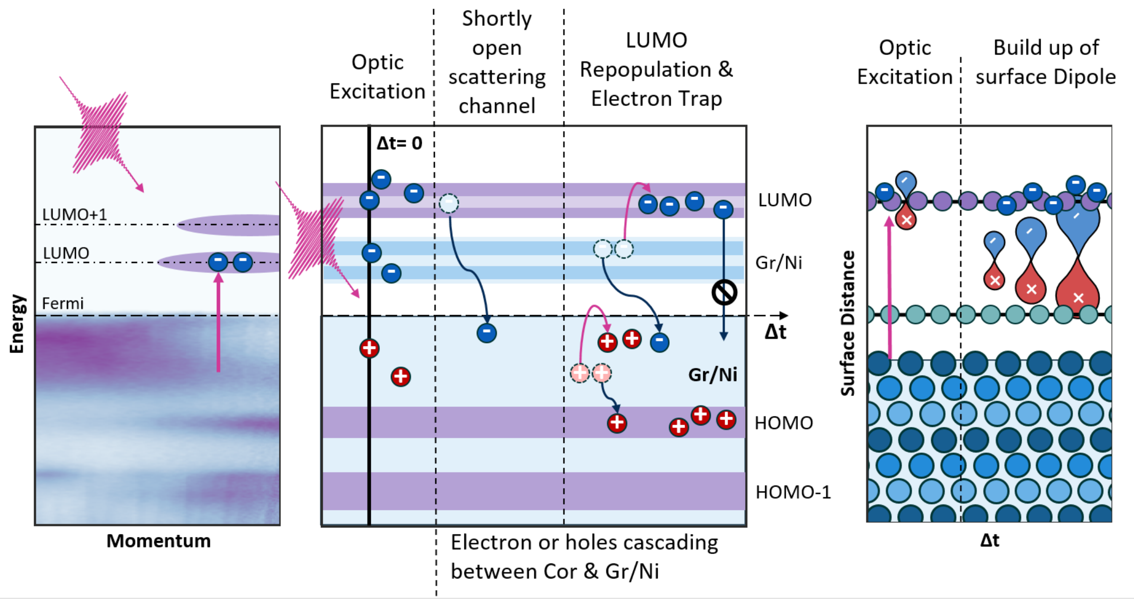

Figure (5.28) Potential electron dynamics at the coronene/graphene/nickel(111) interface.

Secondary (long-lived) LUMO repopulation The selectivity of the signal, confined to the molecular orbital region between 1.1 eV - 1.45 eV, is consistent with the broad k-space signature of the LUMO in both energy and momentum. Such a configuration provides an efficient phase space for inelastic scattering, enabling a redistribution of hot carriers into the LUMO over extended time scales. Given the energetic position of the LUMO and its partial de-localisation in momentum-space "across" the molecule–metal interface, it likely serves as an effective acceptor state for secondary electron population via electron–electron or electron–phonon scattering (e.g. auger-like electron excitations). The peak of the LUMO photoemission cross-section, which lies along the measured momentum direction, facilitates the time-delayed accumulation of spectral weight, hence increasing charge carrier population in its minimum. This interpretation offers a plausible mechanism for the time-dependent band shifts reported in Figure 5.17, where the band structure states exhibit both a prompt shift after the light-driven excitation and a continued evolution on picoseconds time scales after normalisation around 200 fs. The delayed redistribution of charge into the molecular orbital manifold may thus account for the observed long-term band renormalisation, implicating interfacial screening dynamics and non-equilibrium charge transfer.

A potential microscopic origin for the extended lifetime of the excited-state population is found in the electronic structure of the graphene/Ni(111) substrate. As illustrated in Figure A.1, the projected band structure near the K-point reveals a pronounced depletion of unoccupied states in nickel, forming a momentum-selective pseudo-gap. Although nickel exhibits a high density of unoccupied d-states near the Fermi level — contributing to its magnetic and metallic properties — this density is not uniformly distributed in momentum space. In the vicinity of the nickel-K-point, the scarcity of unoccupied states restricts available scattering channels for excited electrons in the LUMO. Only the graphene exhibits unoccupied states near E-Fermi. This phase-space bottleneck may explain why the LUMO population does not efficiently decay via coupling to graphene-derived or substrate bands. An additional factor is the potential spin-polarisation of the excited electrons. The graphene/nickel substrate might serve as a source for spin-polarised electrons [19] which will be injected into the molecular orbitals. Spin-mixing or other effects might change the polarisation preventing a recombination with the initial states. Contradicting this is the de-localisation in k-space of the LUMO momentum signature, intra-band scattering would open a multitude of potential scattering pathways. On the other hand, the long-timescale band shift is only visible in along the K-direction indicating an origin localise in momentum space.

The molecular band broadening or the global band shifts can not easily be explained within this pathway. An electron trapping in the molecule might lead to a charge accumulation localised in real-space at the molecular layer. Potentially, this might effect photo-emitted electrons that pass this area or electrons originating from it (like electrons emitted from the HOMO or HOMO-1).

Prolonged excited state recombination One other possible mechanism is the formation of long-lived molecular excited states. Hole accumulation in the HOMO, combined with trapped electrons in the LUMO, may extend excited-state lifetimes and thus prolong recombination. As discussed earlier, in polycyclic aromatic hydrocarbon molecules, excited-state decay is dominated by "breathing" and "tilting" vibrational modes within a few hundred femtoseconds after photoexcitation [108]. This vibrational relaxation may drive the initial fast decay but becomes less efficient once the system cools and energy is redistributed. If secondary LUMO refilling and cascading hole injection into the HOMO lead to net charge accumulation, electron–hole recombination may become the rate-limiting decay channel. The energetically broad coronene LUMO suggests intrinsic lifetimes on the order of a few femtoseconds. However, for Alq_3 on Cu(111), Aeschlimann *et al.* observed that homogeneous broadening dominated the photoemission linewidth, while the natural linewidth was only 10 meV, corresponding to intrinsic excited-state lifetimes and spin-dependent relaxation times of 400 fs to 800 fs [119]. Whether analogous broadening effects could yield picosecond-range relaxation and account for the long-lived carrier populations observed here remains speculative but warrants future study.

5.4. Discussion of charge-carrier dynamics at the coronene/graphene/nickel(111) interface

This chapter focusses on the light-induced charge-carrier dynamics in the metal-organic heterostructure coronene/graphene/Ni(111). I have systematically investigated the interfacial charge transfer dynamics in the coronene/graphene/Ni(111) system using both static and time-resolved ARPES measurements.

Coronene, a member of the Polycyclic Aromatic Hydrocarbons (PAH), exhibits an electronic structure similar to larger molecules such as perylene or perylenetetracarboxylic dianhydride. On metallic surfaces, the molecular LUMO wave function of PAHs typically overlaps with metallic states, enabling rapid charge transfer and resulting in excited-state lifetimes in the range of tens of femtoseconds. Therefore, the observation of a long-lived LUMO population in the presence of nickel is surprising. Two-photon photoemission (2PPE) studies on C_{60}-molecule adsorbed on graphite however found that photoexcited electrons remain in the C_{60}-molecule LUMO for a decay rate of roughly $1.3\,\mathrm{ps}^{-1}$, corresponding to a lifetime of about 0.8 ps, which was attributed to the weak van-der-Waals coupling between C_{60}-molecule and graphite [33]. Importantly, those authors noted that such long-lived photocarriers were not observed for metallic substrates exhibiting strong interactions.

Generally, the coupling strength between a molecule and its substrate (or interlayer) drastically influences both charge carrier injection and decay times.

For example, time-resolved X-ray photoemission experiments by Ravikumar *et al.* compared electron injection from Ni(111) into the molecule 4,4-bipyridine, showing that when the molecule is separated from the metal by a bi-layer graphene intermediate layer, the electron injection is approximately four times slower [120]. This result highlights that a more decoupling interlayer reduces substrate-to-molecule coupling, yielding longer-lived excited states. In the heterostructure presented in this thesis, coronene is deposited on epitaxial monolayer graphene on Ni(111), which is known to be hybridised with nickel. Thus, one expects a faster injection (and consequently shorter lifetimes) than when using an insulating spacer, but potentially slower injection than for a molecule directly adsorbed on Ni(111). Moreover, because coronene and graphene are only weakly bound, maintaining a separation near their respective van-der-Waals radii, this configuration is very similar to a bi-layer graphene sheet, aligning with observations that even a single layer of hexagonal boron nitride or graphene can prolong excited-state lifetimes of adsorbates by reducing hybridisation [29]. In the coronene/graphene/Ni(111) system, although graphene is not as inert as bulk graphite, it still reduces coupling compared to a direct coronene–Ni contact, making a sub-picosecond or picosecond-scale lifetime component consistent with literature trends.

By contrast, coronene on a noble metal like Ag(111), which interacts via weak chemisorption, might also show extended lifetimes, whereas on strongly interacting metals (where coronene chemisorbs), the excited state would quench almost immediately. Direct comparison with additional measurements on other systems could further elucidate the exact mechanisms, though that exceeds the scope of this thesis.

A system in which interface excitons were studied is WS_2/graphene [34], where resonant excitation of the WS_2 A-exciton led to charge separation, with electrons remaining in WS_2 and holes in graphene, forming a charge-separated state that persisted for approximately 0.8 ps. The long-lived nature of that state was attributed to limited scattering phase space arising from momentum and energy misalignment between WS_2 and graphene, an effect analogous to a charge-transfer exciton or momentum bottleneck that prevents rapid recombination.

While I do not expect excitons in the coronene/graphene/Ni(111) system it might support an excited state with an electron in the coronene LUMO and a screened hole in nickel or graphene, provided the bands are not perfectly aligned for recombination.

My study firstly addresses the question if the buffering effect of a graphene layer (shown in [29]), to influence the electronic structure and charge transfer at the coronene/Ni(111) interface, can be replicated. This task was successfully, as the results demonstrate that the graphene layer effectively decouples coronene from the reactive Ni(111) substrate, restoring a quasi-free-standing character and reducing the strong hybridisation observed with direct adsorption. This finding is consistent with established literature [29, 114] and confirms that the molecular orbital signatures, such as the HOMO and LUMO, become distinctly resolved upon decoupling.

The main objective in this chapter was:

Can a graphene monolayer facilitate the injection of photo-excited charge carriers from a metal into an adsorbed molecular semiconductor, and what are the ultrafast dynamics of such charge-transfer processes?

The stationary-delay configuration measurements reveal a momentum signature for the excited molecular orbitals, with clear features, particularly in the blue-pumped experiments, that align with theoretical expectations. **Thus, the results confirm that light-driven charge carrier injection into the coronene layer does occur, as further evidenced by transient band renormalisation effects (including Fermi level shifts and band broadening) observed in time-resolved ARPES measurements. Most notably, a secondary population mechanism in the LUMO region emerges at longer delay times, leading to the third research question:**

My data suggest that the delayed build-up of spectral weight in the LUMO cannot be solely attributed to prompt two-photon photoemission. Instead, it likely arises from a secondary process that may involve cascading repopulation at the coronene/graphene interface or a phase-space bottleneck due to a momentum-selective pseudo gap in the Ni(111) substrate. Limitations in the signal-to-noise ratio, the low photon flux from the HHG source, and discrepancies in pump power, especially for the blue pump, impose constraints on the quantitative accuracy of these findings. In the context of established literature, my observations align with prior studies on ultrafast charge dynamics in molecule–metal systems and indicate the need for further investigations using higher-flux sources and advanced theoretical models to fully elucidate the underlying microscopic mechanisms.

Conclusion

This chapter provides a detailed and critical evaluation of light-induced charge carrier injection in the coronene/graphene/Ni(111) heterostructure, demonstrating that graphene not only decouples coronene but also facilitates a complex, multi-step population of its unoccupied molecular orbitals. These insights pave the way for future research on spin-polarised charge injection and the design of organic spintronic and optoelectronic devices.

In this chapter, I have investigated the ultrafast photoexcited charge-carrier dynamics in a coronene/-graphene/Ni(111) heterostructure using time- and angle-resolved photoemission spectroscopy. The experimental results revealed an initial sub-picosecond population of the coronene LUMO upon optical excitation, followed by a secondary component that persists for significantly longer times. I interpret the prompt LUMO population as evidence of ultrafast charge injection from the underlying strongly hybridise graphene/Ni(111) substrate into the adsorbed coronene molecules. This interpretation is supported by the alignment of energy levels, which enables electrons from Ni (or hybrid graphene/Ni states) to populate the coronene LUMO on a < 100 fs timescale, analogous to substrate-to-molecule injection observed in related graphene–organic interfaces [33]. The subsequent **long-lived LUMO population** is a central finding of this work, and I discuss two complementary mechanisms that could explain its existence in the context of contemporary literature.

On the one hand, the persistence of excited electrons in the LUMO can be attributed to the formation of an (interfacial) long-lived excited state, wherein an electron resides on coronene while the corresponding hole is located in the graphene/Ni substrate or through cascading relaxation in the HOMO. Such excited state stabilisation is plausible given the partial electronic decoupling provided by the one-atom-thick graphene spacer, which reduces screening enough to sustain an excitation even in proximity to a metal.

On the other hand, a **momentum-space bottleneck** may arise: the injected electron in the coronene LUMO might lack an available state in Ni or graphene to scatter into, due to momentum and energy conservation constraints, thereby prolonging its lifetime. In the coronene/graphene/Ni(111) system, the graphene interlayer might imposes an additional momentum filter and screening buffer, leading to an initial fast decay of unbound electrons and a slower decay of momentum-trapped electrons.

The **limitations of the measurement** must be acknowledged: restricted measurement points due to software constraints, instability of the HHG light source with low countrate, and insufficient pumping power for the blue laser pulse limit the quantitative resolution, particularly in the unoccupied region. Despite these limitations, the consistency of the two-component population and decay dynamics with those observed in other weakly-coupled molecule–metal systems lends confidence to my interpretation. In particular, the long-lived tail of the LUMO population (persisting from a few hundred femtoseconds up to a few picoseconds) is **unprecedented for molecules directly on a metal** but is reasonable for a molecule on graphene/Ni(111), reflecting the reduced electronic coupling in this heterostructure. The analysis shows that the secondary LUMO population likely emerges from a combination of exciton formation and momentum-space bottlenecks, in line with established understanding of interfacial charge dynamics. The results presented here bridge the gap between fully delocalised ultrafast charge transfer at metal–molecule interfaces and the more isolated excitonic behaviour observed in semiconductor–molecule systems, positioning the coronene/graphene/Ni(111) stack as an intermediate regime where both many-body and band structure effects are significant.

Summary

The coronene/graphene/Ni(111) heterostructure exhibits ultrafast charge injection into molecular orbitals followed by an atypically prolonged excited-state lifetime, underscoring the importance of interlayer coupling and interface structure in governing charge-carrier dynamics. This finding not only enriches our fundamental understanding of photoinduced processes at molecule–2D material–metal interfaces but also suggests potential strategies to control excited-state lifetimes through interface engineering. Furthermore, since Ni(111) is ferromagnetic and graphene is known to preserve electron spin coherence, the coronene/graphene/Ni(111) heterostructure could enable ultrafast injection of spin-polarised electrons into an organic molecule, with the long-lived LUMO population providing a time window for spin manipulation. Future experiments with spin-resolved pump-probe photoemission and molecular spin detectors will be crucial for exploring spin injection, transport, and retention in such hybrid systems. The insights gained here pave the way for the development of molecule-based spintronic devices, where a graphene tunnel barrier can facilitate efficient and rapid spin transfer while the molecular layer can be functionalised for spin storage or sensing applications.

This chapter closes the loop: the tuned band structure of Chapter 3 and the femtosecond spin-dynamics of Chapter 4 jointly dictate how spin-polarised, photo-excited carriers inject into coronene. Together, the three studies form a coherent roadmap for interface design — from static band decoupling to dynamic spin control to molecular charge-injection — for next-generation opto-spintronic architectures.

6. Conclusion and Outlook

6.1. Summary of results

This dissertation set out to investigate how interfacial engineering can modulate the ultrafast charge-carrier dynamics in graphene-based heterostructures. Three prototypical systems were studied using time- and angle-resolved photoemission spectroscopy (Tr-ARPES):
1) graphene directly interfaced with a ferromagnetic Ni(111) substrate,
2) the same interface modified by intercalating a monolayer of lead (Pb) between graphene and Ni(111), and
3) a hybrid structure where a graphene/Ni(111) interface is used to electronically couple to an organic molecular layer (coronene).
Across these studies, an unifying theme is that the interface structure profoundly influences graphene's electronic bands and ultrafast carrier dynamics, enabling or suppressing certain phenomena depending on the chosen interface modifications.

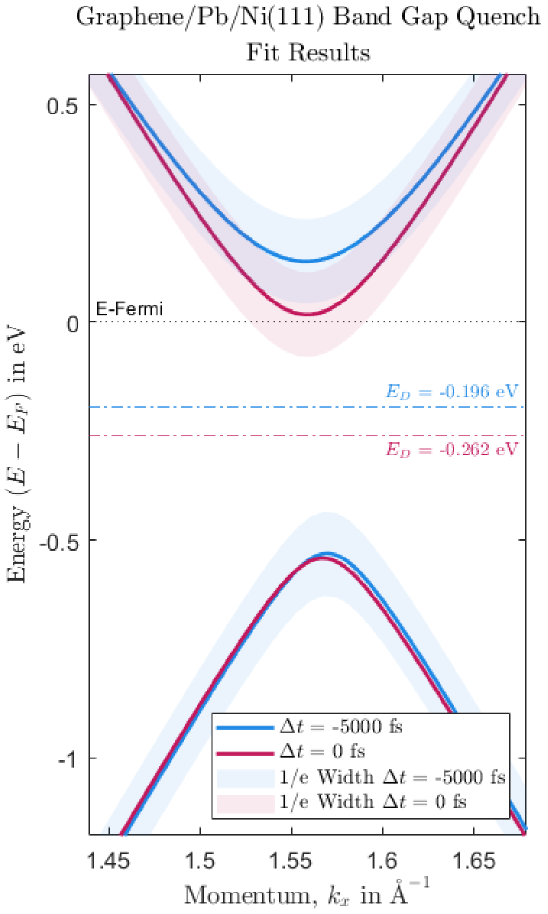

Figure (6.1) Magnitude of optically induced graphene band gap quenching. Depicted are the equilibrium Dirac cone centre position and its 1/e-width (extracted from fitting, blue) compared to its position and 1/e-width at t_0 (red). The respective Dirac point energies E_D and the Fermi energy E_F are marked with horizontal lines.

In the first part, a lead-intercalated graphene/Ni(111) system was explored as a means to tailor graphene's Dirac cone. Static ARPES measurements confirmed that pristine graphene on Ni(111) experiences strong hybridisation with the metal 3d bands, which destroys the characteristic linear dispersion and gapless Dirac point. Upon intercalation of a monolayer of Pb beneath the graphene, the interaction with Ni is substantially reduced and graphene becomes quasi-free-standing. This leads to the recovery of a clear linear Dirac band dispersion and the opening of a sizeable band gap

($\sim 270\,\mathrm{meV}$) at the Dirac point. The gap opening is attributed to the enhanced spin-orbit coupling (SOC) introduced by the heavy Pb atoms in proximity to graphene, together with a breaking of sublattice symmetry. Time-resolved ARPES experiments on this Pb-intercalated graphene/Ni system revealed transient band structure modifications following ultrafast optical excitation (Figure 6.1). In particular, subtle shifts in graphene's Dirac bands and changes in the effective gap were observed on femtosecond timescales, although a fully resolved transient Dirac gap could not be unambiguously distinguished with the available probe photon energy and polarisation and lack of a Tr-EUV momentum microscopy setup. These ultrafast measurements, while preliminary, indicate that optical excitation can dynamically modulate the Dirac cone (e.g. via transient doping or screening effects), and they underscore the need for higher-resolution or spin-resolved probes to capture the SOC-split band dynamics more clearly.

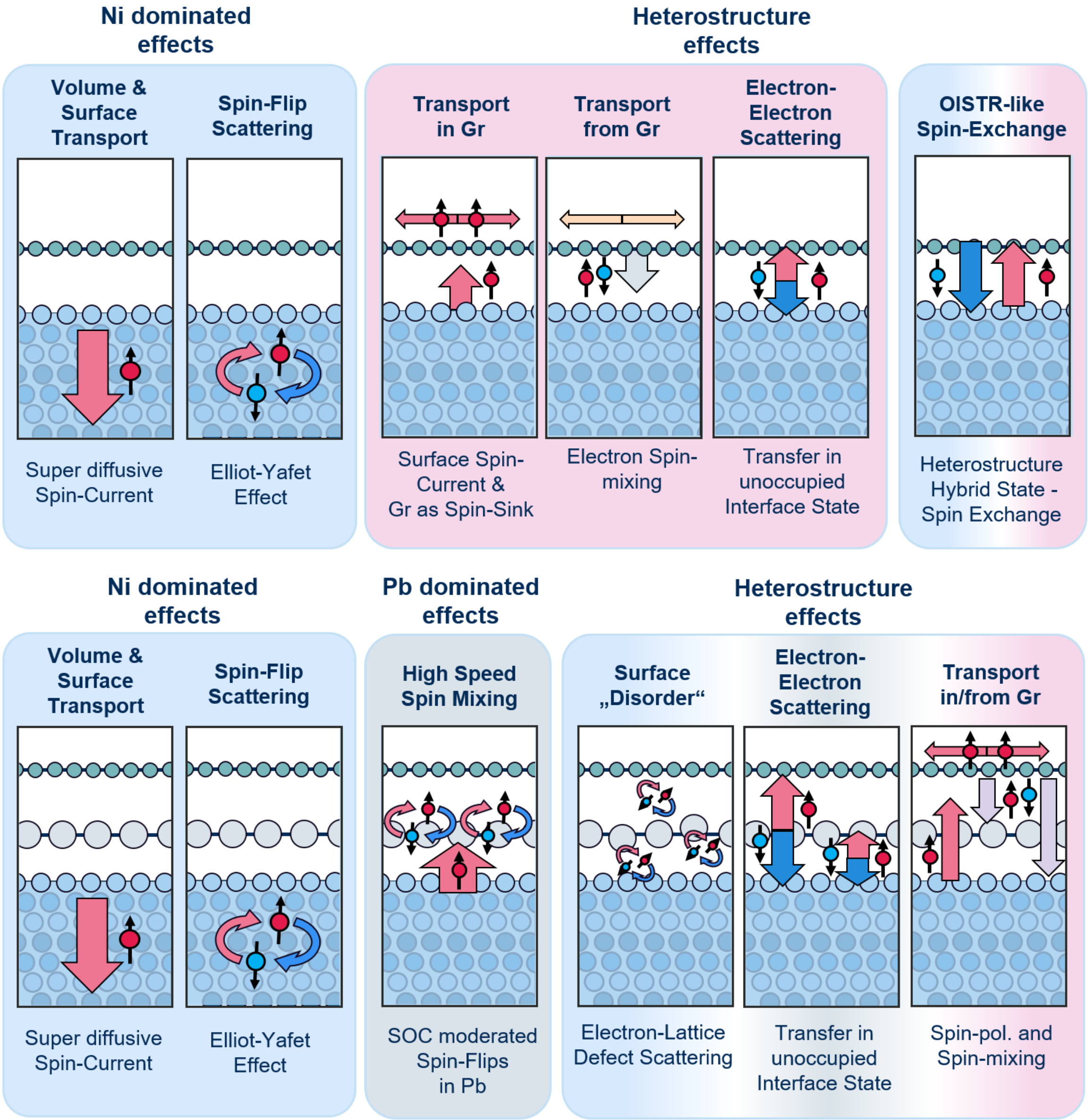

Figure (6.2) Scheme of possible interface spin transport at the graphene/Ni (top) and graphene/Pb/Ni (bottom) interface.

In the second part, the focus shifted to ultrafast magnetisation dynamics at the graphene/Ni interface and how they are altered by Pb intercalation. Using Tr-ARPES to directly monitor the exchange-split Ni $3d$ bands, it was found that all samples exhibit an ultrafast collapse of exchange splitting immediately after a femtosecond laser pulse, signalling a rapid demagnetisation of the Ni layer. Quantitative analysis showed that a bare Ni(111) film (for reference from literature) demagnetise with a characteristic time of ($\sim$ 170 fs, consistent with known values for Ni and governed by spin-flip scattering and super-diffusive spin transport (Page 71). Graphene-capped Ni(111) was observed to demagnetise slightly faster (around 110 fs - 120 fs on average). The presence of the graphene monolayer appears to enhance the demagnetisation rate by providing an additional channel for hot electrons to escape and carry spin angular momentum out of the Ni film. Graphene acts as an ultra-thin conductive layer that can accept spin-polarised electrons and transport them away, consistent with the notion of graphene as a spin-current sink, simultaneously it serves as a source of spin-mixed electrons floating back to the Ni. Meanwhile, the overall demagnetisation amplitude in Ni/Gr was slightly reduced (likely due to limited pump fluence in the experiment), and the magnetisation recovery time was on the order of $\sim$ 0.5 ps, similar to bare Ni. In striking contrast, the Pb-intercalated graphene/Ni(111) sample showed an even more dramatic response. The Ni exchange splitting collapsed almost entirely within tens of femtoseconds, with fitted demagnetisation time constants around 20 fs - 60 fs. At the peak of the response, the Ni spin polarisation was quenched by nearly 100% (exchange splitting collapse), indicating an almost complete ultrafast demagnetisation in this tri-layer structure. This ultrafast and extensive demagnetisation is accompanied by a markedly slower magnetisation recovery (on the order of 0.6 ps $-$ 0.9 ps) compared to the other cases, this is in agreement with the graphene transferring spin mixed electrons back to the substrate over an extended period of time. The data demonstrate that inserting a heavy metal layer (Pb) at the interface enormously accelerates the initial spin angular momentum dissipation from Ni, at the cost of prolonging the re-magnetisation phase [31].

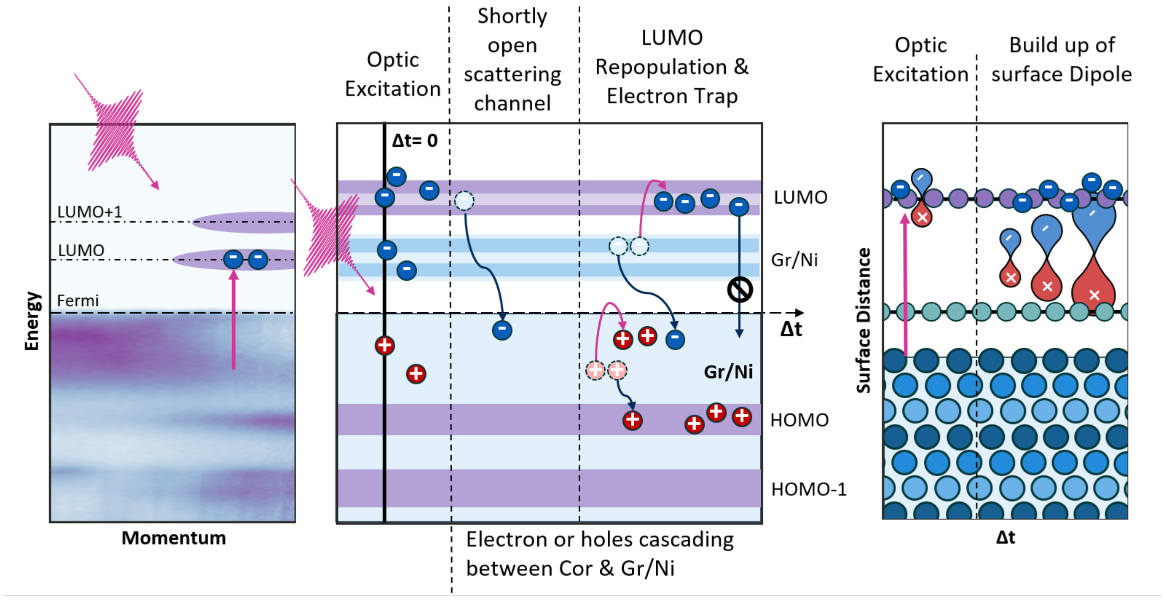

Figure (6.3) Potential electron dynamics at the coronene/graphene/nickel(111) interface.

In the third part, the dissertation investigated a graphene-mediated coupling between Ni(111) and an organic molecular layer (coronene), targeting ultrafast charge transfer across a hybrid inorganic/organic interface. Static measurements showed that coronene molecules adsorbed directly on Ni(111) undergo strong chemisorption and hybridisation, which significantly shifts their molecular orbitals. However, when a monolayer of graphene is introduced as a buffer layer between Ni(111) and coronene, the coronene becomes only weakly bound (physisorbed) and retains molecular orbital features close to those of the free molecule. In particular, the highest occupied molecular orbital (HOMO) and the lowest unoccupied molecular orbital (LUMO) of coronene could be identified in the photoemission spectra of the graphene/Ni(111)/coronene system, confirming that the graphene buffer preserves the molecular electronic structure. Time-resolved experiments were then carried out using a visible pump pulse (at two different photon energies, “red” and “blue” pump) to inject charge carrier, and an extreme-UV probe pulse to capture the ultrafast spectral changes. The Tr-ARPES results revealed a light-induced injection of charge carriers from the substrate into the coronene layer. Specifically, at time-zero at the pump excitation, an immediate transient population appeared in the unoccupied region corresponding to coronene's LUMO. Two distinct features were observed: one at an energy of $\sim 1.15\,\text{eV}$ above E_F and another at $\sim 1.35\,\text{eV}$ above E_F, both of which might be attributed to exited states of the molecular orbitals of coronene. The higher-energy feature ($\sim 1.35\,\text{eV}$) aligns with the expected LUMO resonance of coronene, while the lower feature ($\sim 1.15\,\text{eV}$) is tentatively interpreted as an excited state correlated to the LUMO. This identification of these excited states remains speculative at this point. However, the transient molecular-state populations decay on a sub-picosecond timescale, but notably more slowly than the corresponding graphene/Ni hot electron states (which thermalise within 100 fs - 200 fs). Furthermore, at longer pump-probe delays a second increase in LUMO-region intensity was detected, indicative of a secondary population mechanism occurring after the initial excitation or a continuous filling accompanied by a transient emptying, potentially through band movements of the substrate during demagnetisation, of the state between 200 fs - 700 fs. Concurrently, the graphene/Ni substrate bands exhibited an ultrafast downward shift in energy (and the local electronic Fermi level shifted transiently), consistent with photo-induced charge transfer out of the substrate and into the molecular layer followed by a surface dipole build-up, depicted in Figure 6.3. Together, these observations provide direct evidence of ultrafast charge-carrier injection from the metal/graphene into the coronene, and suggest the formation of long lived excited states and carrier redistribution on picosecond timescales.

6.2. Interpretation and implications

The results of this work highlight how tailored interfaces can endow the graphene layer with properties and dynamics far beyond those of free-standing graphene, which is normally a semi-metal with no band gap and negligible spin-orbit interaction. From a material-engineering perspective, the Pb-intercalated graphene/Ni system demonstrates a viable pathway to overcoming one of graphene's key limitations – the lack of a band gap – while simultaneously introducing strong SOC. The opening of a ($\sim 270\,\text{meV}$) band gap in graphene (comparable to room-temperature thermal energy scales) by Pb intercalation is a remarkable achievement. It is sufficiently large to hinder charge carriers from freely traversing the Dirac point at ambient conditions, thus enabling semiconductor-like behaviour in graphene. Importantly, this band gap is achieved while keeping graphene in close proximity to a ferromagnetic substrate (Ni). In the past, any attempt to decouple graphene from Ni to restore its Dirac cone inevitably meant losing the magnetic proximity effect (since graphene would no longer interact with the ferromagnet). Here, however, I have a tri-layer structure where graphene is electronically decoupled enough to recover its Dirac spectrum and is still adjacent to a ferromagnet (though separated by the Pb layer).

Spintronic implications: Graphene itself is not magnetic and exhibits only very weak intrinsic SOC, which makes it typically passive in terms of spin manipulation. By interfacing it with Pb, we impart significant SOC to the graphene π-bands, providing a platform for spin-dependent phenomena such as the spin Hall effect or other SOC-driven spin currents within the graphene layer. Although the direct exchange coupling between Ni and graphene is lost due to the intercalated Pb (meaning graphene is no longer spin-polarised by Ni's magnetisation), Ni can still serve as a spin injector – injecting spin-polarised electrons through the Pb spacer into graphene. Those spins, once in the graphene layer, can be influenced by the strong SOC from Pb. This combination of a ferromagnet, a heavy-SOC element, and graphene's Dirac fermions creates a hybrid platform (ferromagnet/Pb/-graphene) that is rich in functionality and could be harnessed in future spintronic or topological devices.
For instance, one can envision injecting a spin-polarised current from Ni into the graphene layer (through Pb) and achieving an inverse spin Hall effect or other spin–charge conversion effects within graphene/Pb, which Ni could detect.

In essence, the interface-engineered graphene in this system behaves as a semiconducting Dirac material with enhanced SOC, bridging the gap between two traditionally disjoint requirements for spintronics: high carrier mobility and a manipulable band gap with spin-splitting.

The ultrafast magnetisation dynamics results reinforce and expand the understanding of how interfaces can control spin flow in metallic heterostructures. The observed trend – demagnetisation on Ni(111) being progressively faster for Ni/Gr and fastest for Ni/Pb/Gr – is fully consistent with the mechanism of super-diffusive spin transport and efficient spin sinks at interfaces. Graphene, despite being only one atom thick, provided an additional channel for excited spin-polarised electrons to leave the Ni film, thereby accelerating demagnetisation compared to bare Ni. This is in agreement with recent reports that capping ferromagnet's with graphene can enhance spin loss, for example, experiments by Mondal *et al.* found faster demagnetisation in graphene-covered ferrimagnetic layers than in uncapped ones [99]. In this case, graphene likely allowed spin-polarised hot electrons to delocalise and flow into the graphene plane (across the sample surface), supplementing the usual Elliott–Yafet spin-flip scattering in Ni with an additional non-local spin dissipation channel.

The Ni/Pb/Gr tri-layer took this a step further: The intercalated Pb layer, being a heavy metal with strong SOC and no magnetic moment, acted as a highly efficient sink for spin angular momentum. Immediately after laser excitation, a significant fraction of Ni's majority-spin electrons was emitted into the adjacent Pb layer, where strong spin-orbit scattering rapidly randomise their spins. This led to an almost instantaneous collapse of Ni's exchange splitting. My experimental finding of tens of fs demagnetisation in Ni/Pb/Gr is in line with theoretical predictions by Battiato et al. that adding a heavy-metal contact to a ferromagnet can dramatically speed up demagnetisation by channelling spin carriers out of the ferromagnet [30]. Moreover, the magnitude of demagnetisation we observed (complete quenching of Ni's moment at peak) highlights the potency of using atomic-scale interface engineering to control magnetic switching.

Implications for magnetic switching technologies: Achieving demagnetisation in tens of femtoseconds points to the possibility of terahertz-rate magnetic switching in devices, far exceeding the speed of conventional spintronic writing schemes. However, the concomitant slow recovery in Ni/Pb/Gr (several times slower than in Ni/Gr) indicates that the system remains in a perturbed, spin-depleted state for a longer duration, likely because the spin and energy that flowed into the Pb layer do not quickly return to Ni.

This suggests a trade-off: while a heavy-metal spacer can induce an ultrafast quench of magnetisation, it can also delay the re-magnetisation, potentially limiting the repetition rate of switching. The slow return of magnetisation in the Pb-intercalated case was attributed to the Pb layer trapping spin angular momentum (and excess energy), which must either diffuse out or dissipate to the lattice before Ni can regain its magnetisation.

These insights are crucial for designing multi-layer magnetic heterostructures: by selecting appropriate capping or spacer layers (heavy metals, ferromagnets, or insulators), one can tune the speed and completeness of demagnetisation to suit a given application. My work specifically demonstrates that the inclusion of a heavy metal like Pb at a graphene/ferromagnet interface can serve as an efficient spin dump, thus opening a route to engineering ultrafast magnetic switches.

In a broader context, it showcases the efficacy of time-resolved ARPES as a tool for probing spin dynamics in the band structure perspective, complementing more element-specific techniques like XMCD.

The findings from the graphene/organic (coronene) interface study carry implications for optoelectronics and the development of hybrid materials that integrate organic functionalities with 2D materials. I showed that graphene can function as an effective buffer layer that decouples organic molecules from a reactive metal substrate while still electronically connecting them. This is significant because it enables the organic layer to retain its intrinsic electronic properties (e.g. band gaped molecular orbitals) in proximity to a metal, which is often desired in organic electronics but usually hard to achieve due to molecule–substrate interactions.

In my coronene/graphene/Ni(111) system, the coronene's HOMO–LUMO structure remained intact and the LUMO-area accessible to photoexcitation. Tr-ARPES directly captured ultrafast charge transfer from the metallic substrate into the coronene molecules, a process relevant to how photo-induced charge separation might occur in, say, graphene-organic photodetectors or solar cells. One noteworthy implication is the observation of long lived phase-trapped excited electron states at $\sim 1.15\,\mathrm{eV}$ to $\sim 1.35\,\mathrm{eV}$ in the coronene layer. Excited electron states in proximity to a metal are typically short lived (in comparison to what was observed in this thesis) because the metallic continuum often offers a great amount of scattering partners. We detect a signature consistent with a phase-trapped excited state suggests that the single-layer graphene buffer provides just enough separation and screening such that the coronene can support a transient excitation even when it is close to a metal. This points to the tantalise possibility of using graphene (or other 2D materials) as interlayers to protect and sustain electronic excitations at interfaces, allowing these effects to be utilised in devices (for example, to funnel energy across an interface) while still benefiting from a nearby electrode or spin reservoir.

Additionally, the delayed secondary population in the coronene LUMO at picosecond times hints at complex carrier relaxation pathways or interfacial states in the system. It might indicate a two-step charge transfer: an initial ultrafast injection into the molecule followed by a slower re-filling or trapping of carriers (possibly involving mid-gap states). While further analysis is needed, this behaviour underscores that interfacial charge dynamics can involve multiple timescales and intermediate states. From a technological standpoint, controlling such dynamics could allow one to tune whether an interface primarily performs ultrafast charge injection or instead harbors longer-lived excitations for energy storage.

Overall, the coronene results emphasise the value of graphene as a molecular electrode: it electrically connects to a metal substrate and an organic overlayer, enabling the ultrafast transfer of carriers between the two, all while preserving the molecular identity of the organic layer. This could inform the design of future graphene-based hybrid structures in organic photovoltaics, light-emitting devices, or molecular spintronics, where one needs efficient charge or spin transport across dissimilar materials.

In summary, through the targeted use of interface modifications – heavy metal intercalation and the insertion of a graphene buffer layer – this work has demonstrated control over both electronic and spin dynamics in graphene heterostructures on ultrafast timescales. The ability to open a large band gap in graphene and modulate it transiently, to drastically speed up or tune magnetic switching via interface-induced spin flows, and to inject charge carriers into molecular orbitals while even accessing long lived excited states, all stem from the deliberate engineering of interfaces.

These findings validate the paradigm that “the interface is still the device” in modern materials science, especially for 2D materials: By designing the atomic-scale meeting point between materials, one can realise new functional regimes (e.g. a gapped but high-mobility Dirac fermion system, or a metal-organic junction with ultrafast charge transfer) that are not present in the constituents alone.

6.3. Outlook and future work

The three studies presented here, optical band-structure control (Chapter 3), ultrafast spin dynamics (Chapter 4), and molecular charge injection (Chapter 5), establish a framework for both fundamental understanding and device implementation of graphene-based heterostructures. Nevertheless, several avenues remain to consolidate these findings into a coherent picture.

Spin-resolved and element-resolved dynamics

First, to unambiguously resolve how spin and charge traverse each layer, it will be critical to perform spin-resolved, time-resolved photoemission and complementary magnetic probes on the graphene/Ni(111) and Pb/graphene/Ni(111) interfaces. In particular, combining a spin-filtered ARPES detector — ideally in a time-of-flight momentum-microscope geometry — with complementary time-resolved X-ray magnetic circular dichroism (XMCD) experiments will allow the detailed element sensitive tracing of the sub-100 fs demagnetisation observed in chapter 4. These would directly track the spin polarisation of graphene’s bands, lead and the Ni $3d$ magnetisation separately during the demagnetisation process. Repeating these measurements under rigorously identical pump fluence, spot size and pulse duration for both NiGr and NiPbGr will eliminate laser-parameter artefacts and reveal the true impact of Pb intercalation. Furthermore, acquiring multiple repeats of each trace will yield statistically robust values of the demagnetisation time, and magnetisation drop and remagnetisation, confirming the flow of spin-polarised electrons within the interface, and potentially quantify any transient spin accumulation. Such measurements, coupled with varying pump fluence (to ensure Ni is fully demagnetise), would further elucidate the role of graphene as a spin conduit and Pb as a spin sink.

Furthermore, the findings of surface dependent OISTR-effect in Gd and its possible implications for the graphene/nickel interface are intriguing. As a light driven effect OISTR is a coherent phenomenon, and thereby its signature, visible in the band structure of certain magnetic materials (as demonstrated by [83]), might be explored by a phase-stabilised (and potentially spin-resolved) Tr-ARPES measurements.

Interface variations for graphene Band Engineering

The Pb intercalation successfully opened a band gap while sacrificing direct magnetic coupling. To achieve both a band gap and magnetic proximity in graphene, future studies could explore alternative intercalation or substrate strategies. One idea is to use an ultrathin magnetic insulator (such as EuO or YIG) between graphene and Ni, which might induce a graphene band gap (via symmetry breaking) and introduce exchange splitting in graphene's bands. Recent work by Sheverdyaeva *et al.* suggests EuO on graphene can impart magnetism [26], and combining this with heavy elements could be promising. Additionally, intercalating 3*d* transition metals that alloy with Ni (e.g. Fe or Co) or noble metals (e.g. Au, which was shown to enhance Ni demagnetisation) could be tested to see if they produce an "all-in-one" effect on graphene.
Another pathway is to use different substrates like Pt(111) instead of Ni(111). Graphene/Pb/Pt was previously shown to have a ~0.2 eV gap if one could intercalate a ferromagnet (Co or Ni) beneath graphene on Pt, it might retain the SOC-induced gap from Pt/Pb while reintroducing magnetic coupling. While my own attempts in recreating the findings on Graphene/Pb/Pt in [23], were unsuccessfully (intercalation was not achieved, potentially due to experimental constrains regarding annealing temperature), the lead introduced a band gap even when not intercalated but placed on top of the graphene, depicted in Figure 6.4. The graphene layer grew in multiple rotational domains causing a doubling of the Dirac cone in momentum space. After introduction of a lead layer, which could not be intercalated and remained on top of the graphene, an electron donation from the lead to the graphene is visible (the Dirac cone is moved below E_F) as well as a band gap opening. With the same system revealing a short lift surface state in time-resolved photoelectron emission microscopy (PEEM) measurements using a 2PPE excitation scheme, depicted in Figure 6.5. Exploring a multi-layer stacking (e.g. Gr/Pb/Co/Pt) would help discover whether graphene can simultaneously host robust spin-orbit and exchange effects, and are therefore worth the effort.

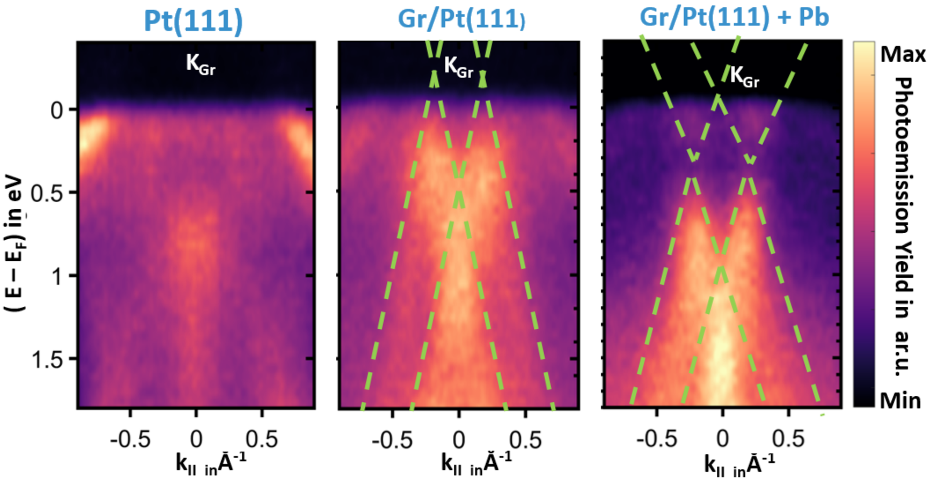

Figure (6.4) nanoscale electron spectroscopy for chemical analysis measurements of, from the left, platinum, graphene/platinum(111) and lead/graphene/platinum interface.

Along similar lines, studying the effects of lattice mismatch and strain at the interface is worthwhile: Varying the graphene-substrate alignment, the intercalants coverage, or using substrates with different lattice constants could tune the degree of sublattice symmetry breaking and hence the size of the induced gap. First-principles calculations (DFT, including SOC and potentially magnetism) could systematically screen combinations of intercalants and substrates to guide experiments.

Advanced Ultrafast Spectroscopy

On the experimental front, using an upgrading the Tr-ARPES setup to higher photon energies, or using high photon energies in combination with a **Spin-Filtered Time-of-Flight Momentum**

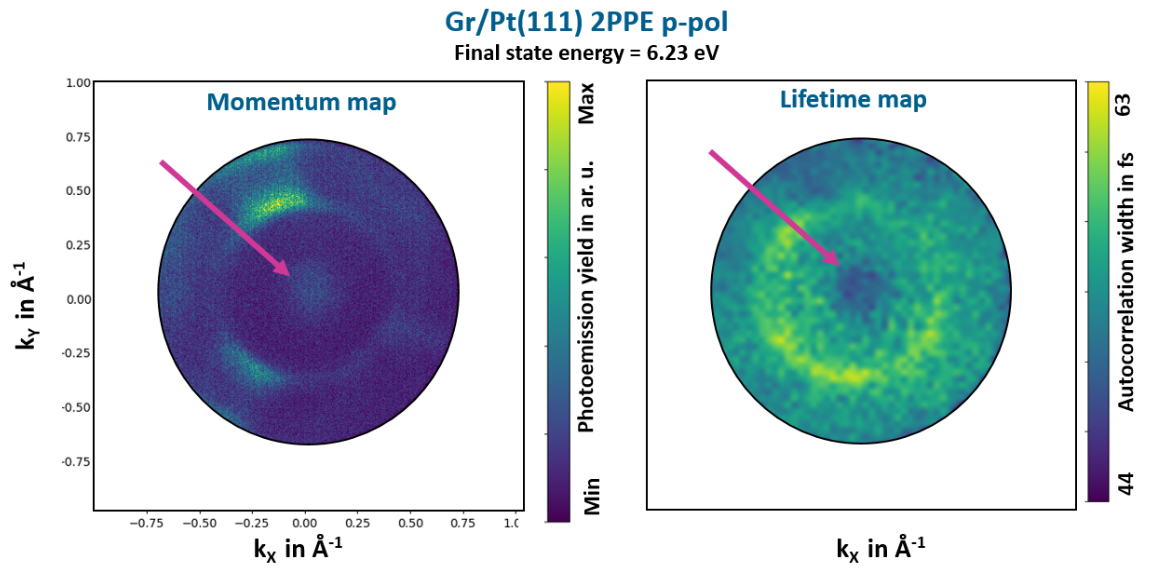

Figure (6.5) PEEM measurements of lead/graphene/platinum interface using a 2PPE excitation scheme were $E_{ph,pump} = E_{ph,probe} = 3.1\,\mathrm{eV}$, with the photoemission yield on the left and the corresponding lifetime map, extracted from the pixel-vise-autocorrelation width on the right. Pink arrows indicate a short lived surface state.

Microscope would greatly benefit these studies. For the graphene/Pb/Ni system, using probe photons in the 40–60 eV range (e.g. from a high-harmonic source or FEL) would enhance the photoemission cross-section of Pb 5d states and allow direct observation of any Rashba-split Pb bands or hybrid states, thereby clarifying the band structure evolution during pumping. A momentum microscope (imaging spin-resolved photoelectron microscope) could capture the full 2D Brillouin zone in a single shot, which is especially useful for the graphene/coronene system where molecular orbital features are spread over momentum. In my work, I employed a rotational scanning ("semi-static") method to map the coronene orbitals. A painstakingly slow method to capture just one time-delay. In combination with an unstable HHG-lightsource, obtaining the "complete" picture is near to impossible. A momentum-microscope would circumvent this and could even track momentum-space dynamics of the transient excited states. Moreover, increasing the available pump wavelengths and fluences (e.g. through using an OPA) could help selectively excite different transitions (such as direct excitations into the graphene Dirac cone or coronenes excited states vs. substrate d-bands) and improve signal-to-noise in the unoccupied region. This would shed light on whether the secondary LUMO population we observed in coronene is due to a specific optical excitation or a general thermalisation effect.

Theoretical modelling of ultrafast processes

To deepen the interpretation of the experimental findings, time-dependent density functional theory (TD-DFT) and spin-transport calculations should be pursued. For the graphene/Pb/Ni system, TD-DFT can be used to simulate an optically excited state and see if a transient band gap change or charge transfer to Pb is expected, helping to confirm the mechanism behind the observed band shifts. For the graphene/coronene interface, many-body calculations could evaluate the lifetime of the excited states. This is a subtle problem since one must include screening from the metal and graphene; advanced approaches might be necessary to capture their formation and annihilation. Other approaches, on the other hand, could model how electrons and spins flow between Ni, graphene, and Pb or coronene under a bias or excitation, thus linking our ultrafast optical experiments to possible device operations (e.g. spin valves or photodiodes). By comparing such theoretical results with our experimental data (for example, matching the timescales of energy shifts or population decays), one can achieve a more rigorous understanding of the microscopic interactions at play.

Expanding to other molecular and 2D systems

Finally, the concept of graphene-mediated ultrafast charge transfer can be extended to other molecular systems and 2D material heterostructures. Future work could replace coronene with molecules that have specific functionalities – for instance, acceptor molecules with high electron affinity to study electron vs. hole transfer, or magnetic molecules to explore spin-dependent transfer. Similarly, incorporating a ferromagnetic layer in the molecular stack (e.g. a magnetic metal-organic framework or a 2D magnet under graphene) could open the door to ultrafast spin injection into molecular orbitals. The successful decoupling of coronene by graphene suggests that other fragile 2D materials (like transition metal dichalcogenide (TMDC) monolayers) could also be protected by graphene on Ni and studied with Tr-ARPES for interfacial charge or energy transfer dynamics.
Such studies would contribute to a broader paradigm of interface-tailored ultrafast phenomena: using 2D material buffers, heavy atom interlayers, and tailored stacking sequences to achieve desired electronic or magnetic responses at extreme time scales.

In conclusion, this dissertation has demonstrated the rich physics that emerges at graphene/ferromagnet and graphene/metal–organic interfaces and provided proof-of-concept that one can modulate graphene's ultrafast carrier dynamics through interface engineering. The findings encourage a deeper exploration of novel interface combinations and advanced spectroscopy. By continuing along these lines – integrating theory and experiment, and exploring new material pairings – we move closer to realise high-speed, interface-defined functionalities for next-generation electronic and spintronic devices.

Appendices

A. Additional Information and Figures

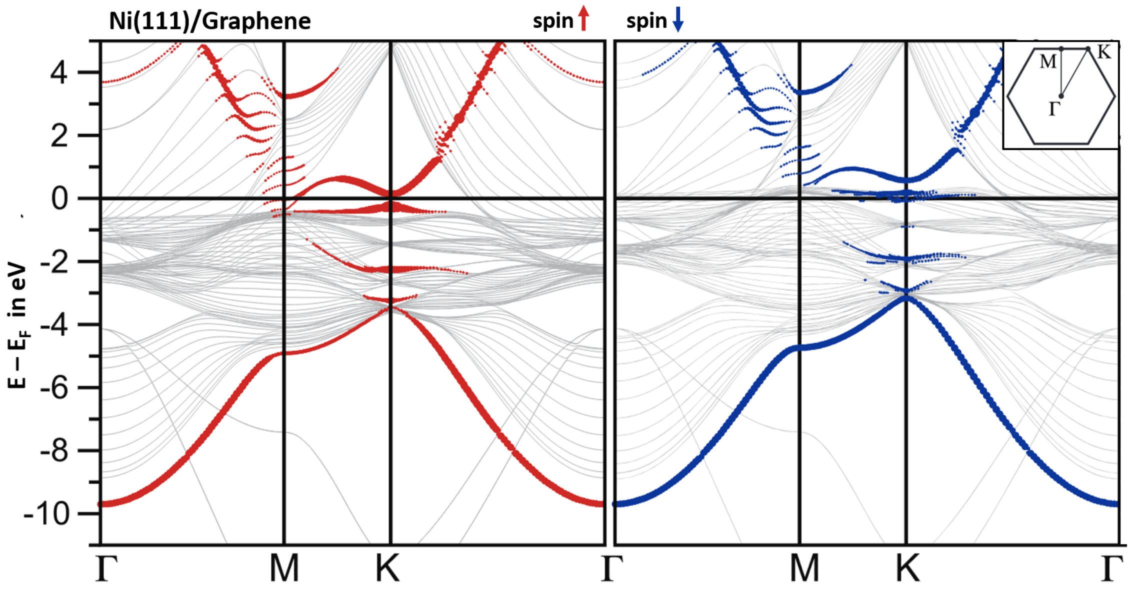

Figure (A.1) Adapted spin-resolved electronic band structure calculation of graphene/Ni(111). Adapted from [117].

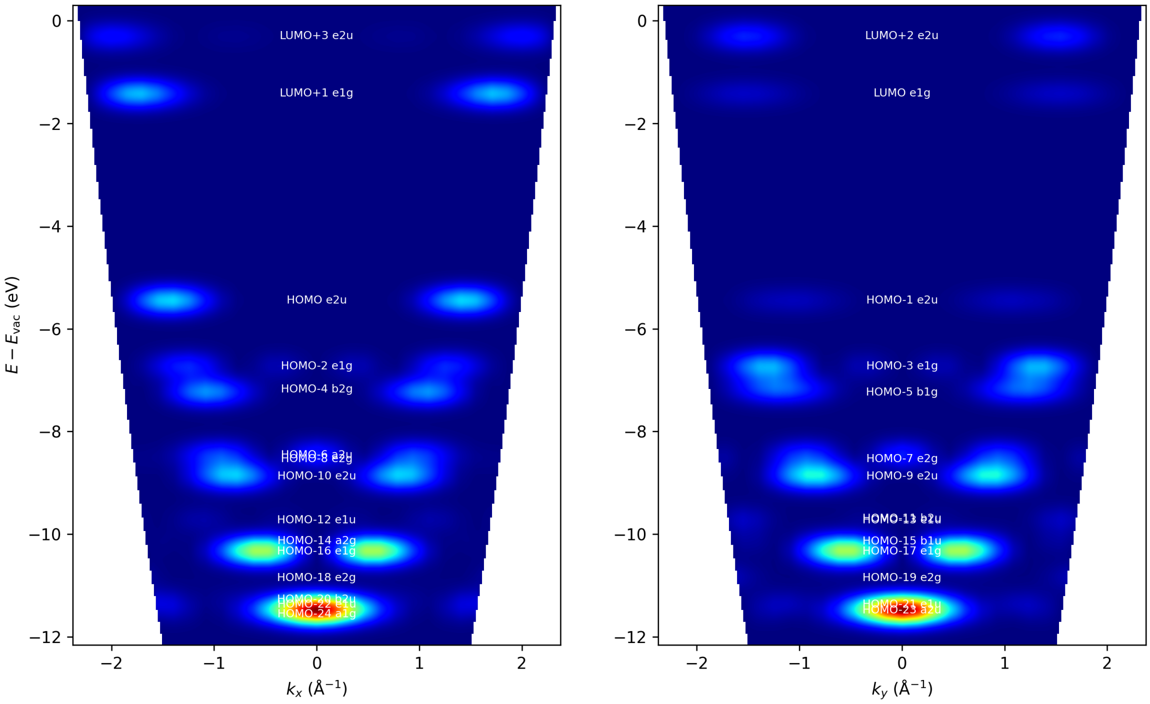

Figure (A.2) Theoretical calculations of the coronene molecules in gas phase. Calculated by P. Puschnig et al. university of Graz.

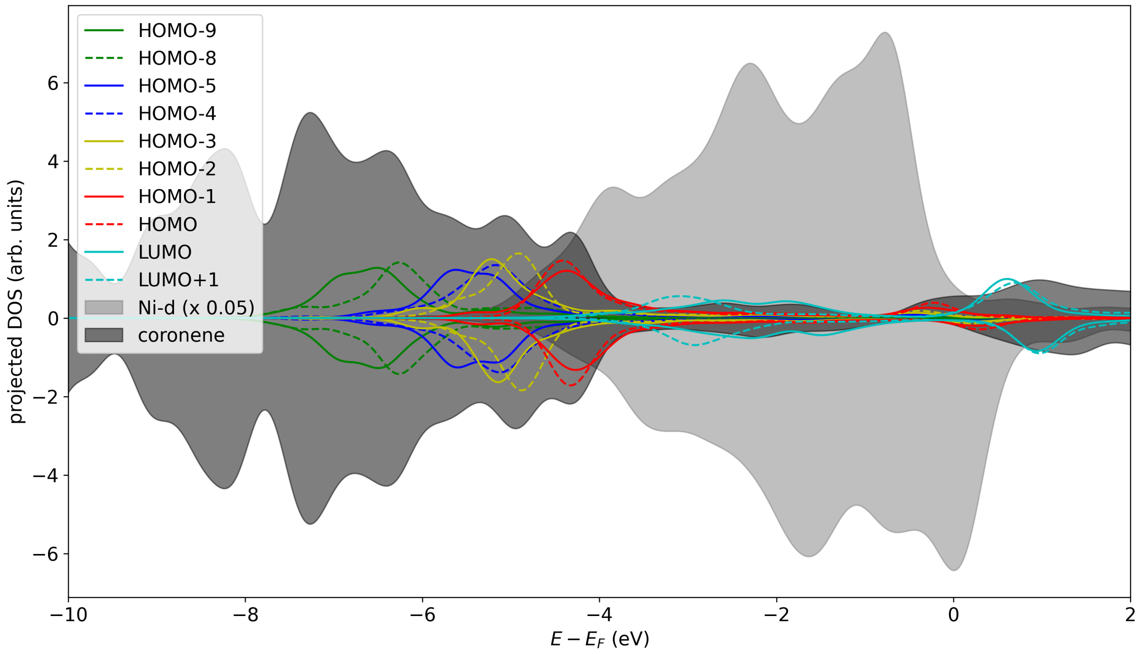

Figure (A.3) spin resolved theoretical calculations of the coronene/Ni(111) system.

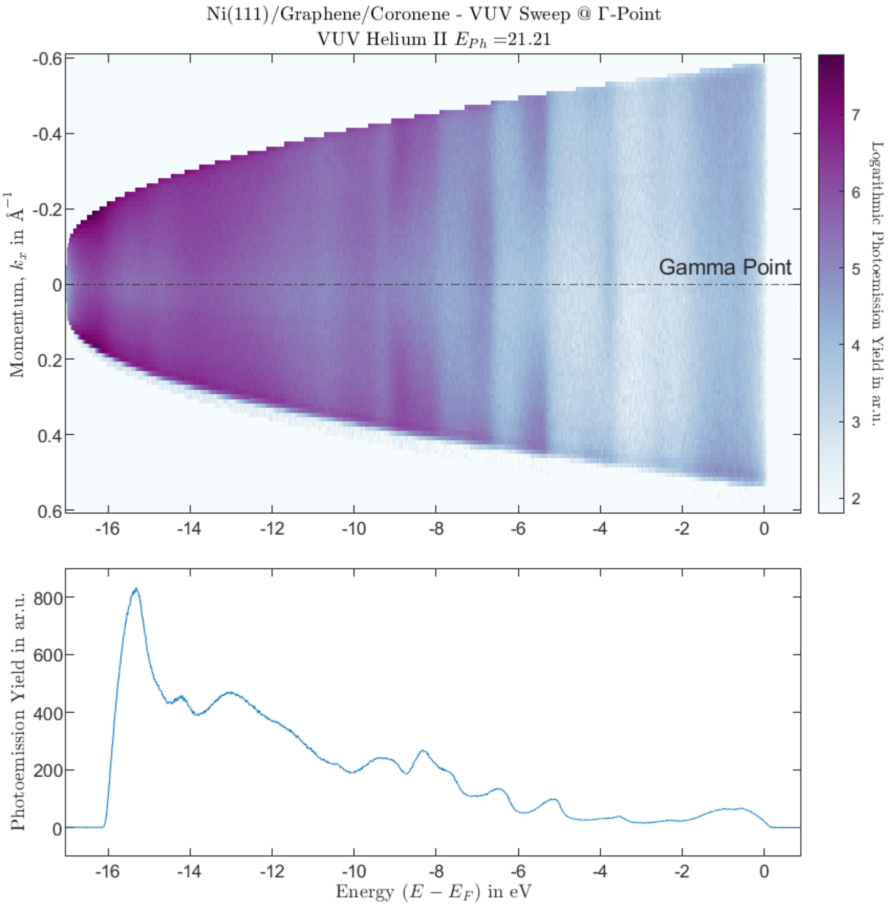

Figure (A.4) Coronene on Graphene on Ni(111), static ARPES VUV(21.21 ev) sweep around Γ-Point.

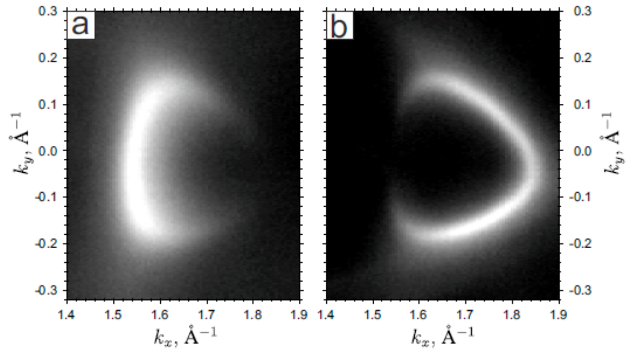

Figure (A.5) constant energy maps from the graphene Dirac cone extracted from ARPES measuring illustrating the "dark corridor". The sample in this image is graphene on Iridium(111) intercalated by Gadolinium. (a) shows the CEM2 1eV below the Dirac point in the π-band and (b) the CEM2 1eV above the Dirac point, hence the π^*-band. Taken from [59]

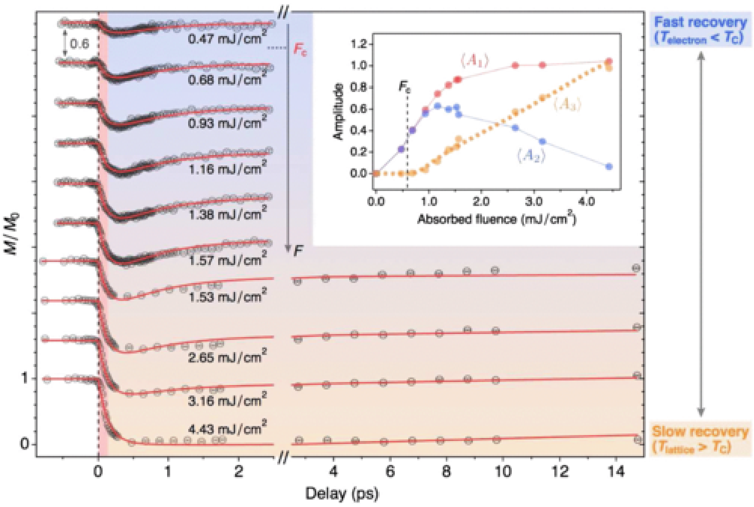

Figure (A.6) Magnetisation dynamics in Ni measured using TR TMOKE over range of laser fluences. For the highest fluence the magnetisation id fully suppressed. The data are offset for clarity. Fits to the microscopic model that considers the critical behaviour and depth-average effects in the Tr-TMOKE measurements are shown in red. The inset presents extracted fluence-dependent amplitudes of the demagnetisation and recovery processes. Reprinted from [44].

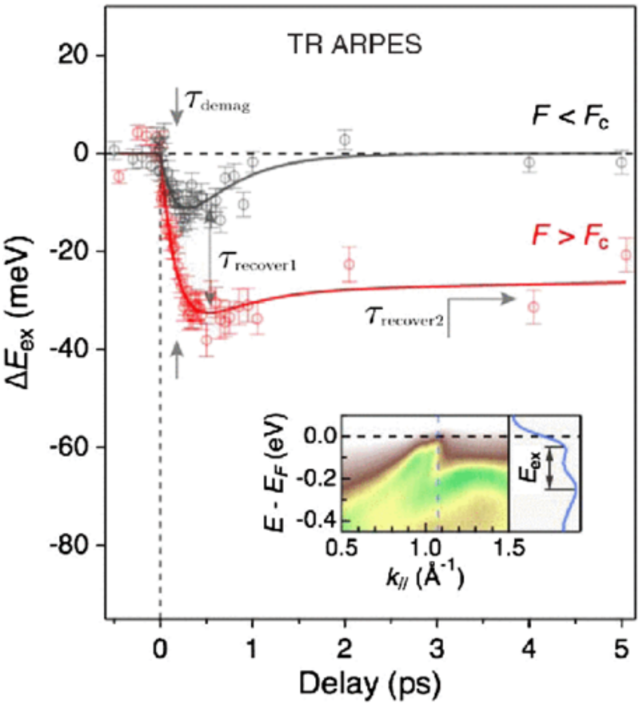

Figure (A.7) Illustration of the exchange splitting ΔE_{ex} collapse of Ni(111) after optical excitation, measured measured using extreme ultraviolet angle-resolved photoemission spectroscopy. The data were taken on pristine Ni(111) at the transverse momentum $k_{||} \sim 1.05\text{angstrom}^{-1}$ along the $\overline{\Gamma}$ $-\overline{K}$ direction. Two measurements were shown for different absorbed laser fluence: below $0.21\frac{\text{mJ}}{\text{cm}^2}$ (grey) and above $1.7\frac{\text{mJ}}{\text{cm}^2}$ (red). The solid lines are the fit, and F_c the so called critical fluence. Inset: Static ARPES spectrum plot along the $\overline{\Gamma}$ $-\overline{K}$ direction recorded using a VUV light source. Reprinted from [44]

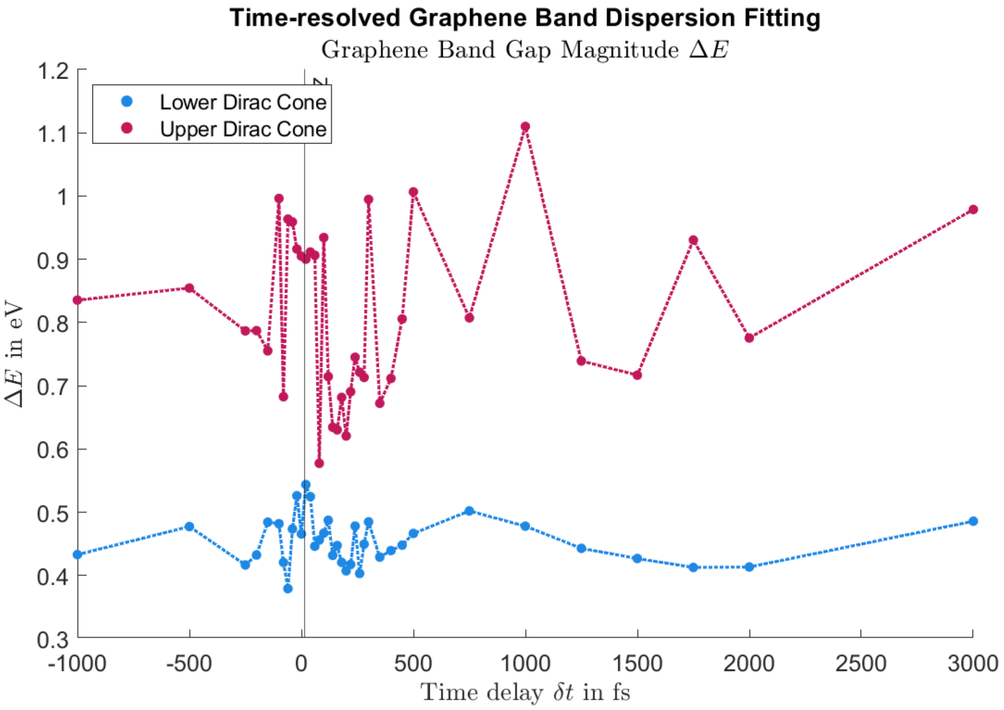

Figure (A.8) Time-resolved graphene π^*-band gab magnitude evolution after optical excitation for free Fermi velocity Fit, showing the results for the upper (green) and lower (blue) Dirac Cone Fit.

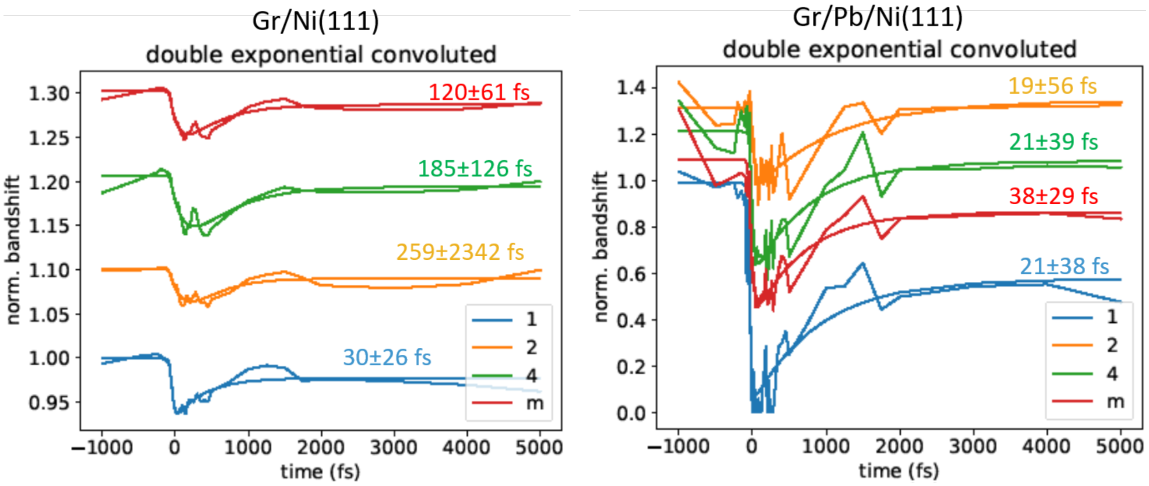

Figure (A.9) Demagnetisation curve fitting results for graphene/Ni(111) and graphene/Pb/Ni(111) . The results for the demagnetisation fit using a convolution between a Gaussian-peak and the double exponential function are shown. Depicted are the extracted exchange splitting curves and the fit-function for both material systems. On each graph the retrieved demagnetisation time is noted. This fit was executed by Paul Herrgen to check if accommodating the pump laser peak width of 55fs changes the results.

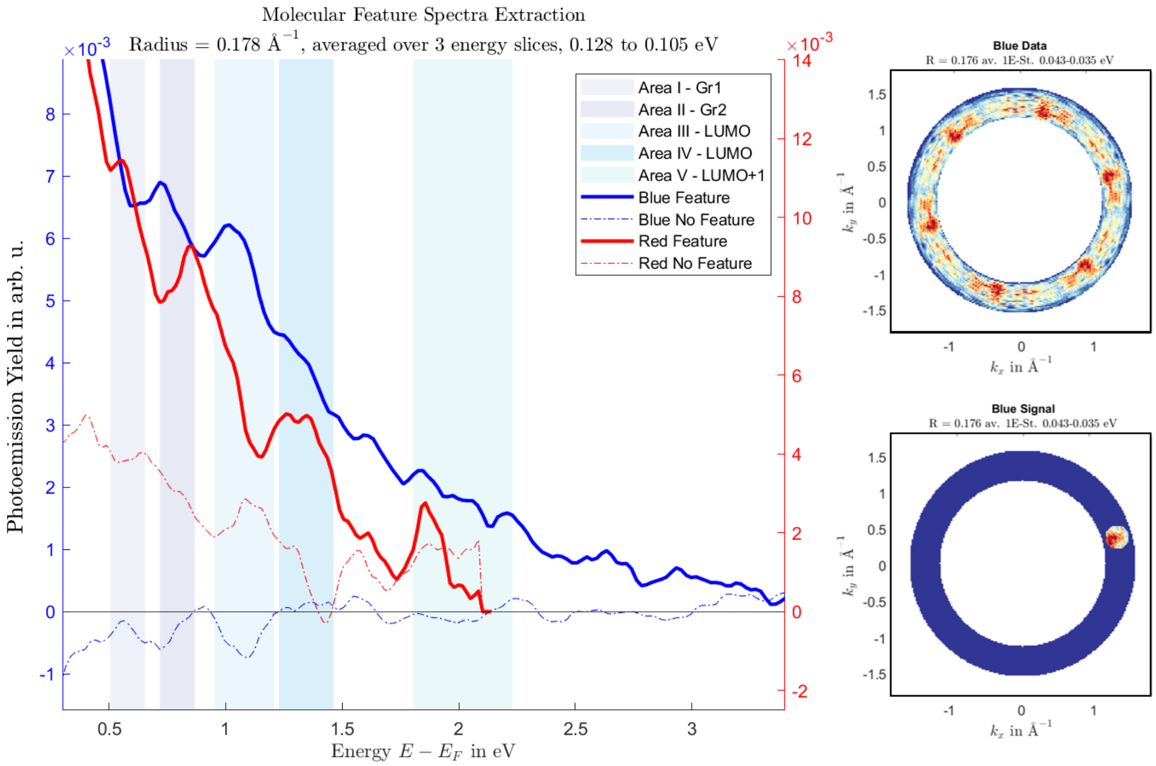

Figure (A.10) Extracted spectra from semi-static ARPES measurements at t_0. Spectra extracted from areas exhibiting prominent molecular features, as well as from regions with no expected molecular signal, are shown for both blue- and red-pumped measurements. The extraction mask had a radius of $0.178\,\text{Å}^{-1}$ and was centred at ($k_x = 1.365\,\text{Å}^{-1}$, $k_y = 0.389\,\text{Å}^{-1}$) and ($k_x = 1.406\,\text{Å}^{-1}$, $k_y = -0.392\,\text{Å}^{-1}$) respectively. Coronene-excited state areas are marked in blue-grey.

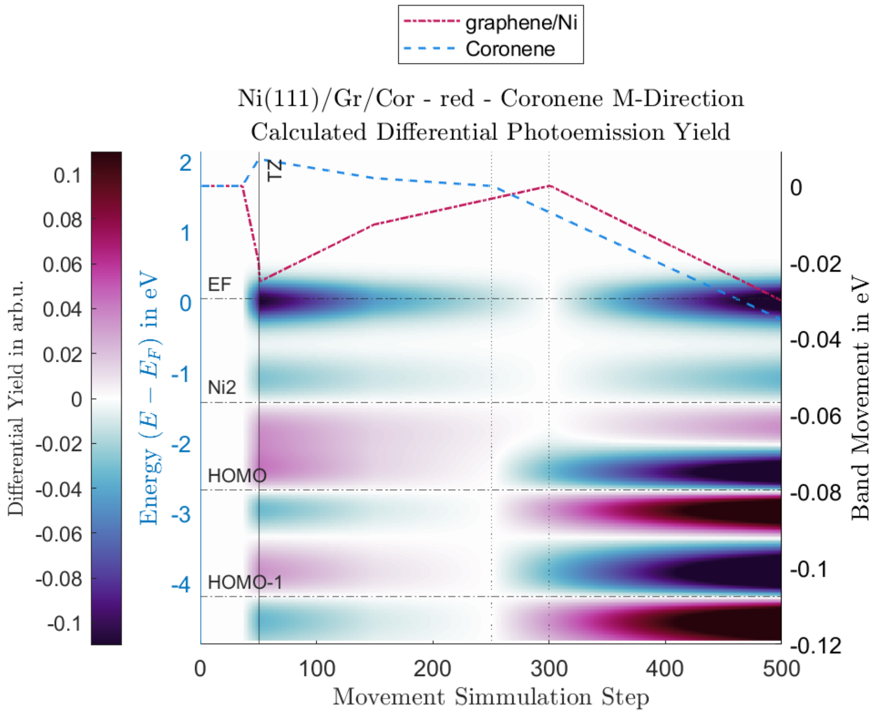

Figure (A.11) Calculated differential photoemission yield for artificial created band movements of the coronene/graphene/Ni(111) system in the HOMO-1-(M)-Direction. Parallel movement of the substrate and the molecular features (left) as well as calculations for an independent movement (right) are presented.

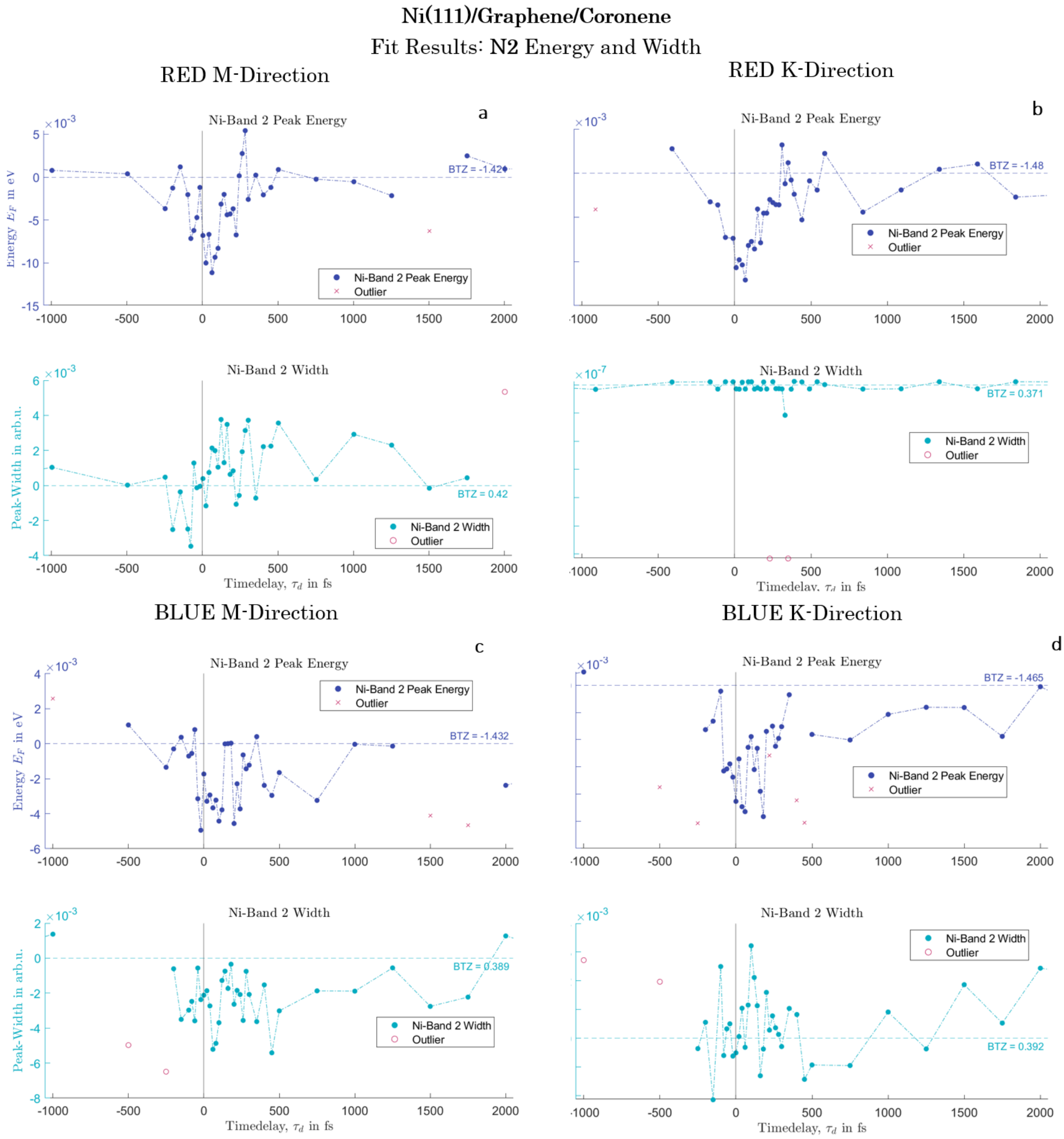

Figure (A.12) Time-resolved spectral fit results for the the nickel 2 Band Peak Energies $E_{Ni,1}$ (top) and widths $\sigma_{Ni,1}$ (bottom) for red- and blue-pumped measurements. The data are normalise to the average of the first five time steps prior to t_0 (dashed lines), and t_0 is indicated by a black vertical line. The results show a clear transient decrease in $E_{Ni,1}$ that nearly coincides with an identical decrease of E_F after laser excitation. Similarly, the respective band widths $\sigma_{Ni,n}$ appear not to exhibit a clear time dependent behaviour.

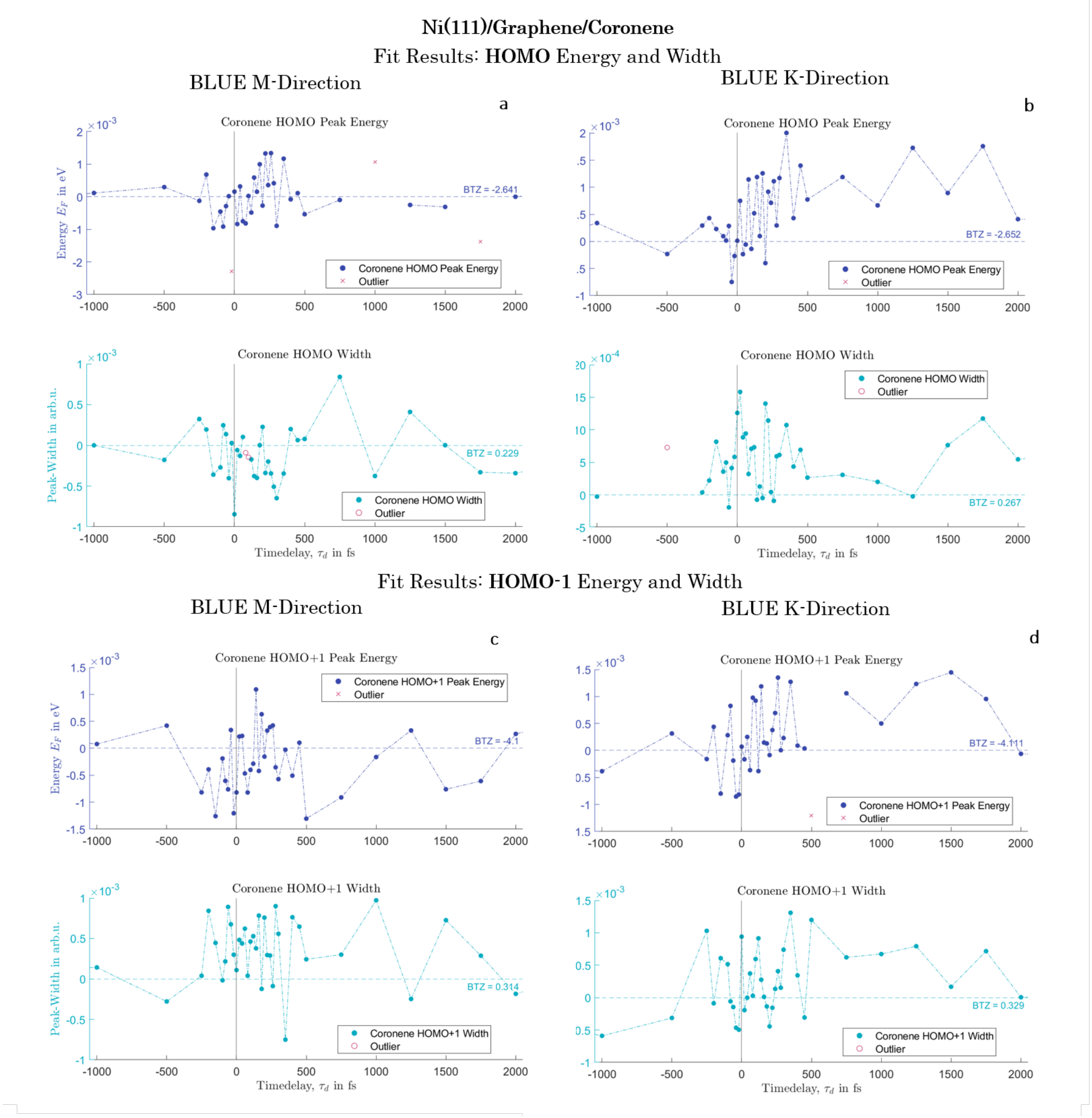

Figure (A.13) All panels depicted the Tr-Spectral Fit results for the HOMO-Peak-Energies $E_{HOMO,HOMO-1}$ and the HOMO-Band-Widths $\sigma_{HOMO,HOMO-1}$ on the bottom for the **BLUE**-pumped data. The results were normalise to their respective average from the first five time-steps far before t_0. As a guide to the eye this average is shown as a dashed line for each value and t_0 is marked with a black line. In comparison to the red-pumped data (Figure 5.23) The results show no clear increase or decrease for the HOMO-Band-Widths $\sigma_{HOMO,HOMO-1}$, but potentially an increase for its energies after the laser excitation along the K-Direction.

B. Resources Overview

The following resources were utilised in the preparation of this dissertation:

B.1. Software and Software Tools

TeXstudio The Software was used to compile the Text. The implemented Spelling correction was used while writing the text.

MATLAB The Software *MATLAB* from the company MathWorks was used for data evaluation as well as figure generation.

DeepL The tools DeepL Write, Linguee and DeepL Translator were used for stylistic text improvement.

ChatCPT The software ChatCPT from openAI was used to improve self written text stylistically and to generate small extemporary code snippets for MATLAB to speed up the coding process. Additionally it was employed to generate some of the glossary entries. Furthermore, the o3-mini and o3-mini-high model was used to find logical inconsistencies within the text or MATLAB code.

Consensus & ScholarAI For literature research the AI powered tool “Consensus” and *ScholarAI* were employed.

Citavi The Software *Citavi, Verison 6* was used to create a literature library and the bibTEX file for this thesis.

SPECS Prodogy The Software SPECS Prodogy was used to collect ARPES measurement data

Engauge Digitaizer The tool Engauge Digitaizer was used to extract measurement data from paper for comparison.

yEd A graphic tool to generate float charts, used in the Method chapter

EVA SOPHIA WALTHER

PHYSIKERIN

BERUFSERFAHRUNG

04/2024 – 01/2025 PERSONAL- UND SACHMITTELPLANUNG
RPTU Kaiserslautern-Landau, Kaiserslautern, Deutschland
Budgetplanung der Forschungsgruppe Aeschlimann

04/2024 – 05/2025 FORSCHUNGSDATEN-MANAGEMENT
RPTU Kaiserslautern-Landau, Kaiserslautern, Deutschland
Sonderforschungsbereich Spin+X: Koordinierung und Vereinheitlichung von Forschungsdaten und deren Speicherung

10/2018 – 05/2025 FORSCHERIN
RPTU Kaiserslautern-Landau, Kaiserslautern, Deutschland
Forschungsgruppe: *Ultrafast Phenomena at Surfaces* von Prof. Dr. Martin Aeschlimann

07/2022 – 09/2022 FORSCHUNGSAUFENTHALT
Okinawa Institute of Science and Technology Graduate University (OIST), Okinawa, Japan
Forschungsgruppe: *Femtosecond Spectroscopy Unit* von Prof. Dr. Keshav Dani

06/2015 – 11/2015 INDUSTRIEPRAKTIKUM
Kapteyn-Murnane-Laboratories Inc., Boulder, CO, USA
Optimierung und Charakterisierung einer kohärenten EUV-Strahlungsquelle

AKADEMISCHER WERDEGANG

10/2018 – 05/2025 PROMOTION in Physik, Dr. rer. nat.
RPTU Kaiserslautern-Landau, Kaiserslautern
Titel: *„Interface-Driven Modulation of Ultrafast Charge-Carrier Dynamics in Graphene/Ferromagnetic Metal-Organic Heterostructures“*.

10/2010 – 02/2018 DIPLOM in Physik
TU Kaiserslautern, Nebenfach: Medizinische Physik
Diplomarbeitstitel: *„Auf dem Weg zum Spin- und Zeit-aufgelösten Photoemissionsimpulsraummikroskop mit Flugzeitspektrometer“*

ZERTIFIKATE

Laserschutzbeauftragte (LSB) nach OStrV§5, 08/2023
Aussteller: Prof. Dr. Neu-Ruffing

Beauftragte zur Einhaltung der Regulierungsvorschriften von Medizinprodukten nach §15 MDR/IVDR, 04/2025 Aussteller: Prof. Dr. Schotten

Lean Six Sigma Yellow Belt, 11/2019
Aussteller: Prof. Dr. Peuckert

SPRACHEN

Deutsch: Muttersprache
Englisch: Verhandlungssicher

EVA SOPHIA WALTHER

PHYSIKERIN

VERÖFFENTLICHUNGEN

2025 **Dissertationsschrift:** *„Interface-Driven Modulation of Ultrafast Charge-Carrier Dynamics in Graphene/Ferromagnetic Metal-Organic Heterostructures”*

2025 **Paper:** *„Optically induced modulation of the graphene band-gap magnitude and high-speed demagnetisation trhough graphene/lead interfacing“* – in Vorbereitung

2020 **Paper:** *“Modification of the charge and magnetic order of a low dimensional ferromagnet by molecule-surface bonding”*
J Seidel, ES Walther, S Mousavion, et al. arXiv:2002.04296

2019 **Paper**: *“Exchange Splitting of a Hybrid Surface State and Ferromagnetic Order in a 2D Surface Alloy”*
J Seidel, PM Buhl, S Mousavion, B Dupé, ES Walther, et al. arXiv:1906.03780

WISSENSCHAFTLICHE BEITRÄGE

2023 **DPG Frühjahrestagung, Dresden:**
Poster: *Band structure and charge carrier dynamics of a Pb-intercalated graphene sheet on Ni(111*

2021 **Summer School: JSSP, Apholda**
Talk: “*Spin- and time-resolved momentum microscopy: A powerfull tool for imaging optically excited carrier dynamics*

2019 **DPG Frühjahrestagung, Regensburg:**
Poster: *“Structure formation and electron dynamics of Pb intercalated graphene/metal interfaces”*

2019 **Summer School: Frontiers in Time-Resolved Science, Bad Honnef**
Poster: *“Momentum dependent quasiparticle lifetime in metals investigated by time-resolved momentum microscopy”*

2018 **DPG Frühjahrestagung, Berlin:**
Poster: *“Time-resolved time-of-flight momentum microscopy at femtosecond lab sources”*

FINANZANTRÄGE

2021 - SEED-FUND PROPOSAL
“Excitons in Low Dimensional Magnetic Metal-Organic Heterostructures”

2022 - PHD-Symposium
Frühjahrestagung der Deutschen Physikalischen Gesellschaft
“The Hitchhiker’s Guide to Spin Phenomena at the Space and Time Limit”

AKADEMISCHE ÄMTER

Steering Committee des transregionalen Sonderforschungsbereiches **Spin+X** – 2 Jahre bis 2022

Fachbereichsrat Physik – 4 Jahre bis 2021

List of Special Terms and Definitions

ARPES angle-resolved photoemission spectroscopy 11, 87–89

angle-resolved photoemission spectroscopy Angle-resolved photoemission spectroscopy (ARPES) is a technique that measures the energy and momentum of electrons ejected from a material's surface when illuminated by ultraviolet or X-ray photons. By analysing these photoemitted electrons, ARPES reveals information about the electronic structure, including energy bands and Fermi surface, of the material. This makes it especially useful in understanding the properties of materials such as 2D materials, where electronic behaviour at the surface is crucial. The used electron detector in the utilise ARPES setup is a PHOIBOS 150 from SPECS GmbH, a half hemispherical electron analyser. When using this setup it was operated in the *wide angle mode (WAD)* which has a high angular acceptance angle for photoelectrons of $\alpha = 26°$ and a resolution down to $\Delta\alpha = 0.3°$. The energetic resolution was experimentally determined to $\Delta E_{analyser} = 23\,\mathrm{meV}$ when using an entrance slit size of $S_{entry} = 0.5\,\mathrm{mm}$ and a Pass-energy of $E_{pass} = 10\,\mathrm{eV}$ [39]. v, 11, 13, 15, 17, 20, 64, 73, 100, 141

4,4-bipyridine 4,4-Bipyridine (abbreviated to 4,4-bipy or 4,4-bpy) is an organic compound with the formula $(C_5H_4N)_2$. 113

BTZ before time zero 101

C_{60}-molecule C_{60} is an organic molecule from the fullerene group, consisting of 60 carbon atomes forming a ball-like structure 96, 99, 104, 113

CEM constant energy map 33, 94, 98

constant energy map A constant energy map shows a cut through a 3D photoemission measurement optained using ARPES for one specific energy. The resulting map shows the photoemission yiel for the two $k_{||}$ coordinats k_x and k_y 33, 131, 141

coronen Coronene is a polycyclic aromatic hydrocarbon (PAH) consisting of six fused benzene rings arranged in a circular pattern, resembling a small graphene fragment. Its chemical formula is $C_{24}H_{12}$, and it is often used as a model compound for studying the properties of larger PAHs and graphene-like materials. Coronene exhibits interesting electronic, optical, and chemical properties, making it relevant in materials science and organic electronics. The used molecules were produced by Sigma-Aldrich and are analysed to have a 99% purity. More information can be found on the sellers web-page: Sigma-Aldrich, Merck Weblink 13, 84

coronene/graphene/Ni(111) coronene on a graphene monolayer on nickel(111) v, 13, 20, 86–96, 99–103, 110, 111, 113–115, 133

coronene/Ni(111) coronene on nickel(111) v, 85–94, 96, 130

cut-off In photoemission experiments, the cut-off refers to the sharp edge in the kinetic energy spectrum of emitted electrons. This cut-off, typically seen at low kinetic energies, marks the minimum energy that electrons need to escape the material's surface. By measuring the cut-off, researchers can determine the work function of the material and gain insight into its electronic properties. 19

CVD chemical vapour deposition 12

DFT density functional theory 37

density functional theory Density functional theory (DFT) is a computational quantum mechanical modelling method used to investigate the electronic structure of many-body systems, particularly atoms, molecules, and condensed phases. By utilising functionals of the electron density, DFT allows for the determination of various properties of these systems, including total energy, electron density distribution, and molecular orbitals. This approach has become a cornerstone in fields such as condensed-matter physics, computational physics, and computational chemistry, due to its balance between computational efficiency and accuracy. [121] 37, 141

differential map An differential map shows the calculated differential picture from measurements taken before t_0 and later time steps. See Section 2.3.1 43, 44, 100, 101

energy momentum distribution map An energy momentum distribution map shows a cut along one k-axis through a 3D photoemission measurement optained using ARPES. The resulting map shows the photoemission yiel for the $k_{||}$ coordinates and the energies 33, 89, 90

extreme ultraviolet EUV, or Extreme Ultraviolet, refers to electromagnetic radiation with wavelengths in the range of approximately 10 to 124 nanometers, between the ultraviolet and X-ray regions of the spectrum. EUV is used in various applications, including lithography for semiconductor manufacturing, spectroscopy, and studies of atomic and molecular processes. 67

EUV-ARPES extreme ultraviolet angle-resolved photoemission spectroscopy 65

extreme ultraviolet angle-resolved photoemission spectroscopy EUV-ARPES, or Extreme Ultraviolet Angle-Resolved Photoemission Spectroscopy, is a technique used to study the electronic structure of materials with high resolution. By utilizise extreme ultraviolet photons to excite electrons, EUV-ARPES provides detailed information about the electronic band structure, including deeper electronic states and finer details of the electronic dispersion in materials. 65, 131, 142

EUV-Tr-ARPES extreme ultraviolet time- and angle-resolved photoemission spectroscopy 67, 94

FWHM full width half maximum 23, 46

graphene/Ni(111) graphene monolayer on nickel(111) 12, 13, 16, 17, 19, 33, 66–77, 79–81, 83, 87–89, 94, 96, 97, 106, 111, 112, 129

graphene/Pb/Ni(111) lead intercalated graphene ML on nickel(111) 13, 16, 21, 33, 35, 41, 43–45, 53, 59, 66, 68, 69, 71–76, 79, 81, 99, 100

high harmonic generation The so called high harmonic generation technique is a method to generate coherent high energy laser pulses. In our case it is driven by the KM-Wyvern Ti:sapphire laser amplifier system and the 7th harmonic is utilise for measurements. Resulting in a wavelenght of ~ 55.73nm, hence in a photon energy of ~ 22.25eV. It has the same temporal FWHM of 55fs as its driving laser. 17, 19, 21, 67

HOMO highest occupied molecular orbital 92, 94, 95, 100

KM-Wyvern Ti:sapphire laser amplifier system The Wyvern laser amplifier system, built by KM-labs in Boulder, Co., USA. is an ultrashort laser amplifier. Its fundamental is at a wavelenght of ~ 782.5nm, resulting in a photon energy of ~ 1.584 eV, and has a temporal FWHM of 55fs. 14, 15, 43, 100, 142

LEED low-energy electron diffraction 11–13, 87

low-energy electron diffraction LEED, or low-energy electron diffraction, is a technique used to determine the surface structure of crystalline materials. By directing a beam of low-energy electrons at a surface and analysing the resulting diffraction pattern, LEED provides information about the atomic arrangement and periodicity of the surface layers. It is widely used in surface science to study clean and adsorbate-covered surfaces. 11, 12, 19, 86, 142

LUMO lowest unoccupied molecular orbital 91, 98

MATLAB curve fitting application The MATLAB curve fitting application is an user interface that provieds a low-code approach to simple, interactive fitting of given data curves. Different fitting algorithms can be easiely applied and the received fitting results can be fed back into the main MATLAB workspace. MathWorks MATLAB Help Center: Curve Fitter 18, 21, 25

MCP micro channel plate 14

micro channel plate A microchannel plate (MCP) is a vacuum device featuring a dense array of microscopic channels that multiply incident electrons (or other particles) via secondary emission, resulting in a high-gain, spatially-resolved signal. 14, 142

ML Mono Layer 13, 142

nanoESCA nanoscale electron spectroscopy for chemical analysis 11, 33

nanoscale electron spectroscopy for chemical analysis A nanoscale electron spectroscopy for chemical analysis (nanoESCA) is a sophisticated photoemission electron microscope (PEEM) that combines high spatial and energy resolution to study surfaces at the nanoscale. It enables imaging and analysis of chemical, electronic, and magnetic properties of materials with spatial resolutions typically down to tens of nanometers. The nanoESCA integrates techniques such as: Photoemission Spectroscopy (PES), Momentum Microscopy and if equiped with a spin-filtering crystal Magnetic Imaging. 11, 123, 143

NIXSW normal incidence X-ray standing wave 86–88

normal incidence X-ray standing wave Normal incidence x-ray standing wave (NIXSW) experiments are a surface-sensitive technique used to determine the precise vertical positions of atoms or molecules adsorbed on crystalline surfaces. By exploiting the interference pattern created when X-rays are incident at angles near the Bragg condition, NIXSW generates standing waves within the crystal. As the phase of these standing waves shifts, the absorption of X-rays by specific atomic species varies, allowing for the determination of their positions relative to the crystal lattice planes with sub-angstrom precision. This method is particularly valuable for studying adsorption geometries and surface interactions in materials science and surface chemistry. The University of Warwick: Department of Physics - NIXSW, Forschungszentrum Jülich: Research Topics - Chemically-Resolved Vertical Structures with sub-Angstrom Resolution 12, 32, 86, 143

polycyclic aromatic hydrocarbon molecules Polycyclic aromatic hydrocarbons (PAHs) are a class of organic compounds that consist solely of carbon and hydrogen atoms in aromatic ring structures. PAHs are uncharged, non-polar and planar. 84, 85, 96, 113

PES photoemission spectroscopy 87

proximity effect The proximity effect, in a condensed matter physics context, generally refers to the influence that a material exerts on an adjacent layer or structure, particularly in altering its physical properties. This effect is often discussed with respect to phenomena like superconductivity, where the properties of a superconducting material affect an adjacent non-superconducting material, or spin-orbit coupling in graphene systems, where spin-orbit interaction in a heavy metal substrate can induce a similar interaction in a nearby graphene layer. This effect occurs at the interface, enabling the transfer of SOC characteristics, which can modify the spintronic and electronic properties of the neighboring material. [122] 30

perylenetetracarboxylic dianhydride Perylenetetracarboxylic dianhydride (PTCDA) is an organic dye molecule and an organic semiconductor. 113

S-ARPES spin- and angle-resolved photoelectron spectroscopy 14, 64

spin- and angle-resolved photoelectron spectroscopy Spin- and angle-resolved photoelectron spectroscopy, short S-ARPES, experiments are used to investigate the spin-dependent electronic structure of materials. By measuring both the kinetic energy and spin orientation of photoemitted electrons, this technique provides detailed information about the spin texture and spin polarization of electronic states in a material. 14, 143

Savitzky–Golay smoothing The Savitzky–Golay smoothing method is a digital filter that smooths data by fitting a low-order polynomial (via least-squares) to a moving window of points and then replacing the central point with the value of that polynomial. This approach preserves important signal features—like peak height and width better than simple averaging, making it especially useful for processing noisy signals. 18

SOI spin-orbit interaction 53

STM scanning tunneling microscopy 12

scanning tunneling microscopy STM, or Scanning Tunneling Microscopy, is a technique used to image surfaces at the atomic level. It operates by scanning a sharp metal tip very close to the surface, allowing electrons to tunnel between the tip and the surface. This tunneling current is used to create detailed images of the surface's atomic structure and can also provide information about the electronic properties of the material. 12, 144

t_0 Time zero is the moment when the pump and probe pulses overlap at the sample, establishing the reference point for delay time measurements. This defines the onset of the photo-induced dynamics observed in pump-probe experiments. 17, 19, 21, 22, 26, 100, 101

Tr-ARPES time- and angle-resolved photoelectron spectroscopy 16, 17, 24, 64–66, 100, 101

time- and angle-resolved photoelectron spectroscopy Time- and Angle-Resolved Photoelectron Spectroscopy, short Tr-ARPES, is an experimental technique to measure photoexited electrons. This method is used to map the elecronic bandstructure dynamics of materials. 15, 16, 19, 43, 44, 144

Tr-MOKE time-resolved magneto-optical Kerr effect 64–66, 73

time-resolved magneto-optical Kerr effect Time-Resolved Magneto-Optical Kerr Effect (Tr-MOKE) experiments are a technique used to study ultrafast magnetic dynamics in materials. In Tr-MOKE, a pump laser pulse excites the sample, and a delayed probe pulse measures the Kerr rotation or ellipticity of reflected light, which changes in response to the sample's magnetisation dynamics. This allows for observation of processes like demagnetisation, spin precession, and relaxation on femtosecond to nanosecond timescales, making Tr-MOKE especially valuable in studying spin dynamics in magnetic materials and thin films. [78, 84, 123] 64, 144

trust-region algorithm The trust-region algorithm is an iterative optimisation method that, at each step, builds a simplified model (typically a quadratic approximation) of the objective function in a neighborhood around the current point—the "trust region." Within this region, the algorithm finds a step that minimise the model function. It then evaluates the actual improvement in the objective function compared to the predicted improvement. Based on this ratio, the trust region is either expanded (if the model was a good approximation) or contracted (if not), ensuring a robust and adaptive approach to converging toward a solution. 18

UHV ultra-high vacuum, vacuum enviroment with extremely low pressure below 1×10^{-9} mbar 11, 20

VUV lamp VUV lamps, or Vacuum Ultraviolet lamps, are light sources that emit radiation in the vacuum ultraviolet range, typically from 10 to 200 nanometers. These lamps are used in applications such as spectroscopy, photochemistry, and surface science, where they provide the high-energy photons needed to study and manipulate materials at the atomic and molecular levels. The used lamp is the VUV-5000 from the company SCIENTA-OMICRON which is a Helium-discharge lamp, optimised to emit the HeI_α and the $HeII_\alpha$ line. Were: $\lambda_{He2} = 30.56$nm, hence in a photon energy of $E_{Ph-He2} = 40.57$eV and $\lambda_{He1} = 58.46$nm, hence in a photon energy of $E_{Ph-He1} = 21.21$eV. The helium plasma is generated using electron cyclotron resonance technique [39] and is equipped with a monochromator. The combination allows for a spectral width of the emitted light of less than 2 meV 14, 35, 67

work function The work function is the minimum energy needed to remove an electron from the surface of a material to a point just outside it (in vacuum). It's essentially the difference between the Fermi level (the highest occupied energy level at absolute zero) and the vacuum level, and it plays a critical role in phenomena like electron emission and surface reactions. 19, 141

X-ray absorption spectroscopy X-ray absorption spectroscopy (XAS) experiments are a technique used to study the electronic structure and local environment of atoms in a material. By measuring the absorption of X-rays as their energy is varied, XAS provides information about the unoccupied electronic states, chemical bonding, and coordination geometry around specific elements in the sample. 64, 145

XAS X-ray absorption spectroscopy 64

XMCD X-ray magnetic circular dichroism 64

X-ray magnetic circular dichroism X-ray Magnetic Circular Dichroism (XMCD) is an experimental technique that probes the magnetic properties of materials by measuring the difference in absorption of left- and right-circularly polarised X-rays. This difference in absorption provides element-specific information on the magnetic moments of atoms, allowing researchers to investigate magnetic ordering, spin configurations, and electronic structure at an atomic level. XMCD is particularly useful in studies of magnetic thin films, multilayers, and nanostructures [18, 65]. 64, 145

XPS X-ray photoelectron spectroscopy 12, 87, 88

X-ray photoelectron spectroscopy XPS, or X-ray Photoelectron Spectroscopy, is a surface-sensitive analytical technique used to study the elemental composition, chemical state, and electronic state of the materials' surface. By irradiating a material with X-rays and measuring the kinetic energy and number of electrons ejected, XPS provides detailed information about the material's surface chemistry and electronic structure. 12, 145

Bibliography

[1] Herbert Krömer. Quasi-electric fields and band offsets: Teaching electrons new tricks: Nobel lecture. 2000. URL `https://www.nobelprize.org/uploads/2018/06/kroemer-lecture.pdf`.

[2] Stefano Ponzoni, Felix Paßlack, Matija Stupar, David Maximilian Janas, Giovanni Zamborlini, and Mirko Cinchetti. Dirac bands in the topological insulator bi 2 se 3 mapped by time–resolved momentum microscopy. *Advanced Physics Research*, 2(5), 2023. ISSN 2751-1200. doi: 10.1002/apxr.202200016.

[3] Daniel Niesner. *Two-photon photoemission studies of graphene and topological insulators: Zugl.: Erlangen-Nürnberg, Univ., Diss., 2013*, volume 1 of *FAU studies mathematics & physics*. FAU Univ. Press, Erlangen, 2013. ISBN 978-3-944057-07-1.

[4] M. S. Dresselhaus, A. Jorio, and R. Saito. Characterizing graphene, graphite, and carbon nanotubes by raman spectroscopy. *Annual Review of Condensed Matter Physics*, 1(1):89–108, 2010. ISSN 1947-5454. doi: 10.1146/annurev-conmatphys-070909-103919.

[5] Siva Böhm. Graphene against corrosion. *Nature nanotechnology*, 9(10):741–742, 2014. doi: 10.1038/nnano.2014.220.

[6] R. R. Nair, P. Blake, A. N. Grigorenko, K. S. Novoselov, T. J. Booth, T. Stauber, N. M. R. Peres, and A. K. Geim. Fine structure constant defines visual transparency of graphene. *Science (New York, N.Y.)*, 320(5881):1308, 2008. doi: 10.1126/science.1156965.

[7] Wencai Ren and Hui-Ming Cheng. The global growth of graphene. *Nature nanotechnology*, 9 (10):726–730, 2014. doi: 10.1038/nnano.2014.229.

[8] Yuanbo Zhang, Tsung-Ta Tang, Caglar Girit, Zhao Hao, Michael C. Martin, Alex Zettl, Michael F. Crommie, Y. Ron Shen, and Feng Wang. Direct observation of a widely tunable bandgap in bilayer graphene. *Nature*, 459(7248):820–823, 2009. doi: 10.1038/nature08105.

[9] Oleg V. Yazyev and Yong P. Chen. Polycrystalline graphene and other two-dimensional materials. *Nature nanotechnology*, 9(10):755–767, 2014. doi: 10.1038/nnano.2014.166.

[10] Sven Aeschlimann. *Ultrafast Quasiparticle Dynamics in Graphene and 2D Heterostructures*. Dissertation, Universität Hamburg, Hamburg, 2018. URL `https://ediss.sub.uni-hamburg.de/handle/ediss/8126`.

[11] Kin Fai Mak, Long Ju, Feng Wang, and Tony F. Heinz. Optical spectroscopy of graphene: From the far infrared to the ultraviolet. *Solid State Communications*, 152(15):1341–1349, 2012. ISSN 00381098. doi: 10.1016/j.ssc.2012.04.064.

[12] A. K. Geim and K. S. Novoselov. The rise of graphene. *Nature materials*, 6(3):183–191, 2007. ISSN 1476-1122. doi: 10.1038/nmat1849.

[13] Arjun Dahal and Matthias Batzill. Graphene-nickel interfaces: a review. *Nanoscale*, 6(5): 2548–2562, 2014. doi: 10.1039/c3nr05279f.

[14] A. Varykhalov, J. Sánchez-Barriga, A. M. Shikin, C. Biswas, E. Vescovo, A. Rybkin, D. Marchenko, and O. Rader. Electronic and magnetic properties of quasifreestanding graphene on ni. *Physical review letters*, 101(15):157601, 2008. doi: 10.1103/PhysRevLett.101.157601.

[15] O. Vilkov, A. Fedorov, D. Usachov, L. V. Yashina, A. V. Generalov, K. Borygina, N. I. Verbitskiy, A. Grüneis, and D. V. Vyalikh. Controlled assembly of graphene-capped nickel, cobalt and iron silicides. *Scientific reports*, 3:2168, 2013. doi: 10.1038/srep02168.

[16] Yu S. Dedkov and M. Fonin. Electronic and magnetic properties of the graphene–ferromagnet interface. *New Journal of Physics*, 12(12):125004, 2010. doi: 10.1088/1367-2630/12/12/125004.

[17] Yu. S. Dedkov, M. Sicot, and M. Fonin. X-ray absorption and magnetic circular dichroism of graphene/ni(111). *Journal of Applied Physics*, 107(9), 2010. ISSN 0021-8979. doi: 10.1063/1.3360340.

[18] L. V. Dzemiantsova, M. Karolak, F. Lofink, A. Kubetzka, B. Sachs, K. von Bergmann, S. Hankemeier, T. O. Wehling, R. Frömter, H. P. Oepen, A. I. Lichtenstein, and R. Wiesendanger. Multiscale magnetic study of ni(111) and graphene on ni(111). *Physical Review B*, 84(20), 2011. ISSN 2469-9950. doi: 10.1103/PhysRevB.84.205431.

[19] Dominik Jonas Jungkenn. *Tuning spin carrier properties in low dimensional multi-compoundmaterials by spin-dependent interactions.* Dissertation, Technische Universität Kaiserslautern, Kaiserslautern, 2019.

[20] D. Marchenko, A. Varykhalov, M. R. Scholz, G. Bihlmayer, E. I. Rashba, A. Rybkin, A. M. Shikin, and O. Rader. Giant rashba splitting in graphene due to hybridization with gold. *Nature Communications*, 3(1):1232, 2012. ISSN 2041-1723. doi: 10.1038/ncomms2227. URL `https://www.nature.com/articles/ncomms2227#further-reading`.

[21] M. Gmitra, S. Konschuh, C. Ertler, C. Ambrosch-Draxl, and J. Fabian. Band-structure topologies of graphene: Spin-orbit coupling effects from first principles. *Physical Review B*, 80(23), 2009. ISSN 2469-9950. doi: 10.1103/PhysRevB.80.235431.

[22] C. L. Kane and E. J. Mele. Quantum spin hall effect in graphene. *Physical review letters*, 95 (22):226801, 2005. doi: 10.1103/PhysRevLett.95.226801.

[23] Ilya I. Klimovskikh, Mikhail M. Otrokov, Vladimir Yu Voroshnin, Daria Sostina, Luca Petaccia, Giovanni Di Santo, Sangeeta Thakur, Evgueni V. Chulkov, and Alexander M. Shikin. Spin-orbit coupling induced gap in graphene on pt(111) with intercalated pb monolayer. *ACS nano*, 11(1):368–374, 2017. doi: 10.1021/acsnano.6b05982.

[24] Yuriy Dedkov and Elena Voloshina. Comment on "spin-orbit coupling induced gap in graphene on pt(111) with intercalated pb monolayer". *ACS nano*, 11(11):10627–10629, 2017. doi: 10.1021/acsnano.7b00737. URL `http://arxiv.org/pdf/1704.00034`.

[25] E. V. Zhizhin, A. Varykhalov, A. G. Rybkin, A. A. Rybkina, D. A. Pudikov, D. Marchenko, J. Sánchez-Barriga, I. I. Klimovskikh, G. G. Vladimirov, O. Rader, and A. M. Shikin. Spin splitting of dirac fermions in graphene on ni intercalated with alloy of bi and au. *Carbon*, 93: 984–996, 2015. ISSN 00086223. doi: 10.1016/j.carbon.2015.05.104.

[26] P. M. Sheverdyaeva, G. Bihlmayer, E. Cappelluti, D. Pacilé, F. Mazzola, N. Atodiresei, M. Jugovac, I. Grimaldi, G. Contini, Asish K. Kundu, I. Vobornik, J. Fujii, P. Moras, C. Carbone, and L. Ferrari. Spin-dependent pi-pi gap in graphene on a magnetic substrate. *Physical Review Letters*, 132(26):266401, 2024. ISSN 0031-9007. doi: 10.1103/PhysRevLett.132.266401. URL `http://arxiv.org/pdf/2404.17887v1`.

[27] Fabian Calleja, Héctor Ochoa, Manuela Garnica, Sara Barja, Juan Jesús Navarro, Andrés Black, Mikhail M. Otrokov, Evgueni V. Chulkov, Andrés Arnau, Amadeo L. Vázquez de Parga, Francisco Guinea, and Rodolfo Miranda. Spatial variation of a giant spin–orbit effect induces electron confinement in graphene on pb islands. *Nature Physics*, 11(1):43–47, 2015. ISSN 1745-2473. doi: 10.1038/nphys3173.

[28] Dongwei Ma and Zhongqin Yang. First-principles studies of pb doping in graphene: stability, energy gap and spin–orbit splitting. *New Journal of Physics*, 13(12):123018, 2011. doi: 10.1088/1367-2630/13/12/123018.

[29] Christina Schott. *Tailoring geometric and electronic properties of a molecule-metal interface by utilization of 2D-materials.* Dissertation, Rheinland-Pfälzischen Technischen Universität, Kaiserslautern, 2024.

[30] M. Battiato, K. Carva, and P. M. Oppeneer. Superdiffusive spin transport as a mechanism of ultrafast demagnetization. *Physical review letters*, 105(2):027203, 2010. doi: 10.1103/PhysRevLett.105.027203.

[31] A. Eschenlohr, M. Battiato, P. Maldonado, N. Pontius, T. Kachel, K. Holldack, R. Mitzner, A. Föhlisch, P. M. Oppeneer, and C. Stamm. Ultrafast spin transport as key to femtosecond demagnetization. *Nature materials*, 12(4):332–336, 2013. doi: 10.1038/nmat3546.

[32] Alex Summerfield and Alexander Allen. Phase transitions in two-dimensional supramolecular assemblies.

[33] Masahiro Shibuta, Kazuo Yamamoto, Tsutomu Ohta, Masato Nakaya, Toyoaki Eguchi, and Atsushi Nakajima. Direct observation of photocarrier electron dynamics in c60 films on graphite by time-resolved two-photon photoemission. *Scientific reports*, 6:35853, 2016. doi: 10.1038/srep35853.

[34] Sven Aeschlimann, Antonio Rossi, Mariana Chávez-Cervantes, Razvan Krause, Benito Arnoldi, Benjamin Stadtmüller, Martin Aeschlimann, Stiven Forti, Filippo Fabbri, Camilla Coletti, and Isabella Gierz. Direct evidence for efficient ultrafast charge separation in epitaxial ws2/graphene heterostructures. *Science advances*, 6(20):eaay0761, 2020. doi: 10.1126/sciadv.aay0761.

[35] Kurt K. Kolasinski. *Surface Science: Foundations of Catalysis and Nanoscience*. John Wiley & Sons, Hoboken, 3. ed. edition, 2012. ISBN 9781119990369. doi: 10.1002/9781119941798.

[36] D. P. Woodruff and T. A. Delchar. *Modern techniques of surface science*. Cambridge solid state science series. Cambridge Univ. Press, Cambridge, 2. ed., reprinted. edition, 1999. ISBN 9780521414678. doi: 10.1017/CBO9780511623172.

[37] Stefan Hüfner. *Photoelectron Spectroscopy: Principles and Applications*. Advanced Texts in Physics. Springer, Berlin and Heidelberg, third revised and enlarged edition edition, 2003. ISBN 978-3-642-07520-9. doi: 10.1007/978-3-662-09280-4.

[38] Toivo Kodas. Chemical vapor deposition: Principles and applications. edited by m. l. hitchman and k. f. jensen , academic press, london 1993, 677 pp., hardback, $ 75, isbn 0–12–349 670–5. *Advanced Materials*, 6(1):87–88, 1994. ISSN 0935-9648. doi: 10.1002/adma.19940060125.

[39] Johannes Stöckl. *Spin-dependent phenomena in molecular thin films on surfaces*. Dissertation, TU Kaiserslautern, Kaiserslautern, 03.07.2020.

[40] Anatol Jurenkow. *Aufbau und Charakterisierung eines UHV-Systems für winkel- und spinaufgelöste Photoelektronenspektroskopie*. Diplomarbeit, Technische Universität Kaiserslautern, Kaiserslautern, 2016.

[41] Benito Arnoldi. *Tailoring of spin-dependent band structures at hybrid inorganic-organic interfaces*. Dissertation, Technische Universität Kaiserslautern, Kaiserslautern, 2023.

[42] Gregor Zinke. *Ultraschnelle Spin- und Ladungsträger-Dynamik in WSe2 und einer CuPc/WSe2-Heterostruktur*. Master-thesis, Rheinland-Pfälzischen Technischen Universität, Kaiserslautern, 2022.

[43] P. Johnson and R. Christy. Optical constants of transition metals: Ti, v, cr, mn, fe, co, ni, and pd. *Physical Review B*, 9(12):5056–5070, 1974. ISSN 2469-9950. doi: 10.1103/PhysRevB.9.5056.

[44] Wenjing You, Phoebe Tengdin, Cong Chen, Xun Shi, Dmitriy Zusin, Yingchao Zhang, Christian Gentry, Adam Blonsky, Mark Keller, Peter M. Oppeneer, Henry Kapteyn, Zhensheng Tao, and Margaret Murnane. Revealing the nature of the ultrafast magnetic phase transition in ni by correlating extreme ultraviolet magneto-optic and photoemission spectroscopies. *Physical review letters*, 121(7):077204, 2018. doi: 10.1103/PhysRevLett.121.077204.

[45] Zhensheng Tao, Cong Chen, Tibor Szilvási, Mark Keller, Manos Mavrikakis, Henry Kapteyn, and Margaret Murnane. Direct time-domain observation of attosecond final-state lifetimes in photoemission from solids. *Science (New York, N.Y.)*, 353(6294):62–67, 2016. doi: 10.1126/science.aaf6793.

[46] M. Krivenkov, D. Marchenko, J. Sánchez-Barriga, E. Golias, O. Rader, and A. Varykhalov. Origin of the band gap in bi-intercalated graphene on ir(111). *2D Materials*, 8(3):035007, 2021. doi: 10.1088/2053-1583/abd1e4.

[47] N. I. Verbitskiy, A. V. Fedorov, G. Profeta, A. Stroppa, L. Petaccia, B. Senkovskiy, A. Nefedov, C. Wöll, D. Yu Usachov, D. V. Vyalikh, L. V. Yashina, A. A. Eliseev, T. Pichler, and A. Grüneis. Atomically precise semiconductor–graphene and hbn interfaces by ge intercalation. *Scientific reports*, 5:17700, 2015. doi: 10.1038/srep17700.

[48] Artem G. Rybkin, Anna A. Rybkina, Mikhail M. Otrokov, Oleg Yu Vilkov, Ilya I. Klimovskikh, Anatoly E. Petukhov, Maria V. Filianina, Vladimir Yu Voroshnin, Igor P. Rusinov, Arthur Ernst, Andrés Arnau, Evgueni V. Chulkov, and Alexander M. Shikin. Magneto-spin-orbit graphene: Interplay between exchange and spin-orbit couplings. *Nano letters*, 18(3):1564–1574, 2018. doi: 10.1021/acs.nanolett.7b01548.

[49] Y. Gamo, A. Nagashima, M. Wakabayashi, M. Terai, and C. Oshima. Atomic structure of monolayer graphite formed on ni(111). *Surface Science*, 374(1-3):61–64, 1997. ISSN 0039-6028. URL `https://waseda.elsevierpure.com/en/publications/atomic-structure-of-monolayer-graphite-formed-on-ni111`.

[50] Wei Zhao, Sergey M. Kozlov, Oliver Höfert, Karin Gotterbarm, Michael P. A. Lorenz, Francesc Viñes, Christian Papp, Andreas Görling, and Hans-Peter Steinrück. Graphene on ni(111): Coexistence of different surface structures. *The Journal of Physical Chemistry Letters*, 2(7): 759–764, 2011. ISSN 1948-7185. doi: 10.1021/jz200043p.

[51] A. Bondi. van der waals volumes and radii. *The Journal of Physical Chemistry*, 68(3):441–451, 1964. ISSN 0022-3654. doi: 10.1021/j100785a001.

[52] Martin Mitkov, Lu Lyu, Eva Sophia Walther, Martin Anstett, Alexander Schmid, Christina Schott, Gyula Halasi, Nikolett Olah, Csaba Vass, Zoltan Filu, Timea Timar-Grosz, Chinmoy Biswas, Peter Jojart, Balazs Major, Laszlo Ovari, Martin Aeschlimann, and Benjamin Stadtmüller. Hot carrier dynamics and band gap formation in pb intercalated graphene on ni(111). In *DPG Frühjahrestagung*, volume 2025 Regensburg, page 1.

[53] Aaron Bostwick, Taisuke Ohta, Thomas Seyller, Karsten Horn, and Eli Rotenberg. Quasiparticle dynamics in graphene. *Nature Physics*, 3(1):36–40, 2007. ISSN 1745-2473. doi: 10.1038/nphys477.

[54] Y. Xia, D. Qian, D. Hsieh, L. Wray, A. Pal, H. Lin, A. Bansil, D. Grauer, Y. S. Hor, R. J. Cava, and M. Z. Hasan. Observation of a large-gap topological-insulator class with a single dirac cone on the surface. *Nature Physics*, 5(6):398–402, 2009. ISSN 1745-2473. doi: 10.1038/nphys1274.

[55] K. Ishizaka, M. S. Bahramy, H. Murakawa, M. Sakano, T. Shimojima, T. Sonobe, K. Koizumi, S. Shin, H. Miyahara, A. Kimura, K. Miyamoto, T. Okuda, H. Namatame, M. Taniguchi, R. Arita, N. Nagaosa, K. Kobayashi, Y. Murakami, R. Kumai, Y. Kaneko, Y. Onose, and Y. Tokura. Giant rashba-type spin splitting in bulk bitei. *Nature materials*, 10(7):521–526, 2011. doi: 10.1038/nmat3051.

[56] Jiahao Han and Luqiao Liu. Topological insulators for efficient spin–orbit torques. *APL Materials*, 9(6), 2021. doi: 10.1063/5.0048619.

[57] Lewis Bawden, Jonathan M. Riley, Choong H. Kim, Raman Sankar, Eric J. Monkman, Daniel E. Shai, Haofei I. Wei, Edward B. Lochocki, Justin W. Wells, Worawat Meevasana, Timur K. Kim, Moritz Hoesch, Yoshiyuki Ohtsubo, Patrick Le Fèvre, Craig J. Fennie, Kyle M. Shen, Fangcheng Chou, and Phil D. C. King. Hierarchical spin-orbital polarization of a giant rashba system. *Science advances*, 1(8):e1500495, 2015. doi: 10.1126/sciadv.1500495.

[58] Xiao-Ming Wang and Shu-Shen Lu. First-principles study of the transport properties of graphene-hexagonal boron nitride superlattice. *Journal of nanoscience and nanotechnology*, 15(4):3025–3028, 2015. doi: 10.1166/jnn.2015.9636.

[59] Maxim Krivenkov. *Spin textures and electron scattering in nanopatterned monolayer graphene*. PhD thesis, Universität Potsdam, 2020.

[60] I. Vurgaftman, J. R. Meyer, and L. R. Ram-Mohan. Band parameters for iii–v compound semiconductors and their alloys. *Journal of Applied Physics*, 89(11):5815–5875, 2001. ISSN 0021-8979. doi: 10.1063/1.1368156.

[61] P. Y. Liu and J. C. Maan. Optical properties of insb between 300 and 700 k. i. temperature dependence of the energy gap. *Physical review. B, Condensed matter*, 47(24):16274–16278, 1993. ISSN 0163-1829. doi: 10.1103/physrevb.47.16274.

[62] Stefan Zollner, Sudha Gopalan, and Manuel Cardona. The temperature dependence of the band gaps in inp, inas, insb, and gasb. *Solid State Communications*, 77(7):485–488, 1991. ISSN 00381098. doi: 10.1016/0038-1098(91)90725-B.

[63] A. L. Cavalieri, N. Müller, Th Uphues, V. S. Yakovlev, A. Baltuska, B. Horvath, B. Schmidt, L. Blümel, R. Holzwarth, S. Hendel, M. Drescher, U. Kleineberg, P. M. Echenique, R. Kienberger, F. Krausz, and U. Heinzmann. Attosecond spectroscopy in condensed matter. *Nature*, 449(7165):1029–1032, 2007. doi: 10.1038/nature06229.

[64] E. L. Shirley, L. J. Terminello, A. Santoni, and F. J. Himpsel. Brillouin-zone-selection effects in graphite photoelectron angular distributions. *Physical review. B, Condensed matter*, 51(19): 13614–13622, 1995. ISSN 0163-1829. doi: 10.1103/physrevb.51.13614.

[65] Alexander M. Shikin, Artem G. Rybkin, Dmitry Marchenko, Anna A. Rybkina, Markus R. Scholz, Oliver Rader, and Andrei Varykhalov. Induced spin–orbit splitting in graphene: the role of atomic number of the intercalated metal and pi –d hybridization. *New Journal of Physics*, 15(1):013016, 2013. doi: 10.1088/1367-2630/15/1/013016.

[66] David A. Siegel, Cheol-Hwan Park, Choongyu Hwang, Jack Deslippe, Alexei V. Fedorov, Steven G. Louie, and Alessandra Lanzara. Many-body interactions in quasi-freestanding graphene. *Proceedings of the National Academy of Sciences of the United States of America*, 108(28):11365–11369, 2011. doi: 10.1073/pnas.1100242108.

[67] Cheol-Hwan Park, Feliciano Giustino, Catalin D. Spataru, Marvin L. Cohen, and Steven G. Louie. Angle-resolved photoemission spectra of graphene from first-principles calculations. *Nano letters*, 9(12):4234–4239, 2009. doi: 10.1021/nl902448v.

[68] Zhen Jiao and Harold J. W. Zandvliet. Determination of the fermi velocity of graphene on mos2 using dual mode scanning tunneling spectroscopy. *Applied Physics Letters*, 118(16), 2021. ISSN 0003-6951. doi: 10.1063/5.0046658.

[69] Federico Mazzola, Thomas Frederiksen, Thiagarajan Balasubramanian, Philip Hofmann, Bo Hellsing, and Justin W. Wells. Strong electron-phonon coupling in the sigma band of graphene. *Physical Review B*, 95(7), 2017. ISSN 2469-9950. doi: 10.1103/PhysRevB.95.075430.

[70] Jens Christian Johannsen, Søren Ulstrup, Marco Bianchi, Richard Hatch, Dandan Guan, Federico Mazzola, Liv Hornekær, Felix Fromm, Christian Raidel, Thomas Seyller, and Philip Hofmann. Electron-phonon coupling in quasi-free-standing graphene. *Journal of physics. Condensed matter : an Institute of Physics journal*, 25(9):094001, 2013. doi: 10.1088/0953-8984/25/9/094001.

[71] E. Pomarico, M. Mitrano, H. Bromberger, M. A. Sentef, A. Al-Temimy, C. Coletti, A. Stöhr, S. Link, U. Starke, C. Cacho, R. Chapman, E. Springate, A. Cavalleri, and I. Gierz. Enhanced electron-phonon coupling in graphene with periodically distorted lattice. *Physical Review B*, 95(2), 2017. ISSN 2469-9950. doi: 10.1103/PhysRevB.95.024304.

[72] Lukas Broers and Ludwig Mathey. Detecting light-induced floquet band gaps of graphene via trarpes. *Physical Review Research*, 4(1), 2022. doi: 10.1103/PhysRevResearch.4.013057.

[73] M. Weser, Y. Rehder, K. Horn, M. Sicot, M. Fonin, A. B. Preobrajenski, E. N. Voloshina, E. Goering, and Yu. S. Dedkov. Induced magnetism of carbon atoms at the graphene/ni(111) interface. *Applied Physics Letters*, 96(1), 2010. ISSN 0003-6951. doi: 10.1063/1.3280047.

[74] Elena N. Voloshina and Yuriy S. Dedkov. Electronic and magnetic properties of the graphene/eu/ni(111) hybrid system. *Zeitschrift für Naturforschung A*, 69(7):297–302, 2014. ISSN 0932-0784. doi: 10.5560/zna.2014-0012.

[75] Wataru Tadano, Masahiro Sawada, Hirofumi Namatame, and Masaki Taniguchi. Magnetic properties of iron ultrathin films intercalated in graphene/ni(111). *e-Journal of Surface Science and Nanotechnology*, 13(0):312–316, 2015. doi: 10.1380/ejssnt.2015.312.

[76] Yuriy Dedkov, Wolfgang Klesse, Andreas Becker, Florian Späth, Christian Papp, and Elena Voloshina. Decoupling of graphene from ni(111) via formation of an interfacial nio layer. *Carbon*, 121:10–16, 2017. ISSN 00086223. doi: 10.1016/j.carbon.2017.05.068.

[77] M. Weser, E. N. Voloshina, K. Horn, and Yu S. Dedkov. Electronic structure and magnetic properties of the graphene/fe/ni111 intercalation-like system. *Physical chemistry chemical physics : PCCP*, 13(16):7534–7539, 2011. doi: 10.1039/c1cp00014d.

[78] E. Beaurepaire, J. Merle, A. Daunois, and J. Bigot. Ultrafast spin dynamics in ferromagnetic nickel. *Physical review letters*, 76(22):4250–4253, 1996. doi: 10.1103/PhysRevLett.76.4250.

[79] Steffen Eich, Moritz Plötzing, Markus Rollinger, Sebastian Emmerich, Roman Adam, Cong Chen, Henry Cornelius Kapteyn, Margaret M. Murnane, Lukasz Plucinski, Daniel Steil, Benjamin Stadtmüller, Mirko Cinchetti, Martin Aeschlimann, Claus M. Schneider, and Stefan Mathias. Band structure evolution during the ultrafast ferromagnetic-paramagnetic phase transition in cobalt. *Science advances*, 3(3):e1602094, 2017. doi: 10.1126/sciadv.1602094.

[80] T. Roth, A. J. Schellekens, S. Alebrand, O. Schmitt, D. Steil, B. Koopmans, M. Cinchetti, and M. Aeschlimann. Temperature dependence of laser-induced demagnetization in ni: A key for identifying the underlying mechanism. *Physical Review X*, 2(2), 2012. doi: 10.1103/PhysRevX.2.021006.

[81] John Kay Dewhurst, Peter Elliott, Sam Shallcross, Eberhard K. U. Gross, and Sangeeta Sharma. Laser-induced intersite spin transfer. *Nano letters*, 18(3):1842–1848, 2018. doi: 10.1021/acs.nanolett.7b05118.

[82] M. Hofherr, S. Häuser, J. K. Dewhurst, P. Tengdin, S. Sakshath, H. T. Nembach, S. T. Weber, J. M. Shaw, T. J. Silva, H. C. Kapteyn, M. Cinchetti, B. Rethfeld, M. M. Murnane, D. Steil, B. Stadtmüller, S. Sharma, M. Aeschlimann, and S. Mathias. Ultrafast optically induced spin transfer in ferromagnetic alloys. *Science advances*, 6(3):eaay8717, 2020. doi: 10.1126/sciadv.aay8717.

[83] Kamil Bobowski, Xinwei Zheng, Björn Frietsch, Dominic Lawrenz, Wibke Bronsch, Cornelius Gahl, Beatrice Andres, Christian Strüber, Robert Carley, Martin Teichmann, Andreas Scherz, Serguei Molodtsov, Cephise Cacho, Richard T. Chapman, Emma Springate, and Martin Weinelt. Ultrafast spin transfer and its impact on the electronic structure. *Science advances*, 10(29):eadn4613, 2024. doi: 10.1126/sciadv.adn4613.

[84] Phoebe Tengdin, Wenjing You, Cong Chen, Xun Shi, Dmitriy Zusin, Yingchao Zhang, Christian Gentry, Adam Blonsky, Mark Keller, Peter M. Oppeneer, Henry C. Kapteyn, Zhensheng Tao, and Margaret M. Murnane. Critical behavior within 20 fs drives the out-of-equilibrium laser-induced magnetic phase transition in nickel. *Science advances*, 4(3):eaap9744, 2018. doi: 10.1126/sciadv.aap9744.

[85] Charles F. Squire. Changes in the absorption spectrum of pb and ni films at low temperatures. *Journal of Applied Physics*, 11(12):779–780, 1940. ISSN 0021-8979. doi: 10.1063/1.1712736.

[86] N. Ahmad, J. Stokes, and M. J. Cryan. Solar absorbers using 1d and 2d periodic nanostructured nickel films. *Journal of Optics*, 16(12):125003, 2014. ISSN 2040-8978. doi: 10.1088/2040-8978/16/12/125003.

[87] M. Cinchetti, M. Sánchez Albaneda, D. Hoffmann, T. Roth, J-P Wüstenberg, M. Krauss, O. Andreyev, H. C. Schneider, M. Bauer, and M. Aeschlimann. Spin-flip processes and ultrafast magnetization dynamics in co: Unifying the microscopic and macroscopic view of femtosecond magnetism. *Physical Review Letters*, 97(17):177201, 2006. ISSN 0031-9007. doi: 10.1103/PhysRevLett.97.177201.

[88] Sven Essert and Hans Christian Schneider. Electron-phonon scattering dynamics in ferromagnetic metals and their influence on ultrafast demagnetization processes. *Physical Review B*, 84 (22), 2011. ISSN 2469-9950. doi: 10.1103/PhysRevB.84.224405.

[89] X. Ma, F. Fang, Q. Li, J. Zhu, Y. Yang, Y. Z. Wu, H. B. Zhao, and G. Lüpke. Ultrafast spin exchange-coupling torque via photo-excited charge-transfer processes. *Nature communications*, 6:8800, 2015. doi: 10.1038/ncomms9800.

[90] Félix Dusabirane, Kai Leckron, Baerbel Rethfeld, and Hans Christian Schneider. Interplay of electron-magnon scattering and spin-orbit induced electronic spin-flip scattering in a two-band stoner model. URL `http://arxiv.org/pdf/2304.14978`.

[91] E. Carpene, E. Mancini, C. Dallera, M. Brenna, E. Puppin, and S. de Silvestri. Dynamics of electron-magnon interaction and ultrafast demagnetization in thin iron films. *Physical Review B*, 78(17), 2008. ISSN 2469-9950. doi: 10.1103/PhysRevB.78.174422.

[92] B. Koopmans, G. Malinowski, F. Dalla Longa, D. Steiauf, M. Fähnle, T. Roth, M. Cinchetti, and M. Aeschlimann. Explaining the paradoxical diversity of ultrafast laser-induced demagnetization. *Nature materials*, 9(3):259–265, 2010. doi: 10.1038/nmat2593.

[93] H-S Rhie, H. A. Dürr, and W. Eberhardt. Femtosecond electron and spin dynamics in ni/w(110) films. *Physical review letters*, 90(24):247201, 2003. doi: 10.1103/PhysRevLett.90.247201.

[94] B. Koopmans, M. van Kampen, J. T. Kohlhepp, and W. J. de Jonge. Ultrafast magneto-optics in nickel: magnetism or optics? *Physical review letters*, 85(4):844–847, 2000. doi: 10.1103/PHYSREVLETT.85.844.

[95] G. Salvatella, R. Gort, K. Bühlmann, S. Däster, A. Vaterlaus, and Y. Acremann. Ultrafast demagnetization by hot electrons: Diffusion or super-diffusion? *Structural dynamics (Melville, N.Y.)*, 3(5):055101, 2016. ISSN 2329-7778. doi: 10.1063/1.4964892.

[96] F. Dalla Longa, J. T. Kohlhepp, W. J. M. de Jonge, and B. Koopmans. Influence of photon angular momentum on ultrafast demagnetization in nickel. *Physical Review B*, 75(22), 2007. ISSN 2469-9950. doi: 10.1103/PhysRevB.75.224431.

[97] Emrah Turgut, Chan La-o Vorakiat, Justin M. Shaw, Patrik Grychtol, Hans T. Nembach, Dennis Rudolf, Roman Adam, Martin Aeschlimann, Claus M. Schneider, Thomas J. Silva, Margaret M. Murnane, Henry C. Kapteyn, and Stefan Mathias. Controlling the competition between optically induced ultrafast spin-flip scattering and spin transport in magnetic multilayers. *Physical review letters*, 110(19):197201, 2013. doi: 10.1103/PhysRevLett.110.197201.

[98] K. Krieger, P. Elliott, T. Müller, N. Singh, J. K. Dewhurst, E. K. U. Gross, and S. Sharma. Ultrafast demagnetization in bulk versus thin films: an ab initio study. *Journal of physics. Condensed matter : an Institute of Physics journal*, 29(22):224001, 2017. doi: 10.1088/1361-648X/aa66f2.

[99] Sucheta Mondal, Yuxuan Lin, Debanjan Polley, Cong Su, Alex Zettl, Sayeef Salahuddin, and Jeffrey Bokor. Accelerated ultrafast magnetization dynamics at graphene/cogd interfaces. *ACS nano*, 16(6):9620–9630, 2022. doi: 10.1021/acsnano.2c02899.

[100] B. T. Lu, J. L. Luo, and Y. C. Lu. A mechanistic study on lead-induced passivity-degradation of nickel-based alloy. *Journal of The Electrochemical Society*, 154(8):C379, 2007. ISSN 00134651. doi: 10.1149/1.2741204.

[101] Shree Ram Acharya, Volodymyr Turkowski, G. P. Zhang, and Talat S. Rahman. Ultrafast electron correlations and memory effects at work: Femtosecond demagnetization in ni. *Physical review letters*, 125(1):017202, 2020. doi: 10.1103/PhysRevLett.125.017202. URL `http://arxiv.org/pdf/1911.01147v1`.

[102] S. Bonetti, M. C. Hoffmann, M-J Sher, Z. Chen, S-H Yang, M. G. Samant, S. S. P. Parkin, and H. A. Dürr. Thz-driven ultrafast spin-lattice scattering in amorphous metallic ferromagnets. *Physical review letters*, 117(8):087205, 2016. doi: 10.1103/PhysRevLett.117.087205.

[103] K. Carva, M. Battiato, and P. M. Oppeneer. Ab initio investigation of the elliott-yafet electron-phonon mechanism in laser-induced ultrafast demagnetization. *Physical review letters*, 107(20): 207201, 2011. doi: 10.1103/PhysRevLett.107.207201.

[104] Shree Ram Acharya, Volodymyr Turkowski, G. P. Zhang, and Talat S. Rahman. Ultrafast electron correlations and memory effects at work: Femtosecond demagnetization in ni. *Physical review letters*, 125(1):017202, 2020. doi: 10.1103/PhysRevLett.125.017202.

[105] *CLEO: Technical conference: 07-12 May 2023, the CLEO hub: 09-11 May 2023, San Jose McEnery Convention Center, San Jose, California, USA*. IEEE, Piscataway, NJ, 2023. ISBN 9781957171258. URL `https://ieeexplore.ieee.org/servlet/opac?punumber=10258511`.

[106] Mirko Cinchetti, V. Alek Dediu, and Luis E. Hueso. Activating the molecular spinterface. *Nature materials*, 16(5):507–515, 2017. doi: 10.1038/nmat4902.

[107] Renhao Dong, Zhitao Zhang, Diana C. Tranca, Shengqiang Zhou, Mingchao Wang, Peter Adler, Zhongquan Liao, Feng Liu, Yan Sun, Wujun Shi, Zhe Zhang, Ehrenfried Zschech, Stefan C. B. Mannsfeld, Claudia Felser, and Xinliang Feng. A coronene-based semiconducting two-dimensional metal-organic framework with ferromagnetic behavior. *Nature communications*, 9 (1):2637, 2018. doi: 10.1038/s41467-018-05141-4.

[108] Alberto Martín Santa Daría, Lola González-Sánchez, and Sandra Gómez. Coronene: a model for ultrafast dynamics in graphene nanoflakes and pahs. *Physical chemistry chemical physics : PCCP*, 26(1):174–184, 2023. doi: 10.1039/d3cp03656a.

[109] Takayuki Suzuki, Dan C. Sorescu, Kenneth D. Jordan, Jeremy Levy, and John T. Yates. The chemisorption of coronene on si(001)-2 x 1. *The Journal of chemical physics*, 124(5):054701, 2006. ISSN 0021-9606. doi: 10.1063/1.2161195.

[110] Davide Curcio, Luca Omiciuolo, Monica Pozzo, Paolo Lacovig, Silvano Lizzit, Naila Jabeen, Luca Petaccia, Dario Alfè, and Alessandro Baraldi. Molecular lifting, twisting, and curling during metal-assisted polycyclic hydrocarbon dehydrogenation. *Journal of the American Chemical Society*, 138(10):3395–3402, 2016. doi: 10.1021/jacs.5b12504.

[111] Benjamin Stadtmüller, Martin Willenbockel, Sonja Schröder, Christoph Kleimann, Eva M. Reinisch, Thomas Ules, Sergey Soubatch, Michael G. Ramsey, F. Stefan Tautz, and Christian Kumpf. Modification of the ptcda-ag bond by forming a heteromolecular bilayer film. *Physical Review B*, 91(15), 2015. ISSN 2469-9950. doi: 10.1103/PhysRevB.91.155433.

[112] Leonardo Spanu, Sandro Sorella, and Giulia Galli. Nature and strength of interlayer binding in graphite. *Physical review letters*, 103(19):196401, 2009. doi: 10.1103/PhysRevLett.103.196401.

[113] Xiaobin Chen, Fuyang Tian, Clas Persson, Wenhui Duan, and Nan-xian Chen. Interlayer interactions in graphites. *Scientific reports*, 3:3046, 2013. doi: 10.1038/srep03046.

[114] Christian Udhardt, Felix Otto, Tobias Huempfner, Bernd Schröter, Roman Forker, and Torsten Fritz. Pi-like band structure observed for coronene monolayers deposited on ag(111). *Journal of Electron Spectroscopy and Related Phenomena*, 227:40–43, 2018. ISSN 03682048. doi: 10.1016/j.elspec.2018.05.010.

[115] Hrvoje Petek and Susumu Ogawa. Surface femtochemistry: observation and quantum control of frustrated desorption of alkali atoms from noble metals. *Annual review of physical chemistry*, 53:507–531, 2002. ISSN 0066-426X. doi: 10.1146/annurev.physchem.53.090701.100226.

[116] A. Varykhalov, D. Marchenko, J. Sánchez-Barriga, M. R. Scholz, B. Verberck, B. Trauzettel, T. O. Wehling, C. Carbone, and O. Rader. Intact dirac cones at broken sublattice symmetry: Photoemission study of graphene on ni and co. *Physical Review X*, 2(4), 2012. doi: 10.1103/PhysRevX.2.041017.

[117] E. N. Voloshina, A. Generalov, M. Weser, S. Böttcher, K. Horn, and Yu S. Dedkov. Structural and electronic properties of the graphene/al/ni(111) intercalation system. *New Journal of Physics*, 13(11):113028, 2011. doi: 10.1088/1367-2630/13/11/113028.

[118] S. C. Veenstra, A. Heeres, G. Hadziioannou, G. A. Sawatzky, and H. T. Jonkman. On interface dipole layers between c 60 and ag or au. *Applied Physics A: Materials Science & Processing*, 75(6):661–666, 2002. ISSN 0947-8396. doi: 10.1007/s003390201311.

[119] Martin Aeschlimann, Tobias Brixner, Mirko Cinchetti, Martin Feidt, Norman Haag, Matthias Hensen, Bernhard Huber, Tristan Kenneweg, Jobynson Kollamana, Christian Kramer, Walter Pfeiffer, Stefano Ponzoni, Benjamin Stadtmüller, and Philip Thielen. Observation of optical coherence in a disordered metal-molecule interface by coherent optical two-dimensional photoelectron spectroscopy. *Physical Review B*, 105(20), 2022. ISSN 2469-9950. doi: 10.1103/PhysRevB.105.205415.

[120] Abhilash Ravikumar, Gregor Kladnik, Moritz Müller, Albano Cossaro, Gregor Bavdek, Laerte L. Patera, Daniel Sánchez-Portal, Latha Venkataraman, Alberto Morgante, Gian Paolo Brivio, Dean Cvetko, and Guido Fratesi. Tuning ultrafast electron injection dynamics at organic-graphene/metal interfaces. *Nanoscale*, 10(17):8014–8022, 2018. doi: 10.1039/c7nr08737c.

[121] André Neubauer. *DFT - Diskrete Fourier-Transformation.* Vieweg+Teubner Verlag, Wiesbaden, 2012. ISBN 978-3-8348-1996-3. doi: 10.1007/978-3-8348-1997-0.

[122] A. Avsar, J. Y. Tan, T. Taychatanapat, J. Balakrishnan, G. K. W. Koon, Y. Yeo, J. Lahiri, A. Carvalho, A. S. Rodin, E. C. T. O'Farrell, G. Eda, A. H. Castro Neto, and B. Özyilmaz. Spin-orbit proximity effect in graphene. *Nature Communications*, 5:4875, 2014. ISSN 2041-1723. doi: 10.1038/ncomms5875.

[123] G. P. Zhang and W. Hübner. Laser-induced ultrafast demagnetization in ferromagnetic metals. *Physical Review Letters*, 85(14):3025–3028, 2000. ISSN 0031-9007. doi: 10.1103/PhysRevLett.85.3025.

Fachbereich Physik

Rheinland-Pfälzische Technische
Universität Kaiserslautern Landau

Postfach 3049
67653 Kaiserslautern, Germany

www.physik.rptu.de/

Rheinland-Pfälzische
Technische Universität
Kaiserslautern
Landau